Small Molecule Adsorption in Layered Materials

Hasnain Sajid

Department of Chemistry and Forensic Sciences

A thesis submitted in partial fulfilment of the requirements of Nottingham Trent University for the degree of

Doctor of Philosophy

February 2023

Copyright Statement

Dedication

Dedicated to my beloved parents Muhammad Sajid and Nagina Shaheen for their endless love, motivation, and support. Your blessings and prayers helped me get through this arduous but rewarding journey.

Acknowledgments

In the name of Allah, whose kindness and guidance have put me through education and knowledge acquisition.

Since the COVID-19 pandemic hits, the scientific community has suffered the most serious anomalies. I have been blessed with leaders Dr. Matthew A. Addicoat, and Prof. Carole C. Perry who contributed significantly to making my PhD research journey a success story. I am grateful to them for their continued supervision, support, and kindness they offered during my research. I believe, my independent research skills have improved with their encouraged freedom of research. The insight and knowledge of the subject from my Director of Study; Dr Matthew A. Addicoat and continuous guidance and valuable suggestions of co-supervisor Prof. Carole C. Perry steered me through this research. I would also express my honest gratitude to Dr. Ian Shuttleworth whose thoughtful comments and recommendations as an independent assessor had a significant influence on steering research. I thank my former colleagues in the Addicoat Computational Research Group, Dr Dinga Wonanke and Dr Maryam Nurhuda whom I have always enjoyed their guidance.

Where I am today is because of my father Mr. Muhammad Sajid and mother Nagina Shaheen. I cannot express adequate gratitude for what you sacrificed for my success. Also, my appreciation goes to my siblings Muhammad Arsalan Sajid, Nimra Sajid, and Kinza Sajid, and my dearest fiancée Kashmala Noor Awan who have stood by me in hard situations.

I am grateful to Prof. Tariq Mahmood, Dr Khurshid Ayub for their assistance to pursue my studies. Their words that "*I would be an excellent researcher"* was enough to rise my horizons. Here, I would thank to my best friends Mr. Muhammad Sohaib, Miss Mishab Asif, Miss Ambreen, Hafiz Muhammad Faisal, and Amir Shahzad for being with me all the time and made me not feel isolated.

Lastly, I have been fortunate to be awarded a funded scholarship from NTU for my PhD study. I would not be able to achieve this goal in my academic life without NTU support.

Hasnain Sajid

February 2023

Abstract

This research mainly focuses on the computational modeling of 2D- Metal and Covalent Organic Frameworks using Quantum Mechanics, Monte-Carlo, hybrid QM/MM, and Molecular Dynamics simulations to investigate their gas adsorption, and thermal properties. In this work, the interlayer slipping effect and the nature of metals on gas adsorption in 2D-Phthalocyanine MOFs have been systematically studied. It is found that the binding strengths and adsorption capacities of MOFs are drastically increased upon shifting the top layers to the energetically stable offsets. For example, the NO adsorption capacity of the slipped-AA structure is approximately 0.69 times higher than the perfect stacked (eclipsed) geometry. The nature of metal (at nodal position) has a remarkable effect on the adsorption properties of eclipsed-AA structures, however, this effect is almost negligible in slipped-AA structures. For example, the NO adsorption capacity difference between Ni and Cu in eclipsed-AA is nearly 100 mg/g, however, it is reduced to 2 mg/g in slipped-AA structures (at 298 K and 75 bar).

The thermal conductivity (*k*) of **BBO** COFs over a wide range of temperatures (800-300 K) is investigated using Non-Equilibrium Molecular Dynamics simulations. The *k* values of **BBO-COFs** are as high as 0.326 W/mK at 300 K, depending on the size of the unit cell.

Hybrid QM/MM simulations for modeling bulk enzymes on 2D **TpAzo-COF** are systematically investigated, indicating the porous site of COF is an energetically suitable site for binding.

The 2D **TpSMe-DPP** COF to serve as a scaffold for mercury adsorption is demonstrated and found that the thioether and imine functional groups facilitate the soft metal binding.

Lastly, the transition state searches for the *bis*-imine and benzimidazole formations are demonstrated to synthesize the 1D-COFs with suitable SBUs. The COF formation with a small benzaldehyde unit is adequate, whereas, the complexity is increase upon increasing the size of SBUs.

Contents

Nomenclature

Acronyms

MOF	Metal Organic Framework
COF	Covalent Organic Framework
MPc	Metallo-Phthalocyanine
GCMC	Grand Canonical Monte-Carlo
MD	Molecular Dynamics
QM	Quantum Mechanics
MM	Molecular Mechanics
AMS	Amsterdam Modeling Suite
SCM	Software for Chemistry and Materials
DFTB	Density Functional Tight Binding
NEMD	Non-Equilibrium Molecular dynamics
LJ	Lennard Jones potential
BBO	BenzoBisoxazole

List of Figures

List of Table

Chapter 1

1 Introduction to Computational Techniques and Tools

This thesis aims to study the computational modeling of conductive 2D Metallo-phthalocyanine-based layered Metal-Organic Frameworks (MOFs) for their chemical sensitivity towards small gaseous molecules. Before proceeding to the main topic, the basic introduction about the computational modeling techniques and methods is explained in Chapter 1. Here, the basic concepts behind the computational methods including, electron-motion-based quantum mechanics and nuclear-position-based molecular mechanics are reviewed, followed by some tools (arranged in alphabetical order) for modeling chemical materials, their energies, thermodynamics, electronic properties, and their reactions. The chapter is finally concluded with general consideration including functionals and basis set selection for materials modeling. The computational approaches discussed here have all been used for investigations in this research. For example, the density functional theory approach is used to search for the transition state for the formation of bis-imine and benzimidazole-based COF products; the tight binding semiempirical approach is implemented to investigate the sensitivity of 2D MOFs; Grand Canonical Monte-Carlo simulations are employed to obtain adsorption isotherms of 2D MOFs; Molecular dynamics and hybrid QM/MM techniques are used to study the heat transport property and bulk biological molecule *i.e.*, enzyme adsorption on 2D Covalent Organic Frameworks (COFs), respectively.

1.1 Computational Modeling Techniques

Computational modeling is an effective approach to investigate the structural, mechanical, and electronic properties of materials using computer tools. Owing to exceptional advances in computer technology and algorithms, a range of computational techniques from Quantum Mechanics (QM) to Heuristic methods have widely been employed in investigating materials with different sizes from a few atoms through to bulk/periodic materials.[1] These techniques are as follows:

1) Quantum Mechanics (QM)

a) *Ab initio* methods either wavefunction-based or density functional-based methods

b) Semi-empirical methods

2) Molecular Mechanics (MM) or Molecular Dynamics (MD)
3) Hybrid QM/MM
4) Heuristic Methods or Monte-Carlo (MC)

1.1.1 Quantum Mechanics

QM methods obtain the accurate solution of the Schrödinger equation.

$$\widehat{H}\Psi = E\Psi \tag{1.1}$$

where *H* and *E* represent the Hamiltonian operator and energy, respectively, while Ψ indicates the wavefunction. The Schrödinger equation is a many-bond problem, the complexity of the solution of the electronic equation *via* computational simulations grows exceptionally with the number of electrons.[2] In QM methods, there are two widely used methods to solve the equation.

1.1.1.1 *Ab initio* Methods

Ab initio methods solve the electronic Schrödinger equation using rigorous mathematical approximations to obtain information about electron densities, their energies, and other related properties.[3] In *ab initio* methods, two approaches are widely used including wavefunction-based and density functional-based to model the electronic structures of materials.

1.1.1.1.1 Wavefunction Approach

These methods solve the time-independent Schrödinger equation based on the Born-Oppenheimer approximation. The Born-Oppenheimer approximation separates the motion of electrons from the nuclei. In 1928, Hartree *et al.*[4] presented an equation to calculate the motion of electrons, later refined by Fock *et al*,[5] based on the Pauli principle. A first *ab initio* method was developed using the Hartree-Fock equation to solve chemical problems of many-electron systems.

$$\Psi = \psi_1\psi_2\psi_3 \ldots \psi_n \tag{1.2}$$

Ψ_i indicates the wave function of orbitals (*i*). Later, it was found that the Hartree-Fock method was unable to account for the electron correlations because a subsequent term for the electrons with opposite spin, was not included in the equation. The Hartree-Fock equation was modified and a post-Hartree-Fock method *e.g.,* second-order Moller-Plesset (MP2) was developed. The MP2 method accurately accounts for the correlation between electrons, but this method was computationally more demanding *e.g.,* MP2 requires four times the CPU time of local DFT methods.[6] Moreover, MP2 is not accurate, especially in systems with van der Waal forces involved. The second well-known post-Hartree-Fock method called CCSD(T); is the Coupled Cluster method containing Single, Double, and perturbative Triple excitation along with the CBS; the complete basis set is a gold standard method in computational modeling because of higher accuracy in estimating electron correlation. On the other hand, the CCSD(T) method demands huge computer time and is suitable for small systems with about thirty to thirty-five atoms.[7] The wavefunction methods have widely been applied in modeling materials in organic (acetone, ethylene butane, & glycine),[8] inorganic complexes (*e.g.*, $ReH_5(PR_3)_2(SiR_3)_2$),[9] polymeric (furan & thiophene),[10] micro- (*e.g.*, N-Acetyl-Phenylalanyl-NH_2),[11] macro-, and biomolecules (nucleic acids base pairs).[12]

1.1.1.1.2 Density Functional Theory Approach

Density functional theory (DFT) is the most popular approach to determine the electronic (or nuclear) structure and total energy of a system based on electron density.[13] The electronic density depends on the three coordinates (*3N*) of the number of electrons (*N*) which escapes the problem of solving the complicated electronic wave equation. Due to this reason, DFT methods are more accurate and computationally effective as compared to wavefunction approaches.[13] In DFT simulations, the total energy of an electronic system is computed based on the Kohn-Sham equation,[14]

$$E_T[\rho] = T[\rho] + U[\rho] + E_{xc}[\rho] \tag{1.3}$$

where ρ, *T*, & *U* are the electron density, kinetic energy, and electrostatic energies of the system, while the E_{xc} represents the sum of exchange and correlation energies as a function of electron density.

$$E_{xc} = E_x + E_c \tag{1.4}$$

The accurate approximation of the E_{xc} term is essential in DFT functionals. In this context, a hierarchy of exchange-correlation in DFT functionals with computational demand and increasing accuracy has been described as "Jacob's Ladder" by John Perdew (**Figure 1.1**).[15]

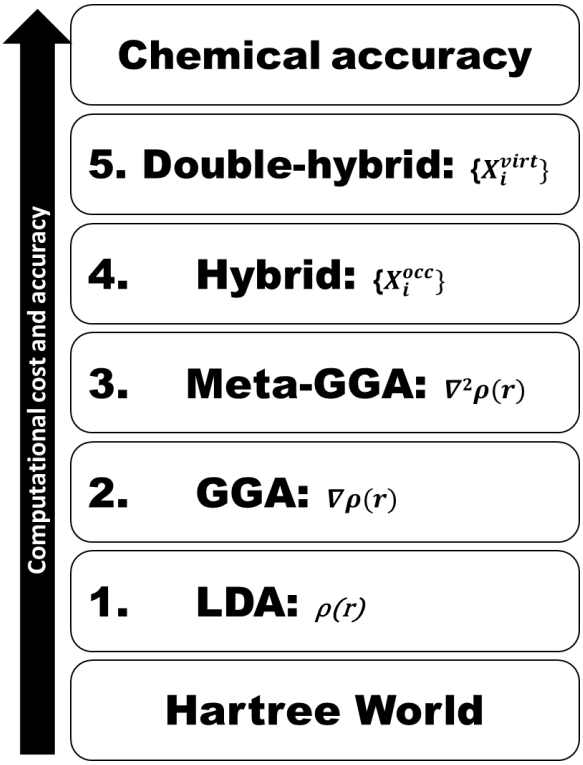

Figure 1.1. DFT functional categories based on Perdew's "Jacob's ladder", where, ρ = electron density, $\boldsymbol{\nabla}$ = local gradient, $\boldsymbol{\nabla^2}$ = higher-order local gradient, $\{\mathbf{X_i^{occ}}\}$ exact exchange with correlation, and $\{\mathbf{X_i^{virt}}\}$ partial exact correlation.[15]

The Local Density Approximation, simply called LDA, is the most popular and simplest approximation[16,] where E_{xc}/electron of a real/inhomogeneous system is acquired from the uniform electron gas of density (ρ) which is parametrized from the Monte-Carlo calculations.[17] The total LDA E_{xc} of a real (inhomogeneous) system can be written as;[18]

$$E_{xc}^{LDA}[\rho] = \int \rho \epsilon_{xc}^{unif}(\rho) d^3r \tag{1.5}$$

Since LDA solves the electronic structures of many bulk systems,[19] but usually overestimates the energies and is less reliable for determining trends in chemical binding.[20]

In the methods of the second rung of Jacob's Ladder, the electron density gradient ($\nabla\rho$) is introduced to model the inhomogeneity of the electron gas, and the resulting approach is known as the semi-local or generalized gradient approximation; in short GGA.[21]

$$E_{xc}^{GGA}[\rho] = \int f^{GGA}(\rho, \nabla\rho) d^3 r \tag{1.6}$$

f^{GGA}, exchange-correlation energy (E_{xc}) density per volume, is a function of electron density (ρ) and its first derivative ($\nabla\rho$) in the generalized gradient approximation.[22] The most popular GGA functionals are PBE, PW91, and BLYP.[23,24] These GGA functionals tend to improve structural total energy and energy barriers.[25] The high computer time, the inability of accounting for van der Waals interactions, and self-interaction errors (SIEs) are the major drawbacks of GGA functionals. SIEs represent the non-zero interactions of an electron with its own density, causing failures in accuracy in estimating dissociation energies and electronic properties such as band gaps.[26–28]

The third rung of Jacob's Ladder called meta-GGA introduces the higher order terms for electron gradient $\nabla^2\rho(r)$ with additional kinetic energy and extra degrees of freedom.[29] The meta-GGA functionals show improved performances in estimating structural energies[30–32] but the ability to determine electronic properties is still poor.[33]

The 4th generation DFT functionals in subsequent rungs add exact exchange terms from the Hartree-Fock methods and are known as hybrid GGA functionals.[34] Such functionals contain rigorous *ab initio* formula for E_{xc} known as the adiabatic connection.

$$E_{xc} = \int_0^1 U_{xc}^{\lambda}\, d\lambda \tag{1.7}$$

Herein, the E_{xc} connects the non-interacting reference systems (λ = 0) with a fully interacting real system (λ = 1). The formula refers to the potential energy explicitly, however, integrates over λ, which generates the kinetic energy part.

The hybrid functionals provide high accuracy to all properties of electronic or molecular systems. The B3LYP is the most popular hybrid functional but fails to account for the exact atomization energies of the metallic and semiconductor systems[35] due to the inaccuracy of the correlation part in the homogeneous electron gas limit.[36] However, some hybrid functionals *e.g.,* HSE0[37] and PBE0[38] have typically been employed to estimate lattice parameters and electronic gaps in insulating and semiconducting materials.[36] In addition, hybrid functionals are well suited for rare-earth metals and transition metal oxides in describing their insulating antiferromagnetic properties.[45] Owing to the calculation of additional HF terms in hybrid functionals, their computational cost is high compared to the GGA functionals. One of the best hybrid-DFT functionals; BL3YP, along with the Grimme dispersion (D3) has been used in this study for the calculation of the activation barrier and transition states for the formation of bis-imine and imidazole products from the reaction of a diamine with aldehydes (*e.g.*, benzaldehyde or tetraldehyde) in the presence of acetic acid catalysts (see **Chapter 8** for further detail).

The last rung of Jacob's Ladder is double hybrid functionals, that mix local Hartree-Fock with semi-local exchanges and MP2 and semi-local correlations.[39]

$$E_{xc}^{\lambda_{DH}} = \lambda_x E_x^{HF} + (1-\lambda_x)E_x[\rho] + (1-\lambda_c)E_c[\rho] + \lambda_c E_c^{MP2} \qquad (1.8)$$

Where the $\lambda_c E_c^{MP2}$ term is estimated with Kohn-Sham orbitals while the remaining terms are estimated with self-consistent hybrid functionals. In double hybrid functionals, the nonlocal both exchange and correlations terms with the orbital dependent correlation term improve the description of short-range van der Waals (hydrogen bonding) and long-range London dispersion forces.[40] Numerous studies in the literature report the higher accuracy of double-hybrid DFT functionals in determining the structural energies and electronic parameters.[41–44] In the Jacob's Ladder of DFT, every rung has some strengths and weaknesses with the surge in computational cost, but each step introduces improvements to yield better results.

1.1.1.2 Semiempirical Method

Since the beginning of computational studies, there has been a continuous struggle to design or develop a quantum chemical method that has the ability to treat large and periodic materials with high accuracy in a short time frame. In this regard, introducing empirical corrections, either derived from high-level calculations or experimental data to the Hartree-Fock methods as semiempirical parameters is the most popular approach. The frequently used semiempirical methods including PM3, PM6, AM1, and MNDO are based on the NDDO[(1)] (Neglect of diatomic differential overlap) integral approximation.[45]

The tight binding approach is also a semiempirical approach in which the wavefunction of an electronic system is built as a superposition of isolated atomic wavefunctions located at the corresponding atomic nucleus. The tight binding models have been applied to a wide variety of materials from small to large periodic systems with superior accuracy than that of DFT methods.[46,47] This tight binding approach has been generalized and led to the design and development of electronic density-based density functional methods e.g., DFTB. An improved DFTB method *via* incorporation of self-consistent redistribution of Mulliken charge density has also been developed called SCC-DFTB.[48] DFTB is parametrized with precomputed interactions of element pairs, thus it is ca. 2 orders of magnitude faster than conventional DFT.[49] However, similarly to force fields, the lack of availability of parameters, especially for transition metals, where parameters are required for both element pairs and description of spin-polarization,[50] has limited their applicability to MOFs.[51] To overcome the problem of the non-generality of DFTB, extended tight-binding (xTB) methods have been developed.

A special purpose extended tight binding variant has been proposed by Grimme *et al*.,[52,53] which results in a novel semiempirical method called GFN1-xTB. The GFN represents the semiempirical approach to optimize accurate structural geometries, infrared frequency, and noncovalent forces, whereas *x* attributes the extension of atomic orbitals basis set. In this extended semiempirical approach, the resulting total

[1] NDDO approximation: "adds all two centre integrals for the repulsion between a charge distribution on one centre and a charge distribution on another centre"

energy is the sum of electronic attractions (E_e), repulsions (E_r), dispersions (E_d), and halogen-bonds (E_{XB}) energies.

$$E = E_e + E_r + E_d + E_{XB} \tag{1.9}$$

These semiempirical methods have been employed to simulate large periodic molecules, especially metal-organic frameworks (MOF), and the resulting mean average deviations of structural parameters of porous materials[54,55] from the experimental values were comparable to the high-level DFT methods.[56–58] The parametrization of GFN-xTB covers s/p/d-block elements up to atomic number 86 which makes it applicable to a wide range of metallic elements including some lanthanide and actinide elements.[53]

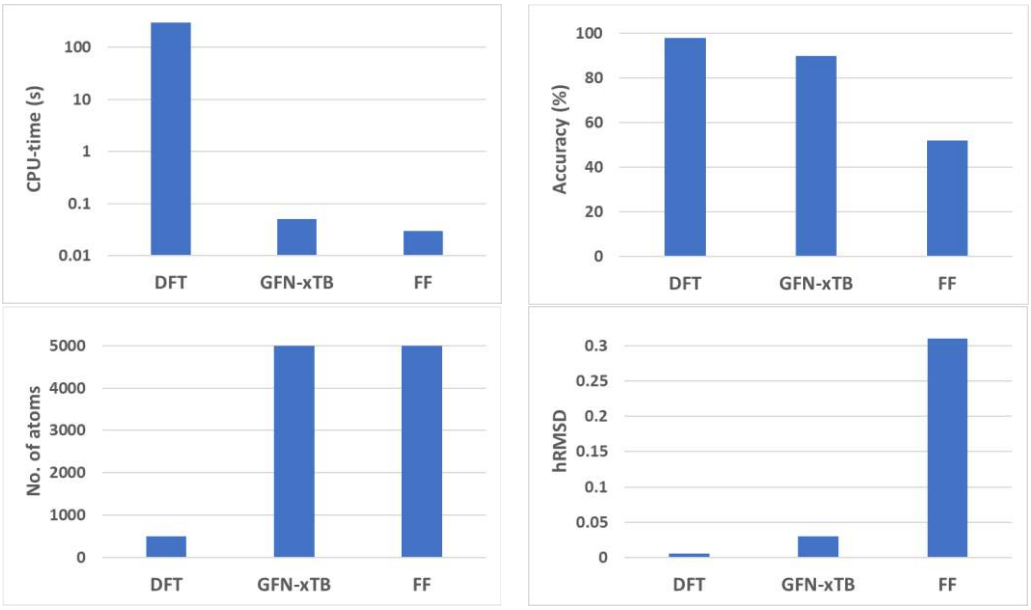

Figure 1.2. GFN-xTB performance for geometry optimization of MOFs compared with DFT and force field methods based on Ref[59–61] where the CPU-time and percentage accuracy are compared between the TPSSh/TZ DFT, GFN1-xTB and UFF given in Ref.[60] while hRMSD values are the average of results presented by Grimme *et al.*[59]

Grimme and co-workers attempted to explore the accuracy of GFN methods in mapping transition metal[56,59] and lanthanide[61] containing MOF structures by comparing the results with high DFT level (PBE0-D4/def2-TZVP) and force field

methods. The GFN$_n$-xTB methods not only performed well (with hRMSD[(2)62] less than 0.5 Å) for full geometry optimization of medium (309 atoms) to large (2784 atoms) non-periodic MOF units but also 6-8 times faster (CPU time per optimization cycle less than 10^2 s) than high-level DFT optimizations. The comparative performance of GFN-xTB with DFT and force field in terms of computational or CPU-time (s), percentage accuracy, number of atoms, and heavy atoms root mean square deviation is graphically represented in **Figure 1.2**. GFN-xTB has great potential to rationalize the structure-property relationships of porous materials, including MOFs, COFs, ZIFs[(3)], and PPNs[(4)]. The xTB program as implemented by the Grimme group [https://github.com/grimme-lab/xtb/], has recently been extended to include periodic optimization. Direct calculation of periodic systems is also available *via* the GFN1-xTB method implemented in Amsterdam Density Functional (AMS) software developed by Software for Chemistry and Materials (SCM)[63] and the implementation in DFTB+.[64] The research of this thesis; the adsorption of small gas molecules on the layer 2D MOFs, is mainly based on GFN1-xTB method. The theoretical background and importance of using GFN1-xTB for this research is discussed in Chapter 3.

1.1.2 Molecular Mechanics (MM) and Molecular Dynamics (MD)

Molecular mechanics (or so-called "empirical force field") is a non-quantum mechanical method that uses classical mechanics for computing geometrical structures and their energies.[65] The total energy (E) of a molecule, a collection of atoms bound together *via* elastic or harmonic forces, in a force field method can be described by position (potential energy) functions of geometric features *i.e.*, bond length, angles, and nonbonding interactions, *etc*.[66]

$$E = E_{stretch} + E_{bend} + E_{tors} + E_{nonbond} + \cdots \qquad (1.10)$$

E is the total "steric" energy, which is the difference between the energy of real and hypothetical molecules. $E_{stretch}$ is the energy of a bond between atoms being compressed and stretched form from its equilibrium stage, E_{bend} is the energy of an

[2] hRMSD, heavy atoms (all elements except hydrogen) root-mean-square deviation, is a matric often used to compare molecular geometries produced from different methods.
[3] ZIFs: Zeolite Imidazolate Frameworks
[4] Porous Polymer Networks

angle in bending position from its natural value, E_{tors} is the torsional energy because of twisting of a bond, $E_{nonbond}$ is the energy of non-bonding interactions. In the case of other intramolecular mechanisms that affect the total energy including columbic/electrostatic or hydrogen bonding, these terms may also be added to the equation of a particular force field.

Unlike quantum mechanics, molecular dynamic (MD) simulations account for the nuclear motion and quantify the associated chemical, physical and thermodynamic properties. Similar to MM, MD is based on the law of classical mechanics such as Newton's laws to examine the time-dependent dynamics of molecular systems.[7]

$$F_i = m_i \frac{d^2}{dt^2} r_i(t), \qquad i = 1,2, \dots, n \tag{1.11}$$

Where *F* is the forces acting on atoms (*i*) with position (*r*) and mass (*m*) can be examined at the time (*t*). In classical molecular dynamics, the force (*F*) acting on atoms (*i*) is enumerated as the negative potential energy gradient with respect to the position of atoms.

$$F_i = -\nabla_i E(r_1, r_2, \dots, r_n) \tag{1.12}$$

Classical molecular dynamics uses potential energy surface (PES) as the predefined potentials based on the empirical force field parametrization which is independent of electronic structure calculations. If the electronic structures or energies are considered during MD simulations, the run is called *ab initio* MD or simply (AIMD).[67]

In MD calculations, once the force acting on atoms is known, the velocities and new positions at any time ($t + \delta t$) are obtained by numerically solving equations. δt indicates the time steps provided in the MD input, appropriate time steps are highly desirable in order to achieve an exact equilibrium state. Typically, the appropriate time steps for an MD run are between 1 and 2 fs, the chance of instability in a system may increase with larger time steps because of the growing inaccuracy in the integration procedure. The MD simulations with Universal Force Field (UFF) have been applied for computing the phonon-based thermal transport properties of layered 2D COFs in this research. One may refer to Chapter 5 for a detailed discussion.

1.1.2.1 Force Fields

Potential energy computation to demonstrate the interaction between atoms is a crucial part of molecular dynamic simulations. A set of specific parameters named force fields are incorporated into the algorithms. A specific force field can be developed by high-level quantum mechanics with experimental parametrizations. Many force fields, including AMBER,[76] CHARMM,[68] CoMPASS,[69] MM2,[70] MM3,[71] and UFF,[72] are well-known to produce reliable energies. Most of these produce comparable results with a slight variation to define potential energy, however, it is essential to choose an appropriate force field.

In the force field algorithm, the total energy is expressed as a sum of different components including, the energy of bonded atoms ($E_{valance}$), the energy of nonbonded atoms ($E_{nonbond}$), and energy of cross-term ($E_{crossterm}$).[73]

$$E_{total} = E_{valence} + E_{nonbond} + E_{crossterm} \tag{1.13}$$

The $E_{nonbond}$ term further includes the energies of van der Waals forces (E_{vdw}), Columbic electrostatic forces (E_{elec}), and hydrogen bond (E_{HB}).

$$E_{nonbond} = E_{vdW} + E_{elec} + E_{HB} \tag{1.14}$$

The $E_{valance}$ is the sum of the energy components including bonds stretching (E_{bond}), angles bending (E_{angle}), dihedral angles torsion (E_{tors}), out-of-plane interactions (E_{oop}), and interactions between atoms of common linkage namely the Urey-Bradley term (E_{UB}).

$$E_{valence} = E_{bond} + E_{angle} + E_{tors} + E_{oop} + E_{UB} \tag{1.15}$$

The $E_{crossterm}$ is the collection of bonds and angles energies affected by their surrounding atoms.

$$E_{crossterm} = E_{bond-bond} + E_{angle-angle} + E_{bond-angle} + E_{end-bond-torsion} + E_{middle-bond-torsion} + E_{angle-torsion} + E_{angle-angle-torsion} \tag{1.16}$$

By taking advantage of empirical force field methods, MD calculations use specific techniques *i.e.*, NVT[5], NVE[6] and NPT[7] to estimate the thermodynamic properties. In these MD calculations, control over the pressure and temperature is typically achieved by augmenting the system with additional (dynamical) variables to create a barostat and a thermostat, respectively.[74] Since molecular dynamics are of wide interest for thermodynamic properties, it has certain limitations including a considerable amount of time required because these simulations consider the movement of each atom at all instants of time. On the contrary, the time required for Monte-Carlo simulations is considerably less because such calculations focus only on the final configurations.

1.1.3 Hybrid QM/MM

Computational modeling of bulk biological molecules *e.g.,* DNA, RNA, *etc* are commonly based on two standard approaches; MD and QM. In MD simulations the link between bio-molecular structures and their energies at atomistic levels are described by classically or empirically derived force fields.[75] The outcomes of MD simulations are critically dependent on the quality of experimentally or high-level QM-derived potentials. However, the formation and breaking of chemical bonds as well as the electronic properties consideration are not possible *via* classical MD simulations.[76] On the other hand, QM methods are readily available for modeling the electronic structures of molecules. Unfortunately, QM-based simulations with higher accuracy especially for bulk biomolecules are time-demanding. The only solution to such limitations is the use of hybrid QM/MM; quantum mechanics/molecular mechanics methods. In the hybrid QM/MM method, the studied system is partitioned into two or more regions (**Figure 1.3A**). Typically, a QM region where a specific process is taking place, consisting of a small number of atoms, is treated with a highly accurate QM method, while an MM region with supported atoms that are not participating in the process, is treated with computationally cheap MD methods.[77]

[5] constant number of atoms, volume, and temperature

[6] constant number, volume, and energy

[7] isothermal-isobaric system

The QM/MM hybrid method can be classified into two distinct approaches,[78,79] additive[80] and subtractive.[81] In the additive approach, the total potential energy is calculated using the expression given in equation 1.17.[82]

$$E_{tot}^{add} = E_{QM} + E_{MM} + E_{QM/MM} \tag{1.17}$$

The total energy (E_{tot}^{add}) of a QM/MM implemented system is the integral sum of energy of the QM region, computed at a high-level *ab initio* method, E_{QM}, the energy of MM region, E_{MM}, computed at a cheap force field and the interaction energy between both QM and MM region ($E_{QM/MM}$) (refer to **Figure 1.3C**).

The subtractive approach also called as IMOMM "integrated molecular-orbital molecular mechanics",[83,84] but commonly known as ONIOM, abbreviated from, "Our own N-layered Integrated Molecular Orbital + Molecular Mechanics".[85] This approach computes the total energy as follows; (**Figure 1.3B**)

$$E_{tot}^{sub} = E_{whole}^{MM} + E_{region}^{QM} - E_{QM-region}^{MM} \tag{1.18}$$

In the subtractive approach, the total energy of a system is computed as; the collective sum of a MM energy of the whole system (E_{whole}^{MM}) and a QM energy of QM region (E_{region}^{QM}) is subtracted from the MM energy of QM region ($E_{QM-region}^{MM}$). Both the subtractive and additive approaches of QM/MM are in principle equivalent and differ only in their implementation. The subtractive approach is relatively easy and straightforward because it does not account for communication between QM and MM regions. However, a major drawback of this method is that a specific force field is required for the QM sub-region, which may not always be available.

The former approach has a major advantage over the latter because in this case all interactions between sub-regions are handled explicitly, $E_{QM/MM}$ at the force field level. The chemical bonds and angles between the atoms of MM and QM regions, one from each region for bond and one QM and two MM atoms for angle, are modelled via harmonic potentials (E^{bond} and E^{angle}, respectively). The torsion involving two atoms from both the sub-regions are modelled with periodic potential function, $E^{torsion}$. Noncovalent interactions including, van der Waals and electrostatic between the atoms of both regions, separated by two or more atoms, are modelled via the force fields Lennard-Jones potential and the Coulomb potential (E^{Coul}), respectively. The

evaluation of the QM wave-function requires extreme care for the chemically bonded atoms of the QM and MM regions because QM/MM boundary creates unpaired electron QM region, however, these unpaired electrons are paired in (bonding) orbitals with the electrons of the MM region. A link atom approach has been proposed to remedy such open valances, where a monovalent link atom is introduced *i.e.*, hydrogen atoms or methyl groups, at the appropriate positions along the bond vector in between the MM and QM atoms. The additionally linked atoms are only presented in the QM region and invisible to the MM region. In a Springer book, entitled; "Biomolecular simulations: methods and protocols" a chapter titled "Introduction to QM/MM Simulations" by Gerrit Groenhof[86] describes the QM/MM methodology in detail.

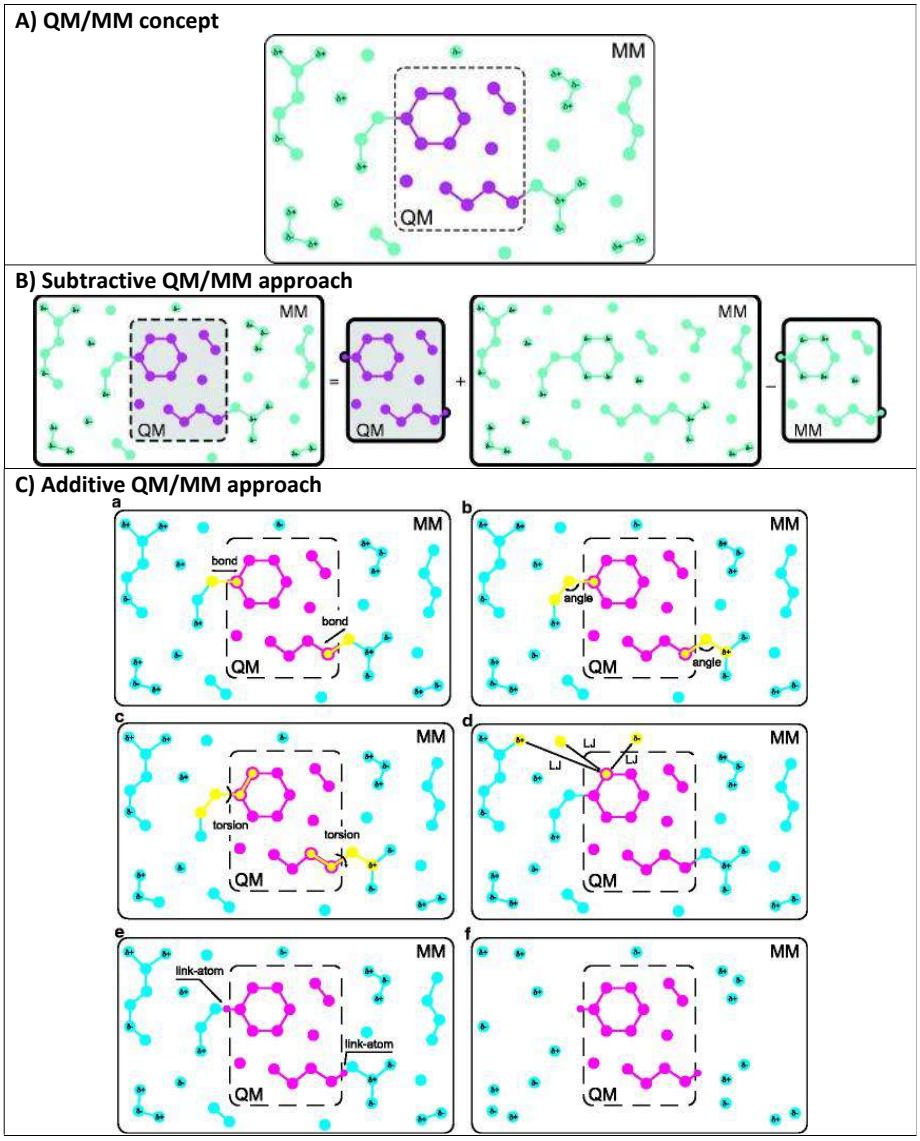

Figure 1.3. A) Illustration of the QM/MM concept: A small region in the dotted boundary represents the region where the process is taking place and modelled with a

high-level of the QM method. The remaining area is treated with the computationally 'cheap' MM method. B) Subtractive QM/MM approach: the total QM/MM energy (left hand side of the expression B) is equal to the energy of the small region, evaluated by the QM method, plus the MM energy of the whole system, minus the MM level evaluated energy of the bare QM region. C) Additive QM/MM approach: coupling between the MM and QM sub-regions. Panels (a–c) illustrate the bonded interactions between MM and QM atoms. Such interactions are treated at the force field level. d) the van der Waals interactions between the three MM atoms and one atom in the QM region, modelled by the Lennard-Jones potential. e) Link atom concept: the linked atom caps the QM region and is only present in the QM calculation. f) the electrostatic embedding approach illustrates the electrostatic QM/MM interactions, where the charged MM atoms enter the electron Hamiltonian of the QM region. In the mechanical embedding, partial MM charges are assigned to the QM atoms and the electrostatic interactions are computed by the pairwise Coulomb potential. Reprinted from Groenhof *et al.*,[86] with permission from Springer Nature.

Due to the advantages *i.e.*, effectiveness and fast processing over MD and QM, respectively, the QM/MM hybrid approach is often used for modeling bulk biological molecules that are difficult or even impossible with high level DFT approaches. This approach has been used in one of the studies presented in the thesis, in which interaction energies and the interaction site of three bulk enzyme molecules (with more than 10,000 atoms each) on a layered COF adsorbent was performed. The detail of this research is discussed in Chapter 6.

1.1.4 Heuristic Methods or Monte-Carlo (MC) Approaches

Monte-Carlo methods compute the desired properties from the equilibrium configuration that is obtained by varying the position and orientation of specific atoms. In MC simulations, the new configuration is obtained for the *N* number of particles by systematically changing the initial positions (*i*) of selected atoms. Subsequently, the Hamiltonian for the new configuration (*j*) is obtained. The change in Hamiltonian (ΔH) is computed by subtracting the generated Hamiltonian at the new configuration (H_j) from the initial position (H_i);[87]

$$\Delta H = H_j - H_i \tag{1.19}$$

The negligible ΔH (ΔH < 0) refers to the acceptable change in positions and the structure is brought to the low energy state and subsequently starts the shifting of atoms to new positions. On the other hand, if $\Delta H \geq 0$, the change is accepted based on the following rules of probability (ξ);[88]

$$\xi \leq exp\left(-\frac{\Delta H}{k_B T}\right), \quad \text{the move is accepted} \tag{1.20}$$

$$\xi > \exp\left(-\frac{\Delta H}{k_B T}\right), \quad \text{the move is rejected} \tag{1.21}$$

On the rejection of the new configuration, the change is resumed, and the new configuration is studied by changing the position of some other atoms.

In Grand Canonical (μTV) Monte-Carlo (GCMC) simulations, the terms including chemical potential; μ, volume; *V*, and temperature *T* are kept constant, while pressure; *P*, and molecules: *N* are allowed to vary. During these simulations, a new configuration (*j*) is proposed by changing the composition of atoms, and the probability of acceptance is associated with the deviation in energy (ΔU), which is given as;

$$p_{i\to j} \propto \left(-\frac{\Delta U}{k_B T}\right) \tag{1.22}$$

During GCMC calculations, the van der Waals interactions are described *via* a Lennard-Jones potential model,[89] which illustrates the noncovalent interaction energies between atoms (*i* and *j*) as;

$$U_{LJ}(r_{ij}) = 4\varepsilon_{ij}\left[\left(\frac{\sigma_{ij}}{r_{ij}}\right)^{12} - \left(\frac{\sigma_{ij}}{r_{ij}}\right)^{6}\right] \tag{1.23}$$

where r_{ij} indicates the separation between two nonbonded atoms while σ_{ij} and ε_{ij} are the L-J parameters and the depth of the potential well for van der Waals radius. These parameters are specific for specific atoms and can be calculated using ab initio calculations or taken from the literature.[90]

The electrostatic interactions are expressed *via* a Coulomb potential that can be described as;[91]

$$U_{elec}(r_{ij}) = \frac{1}{4\pi\varepsilon_r\varepsilon_o}\frac{q_i q_j}{r_{ij}} \tag{1.24}$$

In the expression, the ε_r represents the permittivity of charged atoms (q_j and q_i), ε_o indicates the relative permittivity of vacuum ($83.85 \times 10^{-12}\ C^2s^2/kgm^3$).

The MC method is widely used for examining properties at equilibrium *i.e.*, free energies and phase equilibria, *etc*. A detailed discussion of the properties computed via GCMC simulations can be found in Chapter 4. The GCMC approach is one of the principal methods used in this PhD research and was used to study the adsorption capacities/isotherms of 2D layered MOFs for the adsorption of small gas molecules.

1.2 Introduction to the Computational Tools/Software

Computational tools in computational chemistry are software packages that are used to simulate the desired properties of electronic or molecular systems. Most of the tools can perform all the above-mentioned methods. It is important to specify the method because different methods generate different results based on their algorithms. These computational tools include commercial as well as open-source packages. Some of the most familiar software packages in computational chemistry are described here:

1.2.1 Amsterdam Modeling Suite (AMS)

Amsterdam Modeling Suite (AMS) formerly named Amsterdam Density Functional (ADF) is a powerful computational package that simulates properties using all types of computational methods.[92] AMS was primarily developed in the 1970s by *Prof.* E. J. Baerends (Vrije University in Amsterdam), T. Ziegler (University of Calgary), and Snijders (University of Groningen).[93,94] Since 1995, a company named Software for Chemistry and Materials (SCM) is contributing to developing the AMS software. The detailed documentation, including user manual, licensing, and distribution information can be found on the SCM website http://www.scm.com. Since the 90s, AMS has evolved as a state-of-the-art software package for quantum chemical research in industries as well as academia.[95] The AMS package allows *ab initio* and semiempirical calculations for structural optimization, ground/excited state energies, harmonic/vibrational frequencies, and other properties i.e., NMR spin coupling, *etc*.[63] Over a decade, the AMS abilities have substantially expanded to semi-empirical MOPAC methods, Quantum ESPRESSO plane-wave code, a density-functional based tight-binding (DFTB) module, a reactive force field module ReaxFF, and python

library for automating molecular simulations (PLAMS), etc. AMS is highly recommended for ease of use and a wide variety of treatments for chemical problems. Since 2018, the AMS software can handle all types of jobs including structural optimization, and electronic and thermodynamic properties, using the different "engines", for example, ADF performs *ab initio* simulations for molecular systems, DFTB performs semi-extended tight-binding empirical simulations, BAND performs both *ab initio* and semiempirical calculations for geometry optimizations as well as the electronic properties calculations of both molecular and periodic systems, MOPAC for semiempirical calculations, Force Field and ReaxFF for MD and GCMC calculations, and Hybrid engine for combined MM/QM calculations. SCM-AMS is the main research tool in the Addicoat research group, and is used to investigate different types of simulations *i.e.*, QM, MD, MM, QM/MM hybrid, *etc* for both periodic and molecular systems. SCM-AMS offers different engines such as ADF, BAND, DFTB, Force field, hybrid, and many others for QM calculations for molecular systems, QM plus electronic properties for periodic materials, tight-binding for both types of systems, MD & MC studies, QM/MM for bulk molecules, respectively. Furthermore, it provides opportunity to investigate other properties using external interfaces including CP2K, Crystal, DFTB+, MOPAC, ORCA and RASPA, *etc* within the AMS domain *via* PLAMS functionality. Herein, SCM-AMS is used for all the research investigations presented in this thesis.

1.2.2 CP2K

CP2K[96] is an open-source computational program to perform atomistic calculations to simulate the electronic structure and molecular dynamic properties of bulk/periodic solids, liquids, gases, and biological systems. CP2K provides a wide range of simulations including, DFT calculations through LDA, GGA, and MP2, *etc*, semi-empirical *via* AM1, PM3/6, and MNDO, tight-binding, and hybrid MM/QM. CP2K can also simulate Classical as well as *ab initio* molecular dynamics, Monte-Carlo, frequency calculations, energies minimization, spectroscopy, and transition state search using the Nudged-elastic band (NEB) method. A review article has recently been published by T. D. Kühne and co-workers that describes the efficiency of the CP2K package.[97]

1.2.3 Crystal

CRYSTAL[98] is a quantum tool that was initially developed in the 70's by the theoreticians from the Theoretical Chemistry Group in Torino (Italy), and the Computational Materials Science group, (England). CRYSTAL software is suitable for the atomistic characterization of nonperiodic molecules and periodic crystals using first-principles calculations.[99] Various updates for CRYSTAL have been released in 1988, 1992, 1995, 1998, 2003, 2006, 2009, 2014, and 2017. The early versions permit the evaluation of energies on the basis of periodicity,[100] geometric stability,[101] and magnetic states.[102] In the later versions, the computation of frequencies, IR, and Raman properties have been updated.[103] Moreover, the CRYSTAL-2014 release contains improve algorithms for simulating tensor properties, anisotropic displacements parameters, and phono dispersion.[104] The last update in CRYSTAL-2017 has updated algorithms for electronic transport properties including, thermal conductivity.[103]

1.2.4 Cambridge Serial Total Energy Package (CASTEP)

The CASTEP[105] is fully featured with *ab initio* quantum mechanics to enumerate the electronic properties of inorganic crystals, organic molecules, and liquids as well as amorphous materials. In detail, CASTEP is capable of simulating:[106]

- Total energies, stress, or elastic properties.
- Electronic properties including, charge densities, total and partial density of states, frontier molecular orbital energies, electronic band structure, molecular electrostatic potential, Mulliken charge analysis, and absorption properties.
- Geometry optimization of both periodic and molecular systems
- MD simulations at various conditions i.e., NVE, NVT, NPT, etc.
- Transition state search for organic reactions.
- Thermodynamic properties including Gibbs free energy, enthalpy, entropy, heat capacity, etc.
- Nonlinear electric responses *i.e.*, polarizabilities and dielectric constants.

1.2.5 DMol^3

DMol^3 is a first-principles quantum chemistry software,[107] implements DFT-based *ab initio* methods together with a numerical radial basis set to simulate the electronic structure and energy of molecular, periodic systems. Furthermore, it can include either 3D periodicity as well as gas phase boundary conditions for lower-dimensional periodic systems. DMol^3 has been widely used for geometric optimization and transition state search through LST/QST techniques. DMol^3 is also one of the first computational tools that perform the COSMO (conductor-like screening model) of solvated molecules.[108] DMOl^3 is only a commercially available package, which can be accessed *via* two separate licenses including DMol^3 Molecular and DMol^3 Solid State.[109]

1.2.6 Gaussian

Gaussian is a general-purpose computational software and was initially developed by Sir John A. Pople[110] in 1970. The first released version was Gaussian70. Since, it is continuously updating. The latest release Gaussian is Gaussian16, which offers applications in predicting total energies with molecular structures and their vibrational electronic, excited states, linear and nonlinear properties using a variety of methods including molecular mechanics, wavefunction-based and density functionals-based *ab initio,* and semiempirical methods.

1.2.7 ORCA

ORCA is a quantum chemical package that features all the electronic structure methods including DFT, semi-empirical methods, multireference correlation methods, and classical molecular dynamics calculations.[111] The main features of ORCA are to simulate optimization, frequency, absorption property, and thermodynamics calculations. Recently, the *ab initio* molecular dynamic (AIMD) module is introduced in ORCA's latest release.[116]

1.2.8 Quantum ESPRESSO

The acronym ESPRESSO is "*opEn Source Package for Research in Electronic Structure, Simulation, and Optimization*".[112] Quantum ESPRESSO is a freely

available software. Quantum ESPRESSO is a suite of codes for modeling and *ab initio* electronic-structure calculations using density functional theory, density functional-perturbation theory, plane-wave pseudopotentials, and projector augmented-wave methods. It is capable of computing ground state energies, structural optimization, *ab initio* MD (AIMD), transition states optimizations, frequency calculations, nuclear magnetic and electronic paramagnetic resonance.

1.2.9 VASP

Vienna Ab initio Simulation Package (VASP) is a plane-wave algorithm, which uses the DFT approach to perform energy calculations and structural optimizations of molecular and periodic systems. VASP's applications in structural stability, mechanical, dynamic, semiconducting properties, chemical reactions, and catalysis are reviewed by Hafner *et al*.[33]

1.2.10 SIESTA

Spanish Initiative for Electronic Simulations with Thousands of Atoms (SIESTA) is a general-purpose program to perform mainstream DFT including LDA & GGA and AIMD simulations for geometry optimization, energy calculations, electronic density of state, and band structures analysis.[113] SIESTA is a freely available software for the research community (http://www.uam.es/siesta).

1.2.11 Computational Visual Software

In computational chemistry, efficient computer programs to build molecular structures and visualize the results are required. The field of molecular designing is dominated by freely available software. Among them, the more well-known visualization software/s are BALLView,[114] GaussView,[115] Jmol,[116] PyMOL,[117] QuteMol,[118] RasMol,[119] VESTA,[120] VMD,[121] and XCrySDen.[122] Many of them work on common operating systems like Microsoft Windows and Linux. The choice of visualization software/s capable of designing structures in three dimensions is limited. These include ChemBio3D,[123] GaussView,[115] HyperChem,[124] Materials Studio,[125] and Avogadro.[126] Many of these packages are commercially available. They are, however, not available for all operating systems, most of them only run-on Microsoft Windows.

1.3 General Consideration in Material Modeling

Computational chemists seek to model molecular/crystal structures, dynamics, and thermodynamic properties of materials using atomistic scale description.[127] Since the materials vary widely in size or length, and the observable processes can differ significantly in their time scales, different levels of algorithms are used with different computational methodologies. This may include either explicitly treating the electrons via quantum chemical approaches or treating groups of atoms as a single unit using classical approaches. However, the aim of computational modeling, in all cases, is the same; to model the macroscopic properties of materials and their interactions under external (experimental) stimuli.

1.3.1 Functional Selection

Methods of evaluating structures, energies, and electronic states with the physicochemical properties of materials with higher accuracy can use complex quantum chemistry methods, especially density function-based methods. In the quantum chemical DFT approach, a reliable approximation for the exchange and correlation energies, simply referred to as a functional, is required for the exact solution of the Kohn-Sham equations. Various approaches (*vide supra*), including LDA, GGA, metal GGA, and hybrid and double hybrid functionals are designed for treating E_{xc} (exchange-correlation energies) to predict the hypothetical structures of new materials. In DFT calculations, the approximations of E_{xc} are the main cause of accuracy or inaccuracy!.

The simplest DFT calculation on structures is “static” including single-point energy calculations, molecular energy minimization, vibrational frequency modes, and so on to compute the local features of the energy landscape. The DFT-based methodology is effective in materials especially porous materials (zeolites and MOFs) as compared to wavefunction-based methods. The DFT functionals are further categorized in Perdew’s “Jacob’s ladder” according to increasing accuracy, described in section 1.1.1.2. Even though DFT is categorized on the basis of a fundamental theoretical algorithm factors, such as accuracy is being improved in higher rungs, the performance between functionals of the same rung can vary considerably.[128] Comprehensive benchmarks are required to access the performance of different functionals for the

desired properties. Moreover, Perdew's functional categorization allows the estimation of some systematic errors. Perhaps, the most important distinction is made on the basis of nonlocal/exact exchange, also termed Hartree-Fock exchange. The LDA, GGA, and meta-GGA are called local/semi-local functionals because these do not include Hartree-Fock exchange, while hybrid and double-hybrid DFT functionals include the exact exchange.

Moreover, the self-interaction error (SIE)[129] plus missing long-range correlation effects,[130] specifically required in noncovalent interactions are the two critical errors in DFT approximations. The SIE is traditionally viewed in the one-electron system and can be defined as the self-interaction of an electron. For a perfect one-electron system, there are no electron-electron interactions, which leads to cancelation of exchange (E_{x}), coulomb (E_{coul}), and correlation (E_{c}) energies for the density (ρ (r)) of one electron.[129]

$$E_x[\rho_1(r)] + E_{\mathrm{coul}}[\rho_1(r)] = 0; \qquad E_c[\rho_1(r)] = 0 \tag{1.25}$$

However, in SIE, there is imperfect cancellation of self-exchange, correlation and columbic interactions. Although, this problem seems to be simple, the proper mathematical formulation is still challenging. The HF and wavefunction approach are SIE-free because a mathematical description in the formulation of describing Coulomb interaction cancels the self-interactions. However, in density functional based approaches especially in semi-local approaches, where the electron density is the basic variable, it is not trivial to construct such approximations that completely cancel the SIE error. The hybrid DFT functionals partially cancel the self-Coulomb interactions[131] by replacing approximate DFT exchange with exact Hartree-Fock exchange.[132] For example, the hybrid functionals B3LYP[133,134] and PBE0[38] contain 20% and 25% of exact Hartree-Fock exchange contribution, respectively. The SIE error can be reduced but does not eliminate completely because employing 100 % of Hartree-Fock exchange leads to a poor performance.[135] The largest amount of Hartree-Fock exchange (> 75 %) typically makes double-hybrid functionals resilient toward SIE but it increases the computational time which further introduces limitations in their applicability.[136] Another fundamental shortcoming of DFT is its lack of long-range correlation descriptions.[137] However, nowadays it can easily be overcome by including available dispersion corrections[138] (D3, D4, and VV10, *etc*).

In order to determine the suitable functional, a benchmark of single point energy calculations with multiple DFT functionals are run and the results obtained compared to the best of chemical knowledge, experimental available data or high-level quantum calculations.

1.3.2 Basis Set Selection

The selection of a suitable atomic-orbital basis set is an important aspect of computational chemistry in order to achieve high accuracy with low computational cost. In DFT, the errors associated with basis set are much smaller than that of wavefunction-based approaches, which is an important plus point of the DFT approach. The basis set size or "completeness" of a basis set is an important characteristic, which reflects the available functions to represent specific electrons. Generally, the DFT approach uses Gaussian basis functions in order to describe the system's orbitals based on the numerically converged complete basis set (CBS). If the employed Gaussian basis set is not fully or nearly complete, resulting an additional error, called BSIE; basis-set incompleteness error, arises, reflecting the incorrect description of orbitals for the available electron density.[139] A detailed description of BSIE including formalism and development is given by Roza and DiLabio.[140] Based on the energy, the basis-set incompleteness error can be defined as

$$E_{BSIE} = E_{CBS} - E_x \tag{1.26}$$

where E_x and E_{CBS} are the energies computed at the applied basis set (x) and complete basis set limit *i.e.*, aug-cc-pVQZ.

In most cases, the accurate description of valence electrons is pivotal, thus basis sets are categorized based on the cardinal number that represents the number of independent (basis) functions per valence-occupied orbital. The corresponding basis size is usually called double-zeta (DZ), triple-zeta (TZ) and quadruple-zeta (QZ), *etc*. The word zeta represents the independent atomic functions for a valence occupied orbital in their ground state.

BSSE: "basis set superposition error" is another basis set related error, it arises when the applied basis set is too small and the basis functions of close lying neighboring atoms overlap which results in lowering of energies.[141] BSSE is mainly associated with weak or noncovalent bonded systems. The BSSE error is commonly reduced using

counterpoise (CP) correction.[142,143] The CP-based corrections with a small basis set are highly recommended for geometry optimizations and it supports HF and DFT. The CP-corrected noncovalent energy can be computed as,[144]

$$E_{CP} = E_{CBS} + E_{BSSE} \tag{1.27}$$

The commonly used constructed Gaussian-type basis sets are Pople type (6-31G),[145] Dunning (cc-pVXZ),[146] Jensen (pc(seg)-X),[147,148] and Ahlrichs (def2-XVP).[149,150] Ahlrich's type basis sets are highly recommended over Pople and Dunning types because of higher efficiency and availability for a larger part of the periodic table.[151] The applied basis sets can be extended by additional parameters such as polarization and diffuse function. The polarization introduces a higher angular momentum function whilst the diffuse function introduces more flexibility when required, especially for anions. For the polarization function, the general nomenclature is to add the letters "d/p, where d is to add polarization effect only on hydrogen atoms and p for all other atoms in Pople-type" and "P in Dunning and Ahlrichs basis sets" *e.g.*, "6-31G(d,p) or DZP" added a single polarization function, and DZ2P or DZPP with two polarization functions. Similarly, the notations "+", "aug-" or "D" are respectively added to Pople-, Dunning- and Ahlrichs-type basis sets to introduce diffuse functions, *e.g.*, 6-31+G(d), aug-cc-pVDZ and def2-TZVPD, respectively.[152,153] The basis sets with added polarization and diffuse functions are termed as large basis sets. In order to examine that the results are converged with respect to the size of applied basis set, the same calculations at higher basis sets are performed by increasing the cardinal number including additional polarization and diffuse functions.

1.4 Conclusion

Computational chemistry is a useful tool for modeling a very large diversity of materials with an accurate understanding of their physical, chemical and electronic phenomenon. Herein, the wide variety of computational modeling approaches, methods and basis functions have been outlined to elucidate the geometries, energies and properties of materials. The available simulations approach at different "algorithms" or "levels of theory" and time cost and accuracy have been described. Computationally demanding approaches such as DFT are widely used to investigate electronic processes, by treating electrons explicitly. Alternatively, large systems

(>1000 atoms), phonon-based applications, and adsorption can be examined *via* cheap classical methods. Some of the computational modeling engines or suites are illustrated that are used to simulate and visualize the structures and properties of materials. Finally, the basic considerations for choosing suitable functional and basis sets are explained in detail. The discussed computational modeling approaches used in the research presented in this thesis have been noted.

1.5 References

1 T. Zhang, Q. Xue, S. Zhang and M. Dong, *Nano Today*, 2012, **7**, 180–200.

2 R. A. Friesner, *Proc. Natl. Acad. Sci. U. S. A*, 2005, **102**, 6648–6653.

3 D. and H. J. Marx, *Ab initio molecular dynamics: basic theory and advanced methods*, Cambridge University Press, 2009.

4 D. R. Hartree, *Math. Proc. Camb. Philos. Soc.*, 1928, **24**, 89–110.

5 V. Fock, *Z. Phy.*, 1930, **61**, 126–148.

6 M. D. Halls and H. B. Schlegel, *J. Chem. Phys.*, 1998, **109**, 10587–10593.

7 C. Müller and B. Paulus, *Phys. Chem. Chem. Phys.*, 2012, **14**, 7605.

8 R. Knaanie, J. Šebek, J. Kalinowski and R. Benny Gerber, *Spectrochim. Acta A Mol. Biomol. Spectrosc.*, 2014, **119**, 2–11.

9 G. Barea, F. Maseras, Y. Jean and A. Lledós, *Inorg. Chem.*, 1996, **35**, 6401–6405.

10 A. A. El-Azhary and R. H. Hilal, *Spectrochim. Acta A Mol. Biomol. Spectrosc.*, 1997, **53**, 1365–1373.

11 G. A. Chass, R. S. Mirasol, D. H. Setiadi, T.-H. Tang, W. Chin, M. Mons, I. Dimicoli, J.-P. Dognon, B. Viskolcz, S. Lovas, B. Penke and I. G. Csizmadia, *J. Phys. Chem. A*, 2005, **109**, 5289–5302.

12 I. Dąbkowska, P. Jurečka and P. Hobza, *J. Chem. Phys.*, 2005, **122**, 204322.

13 R. G. Parr, *Annu. Rev. Phys Chem.*, 1983, **34**, 631–656.

14 L. J. Sham and W. Kohn, *Phys. Rev.*, 1966, **145**, 561–567.

15 J. P. Perdew, in *AIP Conf. Proc.*, AIP, 2001, pp. 1–20.

16 W. Kohn and L. J. Sham, *Phys. Rev.*, 1965, **140**, A1133–A1138.

17 J. P. Perdew, *Phys. Rev. B*, 1986, **33**, 8822–8824.

18 B. Santra, *Density-Functional Theory Exchange-Correlation Functionals for Hydrogen Bonds in Water*, Technische Universität Berlin, 2010.

19 P. Haas, F. Tran and P. Blaha, *Phys. Rev. B*, 2009, **79**, 085104.

20 J. L. F. Da Silva, C. Stampfl and M. Scheffler, *Phys. Rev. Lett.*, 2003, **90**, 066104.

21 P. Ziesche, S. Kurth and J. P. Perdew, *Comput. Mater. Sci.*, 1998, **11**, 122–127.

22 F. Tran, J. Stelzl and P. Blaha, *J. Chem. Phys.*, 2016, **144**, 204120.

23 J. P. Perdew, J. A. Chevary, S. H. Vosko, K. A. Jackson, M. R. Pederson, D. J. Singh and C. Fiolhais, *Phys. Rev. B*, 1993, **48**, 4978–4978.

24 A. D. Boese and N. C. Handy, *J. Chem. Phys.*, 2001, **114**, 5497–5503.

25 J. P. Perdew, K. Burke and M. Ernzerhof, *Phys. Rev. Lett.*, 1996, **77**, 3865–3868.

26 A. K. Kelkkanen, B. I. Lundqvist and J. K. Nørskov, *J. Chem. Phys.*, 2009, **131**, 046102.

27 R. W. Godby, M. Schlüter and L. J. Sham, *Phys. Rev. Lett.*, 1986, **56**, 2415–2418.

28 J. L. F. Da Silva, M. V. Ganduglia-Pirovano, J. Sauer, V. Bayer and G. Kresse, *Phys. Rev. B*, 2007, **75**, 045121.

29 J. P. Perdew, S. Kurth, A. Zupan and P. Blaha, *Phys. Rev. Lett.*, 1999, **82**, 2544–2547.

30 Y. Zhao and D. G. Truhlar, *J. Phys. Chem. A*, 2005, **109**, 5656–5667.

31 Y. Zhao and D. G. Truhlar, *J. Chem. Theory Comput.*, 2005, **1**, 415–432.

32 V. N. Staroverov, G. E. Scuseria, J. Tao and J. P. Perdew, *J. Chem. Phys.*, 2003, **119**, 12129–12137.

33 J. Hafner, *J. Comput. Chem.*, 2008, **29**, 2044–2078.

34 R. Peverati and D. G. Truhlar, *J. Phys. Chem. Lett.*, 2011, **2**, 2810–2817.

35 J. Paier, M. Marsman and G. Kresse, *J. Chem. Phys.*, 2007, **127**, 024103.

36 J. Paier, R. Hirschl, M. Marsman and G. Kresse, *J. Chem. Phys.*, 2005, **122**, 234102.

37 J. Heyd, G. E. Scuseria and M. Ernzerhof, *J. Chem. Phys.*, 2003, **118**, 8207–8215.

38 C. Adamo and V. Barone, *J. Chem. Phys.*, 1999, **110**, 6158–6170.

39 K. Sharkas, J. Toulouse and A. Savin, *J. Chem. Phys.*, 2011, **134**, 064113.

40 L. Goerigk and S. Grimme, *Wiley Interdiscip. Rev. Comput. Mol. Sci.*, 2014, **4**, 576–600.

41 S. Kossmann, B. Kirchner and F. Neese, *Mol. Phys.*, 2007, **105**, 2049–2071.

42 L. Goerigk, J. Moellmann and S. Grimme, *Phys. Chem. Chem. Phys.*, 2009, **11**, 4611.

43 M. Sheng, F. Silvestrini, M. Biczysko and C. Puzzarini, *J. Phys. Chem. A*, 2021, **125**, 9099–9114.

44 J. C. Sancho-García and A. J. Pérez-Jiménez, *J. Chem. Phys.*, 2009, **131**, 084108.

45 J. A. and B. D. L. Pople, *Molecular orbital theory*, McGraw-Hill, Inc. , NEW YORK, 1970.

46 S. Yuan, M. Rösner, A. Schulz, T. O. Wehling and M. I. Katsnelson, *Phys. Rev. Lett.*, 2015, **114**, 047403.

47 G. Fiori, S. Lebègue, A. Betti, P. Michetti, M. Klintenberg, O. Eriksson and G. Iannaccone, *Phys. Rev. B*, 2010, **82**, 153404.

48 M. Elstner, D. Porezag, G. Jungnickel, J. Elsner, M. Haugk, Th. Frauenheim, S. Suhai and G. Seifert, *Phys. Rev. B*, 1998, **58**, 7260–7268.

49 M. Van den Bossche, *J. Phys. Chem. A*, 2019, **123**, 3038–3045.

50 G. Zheng, H. A. Witek, P. Bobadova-Parvanova, S. Irle, D. G. Musaev, R. Prabhakar, K. Morokuma, M. Lundberg, M. Elstner, C. Köhler and T. Frauenheim, *J. Chem. Theory. Comput.*, 2007, **3**, 1349–1367.

51 M. Addicoat, C. S. Adjiman, M. Arhangelskis, G. J. O. Beran, D. Bowskill, J. G. Brandenburg, D. E. Braun, V. Burger, J. Cole, A. J. Cruz-Cabeza, G. M. Day, V. L. Deringer, R. Guo, A. Hare, J. Helfferich, J. Hoja, L. Iuzzolino, S. Jobbins, N. Marom, D. McKay, J. B. O. Mitchell, S. Mohamed, M. Neumann, S. Nilsson Lill, J. Nyman, A. R. Oganov, P. Piaggi, S. L. Price, S. Reutzel-Edens, I. Rietveld, M. Ruggiero, M. R. Ryder, G. Sastre, J. C. Schön, C. Taylor, A. Tkatchenko, S. Tsuzuki, J. van den Ende, S. M. Woodley, G. Woollam and Q. Zhu, *Faraday Discuss.*, 2018, **211**, 325–381.

52 S. Grimme, C. Bannwarth and P. Shushkov, *J. Chem. Theory Comput.*, 2017, **13**, 1989–2009.

53 C. Bannwarth, S. Ehlert and S. Grimme, *J. Chem. Theory Comput.*, 2019, **15**, 1652–1671.

54 S. Raaijmakers, M. Pols, J. M. Vicent-Luna and S. Tao, *J. Phys. Chem. C*, 2022, **126**, 9587–9596.

55 J. M. Vicent-Luna, S. Apergi and S. Tao, *J. Chem. Inf. Model.*, 2021, **61**, 4415–4424.

56 Q. Cui, M. Elstner, E. Kaxiras, T. Frauenheim and M. Karplus, *J. Phys. Chem. B*, 2001, **105**, 569–585.

57 S. Dohm, M. Bursch, A. Hansen and S. Grimme, *J. Chem. Theory Comput.*, 2020, **16**, 2002–2012.

58 O. Perkal, Z. Qasem, M. Turgeman, R. Schwartz, L. Gevorkyan-Airapetov, M. Pavlin, A. Magistrato, D. T. Major and S. Ruthstein, *J. Phys. Chem. B*, 2020, **124**, 4399–4411.

59 S. Spicher, M. Bursch and S. Grimme, *J. Phys. Chem. C*, 2020, **124**, 27529–27541.

60 M. Bursch, H. Neugebauer and S. Grimme, *Angew. Chemie Int. Ed.*, 2019, **58**, 11078–11087.

61 M. Bursch, A. Hansen and S. Grimme, *Inorg. Chem.*, 2017, **56**, 12485–12491.

62 A. V. Kalikadien, E. A. Pidko and V. Sinha, *Digital Discovery*, 2022, **1**, 8–25.

63 Y. J. Bomble, *J. Am. Chem. Soc.*, 2006, **128**, 3103–3103.

64 B. Hourahine, B. Aradi, V. Blum, F. Bonafé, A. Buccheri, C. Camacho, C. Cevallos, M. Y. Deshaye, T. Dumitrică, A. Dominguez, S. Ehlert, M. Elstner, T. van der Heide, J. Hermann, S. Irle, J. J. Kranz, C. Köhler, T. Kowalczyk, T. Kubař, I. S. Lee, V. Lutsker, R. J. Maurer, S. K. Min, I. Mitchell, C. Negre, T. A. Niehaus, A. M. N. Niklasson, A. J. Page, A. Pecchia, G. Penazzi, M. P. Persson, J. Řezáč, C. G. Sánchez, M. Sternberg, M. Stöhr, F. Stuckenberg, A. Tkatchenko, V. W. -z. Yu and T. Frauenheim, *J. Chem. Phys.*, 2020, **152**, 124101.

65 K. B. and P. M. A. Lipkowitz, *Chem. Rev.*, 1993, **93**, 2463–2486.

66 D. B. and L. K. B. Boyd, *J. Chem. Educ.*, 1982, **59**, 269.

67 J. Grotendorst, *Modern methods and algorithms of quantum chemistry*, NIC, 2000.

68 V. Zoete, M. A. Cuendet, A. Grosdidier and O. Michielin, *J. Comput. Chem.*, 2011, **32**, 2359–2368.

69 S. S. Gupta and R. C. Batra, *J Comput. Theor. Nanosci.*, 2010, **7**, 2151–2164.

70 A. Hocquet and M. Langgård, *J. Mol. Model.*, 1998, **4**, 94–112.

71 J.-H. Lii and N. L. Allinger, *J. Comput. Chem.*, 1991, **12**, 186–199.

72 A. K. Rappe, C. J. Casewit, K. S. Colwell, W. A. Goddard and W. M. Skiff, *J. Am. Chem. Soc.*, 1992, **114**, 10024–10035.

73 M. Grujicic, G. Cao and W. N. Roy, *Appl. Surf. Sci.*, 2004, **227**, 349–363.

74 R. A. Lippert, C. Predescu, D. J. Ierardi, K. M. Mackenzie, M. P. Eastwood, R. O. Dror and D. E. Shaw, *J. Chem. Phys.*, 2013, **139**, 164106.

75 S. E. McDowell, N. Špačková, J. Šponer and N. G. Walter, *Biopolymers*, 2007, **85**, 169–184.

76 P. Banáš, P. Jurečka, N. G. Walter, J. Šponer and M. Otyepka, *Methods*, 2009, **49**, 202–216.

77 G. de M. Seabra, R. C. Walker, M. Elstner, D. A. Case and A. E. Roitberg, *J. Phys. Chem. A*, 2007, **111**, 5655–5664.

78 S. Roßbach and C. Ochsenfeld, *J. Chem. Theory Comput.*, 2017, **13**, 1102–1107.

79 L. Cao and U. Ryde, *Front. Chem.*, 2018, **6**, 89.

80 H. M. Senn and W. Thiel, *Angew. Chemie Int. Ed.*, 2009, **48**, 1198–1229.

81 F. Maseras and K. Morokuma, *J. Comput. Chem.*, 1995, **16**, 1170–1179.

82 P. Sherwood, A. H. de Vries, M. F. Guest, G. Schreckenbach, C. R. A. Catlow, S. A. French, A. A. Sokol, S. T. Bromley, W. Thiel, A. J. Turner, S. Billeter, F. Terstegen, S. Thiel, J. Kendrick, S. C. Rogers, J. Casci, M. Watson, F. King, E. Karlsen, M. Sjøvoll, A. Fahmi, A. Schäfer and C. Lennartz, *J. Mol. Struct-THEOCHEM*, 2003, **632**, 1–28.

83 M. Svensson, S. Humbel and K. Morokuma, *J. Chem. Phys.*, 1996, **105**, 3654–3661.

84 R. D. J. Froese, D. G. Musaev and K. Morokuma, *J. Am. Chem. Soc.*, 1998, **120**, 1581–1587.

85 L. W. Chung, W. M. C. Sameera, R. Ramozzi, A. J. Page, M. Hatanaka, G. P. Petrova, T. V. Harris, X. Li, Z. Ke, F. Liu, H.-B. Li, L. Ding and K. Morokuma, *Chem. Rev.*, 2015, **115**, 5678–5796.

86 G. Groenhof, *Introduction to QM/MM Simulations*, Humana Press, Totowa, 2013, pp. 43–66.

87 Q. H. Zeng, A. B. Yu and G. Q. Lu, *Prog. Polym. Sci.*, 2008, **33**, 191–269.

88 N. Metropolis, A. W. Rosenbluth, M. N. Rosenbluth, A. H. Teller and E. Teller, *J. Chem. Phys.*, 1953, **21**, 1087–1092.

89 J. E. Lennard-Jones, *Mathematical Proceedings of the Cambridge Philosophical Society*, 1931, **27**, 469–480.

90 J. J. Potoff and J. I. Siepmann, *AIChE J.*, 2001, **47**, 1676–1682.

91 M. Kotzabasaki and G. E. Froudakis, *Inorg. Chem. Front.*, 2018, **5**, 1255–1272.

92 D. Young, *Computational chemistry: a practical guide for applying techniques to real world problems*, John Wiley & Sons, 2004.

93 E. J. Baerends and P. Ros, *Int. J. Quant. Chem.*, 2009, **14**, 169–190.

94 G. te Velde, F. M. Bickelhaupt, E. J. Baerends, C. Fonseca Guerra, S. J. A. van Gisbergen, J. G. Snijders and T. Ziegler, *J. Comput. Chem.*, 2001, **22**, 931–967.

95 G. te Velde, F. M. Bickelhaupt, E. J. Baerends, C. Fonseca Guerra, S. J. A. van Gisbergen, J. G. Snijders and T. Ziegler, *J. Comput. Chem.*, 2001, **22**, 931–967.

96 J. Hutter, M. Iannuzzi, F. Schiffmann and J. VandeVondele, *Wiley Interdiscip. Rev. Comput. Mol. Sci.*, 2014, **4**, 15–25.

97 T. D. Kühne, M. Iannuzzi, M. Del Ben, V. V. Rybkin, P. Seewald, F. Stein, T. Laino, R. Z. Khaliullin, O. Schütt, F. Schiffmann, D. Golze, J. Wilhelm, S. Chulkov, M. H. Bani-Hashemian, V. Weber, U. Borštnik, M. Taillefumier, A. S. Jakobovits, A. Lazzaro, H. Pabst, T. Müller, R. Schade, M. Guidon, S. Andermatt, N. Holmberg, G. K. Schenter, A. Hehn, A. Bussy, F. Belleflamme, G. Tabacchi, A. Glöß, M. Lass, I. Bethune, C. J. Mundy, C. Plessl, M. Watkins, J. VandeVondele, M. Krack and J. Hutter, *J. Chem. Phys.*, 2020, **152**, 194103.

98 R. Dovesi, F. Pascale, B. Civalleri, K. Doll, N. M. Harrison, I. Bush, P. D'Arco, Y. Noël, M. Rérat, P. Carbonnière, M. Causà, S. Salustro, V. Lacivita, B. Kirtman, A. M. Ferrari, F. S. Gentile, J. Baima, M. Ferrero, R. Demichelis and M. De La Pierre, *J. Chem. Phys.*, 2020, **152**, 204111.

99 B. Civalleri, P. Ugliengo, C. M. Zicovich-Wilson and R. Dovesi, *Z. Kristallogr. Cryst. Mater.*, 2009, **224**, 241–250.

100 Y. A. Abramov, A. Volkov, G. Wu and P. Coppens, *J. Phys. Chem. B*, 2000, **104**, 2183–2188.

101 N. Wilson and J. Muscat, *Mol. Simul.*, 2002, **28**, 903–915.

102 G. Zheng and C. H. Patterson, *Phys. Rev. B*, 2003, **67**, 220404.

103 M. De La Pierre, R. Orlando, L. Maschio, K. Doll, P. Ugliengo and R. Dovesi, *J. Comput. Chem.*, 2011, **32**, 1775–1784.

104 A. Erba, M. Ferrabone, R. Orlando and R. Dovesi, *J. Comput. Chem.*, 2013, **34**, 346–354.

105 M. D. Segall, P. J. D. Lindan, M. J. Probert, C. J. Pickard, P. J. Hasnip, S. J. Clark and M. C. Payne, *J. Phys. Condens. Matter*, 2002, **14**, 2717–2744.

106 V. Milman, K. Refson, S. J. Clark, C. J. Pickard, J. R. Yates, S.-P. Gao, P. J. Hasnip, M. I. J. Probert, A. Perlov and M. D. Segall, *J. Mol. Struct-THEOCHEM*, 2010, **954**, 22–35.

107 B. Delley, *J. Chem. Phys.*, 2000, **113**, 7756–7764.

108 J. Andzelm, C. Kölmel and A. Klamt, *J. Chem. Phys.*, 1995, **103**, 9312–9320.

109 Y. Kolokoltsev, O. Amelines-Sarria, T. Yu. Gromovoy and V. A. Basiuk, *J. Comput. Theor. Nanosci.*, 2010, **7**, 1095–1103.

110 W. J. Hehre, R. Ditchfield, R. F. Stewart and J. A. Pople, *J. Chem. Phys.*, 1970, **52**, 2769–2773.

111 F. Neese, *WIREs Computat. Mol. Sci.*, 2012, **2**, 73–78.

112 P. Giannozzi, S. Baroni, N. Bonini, M. Calandra, R. Car, C. Cavazzoni, D. Ceresoli, G. L. Chiarotti, M. Cococcioni, I. Dabo, A. Dal Corso, S. de Gironcoli, S. Fabris, G. Fratesi, R. Gebauer, U. Gerstmann, C. Gougoussis, A. Kokalj, M. Lazzeri, L. Martin-Samos, N. Marzari, F. Mauri, R. Mazzarello, S. Paolini, A. Pasquarello, L. Paulatto, C. Sbraccia, S. Scandolo, G. Sclauzero, A. P. Seitsonen, A. Smogunov, P. Umari and R. M. Wentzcovitch, *J. Phys. Condens. Matter*, 2009, **21**, 395502.

113 A. García, N. Papior, A. Akhtar, E. Artacho, V. Blum, E. Bosoni, P. Brandimarte, M. Brandbyge, J. I. Cerdá, F. Corsetti, R. Cuadrado, V. Dikan, J. Ferrer, J. Gale, P. García-Fernández, V. M. García-Suárez, S. García, G. Huhs, S. Illera, R. Korytár, P. Koval, I. Lebedeva, L. Lin, P. López-Tarifa, S. G. Mayo, S. Mohr, P. Ordejón, A. Postnikov, Y. Pouillon, M. Pruneda, R. Robles, D. Sánchez-Portal, J. M. Soler, R. Ullah, V. W. Yu and J. Junquera, *J. Chem. Phys.*, 2020, **152**, 204108.

114 A. Moll, A. Hildebrandt, H.-P. Lenhof and O. Kohlbacher, *J. Comput. Aided Mol. Des.*, 2005, **19**, 791–800.

115 A. and N. A. and H. A. and others Frisch, *Gaussian Inc., Pittsburgh, PA*.

116 L. Glasser, A. Herráez and R. M. Hanson, *J. Chem. Educ.*, 2009, **86**, 566.

117 N. Alexander, N. Woetzel and J. Meiler, in *2011 IEEE 1st International Conference on Computational Advances in Bio and Medical Sciences (ICCABS)*, IEEE, 2011, 13–18.

118 M. Tarini, P. Cignoni and C. Montani, *IEEE Trans. Vis. Comput. Graph.*, 2006, **12**, 1237–1244.

119 R. Sayle, *Trends Biochem. Sci.*, 1995, **20**, 374–376.

120 K. Momma and F. Izumi, *J. Appl. Crystallogr.*, 2011, **44**, 1272–1276.

121 W. Humphrey, A. Dalke and K. Schulten, *J. Mol. Graph.*, 1996, **14**, 33–38.

122 A. Kokalj, *J. Mol. Graph. Model.*, 1999, **17**, 176–179.

123 G. W. A. Milne, *J. Chem. Inf. Model.*, 2010, **50**, 2053–2053.

124 D. Laxmi and S. Priyadarshy, *Biotech. Software Internet Report*, 2002, **3**, 5–9.

125 M. Meunier and S. Robertson, *Mol. Simul.*, 2021, **47**, 537–539.

126 M. D. Hanwell, D. E. Curtis, D. C. Lonie, T. Vandermeersch, E. Zurek and G. R. Hutchison, *J. Cheminform.*, 2012, **4**, 17.

127 J. D. Evans, G. Fraux, R. Gaillac, D. Kohen, F. Trousselet, J.-M. Vanson and F.-X. Coudert, *Chem. Mater.*, 2017, **29**, 199–212.

128 M. Bursch, J. Mewes, A. Hansen and S. Grimme, *Angew. Chem.*, 2022, **42**, e202205735.

129 P. Mori-Sánchez, A. J. Cohen and W. Yang, *J. Chem. Phys.*, 2006, **125**, 201102.

130 H. Iikura, T. Tsuneda, T. Yanai and K. Hirao, *J. Chem. Phys.*, 2001, **115**, 3540–3544.

131 A. D. Becke, *J. Chem. Phys.*, 1993, **98**, 1372–1377.

132 D. R. Lonsdale and L. Goerigk, *Phys. Chem. Chem. Phys.*, 2020, **22**, 15805–15830.

133 A. D. Becke, *J. Chem. Phys.*, 1993, **98**, 5648–5652.

134 P. J. Stephens, F. J. Devlin, C. F. Chabalowski and M. J. Frisch, *J. Phys. Chem.*, 1994, **98**, 11623–11627.

135 E. Vessally, S. Soleimani-Amiri, A. Hosseinian, L. Edjlali and A. Bekhradnia, *Physica E Low Dimens. Syst. Nanostruct.*, 2017, **87**, 308–311.

136 J.-D. Chai and S.-P. Mao, *Chem. Phys. Lett.*, 2012, **538**, 121–125.

137 T. Tsuneda and K. Hirao, *Wiley Interdiscip. Rev. Comput. Mol. Sci.*, 2014, **4**, 375–390.

138 S. Grimme, A. Hansen, J. G. Brandenburg and C. Bannwarth, *Chem. Rev.*, 2016, **116**, 5105–5154.

139 A. Otero-de-la-Roza and G. A. DiLabio, *J. Chem. Theory Comput.*, 2020, **16**, 4176–4191.

140 A. Otero-de-la-Roza and G. A. DiLabio, *J. Chem. Theory Comput.*, 2017, **13**, 3505–3524.

141 R. M. Balabin, *J. Chem. Phys.*, 2008, **129**, 164101.

142 J. Witte, J. B. Neaton and M. Head-Gordon, *J. Chem. Phys.*, 2016, **144**, 194306.

143 S. F. Boys and F. Bernardi, *Mol. Phys.*, 1970, **19**, 553–566.

144 L. Turi and J. J. Dannenberg, *J. Phys. Chem.*, 1993, **97**, 2488–2490.

145 T. D. Padrick and G. C. Pimentel, *J. Chem. Phys.*, 1971, **54**, 720–723.

146 T. H. Dunning, *J. Chem. Phys.*, 1989, **90**, 1007–1023.

147 F. Jensen, *J. Chem. Phys.*, 2001, **115**, 9113–9125.

148 F. Jensen, *J. Chem. Phys.*, 2002, **116**, 7372–7379.

149 F. Weigend, M. Häser, H. Patzelt and R. Ahlrichs, *Chem. Phys. Lett.*, 1998, **294**, 143–152.

150 F. Weigend and R. Ahlrichs, *Phys. Chem. Chem. Phys.*, 2005, **7**, 3297.

151 M. Bursch, J. Mewes, A. Hansen and S. Grimme, *Angew. Chemie Int. Ed.*, 2022, **61**, e202205735.

152 C. E. Check, T. O. Faust, J. M. Bailey, B. J. Wright, T. M. Gilbert and L. S. Sunderlin, *J. Phys. Chem. A*, 2001, **105**, 8111–8116.

153 F. Jensen, *J. Chem. Phys.*, 2002, **117**, 9234–9240.

Chapter 2

2 Literature Review on Computational Modeling and Metal-Organic Frameworks

Computational modeling has a long history of aiding in rationalizing experimental observations at atomistic levels, which allows the understanding of the structure-property relationships and optimization of desired properties. In another way, computational modeling could be used to design, develop and identify the most promising new materials for synthesis and to rationalize their properties. The main theme of this thesis is to evaluate the effect of metal nodes, and interlayer slipping on the sensing or adsorption phenomenon of 2D layered MOFs using computational modeling techniques. Prior to the discussion about our main study, one should know about the Metal-Organic Frameworks and the role of computational chemistry in modeling the structure and properties of these materials. In this chapter, the motivation behind the main project will be described. Thus, this chapter is organized as follows. First, the introduction to Metal-Organic Frameworks (MOFs), which is subdivided into; definition, Secondary Building Units (SBUs), binding forces to hold these units together, and properties & features of MOFs. In section 2, the role of computational modeling in describing the topological crystal structure and electronic structure of MOFs is presented. Section 3 describes two-dimensional (2D) MOFs including the topology of 2D MOFs, and structure-property-relationships. The structure-property relationships section describes recent advancements in modeling 2D MOF structure *i.e.*, metal nodes, organic linkers, and layer slipping, and their role in various applications such as conductive devices, catalytic and sensor applications. Finally, the motivation for the main thesis project entitled, “Small gas molecule adsorption on layered Metal-Organic Framework” is described.

2.1 Metal-Organic Frameworks (MOFs)

Definition: MOFs, a subclass of coordination polymers, are porous and crystalline organic-inorganic hybrid materials.[1] Generally, the inorganic metal ions or clusters (called nodes) and the organic ligands (called linkers) which are the building blocks of

MOFs, connect through coordination bonding or weak van der Waals forces to form small molecular units, and then, attain the crystalline/bulk architecture *via* self-assembly processes (**Figure 2.1**).[2,3]

SBUs: The prediction of the MOFs structures on the basis of metal ions/clusters with organic linkers is difficult. For this purpose, the concept of simple geometrical entities called SBUs: Secondary Building Units and binding interactions between inorganic metallic and organic linker units has been useful.[4,5] The SBUs approach has been adapted to rationalize MOF structural topologies because it allows the use of a large number of organic and inorganic SBUs with a variety of geometries.[6–14] These SBU entities with specific geometries are generated *in situ* with precisely defined reaction conditions.[15] This strategy allows control of the overall coordination number of MOF units and therefore, the need to identify their network becomes important.

Binding: The process of building MOFs is generally directed by coordination bonding. *Coordination bonds* are the columbic/electrostatic interactions between the negatively charged/polarized atoms of donor ligands and positively charged metal ions.[16] Generally, it can be defined as the donation of an electron lone pair to the metal cation from the organic ligand and the reported energy of such bonds is nearly 50.0 kJ/mol.[3] Weak van der Waals forces strongly influence the formation and stability of these coordination polymeric MOFs that are shortly described hereby;

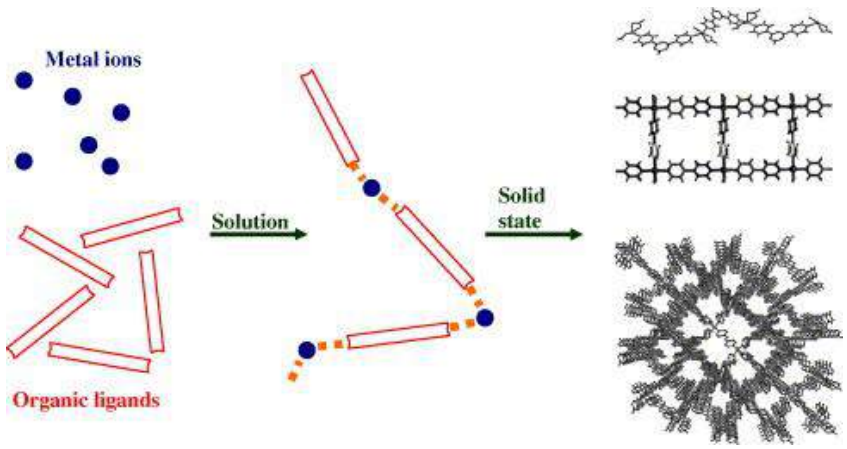

Figure 2.1. The phenomenon of MOF's crystal building; two building blocks *e.g.*, Metal ions (node) and organic ligands bond together *via* coordinate covalent bonds in the solution of their molecular units, followed by self-assembly processes to grow crystal structures in one-, two-, and three-dimensions. Reprinted from Robin *et al.*,[3] with permission from Elsevier.

Hydrogen bond (H-bond) defined by Steiner *et al.*,[17] an X—H•••Y is referred to as a "hydrogen bond", if X—H constitutes a local bond, and acts as a proton donor to Y. Several systematic studies have been reported, with the use of coordination polymer-based structural databases especially, the Cambridge Structural Database (CSD), to understand the energetic strength and the directional preferences of H-bonds.[18,19] Grabowski *et al.*,[20] classified the H-bond into weak, moderate, and strong based on energetic strength. The energy range for weak, moderate, and strong H-bonds are 2.09 to 16.74 kJ/mol (0.5 to 4 kcal/mol), 16.74 to 62.76 kJ/mol (4 to 15 kcal/mol), and 62.76 to 251.04 kJ/mol (15 to 60 kcal/mol); correspondingly, the H•••Y distances for strong (O—H•••O/N) and weak (C—H•••O/N) H-bonds are in the range of 1.5 to 2.2 Å and 2.0 to 3.0 Å, respectively. The H-bond of weak to moderate strength can be described with an "electrostatic plus van der Waals" model. These models fail for strong hydrogen bonds, the quasi-covalent nature of those MOFs must be fully considered.[21]

The 2nd dominant important interaction in coordination polymeric MOF formation is *π-π interactions*. These kinds of interactions have been reviewed in metal complexes with nitrogen-containing aromatic ligands by Janiak *et al*.[22] The π-interactions include aromatic rings preferably stacked in a way to minimize all the repulsions and maximize attractive forces. Such interactions may involve face-to-face side alignment and edge-to-face (C-H •••π) orientations. In face-to-face interactions, the centroid distances between aromatic rings are reported between 3.4 to 3.8 Å long with the offset angle and estimated energy between 16 & 40° and 5 & 10 kJ/mol, respectively. Based on the d^{10} metal cations rule, metal-to-metal interactions are discussed. The estimated energy and bond length of these kinds of interactions are ca. 5.00 kJ/mol and 2.58 Å for Ag-Ag[23] and Fe-Ag,[24] respectively.

Metal-π/aromatic interactions can be found when a metal cation accepts π-electrons from unsaturated organic/aromatic molecules. The interaction distances between Ag^+ and aromatic rings range between 2.8 and 3.3 Å.[16] The energy of these interactions is not well-known, however, it is expected to be around 5 to 10 kJ/mol.[3]

Properties and features: The structural crystallinity, permanent and exceptionally high porosity from several angstroms (Å) to 10 nm scale high surface area (Langmuir 10,000 m^2/g and BET 1000-3000 m^2/g) are fascinating features of MOFs.[25–27] In the current century, MOFs became the most rapidly growing class of materials in material

sciences,[28] due to their versatile structural tailorability, which provides a remarkable tunability to chemical as well as physical properties with a potential role in structure-based applications including, electronic, catalytic,[29] adsorption and storage applications.[30–32] The reasons for the rapidly growing interest in coordination polymers, especially MOFs, are listed by Fromm *et al.*, in a review;[3]

A) Metal ions incorporated in coordination networks and distances between them permit controlling the properties of functional materials.
B) SBUs including numerous types of inorganic nodes and organic linkers offer infinite possibilities for designing new species with intriguing topologies and architectures.

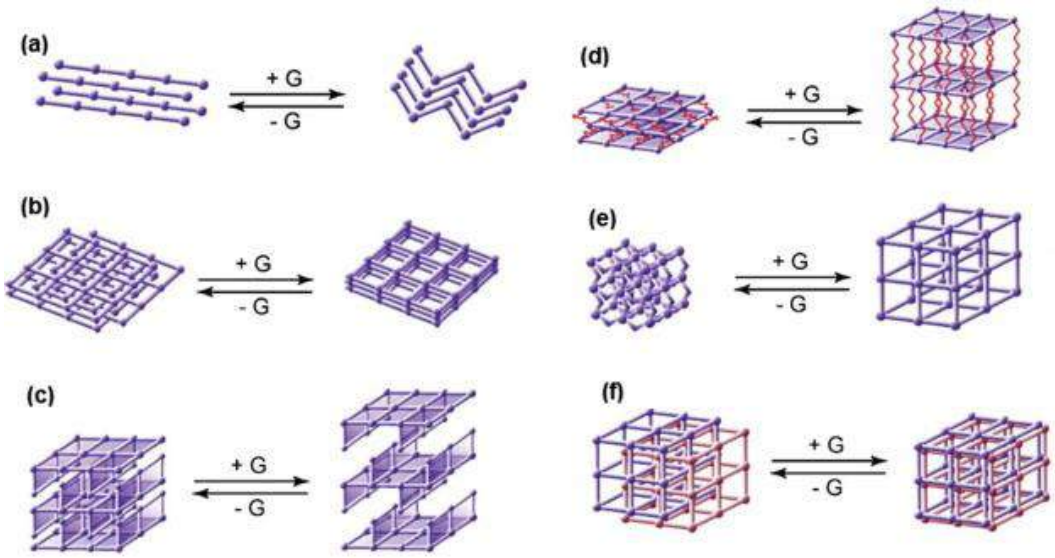

Figure 2.2. The structural dimensionality of (a) 1D/chains MOF, (b) 2D stacked, (c) 2D-interdigitated (layers) MOFs, (d) 3D pillared, (e) 3D shrinking grids & expanding and (f) 3D interpenetrated grids MOFs, where +G and -G represent the addition and removal of the guest molecules, respectively. Reprinted from Kitagawa *et al.*,[33] copyright© 2005, with permission from The Royal Society of Chemistry.

Dimensionality: The dimensional network topology of MOFs can be rationally controlled based on the structural dimensionality of SBUs.[33,34] In 1D (chain) MOFs, the unit crystals are packed in a one-dimensional structure, and voids are accommodated by small rigid molecules.[35] The sheet-like layers of 2D MOFs are superimposed either by staggered or edge-to-edge types of stacking, where the weak interactions operate along the perpendicular direction. The stacking of the layers and their interior functionalities can be controlled by modifying the ligands, which

constitute the main body of the 2D sheets. In 3D porous MOFs, the SBUs are arranged in three dimensions *via* coordination bonds, therefore, such frameworks are highly stable. Detailed descriptions of dimensional MOFs (**Figure 2.2**), especially 3D-MOFs have been reviewed by Kitagawa and Uemura *et. al*.[33] The noncovalent π-stacking and H-bonds not only facilitate the linkages among the building units of 1D, 2D, and 3D frameworks but also control the strength and dimensionalities of the structure.

2.2 MOFs Crystal & Electronic Structure Prediction *via* Computational Modeling

The past two decades have seen enormous success in the design, synthesis, and characterization of MOFs, where the building blocks, inorganic metal units, and organic linkers, are bonded together by strong coordination bonds. Over two decades ago, Yaghi and coworkers introduced a concept called reticular chemistry, illustrating that MOFs can be designed by the endless combinations of secondary building units (SBUs) and create frameworks with various structures, topologies, and elemental compositions. Besides numerous approaches for the experimental designing of MOFs, many hypothetical structures modeled computationally have been reported. The increasing focus on such MOFs is the targeted pre-synthesis design of crystal frameworks with desired properties. Such modeling involves the screening of a million possible MOFs structures in order to search for the most suitable one for targeted properties, the resulting structures are the ideal candidates for the rational designing of syntheses to be attempted.[36,37]

In the recent century, several computational MOFs building algorithms/simulations have arisen. The first computational approach in developing a hypothetical MOF was reported in 2000,[38] entitled “automatic assembly of secondary building units (AASBU)”. The AASBU approach is based on the global optimization technique, where the SBUs containing “sticky” atoms are treated as rigid units and are perturbed randomly in a simulation box as a function of temperature. The sticky atoms serve as “glue” and dictate to adhere SBUs to form extended coordination polymers. This approach samples relatively large degrees of freedom, which permits the building of infinite unique structures even from a single type of SBU. The many degrees of freedom make this algorithm more and more expensive to identify a unique crystalline material with targeted properties, which limits the use of the AASBU method.

Although methods with fewer degrees of freedom, by using larger SBUs with less sticky atoms have been presented (**Figure 2.3a**),[39,40] this demands a preconceived idea of the desired or final framework structure.

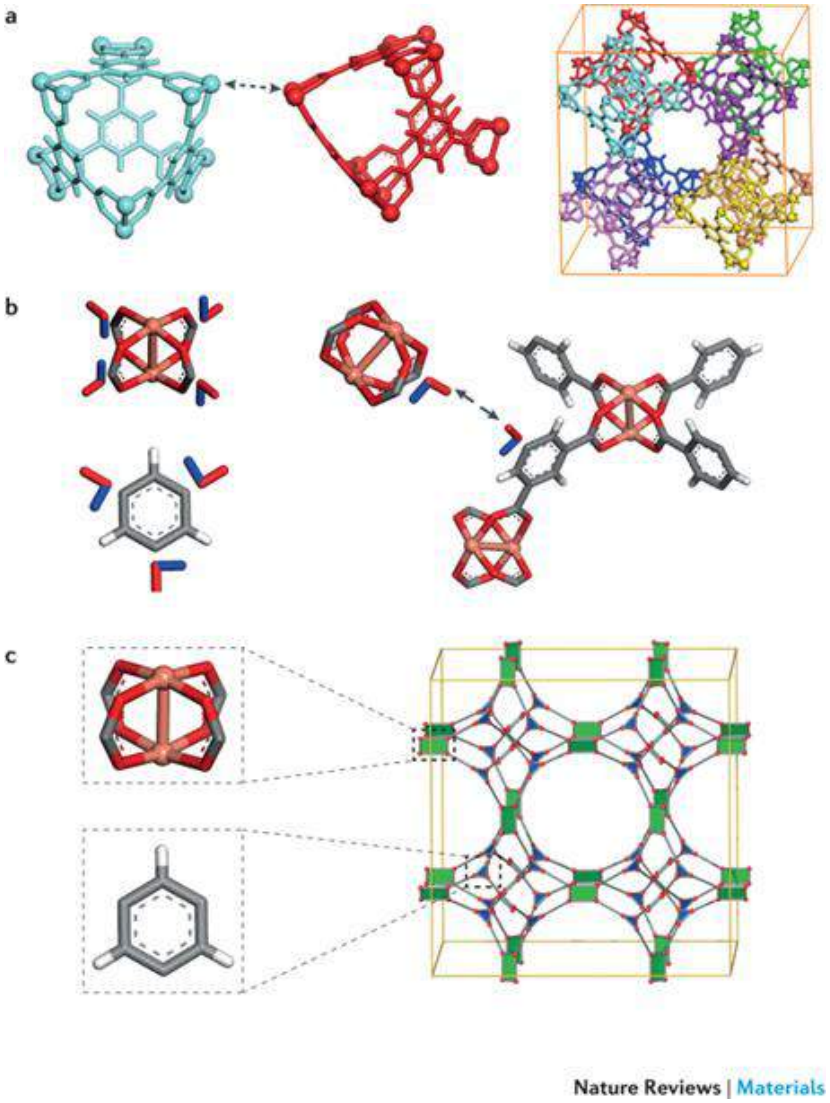

Figure 2.3. The designing of the prototypical HKUST-1 MOF, using different computational assembly approaches. a) The building of HKUST-1 (right) from large hybrid building blocks (left) by joining the sticky atoms' (large balls on the edges of each substituent). Each SBU is represented with eight different colours in the periodic MOF, b) the 'Tinkertoy' method assembling HKUST-1 until there is no free bond (right) using alignment parameters for each SBU, illustrated as blue and red lines, c) the topology-based approach uses known topologies as templates for building MOFs. For HKUST-1 with the ***tbo***; twisted boracite topology (right), in which the aromatic benzene and metal ions (Cu) SBUs are orientated on the 'triangular' and 'square'

nodes, respectively. Atom colours: Cu (orange), O (red), C (grey), and H (white). Reprinted from Boyd *et al.*,[37] with permission from Springer Nature.

The other computational approaches simplify the process of constructing frameworks by assuming that building blocks self-assemble to form predefined 2D networks. The first among these approaches was published a decade ago along with the 13,7953 new theoretical MOFs, generated from 102 SBUs.[41] In this approach, the chemical building units are extracted from experimental X-ray crystallographic data, such that each building unit represents simple geometries including triangles, squares, tetra-, and octahedra. The method of assembling the new hypothetical MOF starts with a single SBU and allows binding freely with iteratively added building units until all the possible positions are saturated. This approach is named Tinkertoy because it seems like the snapping of bricks to form a crystal lattice. The building of MOF-14[8] is a closely related example of the Tinkertoy approach (**Figure 2.3b**), where the inorganic di-copper paddlewheel and aromatic tri-benzoic acid organic linker are two distinct building units. The time complexity of sampling accurate MOF combinations is known to be the n^{th} order, where n is the number of building units of the growing MOFs. This method, therefore, could take years to elucidate the accurate combination of SBUs.

The first topology-based approach for generating crystalline porous materials was presented by Martin and Haranczyk in 2014.[42] This algorithm can be applied using the porous properties characterization software namely, Zeo++.[43,44] In this approach, the SBUs are identified by their binding sites, thus the method can extract the coordination number of atoms and their shapes. However, Smit and coworkers stressed that such connection sites identify how the SBUs are oriented in the template rather than guiding the formation of specific topologies.[37]

The 3D network with predefined unit cell dimensions along with the placement of inorganic nodes and organic edges are obtained from Yaghi *et. al.*,[45] defined Reticular Chemistry Structure Resource method (RCSR), in which the cell dimensions are adjusted to closely fit the SBUs geometries (**Figure 2.3c**). Structures are relaxed with their suitable atomic position to produce energetically more feasible configurations. The approach recommends performing relaxation with a classical force field. Prior to energetic relaxation, it is important that the intra-building units bonding are known or tabulated to avoid ambiguity in describing the structures which could cause

convergence problems during relaxation in the optimization process. The electronic structures of hypothetical frameworks can be further refined using *ab initio* methods, especially the density functional-based approach.

The DFT and other high-level approaches provide quantitative information for framework structures and electronic parameter determination. With this regard, the general approaches with their features and benefits are discussed in detail in a review article by Hendon *et al*.[46] Some of their discussion regarding the role of DFT in MOFs structures elucidation is summarized here. The reliability of DFT calculations depends not only on the structure of the chemical system but also on the implied functional as well as basis sets. To judge the accuracy of the method, the obtained results are compared with experimental or high-level computations *e.g.*, CCSD(T) data. In this regard, Sholl and coworkers reported a benchmark study on predicting the structural parameters of MOFs using a variety of DFT functionals, including M06L, PBE, PBE-D2/D3, PW91, and vdW-DF2 and compared the results with experimentally derived PXRD lattice parameters.[47] They found that PBE-D2, –D3, and DF functional predicted MOF structures exhibit excellent agreement with experimentally available data, where the deviations in pore diameters were less than 0.5 Å of experimental results. However, the interdependence of crystal structures and functional poses a challenge of suitable functional selection to generate both realistic atomic coordinates and electronic wavefunctions.

In DFT, functionals are broadly classified based on their electron density gradient treatment. The hierarchy of electron density approaches is discussed in Chapter 1. Herein, the discussion is only restricted to their application in porous materials, especially MOFs. The local spin density approximations;[48] LDA or LSDA, the bottom rung of Jacob's ladder, are readily applied to metal-containing porous materials *i.e.*, the materials with a nonzero density of state (DOS) at the Fermi level. Despite the nonzero DOS of MOFs,[49–52] their electronic structure would be misguided at any variation of LDA because the electron density is not distributed homogeneously, especially for 2D layered MOFs *e.g.*, $Ni_3(HITP)_2$,[53,54] where the electron density on covalently bonded N and Ni are vastly different.

Instead, GGA[55,56] functionals are based on electron density and the electron density gradient, thus enabling better descriptions for materials with inhomogeneous charge

density, *i.e.*, MOFs or other metal-organic hybrids. A GGA functional including PW91[57] and PBE[58] has been widely implicated in computational experiments on molecular materials as well as solid-state crystals for both structural and electronic properties analysis.[47,59] The inability of GGA functionals to correctly describe electron exchange and correlations is a core shortcoming of their implementation in MOF chemistry.[60,61] Many other extravagant DFT functionals with more complicated algorithms have been implemented to obtain better accuracy in describing the exchange and correlation of electron structure theory. The higher rung meta-GGA functionals *i.e.*, MO6-L or TPSS, invoke the first and second derivatives of the density, whilst so-called hybrid DFT functionals contain exact electron exchange from HF theory, for example, PBE0[62] is the hybrid form of the PBE functional with 25% Hartree-Fock exchange.

By far, the hybrid GGA functionals are widely considered the minimum level of DFT necessary to describe the structure of materials, particularly MOFs with spin-polarized transition metals (TM).[63] In TM containing MOFs, the exchange not only plays a pivotal role in the energy of the system but also describes the nature and structure of the frontier molecular orbitals and the electronic band gaps. Despite their significant cost in terms of computational demand, the most commonly used hybrid functionals in modeling MOF structures are B3LYP, PBE0, HSE06, and M06.[64–68]

2.3 Two-dimensional Metal-Organic Frameworks (2D-MOFs)

2.3.1 Introduction to 2D-MOFs

The word MOF sketches a giant three-dimensional (3D) crystalline network in the mind, which is built-up with metal centers connected by organic linkers through coordination bonds.[69,70] A variety of inorganic metal nodes and a diversity of organic linker units allow MOFs to develop topologically diverse crystal structures *i.e.*, 0D, 1D, 2D, and 3D MOFs.[71] 3D MOFs are widely explored by the research community due to their ultra-high porosity in all dimensions and large surface area.[72,73] 2D layered MOFs have recently gained more interest since 3D MOFs do not completely satisfy some particular requirements for various applications. For example, 2D layered MOFs exhibit lower porosity in comparison to their 3D counterpart, the isolation of single

and atomically thin layers would provide for an in-depth investigation of the surface phenomenon, electronic band structure, and chemical reactivity, *etc*.[74] Since monolayers, with regular repeating metallic sites as well as organic linkers, are expected to show unique physical, chemical, and electronic properties, which may be promising membranes for surfaces applications such as storage,[75] separations,[76,77] sensing[78] and catalysis.[79]

The synthesis of 2D layered MOFs however is trivial because of strong interlayer interactions the 2D MOF layers tend to stack *via* van der Waal, π-π stacking forces, and/or H-bonding.[80] In order to hinder these interactions and generate isolated 2D layers of MOFs with thicknesses between atomic up to the 1 Å (0.1 nm), different approaches including top-down and bottom-up, have been proposed.[81,82] Among them, the preferred method, in which a layer is separated from the well-established 3D crystal, is a top-down approach. In this approach, 2D-monolayers can be separated from a bulk crystalline MOF *e.g.*, $M_2(BDC)_2$ also referred to as MOF-2 (where M^{2+} are Cu^{2+},[83] Zn^{2+},[13] Co^{2+},[84] and Ni^{2+},[85]) either *via* treating with appropriate reagents, including acetone,[86] ethylamine/octylamine,[87] sodium dodecyl sulfate[88] or functionalization of linker units with alkoxy substituents (*e.g.*, $Zn_2(bim)_4$, where *bim* = benzimidazole).[89]

2.3.2 Topology of 2D Layered MOFs

The topology of 2D layered MOFs mainly exhibits single three-, four-, six- and mixed multi-connected topological networks. Some of the common topologies encountered in 2D MOFs, including ***hxl***; hexagonal, ***sql***; square lattice, ***hcb***; honeycomb, ***kgm***; Kagomé, ***fes***; four eight square, ***kgl***; Kangomé, *etc* are shown in **Figure 2.4**.[81] These topologies can be obtained from six-connected nodes (triangle), four-connected nodes (square), and 3-connected nodes (hexagon). These are uniform networks containing nodes (uninodal) and polygons, that are represented by the alphabetic symbols (*n, p*), where *n* represents the size of the shortest circuit while *p* indicates the connectivity of the node. Hence, the ***hcb***, ***hxl***, and ***sql*** networks (**Figure 2.4(a-c)**) are represented as (6,3), (3,6), and (4,4) respectively.[90] The 4-connected nodes either construct 4^4 sql or $3^2 6^2$-based lattice networks called ***kgm*** (**Figure 2.4d**). In rare cases, the bimetallic 4-connected nodes and 3-connected nodes are combined, and a complex 2D-layer structure is simplified with Schläfli symbols $(4.6^2)_4(6^4.10^2)$ (**Figure 2.4e**). In some

cases *e.g.*, ***fes*** contains three-connected nodes with two different rings (**Figure 2.4f**), Schläfli symbols are used to represent such types of networks. The ***fes*** is represented by the Schläfli symbol; 4.8^2, where 4 and 8 are two (2) rings. Moreover, this representation is also used to represent more than one node. In addition, when two nodes are joined together *e.g.*, both three- and six-connected nodes in (**Figure 2.4g**), it constructs a unique bi-nodal (3,6) ***kgd*** network. A unique ***kla*** "parquet floor" topology is obtained when two layers at a 90° angle are joined by bridging the metal nodes (**Figure 2.4h**). These and overall topologies of any periodic network can be identified and studied by OLEX,[91] Systre,[92] and ToposPro[93,94] computer software. The topological networking of the porous framework materials is a vast topic, which has extensively been reviewed in the literature.[95–101] The in-depth discussion about the topological networking of MOFs is behind the scope of this study.

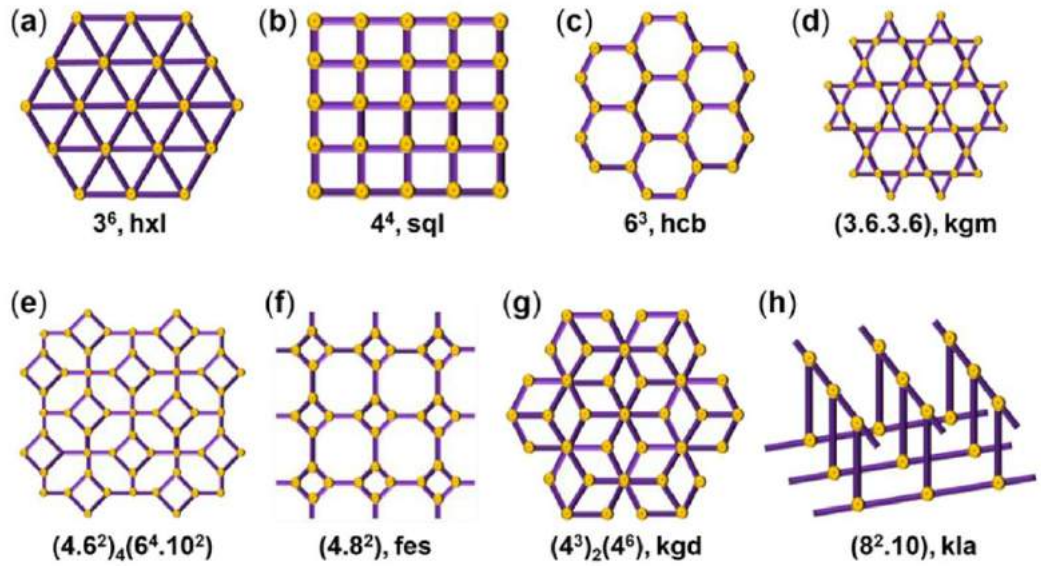

Figure 2.4. The illustration of some common topologies encountered in 2D MOFs. Reprinted from Chakraborty *et al.*,[90] with permission from the American Chemical Society.

2.3.3 Structure-Property Relationships and Computational Modeling of 2D MOFs

2.3.3.1 Structural Features of 2D Layered MOFs

The established strategies for building 2D conductive layer MOFs depends on either square planar or octahedral metal/transition metal cations (*e.g.*, Cu^{2+}, Co^{2+}, Ni^{2+}, and

Pd^{2+}, *etc.*) crosslinked with flat and aromatic ligands (*i.e.*, benzene, triphenylene, and phthalocyanine) containing *ortho*-substituted heteroatoms (like O, S) or the group of atoms (NH) (**Figure 2.5**).[102] The choice of inorganic metal nodes and the molecular substitution in terms of the chemical nature of crosslinked heteroatoms or groups (O, S, and NH) in organic ligands can significantly influence the stacking nature of 2D layers (*e.g.*, eclipsed, slipped parallel, and staggered). For example, the incorporation of Cu^{2+} in HHTP; hexahydroxy-triphenylene, (**Figure 2.5**D) forms 2D MOFs with either eclipsed or slipped parallel (AAAA) stacking. Replacing the Cu^{2+} with Ni^{2+} or Co^{2+} drastically changes the stacking to staggered ABAB geometry.[53]

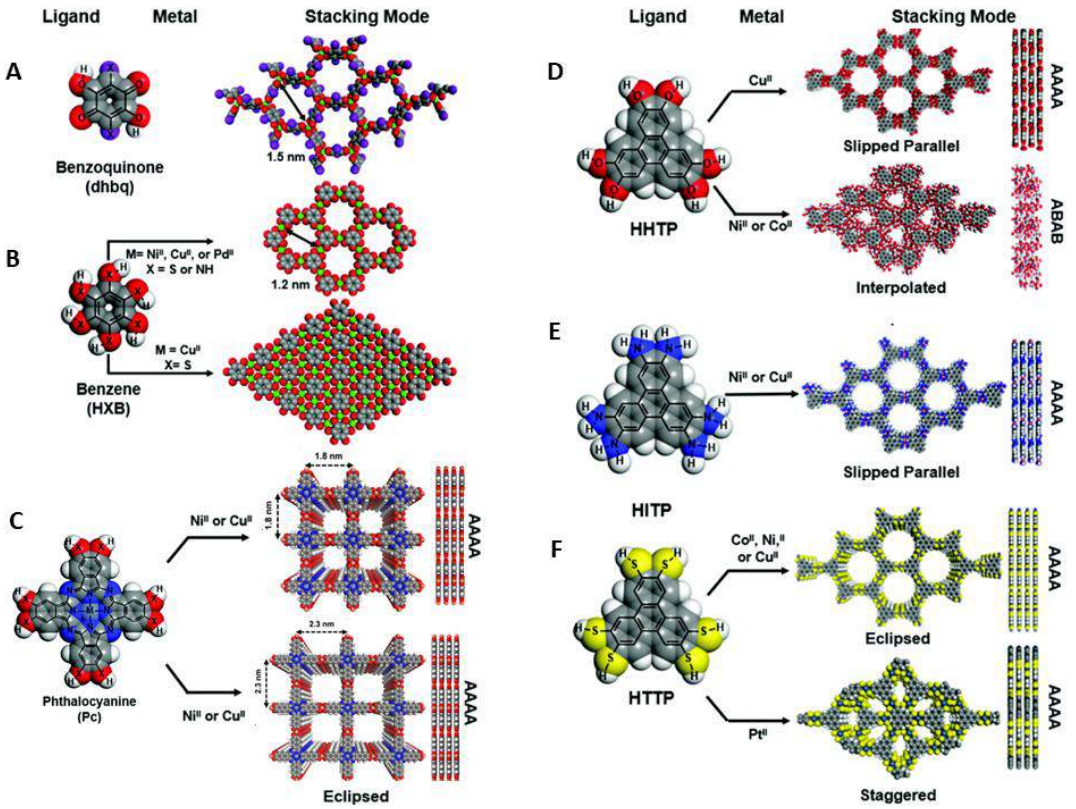

Figure 2.5. Core aromatic ligands with ortho-substituted heteroatoms for the building of 2D layered MOFs. Different topologies with varying pore sizes and shapes can be constructed with different ligands. A) Benzoqinone-type ligands form non-planar 2D MOFs.[103] B) Benzene with six-heteroatom ligands forms continuous non-porous sheets as well as hexagonal porous MOFs.[104] C) Phthalocyanine or naphthalocyanine ligands build square pore stacked 2D MOFs.[105] D-F) Triphenylene with hetero atoms O[53] (D), NH[54] (E), and S[50,106] (F) from different stacked *e.g.*, eclipsed (AAAA), slipped (AAAA) and staggered/interpolated (ABAB) layered MOFs. **Figure 2.5(A, B, & D-F)** are readapted from Michael *et al.*,[107] with permission from The Royal Society of

Chemistry, and the **Figure 2.5C** is reprinted from Meng *et al.*,[105] with permission from the American Chemical Society.

Similarly, the Ni^{2+} incorporated with HITP; hexaiminotriphenylene, generates a 2D slipped parallel (AAAA) stacking pattern (**Figure 2.5E**).[102] Dincă *et al.*,[54] confirmed the slipped parallel stacking of Ni_3HITP_2 MOF by comparing powder X-ray diffraction (PXRD) with computationally generated XRD. For this purpose, the author used Avogadro v1.1.1[108] software with a threshold (the force for max. adjustment of coordinate) of 1.7 pm. For further detailed analysis, the single point energies of a total of 82 *ab*-parallelly slipped structures, the two layers with a separation of 3.3 Å and the top layer translated to either *a (x-), b (y-),* or *ab (xy-plane)* directions, were generated using a GGA-DFT (PBE) functional in addition to Grimme's D2 corrections on the VASP v5.2[109,110] suite. As a result, the potential energy surface was obtained, which suggested that the eclipsed and staggered structure was energetically unfavorable while a slipped parallel structure with an *ab* offset of around 1.8 Å is energetically more feasible. Moreover, the computationally produced PXRD pattern is quite comparable with the experimental PXRD pattern. This study highlights the importance of slipped geometries in 2D layer MOFs and is of relevance to the main project of this thesis, see Chapter 3 for detail. According to Dincă and co-workers slipped parallel stacking for Ni_3HITP_2 MOF is a preferable geometry as compared to the eclipsed and staggered geometries. However, when the crosslinked NH on triphenylene is replaced with sulfur in hexathiotriphenylene, the eclipsed and staggered stacking modes are more favourable (**Figure 2.5F**), depending upon the incorporated metal nodes. For example, the eclipsed structure is preferable with Ni^{2+}, Co^{2+}, and Cu^{2+}, while the stacking structure is preferred in replacing metal ions with Pt^{2+}.[111]

With the above discussion, it can be concluded that the structural features including inorganic metal nodes, organic linkers, and layer stacking geometries produce a remarkable effect on the stability of 2D-MOFs. In the subsequent sections, the effects of tuneable molecular building units on the mechanical, electrical, and catalytic properties of MOFs *via* computational modeling is discussed.

2.3.3.2 Structure and Conductivity of 2D MOFs

The advent of highly porous and crystalline MOFs has revolutionized the chemistry of solid-state materials.[112,113] The tunable molecular building units of MOFs provide a

remarkable and diverse utility in various applications (*e.g.*, catalysis,[114] gas storage,[115] energy,[116] and chemical sensing[117,118]). Until now, their utility in electrochemical or electronic devices has been limited because of the poor charge transportation of most MOFs.[119] In order to achieve high electrical conductivity in MOF-based materials, maximizing the charge concentration and charge carrier's mobility is desirable. The former can be achieved by; a) hole/electron injection,[120] b) photo/thermal-excitation,[121,122] and c) doping[123,124] while the latter can be maximized by reducing the charge trapping sites[125] and lowering the defect density.[126] Extensive research has been published to summarize experimental design principles as well as structural features that not only enable but enhance charge transport in MOFs.[127–129]

The 2D π-conjugated layered MOFs are currently among the most conductive materials,[54] where both metal ions crosslinked with heteroatoms and organic linkers can serve as the source of electron/charge carriers.[130] Specifically, the redox-active or stable radical linker units together with metallic nodes containing unpaired electrons can be utilized to ensure high charge density delocalization through conjugated systems.[129] The specific charge transport mechanism in 2D conductive MOFs is not well-understood yet, but several approaches[131] have been proposed to display the conduction mechanism in such materials including hopping[132] (**Figure 2.6A**), through-space[133] (**Figure 2.6B**), through-bond[134,135] (**Figure 2.6C**) and band transport.[136]

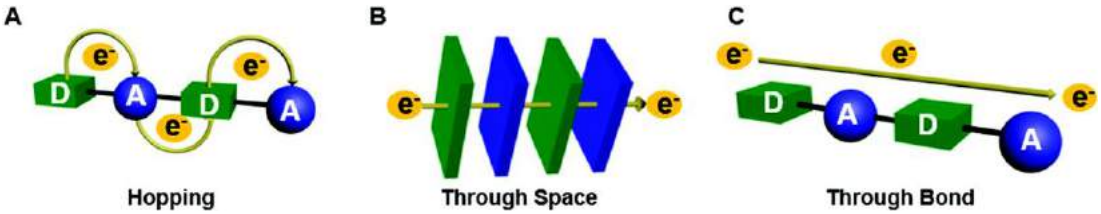

Figure 2.6. The possible mode of electron/charge transportation in 2D MOFs. Reprinted from Michael *et al.*,[107] with permission from the Royal Society of Chemistry.

2.3.3.2.1 Effect of Metal Nodes

Depending on the metallic nodes, metal substitution can affect redox processes *e.g.*, electron injection (reduction) and hole injection (oxidation) within the MOF crystals, and thus, influence their electronic properties.[137] Initially, Dinca *et al.*,[138] experimentally proposed that a 2D-layered MOF *e.g.*, Ni_3HITP_2 film behaves as a

semiconductor. Later, a computational study by Chen *et al*.,[139] proposed the change in conductive nature from semiconductor to metallic by replacing Ni^{2+} with Cu^{2+} to form Cu_3HITP_2. For this purpose, the electronic band structure of periodic two-layered Ni_3HITP_2 and Cu_3HITP_2 are computed at a GGA/PBE exchange-correlation functional. In addition, Grimme dispersion; D3, was also implied to account for the dispersion energies correctly whereas the ion interactions were described by the Projector Wave potentials Augmented (PWA).[140] Based on the generated band structures, it was illustrated that Ni_3HITP_2 is a semiconductor with a narrow band gap (0.13 eV) while Cu_3HITP_2 is a metallic MOF.

2.3.3.2.2 Effect of Heteroatom Crosslinkers

The electron push and pull strategies based on the charge donating or withdrawing nature of additional substituents such as heteroatoms bridging between metal nodes and organic linkers can be employed to modulate charge distribution within MOFs. This particular strategy needs proper energy overlap of the orbitals of the metal nodes and coordinating heteroatoms that can be inferred from the relative electronegativities (EAs) of coordinating atoms. For instance, the EA values of the transition metals (TM) are better matched with sulfur (*e.g.*, in hexathiotriphenylene; HTTP) than oxygen (*e.g.*, in hexahydroxytriphenylene; HHTP).[141] Metal ion and organic linkers connected through metal-sulfur bonds are expected to exhibit better charge transportation than structurally analogous metal-oxygen connectivity.[102,142,143] Recently, the electron transport properties between metal and heteroatom (S, O, & NH) coordinated organic triphenylene (namely, HHTP, HHTP, and HATP, respectively) were compared using a hybrid long-range DFT functional (ωB97X-D). Herein, the reported charge transport between metal and heteroatoms was as follows: HTTP>HHTP>HATP.[144]

2.3.3.2.3 Effect of Organic Linkers

Another strategy in modifying the electronic behaviour of 2D MOFs is the use of inherently redox-active organic linkers such as benzene,[145] triphenylene,[146,147] or phthalocyanine,[148] that show numerous accessible redox states.[117,149] For example, TM_3(hexaiminobenzene)$_2$; TM_3HIB_2 containing Ni as a transition metal are reported to exhibit metallic behaviour based on the computationally computed band gaps.[49] On the other hand, similar studies on Ni_3(hexaiminotriphenylene)$_2$; Ni_3HITP_2 suggested

its semiconducting nature.[52,150] Modifying the organic linker is an important factor that enables changing conductive nature of planar MOFs.

2.3.3.2.4 Effect of Interlayer Slipping and Separation

Band structure simulations showed that the interlayer slipping in 2D layered MOFs can induce significant changes in conduction behaviour.[151] The band structures of eclipsed, slipped-parallel and staggered structures of Ni_3HITP_2 were modeled using a hybrid DFT functional with a large basis set (B3LYP/pob-TZVP) level of theory. Based on these calculations, it was concluded that the pristine, as well as eclipsed Ni_3HITP_2 exhibit a metallic electronic structure, whereas the layer-by-layer displacement governed remarkable changes in the band structure, which lead to the introduction of semiconducting properties. Similarly, Foster *et al.*,[150] performed a DFT study to model the electronic behaviour of the pristine layer, bilayer eclipsed and minimum energy slipped parallel structure of Ni_3HITP_2. The DFT band structure calculations by B3LYP/pob-TZVP predicted that both the eclipsed and slipped Ni_3HITP_2 structures are metallic in nature; in contrast, a pristine 2D layer exhibits a small band gap (**Figure 2.7A-C**). Furthermore, the band gap as a function of the interlayer spacing from interacting; 3.3 Å to noninteracting; 5.0 Å was also evaluated (**Figure 2.7D-F**). The band opening was started when the spacing between layers reached 3.8 Å, whereas at 5.0 Å interlayer spacing the band structure effectively converged to the pristine monolayer value, reflecting the narrow band gap semiconductor nature of Ni_3HITP_2.

Recently, another computational report by Shakib and co-workers reported that the slipping of layers and change of interlayer separation can induce semiconductor-to-metal and *vice versa*.[152] A step further, *ab initio* molecular dynamics (AIMD) simulations were also employed to demonstrate the inherent structural deformations in Ni_3HITP_2 can induce a change in the conductivity from metallic to semiconducting at 0 K and 293 K, respectively.

The experimental study by Sheberla *et al.*,[138] reveals that Ni_3HITP_2 film is a semiconducting with conductivity value of 40 S/cm, in contrast, the computational studies reveal the metallic nature of bulk Ni_3HITP_2.[151] This disconnection between the computational results and experimental analysis may evolve from the existence of transport barriers in the real experimental system (*i.e.*, defects and interfaces), that are

absent in computational modeling. Three known potential defects influence charge transport including layer separation, perpendicular grain boundaries, and strike-slip faults between grains, as described by Foster and co-workers.[151]

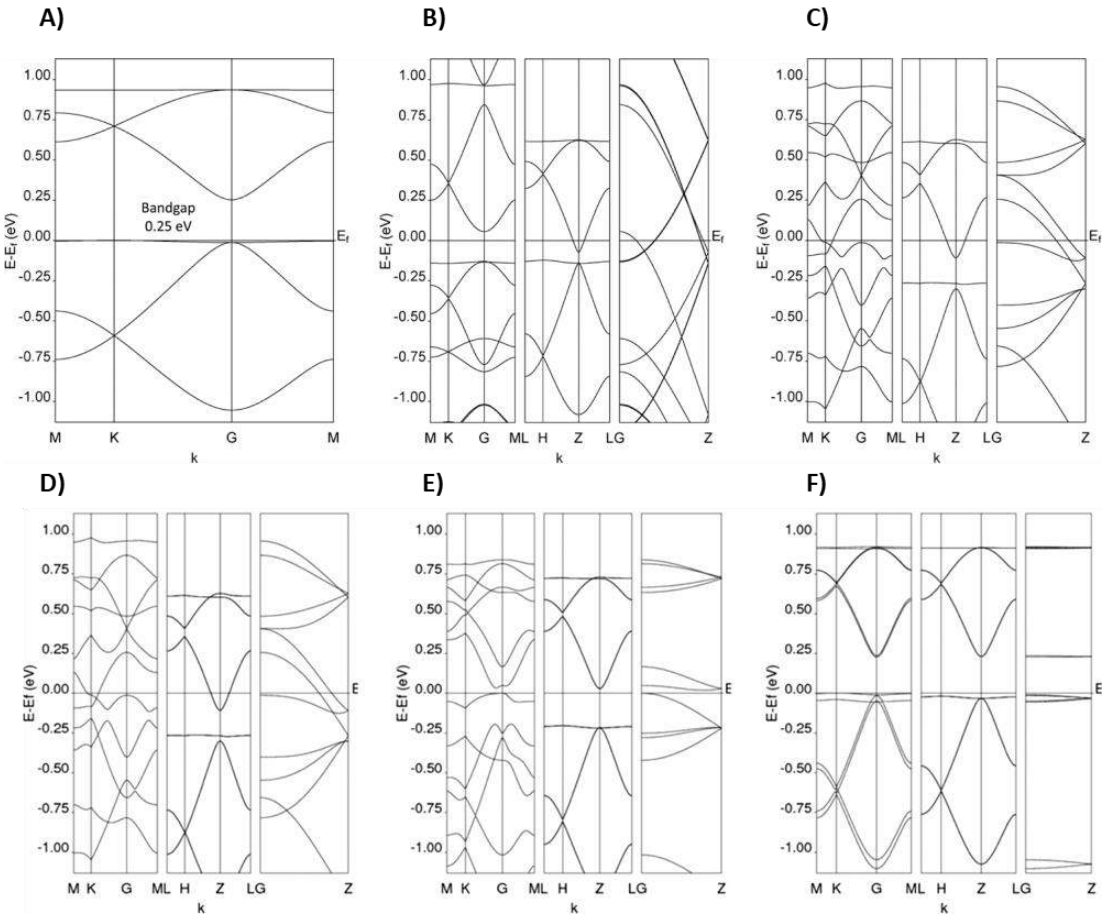

Figure 2.7. Simulated band structures of A) pristine monolayer, B) eclipsed, C) parallel-slipped, parallel-slipped with the interlayer slipping of D) 3.3, E) 3.8, and F) 5.0 Å of Ni_3HITP_2. Reprinted from Foster *et al.*,[150] with permission from the American Chemical Society.

2.3.3.3 Applications of 2D MOFs

Based on the above discussion, three main advantages can be identified for the multifaceted utility of 2D layered MOFs. First, a high degree of controlled structural modulation (*e.g.*, varieties of metal nodes and organic linkers[153]) permits the integration of MOFs into catalysis. Second, the excellent electrical conductivity of 2D MOFs makes them well-suited for electronic devices. Third, the large surface area, high porosity, and exposed surfaces *via* interlayer slipping present numerous active sites available for gas separation and storage.

2.3.3.3.1 Electrocatalysis

Electrocatalysis is fundamentally related to the surface, therefore, the electrocatalytic efficiency of nanomaterials is directly linked with geometric composition. The 2D MOFs offer large surface area, highly exposed active sites along with a variety of compositions in terms of metal nodes and ligands that provide significant performance in electrocatalysis.[154–157] In addition to the structural composition, the electrical conductivity of 2D MOFs is equally important for state-of-the-art electrocatalysis.[158–160] Although the advent of synthetic methodologies and design of 2D MOFs with exceptional charge transport affinity is highly demanding, the role of computational modeling to predict the suitable architectures for electro/catalysis cannot be neglected.

HER; hydrogen evaluation reaction is nowadays the utmost method to generate a highly pure and large quantity of hydrogen. Up until now, water splitting *via* an electrochemical route is a fascinating and eco-friendly method to produce hydrogen.[161] To accelerate the commercialization of the electrocatalytic splitting of water, it is necessary to design or search for earth-abundant, low-cost stable catalytic materials. The integration of this process in 2D MOFs is an effective strategy *via* single-atom catalysis (SAC). In this context, Li *et al*.,[162] performed a computational modeling technique to screen the optimal SAC for HER from 2D MOFs composed of a variety of nodes and heteroatom crosslinked ligands. In this study, the author aimed to find out a suitable transition metal from group-VIIIB TM atoms (*e.g.*, Fe, Co, Ni, Ru, Rh, Pd, Os, Ir & Pt) as a node and a suitable X-atom (X= NH, O, S, Se) crosslinked benzene-containing ligand for the HER electrocatalytic process (**Figure 2.8A**). For these studies, the VASP package[163] was used to perform all the DFT calculations at the PBE-D3 method for geometry optimization, compute formation energies, and perform thermal dynamic analysis. Furthermore, AIMD and nudge elastic band[8] (NEB)[164] were simulated to evaluate the thermal stability and the minimum energy pathway for H_2 evolution, respectively. Among the 36 studied configurations of 2D MOFs, Rh_3BHI_2; Rh_3(benzenehexaimine)$_2$ was predicted as the optimal HER catalyst because of the near-zero Gibbs free energy for hydrogen adsorption; $\Delta G(H^*) = 0.02$

[8] NEB are the types of computational modeling used for optimizing saddle points or finding (minimum) energy paths between reactants and products.

eV (1.93 kJ/mol) (**Figure 2.8B**) and the lowest (0.53 eV or 51.14 kJ/mol) activation barrier (**Figure 2.8C**).

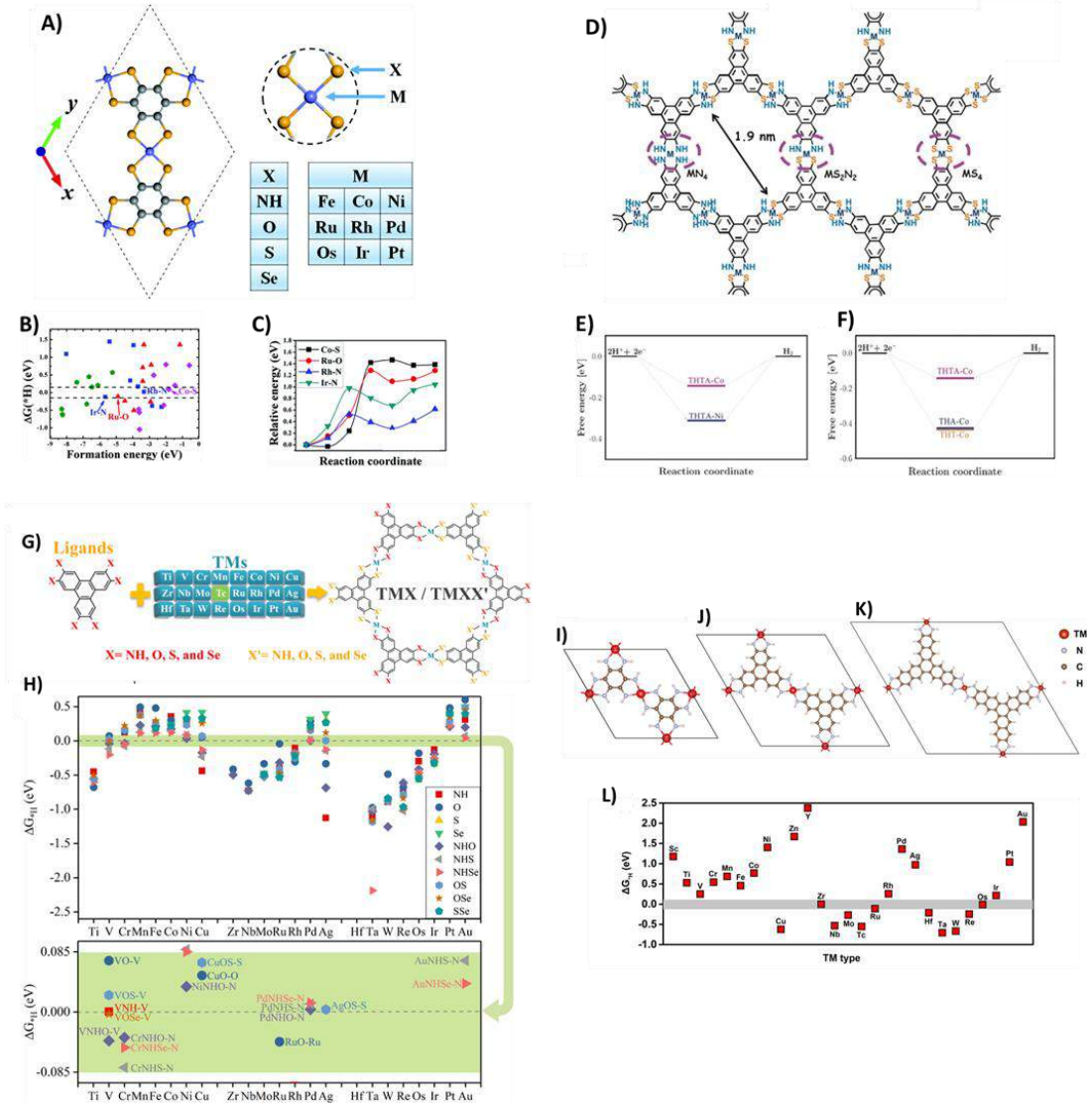

Figure 2.8. A) Top view of 2D-MOF (left) with two possible active sites for HER (right) where M = transition metals and X = "glue/crosslinked heteroatoms". B) ΔG_{H^*} for hydrogen atom adsorption on metal sites, C) relative energies of reaction coordinates on metal sites. **Figure 2.8**(A-C) are reprinted from Li *et al.*,[162] with permission from the Royal Society of Chemistry. D) Metal dithiolene-diamine incorporated 2D MOF sheet, E) ΔG_{H^*} for hydrogen adsorption on NiS_2N_2 and CoS_2N_2 active sites in 2D MOFs, F) ΔG_{H^*} of hydrogen adsorption on CoS_2N_2, CoS_2, and CoN_4. **Figure 2.8**(D-F) are reprinted from Dong *et al.*,[165] with permission from Wiley-VCH GmbH, Weinheim. G) Schematic representation of various combinations of transition metals and linkers produce a variety of MOFs, H) ΔG_{H^*} of most stable hydrogen adsorption site (top), ΔG_{H^*} between 0.085 and -0.085 eV (bottom). **Figure 2.8**(G&H)

is reprinted from Wang *et al*.,[166] with permission from Elsevier. Optimized structures of I) M_3HIB_2, J) M_3HITP_2, K) M_3HITN_2, and L) ΔG_{H^*} on M_3HITN_2, reprinted from Wang *et al.,*[167] with permission from Elsevier.

HER catalysis on 2D MOF with one type of functional material such as MN_4 or MS_4 or MO_4 are promising alternative to expensive Pt-based catalysis. However, the exact active site for HER remained elusive before a combined experimental and theoretical study by Dong and coworkers.[165] Herein, mixed functional groups *e.g.*, MS_4; metal bis(dithiolene), MN_4; metal bis(diamine), and metal mixed dithiolene-diamine were successfully incorporated into 2D MOFs as HER electrocatalysts (**Figure 2.8D**). DFT simulations were performed to compute the Gibbs free energy (ΔG_{H^*}) for H* adsorption on Co and Ni containing S_2N_2 active sites. In comparison, the CoS_2N_2 showed higher free energy (-0.12 eV) than NiS_2N_2 (-0.30 eV) counterpart (**Figure 2.8E**), indicating that Co-containing 2D MOFs exhibit remarkable electrocatalytic activity. In terms of crosslinked heteroatom influence of HER performance of 2D MOFs, the pure ligands *e.g.*, MS_4 or MN_4, showed poor HER activity than hybrid functionals (*e.g.*, MS_2N_2). **Figure 2.8F** illustrates that the ΔG_{H^*} of pure functionalities showed more negative values *i.e.*, -0.40 and -0.42 eV for MN_4 and MS_4, respectively than mixed functionality (-0.12 eV). The strong adsorption (more negative Gibb's energy) is unfavorable to desorb the H_2 molecule in the overall HER kinetic pathway. A similar comparison was established by Chen and co-workers in their study of mixed crosslinked 2D MOF for HER activity (**Figure 2.8G&H**).[166]

The semiconducting nature of 2D MOFs increased with increasing the pore size of organic ligands, which may reduce the HER efficiency. In contrast, due to the increase in intrinsic π-conjugation with increasing the aromatic ring units in organic ligands, it is expected to increase the HER catalytic activity. To the best of our knowledge gained from a survey of the literature, a comprehensive report explaining this phenomenon is still due. However, the phenomenon can be understood by comparing different reports such as Su *et al*.,[167] who computationally modeled the HER activity of TM_3(hexaiminotrinaphthylene)$_2$; TM_3HITN_2 with varying almost all the transition metal nodes. Among all the computationally modeled structures, the Zr_3HITN_2 showed excellent HER performance (**Figure 2.8L**), followed by OS_3HITN_2. In comparison between cobalt containing benzenehexaimine; $Co_3(BHI)_2$, hexaiminotriphenylene; $Co_3(HITP)_2$ and hexaiminotrinaphthylene; $Co_3(HITN)_2$,

shown in **Figure 2.8(I-K)**, the HER performance decreased with the increasing size of the organic ligands. For example, the ΔG_{H^*} of $Co_3(BHI)_2$, $Co_3(HITP)_2$, and $Co_3(HITN)_2$ are 0.34 (**Figure 2.8B**), 0.38 (**Figure 2.8H**) and >0.5 eV (**Figure 2.8L**) as measured in the studies by Li,[162] Chen,[166] and Su,[167] respectively.

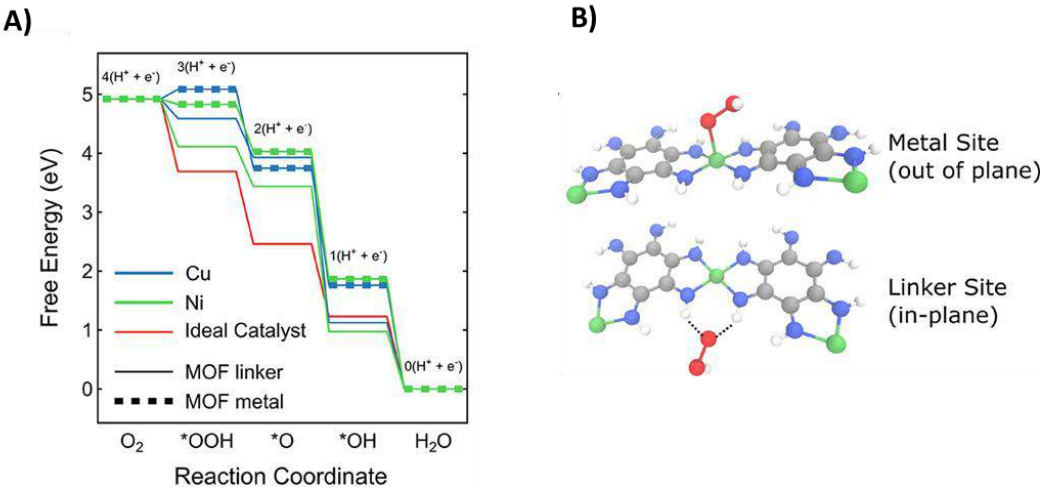

Figure 2.9. A) Gibbs free energy illustration of Ni- and Cu-HAB for ORR mechanism with the ideal catalytic pathway in red. B) Chemical illustration of binding on out-of-plane on metal (top) and in-plane linker site (bottom). Reprinted from Park *et al.*,[171] with permission from American Chemical Society.

ORR: The oxygen reduction reaction is an important electrochemical reaction in fuel cell applications and the production of hydrogen peroxide. Owing to the high cost of noble metal-based catalysts *e.g.*, Pt or Pd their scalability is limited.[168] The ORR catalytic activity of 2D MOFs has recently been demonstrated due to their excellent electrical conductivity and the catalytically active site composed of a single transition metal coordinated to four heteroatoms.[169] Furthermore, the carbon matrix such as the organic ligand can enhance the stability of the structure and the electronic properties of 2D MOFs.[170] Recently, the role of metal nodes and organic linkers in ORR catalysis was probed by Park and coworkers[171] using both experimental and computational modeling approaches. Here, the role of the linker site was analyzed by performing a similar study on M_3HIB_2 and M_3HITP_2 systems while the metal activity was studied by varying the nature of metal between Cu and Ni. The computationally evaluated adsorption energies showed that both Cu and Ni exhibit weak binding relative to the ideal ORR catalytic material (red line in **Figure 2.9**). Moreover, the out-of-plane binding on the metal site is considered weak binding while the in-plane linker binding

is significantly stronger, **Figure 2.9**. Thereby, it was concluded that the organic linker site acts as ORR active more than the metal site. This suggestion is also in accord with a study by Miner *et al*.[172]

In another computational study, an ORR catalytic activity of M_3HIB_2 MOF with a range of transition metals including Fe, Os, Ir, and Pt was studied.[173] DMol^3 software code was used to perform the GGA calculations at PW91/DNP (DNP means the double numerical atomic orbitals with polarization function) level of theory.[174] This study showed that changing the nature of the metal can effectively change the catalytic performance of a material. The best OOR catalytic performance was shown by Ir_3HIB_2, followed by Fe_3HIB_2, Pt_3HIB_2, and Os_3HIB_2, respectively. Jing *et al*.,[175] also studied the effect of metals (Cr to Cu and Ru to Pd) on the ORR catalytic performance of hexahydroxybenzene (HHB) MOF. Due to sufficient π-conjugation and strong interaction between the transition metal and organic linker, M_3HHB_2 are metallic with high electron conductivity and are expected to exhibit high ORR catalytic activity. The thermodynamic simulations for the ORR reaction mechanism were performed at the PBE function with Grimme vdW corrections using VASP software. The catalytic performance of 2D M_3HHB_2 is mainly governed by the nature of the metal node, where the best catalytic activity is shown by a Cu-containing MOF which is in good agreement with other computational studies.[176] Other than a single heteroatom crosslinked 2D MOFs, Jing *et al*.,[177] designed a novel mixed 2D MOF namely $M_3(C_6S_3O_3)_2$ (M = Cr to Cu and Ru to Pd), and explored its ORR catalytic potential by using computational methods. The catalytic activity of these newly designed 2D MOFs was simulated by the GGA-PBE method using VASP software. The simulated structural and electronic properties revealed the higher stability and excellent electrical conductivity of these designed 2D monolayers. Moreover, the catalytic activity of Co-, Fe-, Mn-, and Rh-containing MOFs was higher than ideal Pt complexes. The above studies and many more show that the catalytic performance of 2D MOFs is significantly affected by both the nature of organic ligands,[178–180] as well as the metal node,[181–183] whereas, the interlayer slipping has no significant effect on the ORR catalytic activity of a 2D MOF *e.g.*, Ni_3HITP_2.[184]

OER, CO_2RR, NRR: Similar to HER and ORR, many computational approaches have been applied to model the effect of metal, ligand, or interlayer slipping in other catalytic processes *e.g.*, oxygen evolution reaction (OER), carbon dioxide reduction

reaction (CO2RR), nitrogen reduction reaction (NRR), and Nitrogen oxide reduction reaction (NORR). Discussing each and every study here is behind the scope of this chapter because the aim is to understand the basic concepts behind the chemical properties of 2D MOFs in various fields of science. The detailed discussion on two types of electrocatalytic processes such as HER and ORR illustrates the significant effects of metal nodes, organic ligands, and layer slipping in the catalytic performance of such materials. Similar effects have widely been studied in OER,[185–187] CO_2RR,[188–195] NRR,[196] NORR,[197] and others using computational modeling techniques.

2.3.3.3.2 Gas Adsorption Applications

2D MOFs have drawn considerable attention as emerging candidates for gas sensing applications due to their diverse functionalities including metal nodes, and organic linkers with numerous types of heteroatom functionalities.[198] Experimentally, these 2D MOFs have widely been studied as selective sensors towards a wide variety of molecules including volatile organic molecules and small gaseous materials.[118,199] However, theoretical reports to study the effects of variation of metal, organic linkers and other structural diversities on adsorption selectivity are limited. Liu and co-workers were the first in studying surface gas adsorption and its effects on the electronic behaviour of 2D MOFs using a computational modeling technique.[200] It was proposed that the orbital hybridization of the transition metal node and adsorbed gas molecules led to significant variation in the electronic nature of Ni_3(benzohexathiolene)$_2$; Ni_3BHT_2 MOF. For example, CO and NO adsorbed on Ni_3BHT_2 exhibits metallic character due to the chemisorption of hetero-bi-atomic gas molecules whereas, the physisorption of O_2 molecule did not produce a significant change in the semiconducting nature of 2D Ni_3BHT_2 MOF.[200] This conductivity enhancement of Ni_3BHT_2 MOF was studied by computing the band gaps of the MOF sheet prior to and later after molecule adsorption. The geometry optimization and band gap calculations were carried out within the GGA-PBE-D2 framework using VASP software. Other than Ni_3BHT_2, O_2 adsorption was found to significantly change the semiconducting character of Co- and Rh-containing bis(benzenehexathiolene) to metallic nature.[201] A similar result was shown for $Ni_3(HITP)_2$ upon NO_2 adsorption.[202] Sarkar *et al*.,[203] has systematically investigated the gas sensing properties and their influence on the magnetic and electronic properties of the M=BHT_2 MOF (where, M

indicates Co, Fe, Mn, and Cr) using theoretical modeling. The geometry optimizations and electronic band structure calculations were performed using PBE, a GGA-DFT method along with the DZP basis set on the SIESTA package.[204] Furthermore, the charge transport properties were simulated using a module within the SIESTA package called TranSIESTA, which combines DFT and a nonequilibrium Green's function (NEGF).[205] Based on these computational simulations, remarkable changes were noticed in the electronic and magnetic properties of M_3BHT_2 after CO molecule adsorption. Similarly, the effect of the magnetic nature of metal nodes on the sensing performance of a 2D MOF *i.e.*, M_3BHT_2 was studied in a computational study by Liu *et al.*,[206] GGA-PBE-D3 on VASP software was used to perform the geometry optimization, and electronic properties calculations (*e.g.*, the density of state, electronic band gap, and electronic transportation) of bare and gas adsorbed M_3BHT_2 MOF sheet. It was observed that the ferromagnetic Fe- and Co-containing bis-BHT chemically adsorbed Co, NO, and O_2 molecules, whereas the non-magnetic Pd- and Pt-MOF strongly adsorbed NO but showed weak affinity of binding for CO and O_2 molecules. A step further, Ding and co-workers have recently studied the effect of the organic linker and the crosslinked heteroatoms on molecule adsorption or sensing.[207] By taking advantage of computational modeling, it was shown that there are two active sites for molecule adsorption including, the metal site; where the molecule adsorbs straight on the top of the metal node, and the linker site; where adsorption takes place with the heteroatom of the linker (**Figure 2.10**).[207]

Based on their computed binding energies, the binding strength of the linker site was higher with a binding energy of -0.12 eV (-11.58 kJ/mol) as compared to the metal site (-0.03 eV or -2.90 kJ/mol), whereas the amount of charge transfer was the same (-0.02 |e|) from both active sites. In the case of a defective analogue, in which a linker unit was replaced with hydroxy groups, the metal site, called Ni-2-site; next to the missing linker site, was highly activated and showed maximum binding strength with an energy of -0.80 eV (-77.19 kJ/mol). The second most stable active site was the linker site or N-site with a binding energy of -0.56 eV (-54.03 kJ/mol), followed by the metal-1-site; where the metal was coordinated with hybrid heteroatoms groups *i.e.*, NH and OH, with the binding energy of -0.24 eV (-23.16 kJ/mol), this position showed the highest charge transfer 0.14 |e| as well. Owing to all these computational studies on the modeling of sensing performance of 2D MOFs, it was possible to show that the

metal nodes as well as the heteroatom containing linker units exhibit a significant effect on the sensing performance, which may further affect the electronic and magnetic behaviours of such materials.

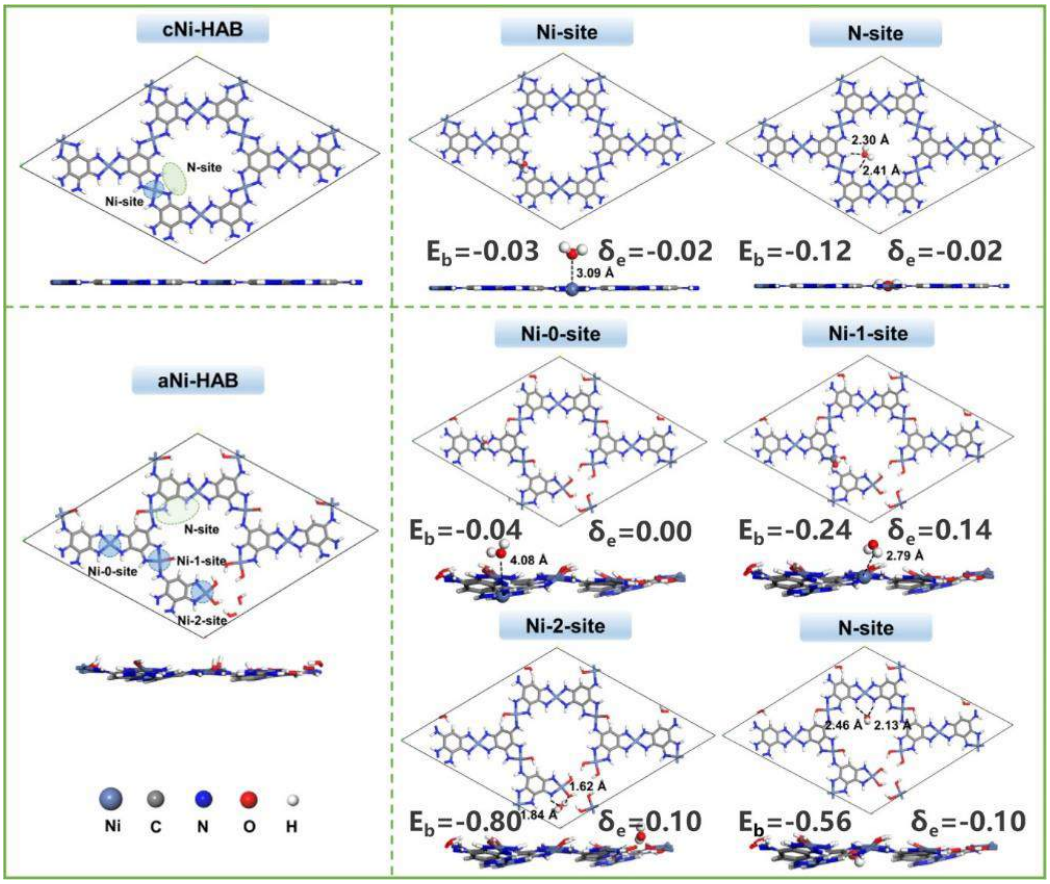

Figure 2.10. The top and side views of the monolayer model of pure and defected M_3HAB_2; where the metal is Ni with possible molecule (H_2O) adsorption. Chemical composition, purple; Ni, grey; C, blue; N, and red; O. Inset: E_b; binding energies in eV, and charge transfer (δ_e) with |e| unit of possible binding sites. Reprinted from Liu *et al.*,[207] with permission from the American Chemical Society.

2.4 Research Aims and Objectives

To the best of our knowledge, and based on the survey of the literature, the effect of MOF layers or layer-by-layer slipping is not yet studied even though this is one of the most important factors in determining properties in such types of layered 2D materials. In 2D structures, the van der Waals (vdW) forces between the MOF layers can physically and chemically integrate into the adsorption phenomenon,[208] which is not considered in most of the studies discussed above. The lack of a real picture such as the effect of multilayers and their slipping on the gas adsorption or sensing

performance of 2D MOFs drove our attention to design such an investigation. Therefore, our aim is to perform a systematic investigation of the effect of layer-to-layer slipping in 2D MOFs on their gas adsorption and sensing using combined tight binding (xTB) semi-empirical calculations and Grand Canonical Monte-Carlo (GCMC) simulations. The xTB simulation's detail, methodology, results, and discussion are described in Chapter 3, while GCMC simulations and their result and discussion are discussed in Chapter 4. For this study, 2D Metallo-phthalocyanine (M-Pth) MOF was chosen to adsorb gas molecules (NO, NH_3, and H_2S), the rationale for this particular MOF and the gases chosen for adsorption is described in the introduction to Chapter 3. For details about the methods for geometry optimization and binding energy calculations, one could refer to the methodology section of Chapter 1.

2.5 References

1 B. F. Hoskins and R. Robson, *J. Am. Chem. Soc.*, 1990, **112**, 1546–1554.

2 B. Moulton and M. J. Zaworotko, *Chem. Rev.*, 2001, **101**, 1629–1658.

3 A. Y. Robin and K. M. Fromm, *Coord. Chem. Rev.*, 2006, **250**, 2127–2157.

4 D. J. Tranchemontagne, J. L. Mendoza-Cortés, M. O'Keeffe and O. M. Yaghi, *Chem. Soc. Rev.*, 2009, **38**, 1257.

5 M. Casarin, C. Corvaja, C. di Nicola, D. Falcomer, L. Franco, M. Monari, L. Pandolfo, C. Pettinari and F. Piccinelli, *Inorg. Chem.*, 2005, **44**, 6265–6276.

6 B. Chen, M. Eddaoudi, T. M. Reineke, J. W. Kampf, M. O'Keeffe and O. M. Yaghi, *J. Am. Chem. Soc.*, 2000, **122**, 11559–11560.

7 Y. Diskin-Posner, S. Dahal and I. Goldberg, *Angew. Chem. Int. Ed.*, 2000, **39**, 1288–1292.

8 B. Chen, M. Eddaoudi, S. T. Hyde, M. O'Keeffe and O. M. Yaghi, *Science (1979)*, 2001, **291**, 1021–1023.

9 M. Eddaoudi, J. Kim, D. Vodak, A. Sudik, J. Wachter, M. O'Keeffe and O. M. Yaghi, *Proceedings of the National Academy of Sciences*, 2002, **99**, 4900–4904.

10 S. Y. Yang, L. S. Long, Y. B. Jiang, R. B. Huang and L. S. Zheng, *Chem. Mater.*, 2002, **14**, 3229–3231.

11 O. M. Yaghi, C. E. Davis, G. Li and H. Li, *J. Am. Chem. Soc.*, 1997, **119**, 2861–2868.

12 H. Li, M. Eddaoudi, M. O'Keeffe and O. M. Yaghi, *Nature*, 1999, **402**, 276–279.

13 H. Li, M. Eddaoudi, T. L. Groy and O. M. Yaghi, *J. Am. Chem. Soc.*, 1998, **120**, 8571–8572.

14 J. Kim, B. Chen, T. M. Reineke, H. Li, M. Eddaoudi, D. B. Moler, M. O'Keeffe and O. M. Yaghi, *J. Am. Chem. Soc.*, 2001, **123**, 8239–8247.

15 O. M. Yaghi, M. O'Keeffe, N. W. Ockwig, H. K. Chae, M. Eddaoudi and J. Kim, *Nature*, 2003, **423**, 705–714.

16 A. N. Khlobystov, A. J. Blake, N. R. Champness, D. A. Lemenovskii, A. G. Majouga, N. v. Zyk and M. Schröder, *Coord. Chem. Rev.*, 2001, **222**, 155–192.

17 T. Steiner, *Angew. Chem. Int. Ed.*, 2002, **41**, 48–76.

18 G. Aullón, D. Bellamy, A. Guy Orpen, L. Brammer and † Eric A. Bruton, *Chem. Comm.*, 1998, 653–654.

19 G. R. Desiraju, *Acc. Chem. Res.*, 1996, **29**, 441–449.

20 S. J. Grabowski, *J. Phys. Org. Chem.*, 2004, **17**, 18–31.

21 D. S. Coombes, S. L. Price, D. J. Willock and M. Leslie, *J. Phys. Chem.*, 1996, **100**, 7352–7360.

22 C. Janiak, *Journal of the Chemical Society, Dalton Trans.*, 2000, 3885–3896.

23 P. Pyykkö, *Chem. Rev.*, 1997, **97**, 597–636.

24 G. Wang, Y. S. Ceylan, T. R. Cundari and H. V. R. Dias, *J. Am. Chem. Soc.*, 2017, **139**, 14292–14301.

25 H. Deng, S. Grunder, K. E. Cordova, C. Valente, H. Furukawa, M. Hmadeh, F. Gándara, A. C. Whalley, Z. Liu, S. Asahina, H. Kazumori, M. O'Keeffe, O. Terasaki, J. F. Stoddart and O. M. Yaghi, *Science (1979)*, 2012, **336**, 1018–1023.

26 H. Furukawa, N. Ko, Y. B. Go, N. Aratani, S. B. Choi, E. Choi, A. Ö. Yazaydin, R. Q. Snurr, M. O'Keeffe, J. Kim and O. M. Yaghi, *Science (1979)*, 2010, **329**, 424–428.

27 O. K. Farha, I. Eryazici, N. C. Jeong, B. G. Hauser, C. E. Wilmer, A. A. Sarjeant, R. Q. Snurr, S. T. Nguyen, A. Ö. Yazaydın and J. T. Hupp, *J. Am. Chem. Soc.*, 2012, **134**, 15016–15021.

28 J. R. Long and O. M. Yaghi, *Chem. Soc. Rev.*, 2009, **38**, 1213.

29 J. Lee, O. K. Farha, J. Roberts, K. A. Scheidt, S. T. Nguyen and J. T. Hupp, *Chem. Soc. Rev.*, 2009, **38**, 1450.

30 L. J. Murray, M. Dincă and J. R. Long, *Chem. Soc. Rev.*, 2009, **38**, 1294.

31 S. Yang, X. Lin, A. J. Blake, G. S. Walker, P. Hubberstey, N. R. Champness and M. Schröder, *Nat. Chem.*, 2009, **1**, 487–493.

32 Y. E. Cheon and M. P. Suh, *Angew. Chem. Int. Ed.*, 2009, **48**, 2899–2903.

33 S. Kitagawa and K. Uemura, *Chem. Soc. Rev.*, 2005, **34**, 109.

34 R. Haldar and T. K. Maji, *CrystEngComm.*, 2013, **15**, 9276.

35 S. Takamizawa, E. Nakata, H. Yokoyama, K. Mochizuki and W. Mori, *Angew. Chem. Int. Ed.*, 2003, **42**, 4331–4334.

36 M. A. Addicoat, N. Vankova, I. F. Akter and T. Heine, *J. Chem. Theory Comput.*, 2014, **10**, 880–891.

37 P. G. Boyd, Y. Lee and B. Smit, *Nat. Rev. Mater.*, 2017, **2**, 17037.

38 C. Mellot Draznieks, J. M. Newsam, A. M. Gorman, C. M. Freeman and G. Férey, *Angew. Chem. Int. Ed.*, 2000, **39**, 2270–2275.

39 C. Mellot-Draznieks, S. Girard, G. Férey, J. C. Schön, Z. Cancarevic and M. Jansen, *Chem. Eur. J.*, 2002, **8**, 4102–4113.

40 C. Mellot-Draznieks, J. Dutour and G. Férey, *Angew. Chem. Int. Ed.*, 2004, **43**, 6290–6296.

41 C. E. Wilmer, M. Leaf, C. Y. Lee, O. K. Farha, B. G. Hauser, J. T. Hupp and R. Q. Snurr, *Nat. Chem.*, 2012, **4**, 83–89.

42 R. L. Martin and M. Haranczyk, *Cryst. Growth Des.*, 2014, **14**, 2431–2440.

43 T. F. Willems, C. H. Rycroft, M. Kazi, J. C. Meza and M. Haranczyk, *Microporous Mesoporous Mater.*, 2012, **149**, 134–141.

44 M. Pinheiro, R. L. Martin, C. H. Rycroft, A. Jones, E. Iglesia and M. Haranczyk, *J. Mol. Graph. Model.*, 2013, **44**, 208–219.

45 M. O'Keeffe, M. A. Peskov, S. J. Ramsden and O. M. Yaghi, *Acc. Chem. Res.*, 2008, **41**, 1782–1789.

46 J. L. Mancuso, A. M. Mroz, K. N. Le and C. H. Hendon, *Chem. Rev.*, 2020, **120**, 8641–8715.

47 D. Nazarian, P. Ganesh and D. S. Sholl, *J. Mater. Chem. A. Mater.*, 2015, **3**, 22432–22440.

48 S. H. Vosko, L. Wilk and M. Nusair, *Can. J. Phys.*, 1980, **58**, 1200–1211.

49 J.-H. Dou, L. Sun, Y. Ge, W. Li, C. H. Hendon, J. Li, S. Gul, J. Yano, E. A. Stach and M. Dincă, *J. Am. Chem. Soc.*, 2017, **139**, 13608–13611.

50 A. J. Clough, J. M. Skelton, C. A. Downes, A. A. de la Rosa, J. W. Yoo, A. Walsh, B. C. Melot and S. C. Marinescu, *J. Am. Chem. Soc.*, 2017, **139**, 10863–10867.

51 A. J. Clough, N. M. Orchanian, J. M. Skelton, A. J. Neer, S. A. Howard, C. A. Downes, L. F. J. Piper, A. Walsh, B. C. Melot and S. C. Marinescu, *J. Am. Chem. Soc.*, 2019, **141**, 16323–16330.

52 S. Chen, J. Dai and X. C. Zeng, *Phys. Chem. Chem. Phys.*, 2015, **17**, 5954–5958.

53 M. Hmadeh, Z. Lu, Z. Liu, F. Gándara, H. Furukawa, S. Wan, V. Augustyn, R. Chang, L. Liao, F. Zhou, E. Perre, V. Ozolins, K. Suenaga, X. Duan, B. Dunn, Y. Yamamto, O. Terasaki and O. M. Yaghi, *Chem. Mater.*, 2012, **24**, 3511–3513.

54 D. Sheberla, L. Sun, M. A. Blood-Forsythe, S. Er, C. R. Wade, C. K. Brozek, A. Aspuru-Guzik and M. Dincă, *J. Am. Chem. Soc.*, 2014, **136**, 8859–8862.

55 J. P. Perdew, J. A. Chevary, S. H. Vosko, K. A. Jackson, M. R. Pederson, D. J. Singh and C. Fiolhais, *Phys. Rev. B*, 1992, **46**, 6671–6687.

56 D. C. Langreth and M. J. Mehl, *Phys. Rev. B*, 1983, **28**, 1809–1834.

57 J. P. Perdew, J. A. Chevary, S. H. Vosko, K. A. Jackson, M. R. Pederson, D. J. Singh and C. Fiolhais, *Phys. Rev. B*, 1993, **48**, 4978–4978.

58 J. P. Perdew, K. Burke and M. Ernzerhof, *Phys. Rev. Lett.*, 1996, **77**, 3865–3868.

59 J. M. Riley, F. Mazzola, M. Dendzik, M. Michiardi, T. Takayama, L. Bawden, C. Granerød, M. Leandersson, T. Balasubramanian, M. Hoesch, T. K. Kim, H. Takagi, W. Meevasana, Ph. Hofmann, M. S. Bahramy, J. W. Wells and P. D. C. King, *Nat. Phys.*, 2014, **10**, 835–839.

60 I. Ciofini, C. Adamo and H. Chermette, *Chem. Phys.*, 2005, **309**, 67–76.

61 P. Borlido, J. Schmidt, A. W. Huran, F. Tran, M. A. L. Marques and S. Botti, *NPJ Comput. Mater.*, 2020, **6**, 96.

62 C. Adamo and V. Barone, *J. Chem. Phys.*, 1999, **110**, 6158–6170.

63 P. Janthon, S. (Andy) Luo, S. M. Kozlov, F. Viñes, J. Limtrakul, D. G. Truhlar and F. Illas, *J. Chem. Theory Comput.*, 2014, **10**, 3832–3839.

64 J. Heyd, G. E. Scuseria and M. Ernzerhof, *J. Chem. Phys.*, 2003, **118**, 8207–8215.

65 Y. Zhao and D. G. Truhlar, *Theor. Chem. Acc.*, 2008, **120**, 215–241.

66 I. I. Vrubel, N. Yu. Senkevich, E. v. Khramenkova, R. G. Polozkov and I. A. Shelykh, *Adv. Theory Simul.*, 2018, **1**, 1800049.

67 F.-M. Zhang, J.-L. Sheng, Z.-D. Yang, X.-J. Sun, H.-L. Tang, M. Lu, H. Dong, F.-C. Shen, J. Liu and Y.-Q. Lan, *Angew. Chem. Int. Ed.*, 2018, **57**, 12106–12110.

68 H. C. Dong, H. L. Nguyen, H. M. Le, N. Thoai, Y. Kawazoe and D. Nguyen-Manh, *Sci. Rep.*, 2018, **8**, 16651.

69 F. ZareKarizi, M. Joharian and A. Morsali, *J. Mater. Chem. A Mater.*, 2018, **6**, 19288–19329.

70 S. Zhang, Q. Yang, X. Liu, X. Qu, Q. Wei, G. Xie, S. Chen and S. Gao, *Coord. Chem. Rev.*, 2016, **307**, 292–312.

71 Y. Gong, C. Liu, H. Wen, L. Yan, Z. Xiong and L. Ding, *New J. Chem.*, 2011, **35**, 865.

72 J. Lei, R. Qian, P. Ling, L. Cui and H. Ju, *TrAC Trends Analyt. Chem.*, 2014, **58**, 71–78.

73 E. M. Miner and M. Dincă, *Nat. Energy*, 2016, **1**, 16186.

74 A. Schneemann, R. Dong, F. Schwotzer, H. Zhong, I. Senkovska, X. Feng and S. Kaskel, *Chem. Sci.*, 2021, **12**, 1600–1619.

75 K. Zhao, W. Zhu, S. Liu, X. Wei, G. Ye, Y. Su and Z. He, *Nanoscale Adv.*, 2020, **2**, 536–562.

76 N. Ahmad, H. A. Younus, A. H. Chughtai, K. van Hecke, Z. A. K. Khattak, Z. Gaoke, M. Danish and F. Verpoort, *Catal. Sci. Technol.*, 2018, **8**, 4010–4017.

77 M. Xu, S. Yang and Z. Gu, *Chem. Eur. J.*, 2018, **24**, 15131–15142.

78 M. Kiani, M. U. Rehman, X. Tian and B. Yakobson, *Adv. Mater. Technol.*, 2022, **7**, 2101252.

79 A. Dhakshinamoorthy, A. M. Asiri and H. Garcia, *Adv. Mater.*, 2019, **31**, 1900617.

80 V. Nicolosi, M. Chhowalla, M. G. Kanatzidis, M. S. Strano and J. N. Coleman, *Science (2013)*, **340**, 1226419.

81 Y. Zheng, F. Sun, X. Han, J. Xu and X. Bu, *Adv. Opt. Mater.*, 2020, **8**, 2000110.

82 J. Wang, N. Li, Y. Xu and H. Pang, *Chem. Eur. J.*, 2020, **26**, 6402–6422.

83 W. Mori, F. Inoue, K. Yoshida, H. Nakayama, S. Takamizawa and M. Kishita, *Chem. Lett.*, 1997, **26**, 1219–1220.

84 H. Wang, J. Getzschmann, I. Senkovska and S. Kaskel, *Microporous Mesoporous Mater.*, 2008, **116**, 653–657.

85 Y. Chi, W. Yang, Y. Xing, Y. Li, H. Pang and Q. Xu, *Nanoscale*, 2020, **12**, 10685–10692.

86 P.-Z. Li, Y. Maeda and Q. Xu, *Chem. Comm.*, 2011, **47**, 8436.

87 C. Kutzscher, A. Gelbert, S. Ehrling, C. Schenk, I. Senkovska and S. Kaskel, *Dalton Trans.*, 2017, **46**, 16480–16484.

88 Z. Wang, G. Wang, H. Qi, M. Wang, M. Wang, S. Park, H. Wang, M. Yu, U. Kaiser, A. Fery, S. Zhou, R. Dong and X. Feng, *Chem. Sci.*, 2020, **11**, 7665–7671.

89 D. Liu, B. Liu, C. Wang, W. Jin, Q. Zha, G. Shi, D. Wang, X. Sang and C. Ni, *ACS Sustain. Chem. Eng.*, 2020, **8**, 2167–2175.

90 G. Chakraborty, I.-H. Park, R. Medishetty and J. J. Vittal, *Chem. Rev.*, 2021, **121**, 3751–3891.

91 O. v. Dolomanov, A. J. Blake, N. R. Champness and M. Schröder, *J. Appl. Crystallogr.*, 2003, **36**, 1283–1284.

92 O. Delgado-Friedrichs and M. O'Keeffe, *Acta. Crystallogr. A*, 2003, **59**, 351–360.

93 E. v. Alexandrov, V. A. Blatov, A. v. Kochetkov and D. M. Proserpio, *CrystEngComm.*, 2011, **13**, 3947.

94 V. A. Blatov, A. P. Shevchenko and D. M. Proserpio, *Cryst. Growth Des.*, 2014, **14**, 3576–3586.

95 I. A. Baburin, V. A. Blatov, L. Carlucci, G. Ciani and D. M. Proserpio, *CrystEngComm.*, 2008, **10**, 1822.

96 M. O'Keeffe, M. Eddaoudi, H. Li, T. Reineke and O. M. Yaghi, *J. Solid State Chem.*, 2000, **152**, 3–20.

97 S. R. Batten and R. Robson, *Angew. Chem. Int. Ed.*, 1998, **37**, 1460–1494.

98 L. Öhrström and K. Larsson, *Dalton Trans.*, 2004, 347–353.

99 M. A. Springer, T.-J. Liu, A. Kuc and T. Heine, *Chem. Soc. Rev.*, 2020, **49**, 2007–2019.

100 V. A. Blatov, O. Delgado-Friedrichs, M. O'Keeffe and D. M. Proserpio, *Acta. Crystallogr. A*, 2007, **63**, 418–425.

101 V. A. Blatov and D. M. Proserpio, *Acta. Crystallogr. A*, 2009, **65**, 202–212.

102 L. Sun, M. G. Campbell and M. Dincă, *Angew. Chem. Int. Ed.*, 2016, **55**, 3566–3579.

103 L. E. Darago, M. L. Aubrey, C. J. Yu, M. I. Gonzalez and J. R. Long, *J. Am. Chem. Soc.*, 2015, **137**, 15703–15711.

104 T. Kambe, R. Sakamoto, K. Hoshiko, K. Takada, M. Miyachi, J.-H. Ryu, S. Sasaki, J. Kim, K. Nakazato, M. Takata and H. Nishihara, *J. Am. Chem. Soc.*, 2013, **135**, 2462–2465.

105 Z. Meng, A. Aykanat and K. A. Mirica, *J. Am. Chem. Soc.*, 2019, **141**, 2046–2053.

106 R. Dong, M. Pfeffermann, H. Liang, Z. Zheng, X. Zhu, J. Zhang and X. Feng, *Angew. Chem. Int. Ed.*, 2015, **54**, 12058–12063.

107 M. Ko, L. Mendecki and K. A. Mirica, *Chem. Comm.*, 2018, **54**, 7873–7891.

108 M. D. Hanwell, D. E. Curtis, D. C. Lonie, T. Vandermeersch, E. Zurek and G. R. Hutchison, *J. Cheminform.*, 2012, **4**, 17.

109 G. Kresse and J. Furthmüller, *Comput. Mater. Sci.*, 1996, **6**, 15–50.

110 G. Kresse, *J. Non. Cryst. Solids.*, 1995, **192–193**, 222–229.

111 J. Cui and Z. Xu, *Chem. Commun.*, 2014, **50**, 3986–3988.

112 M. D. Allendorf, A. Schwartzberg, V. Stavila and A. A. Talin, *Chem. Eur. J.*, 2011, **17**, 11372–11388.

113 D. M. D'Alessandro, J. R. R. Kanga and J. S. Caddy, *Aust. J. Chem.*, 2011, **64**, 718.

114 T. Y. Ma, S. Dai, M. Jaroniec and S. Z. Qiao, *J. Am. Chem. Soc.*, 2014, **136**, 13925–13931.

115 M. Li, H. Schnablegger and S. Mann, *Nature*, 1999, **402**, 393–395.

116 Y. Zhao, Z. Song, X. Li, Q. Sun, N. Cheng, S. Lawes and X. Sun, *Energy Storage Mater.*, 2016, **2**, 35–62.

117 M. K. Smith, K. E. Jensen, P. A. Pivak and K. A. Mirica, *Chem. Mater.*, 2016, **28**, 5264–5268.

118 M. G. Campbell, D. Sheberla, S. F. Liu, T. M. Swager and M. Dincă, *Angew. Chem. Int. Ed.*, 2015, **54**, 4349–4352.

119 A. A. Talin, A. Centrone, A. C. Ford, M. E. Foster, V. Stavila, P. Haney, R. A. Kinney, V. Szalai, F. el Gabaly, H. P. Yoon, F. Léonard and M. D. Allendorf, *Science (1979)*, 2014, **343**, 66–69.

120 N. Karl, *Synth. Met.*, 2003, **133–134**, 649–657.

121 E. M. Kiarii, K. K. Govender, P. G. Ndungu and P. P. Govender, *Chem. Phys. Lett.*, 2017, **678**, 167–176.

122 K. Vandewal, S. Albrecht, E. T. Hoke, K. R. Graham, J. Widmer, J. D. Douglas, M. Schubert, W. R. Mateker, J. T. Bloking, G. F. Burkhard, A. Sellinger, J. M. J. Fréchet, A. Amassian, M. K. Riede, M. D. McGehee, D. Neher and A. Salleo, *Nat. Mater.*, 2014, **13**, 63–68.

123 A. Sengupta, S. Datta, C. Su, T. S. Herng, J. Ding, J. J. Vittal and K. P. Loh, *ACS Appl. Mater. Interfaces*, 2016, **8**, 16154–16159.

124 L. S. Xie, L. Sun, R. Wan, S. S. Park, J. A. DeGayner, C. H. Hendon and M. Dincă, *J. Am. Chem. Soc.*, 2018, **140**, 7411–7414.

125 Y. Li, H. Li, J. He, Q. Xu, N. Li, D. Chen and J. Lu, *Chem. Asian J.*, 2016, **11**, 906–914.

126 O. Basu, S. Mukhopadhyay, S. Laha and S. K. Das, *Chem. Mater.*, 2022, **34**, 6734–6743.

127 D. M. D'Alessandro, *Chem. Comm.*, 2016, **52**, 8957–8971.

128 A. Walsh, K. T. Butler and C. H. Hendon, *MRS Bull.*, 2016, **41**, 870–876.

129 C. F. Leong, P. M. Usov and D. M. D'Alessandro, *MRS Bull.*, 2016, **41**, 858–864.

130 Z. Lin, A. McCreary, N. Briggs, S. Subramanian, K. Zhang, Y. Sun, X. Li, N. J. Borys, H. Yuan, S. K. Fullerton-Shirey, A. Chernikov, H. Zhao, S. McDonnell, A. M. Lindenberg, K. Xiao, B. J. LeRoy, M. Drndić, J. C. M. Hwang, J. Park, M. Chhowalla, R. E. Schaak, A. Javey, M. C. Hersam, J. Robinson and M. Terrones, *2d Mater.*, 2016, **3**, 042001.

131 C. H. Hendon, D. Tiana and A. Walsh, *Phys. Chem. Chem. Phys.*, 2012, **14**, 13120.

132 J. R. Winkler and H. B. Gray, *J. Am. Chem. Soc.*, 2014, **136**, 2930–2939.

133 T. C. Narayan, T. Miyakai, S. Seki and M. Dincă, *J. Am. Chem. Soc.*, 2012, **134**, 12932–12935.

134 S. Takaishi, M. Hosoda, T. Kajiwara, H. Miyasaka, M. Yamashita, Y. Nakanishi, Y. Kitagawa, K. Yamaguchi, A. Kobayashi and H. Kitagawa, *Inorg. Chem.*, 2009, **48**, 9048–9050.

135 Y. Kobayashi, B. Jacobs, M. D. Allendorf and J. R. Long, *Chem. Mater.*, 2010, **22**, 4120–4122.

136 R. Dong, P. Han, H. Arora, M. Ballabio, M. Karakus, Z. Zhang, C. Shekhar, P. Adler, P. st. Petkov, A. Erbe, S. C. B. Mannsfeld, C. Felser, T. Heine, M. Bonn, X. Feng and E. Cánovas, *Nat. Mater.*, 2018, **17**, 1027–1032.

137 C. K. Brozek and M. Dincă, *J. Am. Chem. Soc.*, 2013, **135**, 12886–12891.

138 D. Sheberla, L. Sun, M. A. Blood-Forsythe, S. Er, C. R. Wade, C. K. Brozek, A. Aspuru-Guzik and M. Dincă, *J. Am. Chem. Soc.*, 2014, **136**, 8859–8862.

139 X. Song, J. Liu, T. Zhang and L. Chen, *Sci. China. Chem.*, 2020, **63**, 1391–1401.

140 T. Zhang, Y. Wang, J. Xian, S. Wang, J. Fang, S. Duan, X. Gao, H. Song and H. Liu, *Matter and Radiation at Extremes*, 2021, **6**, 068401.

141 B. J. Holliday and T. M. Swager, *Chem. Comm.*, 2005, 23.

142 D. L. Turner, T. P. Vaid, P. W. Stephens, K. H. Stone, A. G. DiPasquale and A. L. Rheingold, *J. Am. Chem. Soc.*, 2008, **130**, 14–15.

143 D. L. Turner, K. H. Stone, P. W. Stephens, A. Walsh, M. P. Singh and T. P. Vaid, *Inorg. Chem.*, 2012, **51**, 370–376.

144 H. Sajid and T. Mahmood, *Physica E Low Dimens. Syst. Nanostruct.*, 2021, **134**, 114905.

145 T. Berry, J. R. Morey, K. E. Arpino, J.-H. Dou, C. Felser, M. Dincă and T. M. McQueen, *Inorg. Chem.*, 2022, **61**, 6480–6487.

146 P. Miry, V. Safarifard, M. Moradi and A. Massoudi, *FlatChem.*, 2022, **34**, 100382.

147 N. N. Ingle, S. Shirsat, P. Sayyad, G. Bodkhe, H. Patil, M. Deshmukh, M. Mahadik, F. Singh and M. Shirsat, *J. Mater. Sci. Mater. Electron.*, 2021, **32**, 18657–18668.

148 H. Nagatomi, N. Yanai, T. Yamada, K. Shiraishi and N. Kimizuka, *Chem. Eur. J.*, 2018, **24**, 1806–1810.

149 M. Ko, A. Aykanat, M. Smith and K. Mirica, *Sensors*, 2017, **17**, 2192.

150 M. E. Foster, K. Sohlberg, C. D. Spataru and M. D. Allendorf, *J. Phys. Chem. C*, 2016, **120**, 15001–15008.

151 M. E. Foster, K. Sohlberg, M. D. Allendorf and A. A. Talin, *J. Phys. Chem. Lett.*, 2018, **9**, 481–486.

152 Z. Zhang, D. Dell'Angelo, M. R. Momeni, Y. Shi and F. A. Shakib, *ACS Appl. Mater. Interfaces*, 2021, **13**, 25270–25279.

153 M. Wang, R. Dong and X. Feng, *Chem. Soc. Rev.*, 2021, **50**, 2764–2793.

154 J. Cheng, X. Yang, X. Yang, R. Xia, Y. Xu, W. Sun and J. Zhou, *Fuel Process. Technol.*, 2022, **229**, 107174.

155 Z. Zhang, Y. Wang, B. Niu, B. Liu, J. Li and W. Duan, *Nanoscale*, 2022, **14**, 7146–7150.

156 P. Liu, J. Li, J. Yan and W. Song, *Phys. Chem. Chem. Phys.*, 2022, **24**, 8344–8350.

157 G. Hai, H. Gao, X. Huang, L. Tan, X. Xue, S. Feng and G. Wang, *Chem. Sci.*, 2022, **13**, 4397–4405.

158 X. X. Wang, M. T. Swihart and G. Wu, *Nat. Catal.*, 2019, **2**, 578–589.

159 H.-F. Wang and Q. Xu, *Matter.*, 2019, **1**, 565–595.

160 S. Liu, H. Yang, X. Su, J. Ding, Q. Mao, Y. Huang, T. Zhang and B. Liu, *J. Energy Chem.*, 2019, **36**, 95–105.

161 X. Zou and Y. Zhang, *Chem. Soc. Rev.*, 2015, **44**, 5148–5180.

162 Y. Ji, H. Dong, C. Liu and Y. Li, *Nanoscale*, 2019, **11**, 454–458.

163 J. Hafner, *J. Comput. Chem.*, 2008, **29**, 2044–2078.

164 G. Henkelman, B. P. Uberuaga and H. Jónsson, *J. Chem. Phys.*, 2000, **113**, 9901–9904.

165 R. Dong, Z. Zheng, D. C. Tranca, J. Zhang, N. Chandrasekhar, S. Liu, X. Zhuang, G. Seifert and X. Feng, *Chem. Eur. J.*, 2017, **23**, 2255–2260.

166 R. Wang, C. He, L. Fu and W. Chen, *Mater. Today Nano.*, 2022, **20**, 100278.

167 C. Wang, M. Zhang, J. Song, Y.-T. Shan and Z.-M. Su, *Appl. Surf. Sci.*, 2022, **601**, 154241.

168 Z. Chen, S. Chen, S. Siahrostami, P. Chakthranont, C. Hahn, D. Nordlund, S. Dimosthenis, J. K. Nørskov, Z. Bao and T. F. Jaramillo, *React. Chem. Eng.*, 2017, **2**, 239–245.

169 J. H. Zagal and M. T. M. Koper, *Angew. Chem. Int. Ed.*, 2016, **55**, 14510–14521.

170 J. W. F. To, J. W. D. Ng, S. Siahrostami, A. L. Koh, Y. Lee, Z. Chen, K. D. Fong, S. Chen, J. He, W.-G. Bae, J. Wilcox, H. Y. Jeong, K. Kim, F. Studt, J. K. Nørskov, T. F. Jaramillo and Z. Bao, *Nano. Res.*, 2017, **10**, 1163–1177.

171 J. Park, Z. Chen, R. A. Flores, G. Wallnerström, A. Kulkarni, J. K. Nørskov, T. F. Jaramillo and Z. Bao, *ACS Appl. Mater. Interfaces*, 2020, **12**, 39074–39081.

172 E. M. Miner, S. Gul, N. D. Ricke, E. Pastor, J. Yano, V. K. Yachandra, T. van Voorhis and M. Dincă, *ACS Catal.*, 2017, **7**, 7726–7731.

173 X. Yang, Q. Hu, X. Hou, J. Mi and P. Zhang, *Catal. Commun.*, 2018, **115**, 17–20.

174 B. Delley, *J. Chem. Phys.*, 1990, **92**, 508–517.

175 J. Zhang, Z. Zhou, F. Wang, Y. Li and Y. Jing, *ACS Sustain. Chem. Eng.*, 2020, **8**, 7472–7479.

176 Z. Gao, H. Ma, S. Yuan, H. Ren, Z. Ge, H. Zhu, W. Guo, F. Ding and W. Zhao, *Appl. Surf. Sci.*, 2022, **601**, 154187.

177 T. Li, M. Li, X. Zhu, J. Zhang and Y. Jing, *J Mater. Chem. A Mater.*, 2021, **9**, 24887–24894.

178 R. Iqbal, S. Ali, G. Yasin, S. Ibraheem, M. Tabish, M. Hamza, H. Chen, H. Xu, J. Zeng and W. Zhao, *Chem. Eng. J.*, 2022, **430**, 132642.

179 X. Chen, S. Huang, F. Sun and N. Lai, *J. Phys. Chem. C*, 2020, **124**, 1413–1420.

180 Q. Zhao, D. Zhu, X. Zhou, S.-H. Li, X. Sun, J. Cui, Z. Fan, M. Guo, J. Zhao, B. Teng and B. Cheng, *ACS Appl. Mater. Interfaces*, 2021, **13**, 52960–52966.

181 B. Xiao, H. Zhu, H. Liu, X. Jiang and Q. Jiang, *Front. Chem.*, 2018, **6**, 351.

182 K. Dong, J. Liang, Y. Wang, L. Zhang, Z. Xu, S. Sun, Y. Luo, T. Li, Q. Liu, N. Li, B. Tang, A. A. Alshehri, Q. Li, D. Ma and X. Sun, *ACS Catal.*, 2022, 6092–6099.

183 X. Chen, F. Sun, F. Bai and Z. Xie, *Appl. Surf. Sci.*, 2019, **471**, 256–262.

184 Y. Tian, Z. Zhang, C. Wu, L. Yan, W. Chen and Z. Su, *Phys. Chem. Chem. Phys.*, 2018, **20**, 1821–1828.

185 J. Wang, Y. Fan, S. Qi, W. Li and M. Zhao, *J. Phys. Chem. C*, 2020, **124**, 9350–9359.

186 X. Wei, S. Cao, H. Xu, C. Jiang, Z. Wang, Y. Ouyang, X. Lu, F. Dai and D. Sun, *ACS Mater. Lett.*, 2022, **4**, 1991–1998.

187 G. Gao, E. R. Waclawik and A. Du, *J. Catal.*, 2017, **352**, 579–585.

188 Q. Cui, G. Qin, W. Wang, K. R. Geethalakshmi, A. Du and Q. Sun, *Appl. Surf. Sci.*, 2020, **500**, 143993.

189 Y. Xiao, D. Chen and R. Chen, *Electrochim. Acta.*, 2021, **378**, 138028.

190 G. Xing, L. Cheng, K. Li, Y. Gao, H. Tang, Y. Wang and Z. Wu, *New J. Chem.*, 2020, **44**, 12299–12306.

191 Y. Tian, T. Zhao, C. Zhao and Likai Yan, *Appl. Surf. Sci.*, 2022, **597**, 153724.

192 G. Xing, L. Cheng, K. Li, Y. Gao, H. Tang, Y. Wang and Z. Wu, *Appl. Surf. Sci.*, 2021, **550**, 149389.

193 Y. Tian, Y. Wang, L. Yan, J. Zhao and Z. Su, *Appl. Surf. Sci.*, 2019, **467–468**, 98–103.

194 J. Liu, D. Yang, Y. Zhou, G. Zhang, G. Xing, Y. Liu, Y. Ma, O. Terasaki, S. Yang and L. Chen, *Angew. Chem. Int. Ed.*, 2021, **60**, 14473–14479.

195 H. Zhang, L. Cheng, K. Li, Y. Wang and Z. Wu, *Mol. Phys.*, 2022,**14**, e2064785.

196 Q. Cui, G. Qin, W. Wang, G. K. R., A. Du and Q. Sun, *J. Mater. Chem. A Mater.*, 2019, **7**, 14510–14518.

197 B. Huang, B. Chen, G. Zhu, J. Peng, P. Zhang, Y. Qian and N. Li, *ChemPhysChem.*, 2022, **4**, e202100785.

198 S. Suginome, H. Sato, A. Hori, A. Mishima, Y. Harada, S. Kusaka, R. Matsuda, J. Pirillo, Y. Hijikata and T. Aida, *J. Am. Chem. Soc.*, 2019, **141**, 15649–15655.

199 M. G. Campbell, S. F. Liu, T. M. Swager and M. Dincă, *J. Am. Chem. Soc.*, 2015, **137**, 13780–13783.

200 H. Liu, X. Li, L. Chen, X. Wang, H. Pan, X. Zhang and M. Zhao, *J. Phys. Chem. C*, 2016, **120**, 3846–3852.

201 M. Ruan, Q. Yang, M. Wu, B. Wang and J. Liu, *Chem. Phys. Lett.*, 2019, **731**, 136581.

202 H. Liu, L. Chen, D. Wang, C. Shi, X. Li, Y. He and J. Zhao, *Appl. Phys. Lett.*, 2020, **117**, 013105.

203 C. Chakravarty, B. Mandal and P. Sarkar, *J. Phys. Chem. C*, 2016, **120**, 28307–28319.

204 J. M. Soler, E. Artacho, J. D. Gale, A. García, J. Junquera, P. Ordejón and D. Sánchez-Portal, *J. Phys. Condens. Matter.*, 2002, **14**, 2745–2779.

205 S. Datta, *Electronic Transport in Mesoscopic Systems*, Cambridge University Press, 1995.

206 H. Liu, X. Li, C. Shi, D. Wang, L. Chen, Y. He and J. Zhao, *Phys. Chem. Chem. Phys.*, 2018, **20**, 16939–16948.

207 C. Liu, Y. Gu, C. Liu, S. Liu, X. Li, J. Ma and M. Ding, *ACS Sens.*, 2021, **6**, 429–438.

208 Y. Liu, Y. Huang and X. Duan, *Nature*, 2019, **567**, 323–333.

Chapter 3

3 Structures Modeling of Porous 2D-Layered Ni/Ni- and Ni/Cu-Phthalocyanine MOFs and Host-Guest Interactions with Small Gas Molecules

Chapters 2 and 3 describe the main research of this thesis, where we considered layered 2D phthalocyanine (Pc) metal-organic frameworks and studied the effect of interlayer slipping on the small gaseous molecules *i.e.*, NO, NH_3, and H_2S, binding or adsorption properties. We further demonstrated the role of dual-redox-sites of 2D Pc-MOFs with Nickel phthalocyanine ligands linked by MO_4 nodes, M = Ni or Cu. For this purpose, we performed quantum mechanics (QM) and grand canonical Monte-Carlo (GCMC) simulations, where the former describes the binding strength while the latter describes the adsorption capacity of MOF materials. In this Chapter, we only discussed and compared the binding strength of 2D Ni/Ni-, and Ni/Cu-Pc MOFs along with the effect of interlayer slipping using the extended tight binding semiempirical method; GFN1-xTB whereas, the GCMC study is described in the next chapter. At first, energetically stable stacking geometries of considered MOF are explored and discussed, followed by the study of the interlayer slipping effect on the binding strength.

3.1 Abstract

The energetic stability of layered metal-organic frameworks (MOFs) in slipped structures suggests that interlayer slipping remarkably affects gas adsorption and could be used as an essential parameter to design 2D MOFs with excellent binding properties. In this research, the role of interlayer slipping on small gas molecules binding on layered Ni/Ni- and Ni/Cu-Pc MOFs using quantum mechanics has systematically been studied. It is observed that the slipping of layers affects the number of preferred NO binding regions and corresponding binding energies, which results in a drastic increase in the adsorption uptake. The adsorption behaviour is explained using a simplified model of phthalocyanine 2D MOF that also provides an optimal range of parallel slipping distances to surge the gas storage performance. The results

illustrate that optimized and energetically stable slipped-AA MOF structures, with offsets of 6.00 Å, have approximately double the adsorption affinity as compared to eclipsed structures. For example, the gas (NO) binding energies of stable slipped-AA structures are -243 and -242 kJ/mol, which are lower than those of eclipsed-AA counterparts, *e.g.*, -155 and -113 kJ/mol, respectively. This is because the possible active sites to bind gas molecules are hidden in eclipsed-AA structures whereas, these sites are exposed and available for binding in energetically stable slipped-AA structures. This indicates that the binding strength in 2D MOFs is strongly influenced by the parallel slipping of layers, which cannot be neglected practically. The molecular binding insight presented in this research is quantitatively applicable to other slipped MOFs or COFs and is fruitful for the development of similar materials for improved gas storage applications.

3.2 Introduction

Industrial growth has brought immense advancements to mankind but this revolution has also been accompanied by several unwanted consequences. Global warming, among the various environmental issues, produces drastic damage to lives on the globe.[1] Air pollution, containing all kinds of chemical wastes including, dust, greenhouse gases, toxic gases, *etc* are known cause of global warming. Nitrogen oxides, commonly known as NO_x, are highly reactive and toxic gases produced *via* human activities, burning of solid wastes, and fossil fuels.[2,3] In these processes, the nitrogen combines with oxygen in various oxidation states and generates a collection of gaseous products, including nitric oxide (NO), nitrogen dioxide (NO_2), dinitrogen trioxide (N_2O_3), dinitrogen tetroxide (N_2O_4), dinitrogen pentoxide (N_2O_5), and nitrous oxide (N_2O), which are responsible for ozone depletion and other environmental hazards. Among these toxins, NO can cause serious health hazards *i.e.*, gene mutation and limited oxygen-blood supply.[4] Owing to the high toxicity, its control and monitoring have dedicated extreme intentions. Various kinds of materials have been designed for NO treatment in order to reduce NO concentration by adsorption on suitable surfaces[5] or to produce environmental friendly byproducts *via* catalytic conversion.[6] Since the advent of Metal-Organic Frameworks (MOFs), many efforts have been devoted in utilizing MOFs as potential candidates for NO adsorption. A

detailed discussion on this topic can be found in a recent review article by Ho and co-workers.[7]

Like NO_x, ammonia (NH_3) and hydrogen sulfide (H_2S) gases have also been known as serious health hazards, causing irritation to the lungs, respiratory tract, and eyes.[8,9] Long exposure (*e.g.*, 10 minutes) to ≥50 ppm of NH_3 and over 250 ppm of H_2S may cause blindness, blebs, lung disease, and ultimately death.[8,10] Thus, their reliable and rapid detection is vital to safeguard humankind. The role of MOFs as air quantity treatment media especially for NH_3[11] and H_2S[12] are listed in the review articles by Kim and co-workers.

MOF is an emerging family of highly porous, crystalline, and ordered-dimensional polymers composed of metal ion/cluster centers coordinated with organic ligands or linkers.[13] Due to their hybrid functionality, high accessible surface area, and exceptional porosity, MOFs are promising candidates for sensing purposes.[14,15] However, many challenges still prevail in the application of MOFs as chemical sensors. For instance, the crystallinity of some MOF materials may collapse in harsh reactive conditions due to their lack of stability.[16] Furthermore, most MOFs exhibit low electrical/charge conductivity,[17] which restricted the acquisition of chemiresistive signals upon sensing. The synthesis of two-dimensional (2D) conductive MOFs brings their utility in manufacturing chemiresistive sensors.[18,19] Since, Dincă *et al.*,[20] first reported the chemiresistive sensitivity of a 2D MOF towards ammonia gas below ppm level, more efforts have been devoted to search the chemical sensitivity of conductive 2D MOF.[21,22] By now, a variety of conductive 2D MOFs have been known depending on the nature of the organic ligands (*e.g.*, benzene,[23] triphenylene,[24] graphdiyne,[19] and phthalocyanine[25]), metal nodes,[26] and heteroatom functionalities[27,28] (*e.g.*, S, O, Se, & NH, *etc*) to bind both the building units together. Recent studies have predicted the potential role of these 2D MOFs in chemical sensor devices,[20,29,30] which has already been discussed in Chapter 2.

Despite the successful implementation of some 2D MOFs as chemical sensors, the demonstration of chemiresistive sensitivity of 2D Metallo-phthalocyanine (Pc)-MOFs is still under-explored and the underlying mechanisms are not fully known. 2D conductive Pc-MOFs have practically been realized for the electrochemical sensing of nitrites,[31] volatile organic compounds (VOCs),[32] and biological molecules.[33,34] Owing

to the bimetallic nature of phthalocyanine-based MOFs, their gas sensitivity is high as compared to conventional 2D-MOFs (*e.g.*, triphenylene-based MOFs).[18] In such bi-metallic MOFs, each metal comes from a different building block[35,36], however, both the metal centers are equally important to bind the foreign gas molecules. Hence, the 2D conductive Pc-MOFs can serve as potential gas sensors as compared to the traditional 2D MOFs. Kasai *et al*.,[37] attempted to explain the effect of the central metal of a nonperiodic MPc unit on a binding diatomic gas molecule *e.g.*, nitric oxide (NO) using the computational modeling technique. For this purpose, the author investigated the binding strength of NO molecule on the nonperiodic MPc unit, where M was varying between the rare element of the first-row transition metals. Despite the dependence of binding strength on the nature of the metal but the metallic center of MPc is the most active site for adsorbing NO molecules concluded by the author.[38] Aykanat[39] and co-authors compared the binding affinity of both metallic sites *e.g.*, the metal center in the MPc body and a metal node by adsorbing CO molecule. Based on the computational result computed with GGA-PBE exchange-correlation DFT functional with double numerical polarization (DNP) basis set, it was concluded that the gas binding is substantially influenced by the nature of metal (*e.g.*, Ni or Cu) rather than the metal's position in the MOF structure. The literature regarding conductive M-Pc 2D MOFs-based chemical sensors is restricted to either the nonperiodic single metal-containing Pc units or a monolayer of bimetallic 2D Pc-MOFs.[40] Such studies are unable to draw a real picture of the interaction mechanism in Metallo-phthalocyanine-based 2D layered MOFs (MPc) because the role of layers parallel stacking and their slipping in these materials cannot be ignored. Therefore, a comprehensive report to rationalize the effect of interlayer slipping on the molecule binding mechanism and the efficiency of periodic MPc is urgently needed. This motivated us to design a systematic investigation to study the effect of interlayer slipping with different metallic centers (*vide infra*). Moreover, an experimental study by Mirica and co-workers assisted us in this context.[41] Their study demonstrated the activity of 2D $MPc(M'O_4)_2$ MOF (where, M = Ni, inside the Pc body and M' = Ni or Cu node) in chemiresistive sensor applications. The designed devices achieved exceptionally high sensitivity and ultrahigh detection limits for NO, NH_3, and H_2S with a very short exposure time (1.5 min).

Herein, the two $MPc(M'O_4)_2$ analogs are named Ni/Ni-Pc and Ni/Cu-Pc for ease of understanding, where the first metal (Ni) represents the metal inside the Pc-unit, while the second metal (Ni or Cu) indicates the metal nodes between the two phthalocyanine units. Prompted by an experimental study,[41] we are interested to find the answers to the following questions by using a computational modeling tool;

a) which is the most active position for binding NO, NH_3, and H_2S on periodic Ni/Ni- and Ni/Cu-Pc MOFs?

b) How does the interlayer slipping affect the adsorption affinity of these MOFs?

c) What would be the effect of replacing the NiO_4 node with the CuO_4 node on binding strength and behaviour?

d) How the adsorption capacity is affected by changing the nature of metal nodes as well as the interlayer slipping?

This research is organized as; first, the energetic stabilities of slipped layer structures including, AA-eclipsed, AA-slipped, and AB-staggered, of MPcM' MOFs are described on the basis of the potential energy surface (PES) landscape. Secondly, the binding mechanisms and strengths of NO, NH_3, and H_2S onto the various MOF analogs are discussed in the 2nd portion of the Results and Discussion of this Chapter. Finally, the loading capacity comparison of Ni/Ni- and Ni/Cu-Pc MOFs analogs for all considered gas molecules is presented in Chapter 4.

3.3 Computational Methodology

3.3.1 Models for MOF Slipped Structures

All the Density Functional Tight Binding (DFTB) calculations for Ni/Ni- and Ni/Cu-Pc MOFs were implemented in AMS software version 2020.1.[42] The periodic monolayers of Ni/Ni- and Ni/Cu-Pc MOFs consisting of a Ni-Pc ligand and tetrahedrally bonded NiO_4 & CuO_4, respectively, as a node, were constructed and optimized at the GFN1-xTB method (see section 3.2.3) without any geometry constrain (**Figure 3.1**). From the optimized monolayers, the relative energies of bilayer Pc-MOFs in eclipsed-AA, slipped-AA, and staggered-AB structures were calculated using single-point DFTB calculations. To develop the slipped structures of the Ni/Ni- and Ni/Cu-Pc MOFs, the supercells consisting of two layers, separated by 3.3 Å along

the *z*-direction, were used where the top layer slides parallel to the neighbouring bottom layer along *x*-, *y*- and *xy*-plane with the offset increasing by an increment of 0.5 Å. Along all the directions, 361 structures for each MOF were produced in the increasing magnitude of slipping distance from eclipsed-AA (zero slip) to staggered-AB (maximum distance, when Ni-Pc units in both the layers are equally separated from all the directions). The PESs were plotted using R-Studio software[43] based on the relative energies with respect to the eclipsed-AA structure. For both the Ni/Ni- and Ni/Cu-Pc MOFs, the relative stability of the slipped-AA structures was more pronounced, consistent with the literature,[44] with the offset of 6.00 Å in the *xy*-plane because the major portion of all the layers is exposed. Periodically, the slipped-AA with 6.00 Å offset produces slipped-ABC geometries in the *z*-plane thus creating an additional accessible surface area. On the other side, in staggered-AB structures, many of the functional groups are not accessible due to the *z*-plane periodicity showing ABAB structures. The eclipsed-AA is energetically least favourable due to the strong columbic repulsions between the functional groups of each layer that is sandwiched between the two neighbouring layers.[45,46]

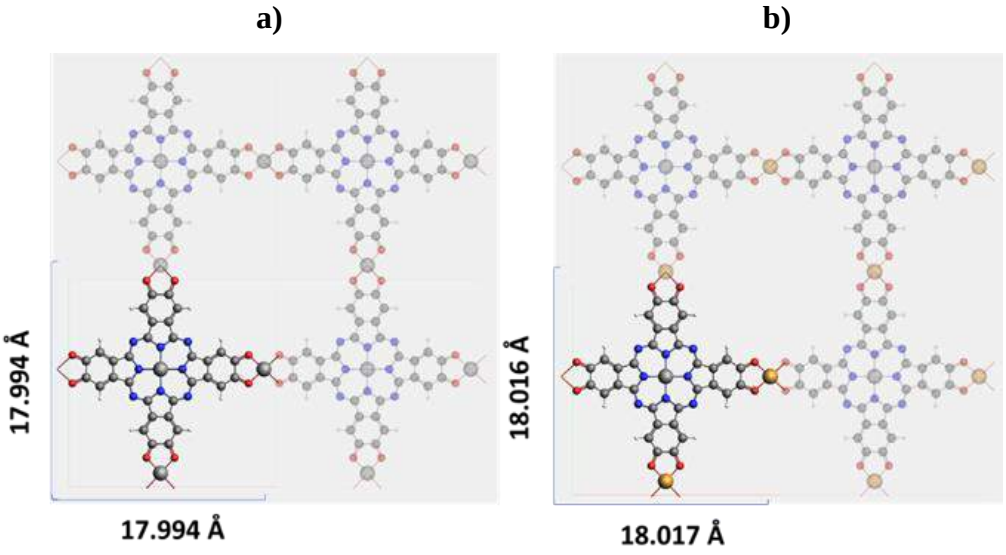

Figure 3.1. Monolayer 2×2 supercells of a) Ni/Ni-Pc MOF, and b) Ni/Cu-Pc MOF. Unit cells (1×1) with lattice parameters are highlighted.

3.3.2 Binding Energy Calculations

In the next step, the six-layers structures of Ni/Ni- and Ni/Cu-Pc MOFs were generated and optimized, to minimize the repulsion by increasing the gap between the adsorbed

gas molecules in a periodic system. To get the periodic structure of slipped-AA MOF, each top layer was allowed to shift at the best possible distance from the lower one *i.e.*, 6.00 Å. Lastly, the gas molecules including, NO, NH_3, and H_2S were individually stochastically placed in both the analogues *i.e.*, less stable eclipsed-AA and stable slipped-AB of Ni/Ni- and Ni/Cu-MOFs for comparison using the Kick3 stochastic structure generator.[47] As a result, 100 structures were generated for each candidate to understand the most likely interaction motif between the gas molecules and MOFs. A total of 600 structures including 100 for each NO@Ni/Ni-Pc, NO@Ni/Cu-Pc, NH_3@Ni/Ni-Pc, NH_3@Ni/Cu-Pc, H_2S@Ni/Ni-Pc, and H_2S@Ni/Cu-Pc MOFs was subjected to geometry optimization at GFN1-xTB method with constrained lattice parameters such as the lattices angles were fixed to be at 90° as well as the length a = b = 17.994 Å (for Ni/Ni-Pc) or 18.017 Å (Ni/Cu-Pc) and c = 19.00 Å. The binding energies (E_B) are estimated as;

$$E_B = E_{(Gas-MOF)} - \left[E_{(Gas)} + E_{(MOF)}\right] \quad (3.1)$$

Subsequently, the closest distances between the binding atoms of adsorbed gas molecules and MOFs were interrogated within the separation of 3.00 Å.

3.3.2.1 GFN1-xTB

Computational modeling including, structure optimizations, frequency calculations, and optoelectronic properties of MOFs is dominated by density functional theory (DFT) calculations.[48] Thousands of research articles have been published to describe the structure-property relationship of both experimental and hypothetical MOFs using DFT calculations, a few examples are described in a review by Cheetham *et al*.[49] DFT methods including, PBE,[50] B3LYP,[51] HSE06[52] and many more are highly accurate in computing the structures of MOFs with heavy atom root mean square deviation (hRMSD) less than 0.05 Å. However, these methods are computationally very expensive for large (containing more than 1000 atoms), periodic MOF systems.[52] For instance, the reported CPU time per optimization cycle is more than 10^4 seconds for the Rh-MOF (480 atoms) on an Intel Xeon-E5-266.V4@2.00 GHz CPU.[53]

Many interesting periodic MOFs with 2000-5000 atoms in a unit cell are not viable for routine DFT optimizations, such investigations are performed by empirical force-field (FF) models.[54] Force fields variously parameterize bond lengths, angles, torsions, and

nonbonded interactions, and are consequently up to five to ten orders of magnitude faster than DFT and therefore applicable for larger MOFs (>1000 atoms).[55] The hRMSD of the Universal Force Field (UFF) is greater than 2.00 Å for the common MOF-5, as compared to only 0.04 Å for the computationally efficient DFT method B97-3c. Initially, this poor and unpredictable accuracy was a serious drawback of force field methods, however, several parameterizations of different Force Fields have variously overcome this limitation.[56,57] Unfortunately, the need for specific parametrizations restricts the applicability of force fields to MOFs where sufficient experimental data is available – most general force fields *i.e.*, AMBER,[58] CHARMM,[59] UFF,[60] MM1, and MM2 are only suitable for specific combinations of (mostly organic) atoms, which limits their usefulness given the wide variety of metal nodes in MOFs. A further limitation on the use of force field methods is the limited range of properties available – while the structure and mechanical properties[61] are readily accessible, electronic properties are not.

The semiempirical approach especially Density Functional Tight Binding (DFTB), which approximates high-level DFT with pre-calculated parameters and a minimal basis set, is a reliable strategy to maintain the accuracy of *ab initio* methods[62] with less computational cost. Although DFTB methods are used in modeling MOFs, however, the lack of parameterization for many of the metal atoms restricts their utility.[63] In order to address this limitation of DFTB, Grimme *et al.*,[64] have recently developed an extended tight binding (xTB) semiempirical method; GFN-1xTB to model reasonable geometrical structures of porous (COFs) and hybrid-porous (MOFs) materials. The bulk materials containing $>10^3$ atoms can reliably be modeled using the GFN1-xTB method in a limited computational time similar to force field methods. The theoretical background of GFN1-xTB is discussed in Chapter 1, section 1.1.1.2.

The GFN-xTB method is recently benchmarked with DFT functional for the adsorption of molecules, including CO_2, N_2, H_2, CH_3OH, and C_6H_6, in MOF by Grimme and coworkers.[53] The mean absolute deviation (MAD) of the GFN method is remarkably close to the high-level DFT functionals, which justified its applications for adsorption screening especially, active site modeling for the binding of small molecules in MOF. Moreover, the performance of GFN*n*-xTB methods (n = 1 & 2) specifically for open-shell transition metal systems *e.g.*, Cu^{2+} has recently been examined by Minenkov *et al.*,[65] *via* reproducing the conformational energies against

M06, ωB97X-V, PBE0-D3(BJ), and PBE-D3(BJ) and concluded the significantly better performance of tight-binding semiempirical methods for open-shell systems in comparison with semiempirical methods (PM6 and PM7) and some of the conventional DFT methods (*e.g.*, B97-3c). Owing to the reliability and fast computations (see Chapter 1, section 1.1.2) than that of DFT and force field methods, the GFN1-xTB method is employed to present the binding energies or binding site screening of small gases molecules (NO, NH_3, and H_2S) in Phthalocyanine-based MOFs. SCM-AMS[66] and DFTB+[67] computational tools allow periodic optimizations of materials with GFN-xTB methods, thus, in this work, all the calculations are performed using the AMS modeling tool.

3.4 Results and Discussion

3.4.1 Model for MOF Structures

The single layer of 2D Ni/Ni- and Ni/Cu-Pc MOFs have a square planner structure with $a = \beta = \gamma = 90°$.[25] The considered MOFs including Ni/Ni-Pc and Ni/Cu-Pc have identical organic linkers *i.e.*, Ni-phthalocyanine (NiPc) while inorganic nodes are composed of tetrahedrally bonded NiO_4 and CuO_4, respectively. Each primitive cell of the MOF consists of one Ni-Pc and two nodes. The lattice parameters of optimized single layer Ni/Ni-Pc and Ni/Cu-Pc MOFs in the *x*/*y*-plane are 17.99 and 18.016 Å (**Figure 3.1**), respectively, which is well consistent with the literature.[68]

3.4.1.1 Stable Interlayer Stacked Structures and Potential Energy Landscape

A monolayer structure of Ni/Ni- and Ni/Cu-Pc MOFs is relaxed by geometry optimization at the GFN1-xTB method, followed by the construction of two layers-stacked structures by varying the horizontal (*x/y*) offsets. Based on the horizontal slip in the *x*-, *y*-, or *xy*-plane, the stacking structures are of different types including eclipsed-AA; both the adjacent layers are on top of one another, slipped-AA; a top layer moves apart either in *x*-, *y*-, or *xy*-direction, and staggered-AB; the top layer slipped haft the offset of the lower layer.[69] In the eclipsed-AA arrangement of 2D MOF layers, the atoms of neighboring layers are fully stacked, forming the one-dimensional tetragonal mesoporous channel. These eclipsed structures are used as a reference to build different slipped structures for both Ni/Ni- and Ni/Cu-Pc MOFs. To construct

the slipped structures, supercells containing two layers are used with an interlayer separation of 3.30 Å (similar to the ref.[35]), and the top layer is allowed to shift parallel to the lower one with a distance of 0.5 Å along *x*, *y*, and *xy* directions.[70] Given different values for shifts in the *x* and *y* directions, a total of 361 slipped structures of each MOF are possible, however here we discuss slipping only either $x = 0$, $y = 0$, and $x = y$. The slipped structures namely slipped-AAX, slipped-AAY, and slipped-AA when *x* is zero, *y* is zero and *x* & *y* are equal, respectively are considered, in the increasing magnitude of slipping distance from eclipsed-AA (zero slipping) to either slipped-AA, when NiPc units of two layers reach to maximum distance in *x* or *y* plane or staggered-AB, where Ni-Pc units are at the centre of the tetragonal pores. In the eclipsed arrangement, the atoms of each layer are a sandwich between two neighbouring layers. On the contrary, the portion of the middle layer becomes exposed, creating an additional surface area in slipped and staggered structures.

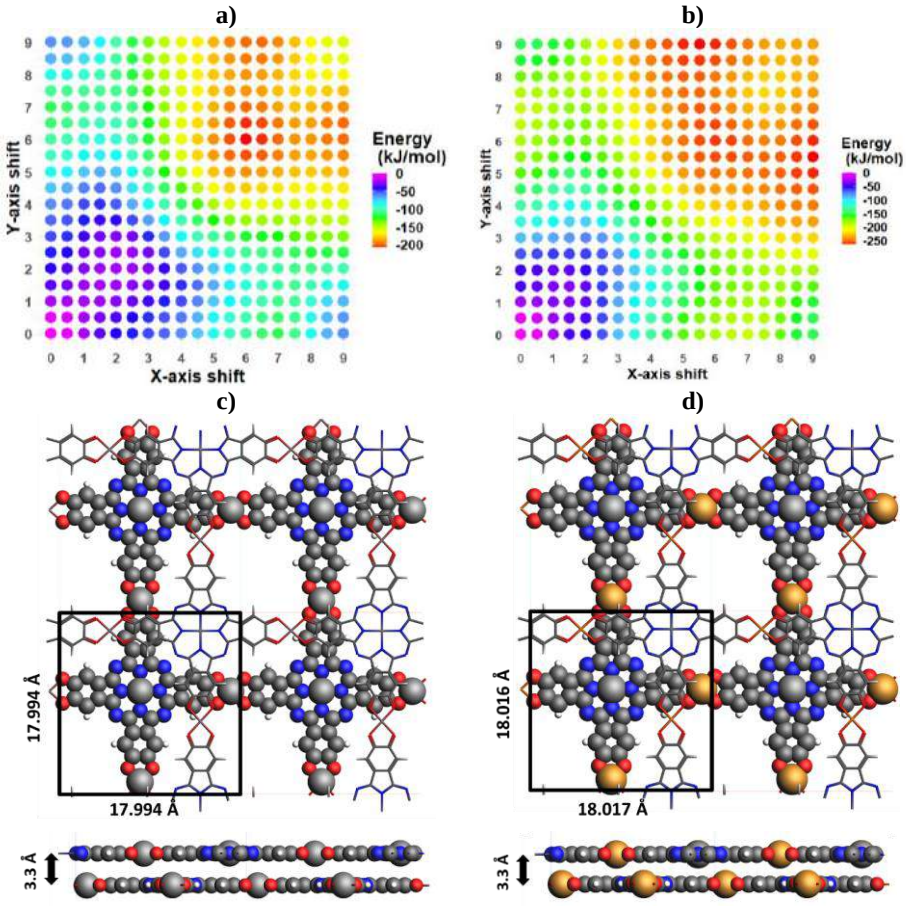

Figure 3.2. a) PES for bilayers slip Ni/Ni-Pc MOFs, b) PES for bilayers slip Ni/Cu-Pc MOFs, c) Top and side view of bilayer Ni/Ni-Pc MOF, most stable structure with the slip of 6.00 Å in XY plane, and d) Top and side view of bilayer Ni/Cu-Pc MOF,

most stable structure with the slip of 6.00 Å in XY plane. The interlayer layer separation is 3.3 Å.

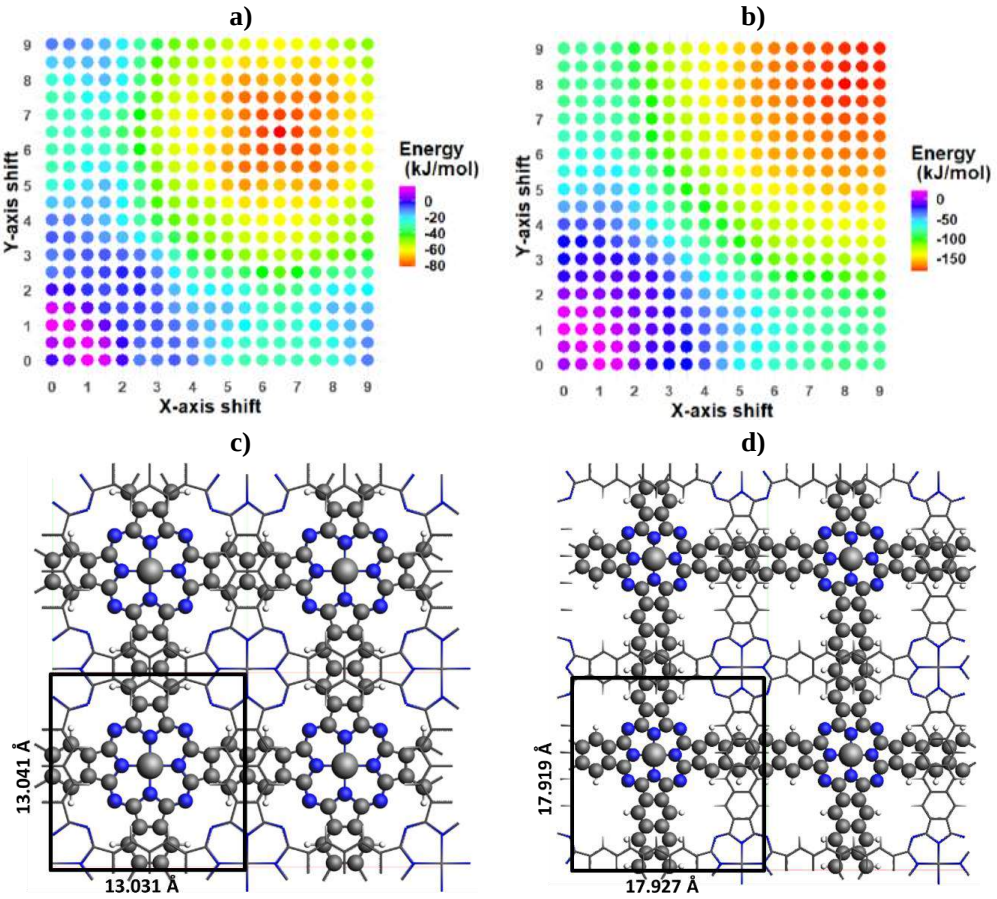

Figure 3.3. a) PES without NiO_4/CuO_4 connectors MOF, b) PES of benzene substituted NiO_4/CuO_4 connectors MOF, c) 2×2 supercell of AB (stable geometry) MOF without NiO_4/CuO_4 connectors with highlighted 1×1 unit cell, d) 2×2 supercell of benzene substituted instead of NiO_4/CuO_4 connectors AB (stable) MOF with highlighted 1×1 unit cell.

Table 3.1. Interaction parameters, including binding atoms (A_b), binding distances (D_b) in Å and binding energies (E_b) in kJ/mol of NO on Ni/Ni- and Ni/Cu-Pc MOFs analogues.

Systems	A_b	D_b	E_b	A_b	D_b	E_b
	Ni/Ni-Pc MOF			Ni/Cu-Pc MOF		
1NO@AAA	ON---O	1.89	-155	ON---O	1.91	-113
1NO@ABC	ON---O	1.42	-243	ON-Ni/N	1.95	-242
24NO@AAA	ON---O	---	-130	ON---O	---	-93
24NO@ABC	ON---O	---	-152	ON---O	---	-138
25NO@AAA	ON---N	1.41	-86	ON---N	1.82	-108
25NO@ABC	ON---O	1.42	-227	ON---O	1.41	-143

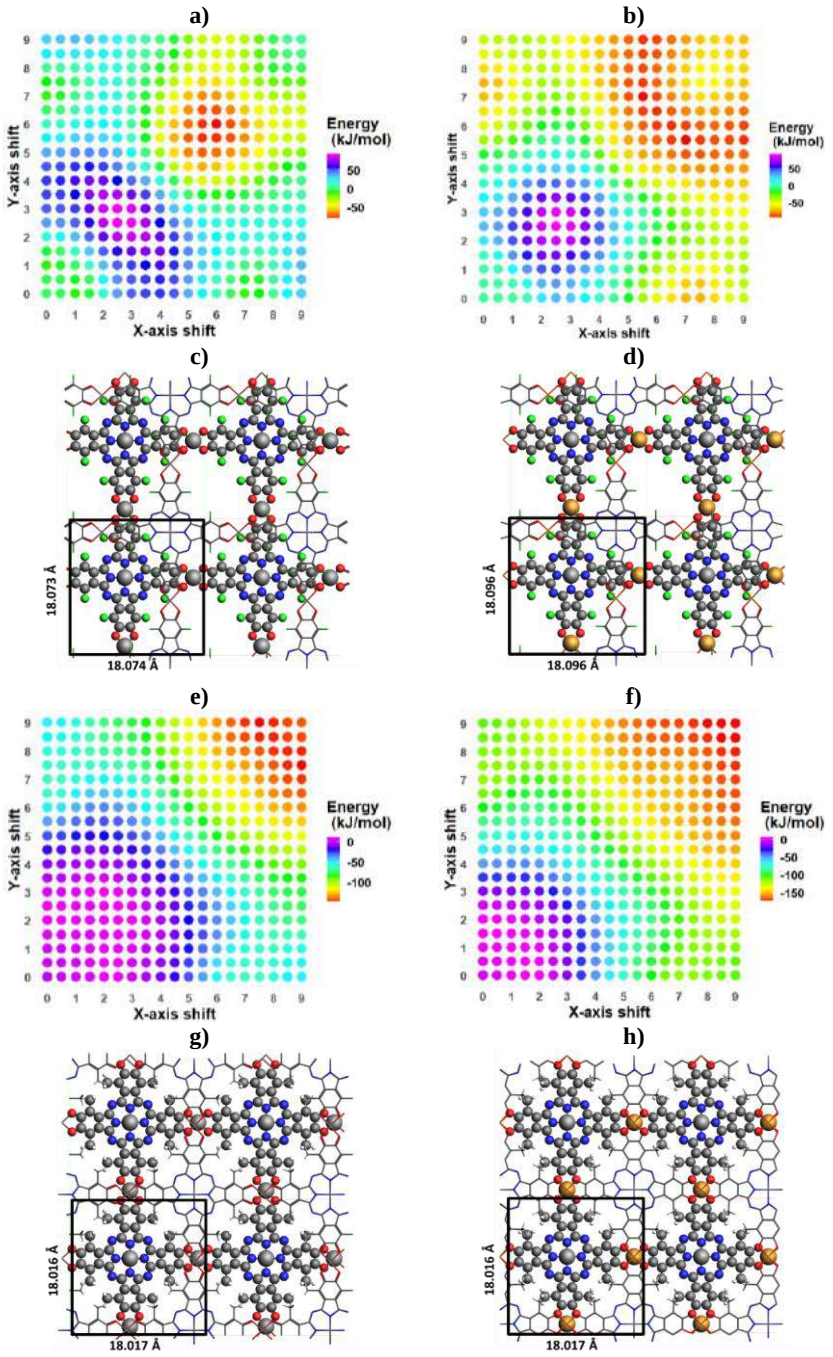

Figure 3.4. PES of fluorine substituted a) Ni/Ni MOF, b) Ni/Cu MOF analogue. c) 2×2 supercell of 6.0 Å slip-AA (stable geometry) fluorine substituted Ni/Ni-MOF, d) Ni/Cu-MOF analogue with highlighted 1×1 unit cells. e) PES of methyl-substituted Ni/Ni MOF, f) Ni/Cu MOF analogue. g) 2×2 supercell of stable structure with the offset of 9.00 Å of methyl-substituted Ni/Ni-MOF cell and h) methyl-substituted Ni/Cu-MOF with highlighted 1×1 unit cell.

For the Ni/Ni- and Ni/Cu-Pc MOFs, the potential energy landscapes are generated, shown in **Figure 3.2** by calculating the relative single point energy with respect to

fully eclipsed structures. Although the van der Waals interactions are maximum in eclipsed-AA configuration, the structures are still highly unstable with the highest positive energies because the columbic or steric repulsions are dominating between the atoms especially metals of the neighbouring layers.[35,71,72] The energy of the slipped-AA gradually decreases when the upper layer is slightly shifted in one of the *x*, *y* & *xy* planes. The decrease in the energy attributes to the increasing stability of MOF structures which might be due to the increasing distance and decreasing steric repulsions[73,74] between the metal atoms as well as the NiPc units of the adjacent layers. In addition, the energies of slipped-AA for Ni/Ni- and Ni/Cu-Pc MOFs with the offset of 6.00 Å in the *x*- and *y*-plane ($x = y = 6.0$ Å) are found to be around -206.0 and -260.0 kJ/mol, respectively, lowest as compared to that of eclipsed-AA, slipped-AA, and staggered-AB structures. It can be inferred that in the slipped-AA structure with the offsets $x = y = 6.0$ Å, **Figure 3.2(c & d)** the NiPc units as well as the metal nodes of both the adjacent layers are fully exposed, causing the least steric repulsion. Thus, slipped-AA structures are indeed highly stable for both Ni/Ni- and Ni/Cu-Pc MOFs. In further separation, the metal nodes of the top layer encounter a similar environment to the bottom layer, resulting in an increase in steric repulsions, correspondingly decreasing their relative stability.

3.4.1.2 Role of Metal Atoms and Substitutions in Increasing Dispersion Forces

To examine the potential role of tetrahedrally bonded metal (NiO_4 and CuO_4) nodes, the relative PE landscapes of two COF-derivatives of the Pc-MOF have been generated, see **Figure 3.3(a & b)**. These derivatives are generated a) by eliminating the tetrahedral metal nodes (NiO_4 or CuO_4) (**Figure 3.3c**), and b) by replacing the MO_4 with aromatic six-membered rings (**Figure 3.3d**). The former derivative exhibits small lattice parameters; $a = b = 13.04$ Å, while the latter exhibits lattice parameters ($a = b =$ 17.93 Å) similar to the reference MOFs. Unlike Ni/Ni- or Ni/Cu-Pc MOFs, the PESs of both the COF-derivatives of Pc-MOFs show that the perfect AB stacked structures are energetically favorable, where the NiPc units of both the layers are at maximum offsets, similar to the other covalent organic frameworks.[75] Due to the absence of metal nodes, steric repulsion is not contributing to these derivatives. In addition, the NiPc linker units of both layers are located at maximum distances, resulting in maximum

dispersion forces in AB geometries. The PES landscapes along with their AB-stacked 2×2 supercell structures of both derivatives are displayed in **Figure 3.3(a & b)**.

Subsequently, the effect of substituents on the dispersion forces between the layers of Ni/Ni and Ni/Cu-Pc MOFs has been explored *via* substituting phenyl hydrogens with fluorine atoms as well as methyl groups. The 2×2 supercells of functionalized MOFs with highlighted primitive unit cell parameters and their respective PES landscapes are displayed are in **Figure 3.4**. Fluorine functionalization is a common approach in order to tune the physical and chemical properties, which produces a significant improvement in their structural stability and electronic applications.[76–78] In this research, the PESs of fluorine functionalized Pc-MOFs (**Figure 3.4a & b**) illustrate that fluorine substitution cannot produce a significant effect on the interlayer dispersion stability of 2D MOFs. Moreover, the geometric stability of the fluorinated Pc MOFs is reduced because the aromatic C-F bonds tend to be stronger than that of corresponding C-H bonds, thus fluorination weakens the neighbouring bonds.[79] Therefore, the stabilization energies of fluorinated Ni/Ni- and Ni/Cu-Pc MOFs are reduced to -79.0 and -92.0 kJ/mol, respectively. On the contrary, by substituting methyl groups, the Columbic repulsions between the metal atoms of neighbouring layers decrease because the interlayer separation increase to 3.8 Å. As a result, the perfect AB-staggered structure is energetically more stable. In the perfect AB structures of methylated Ni/Ni- and Ni/Cu-Pc MOFs, the steric repulsions are neglected[80] between the NiPc units of consecutive layers, resulting in the maximum dispersion forces contribute in stabilizing the structures.

3.4.2 MOF Models for Gas Molecules Binding

Conventionally, the DFT studies of gas binding in 2D COFs/MOFs are performed on either monolayer or AA structures.[81–83] However, our single point calculations (*vide supra*) suggest that π-π stacking arrangements are energetically more favorable in the slipped-AA structures especially when $x = y = 6.00$ Å, which is well consistent with the recent computational studies.[46] To understand the significant difference in the gas adsorption due to slipping, the comparative binding of NO, NH_3, and H_2S in the eclipsed-AA and the most stable slipped-AA 2D MOFs structures ($x = y = 6.00$ Å) are studied. For this purpose, the six layers of periodic Ni/Ni- and Ni/Cu-Pc MOFs analogues are chosen as model structures for the gas adsorption, thus the separation

between the adsorbed molecules is over 10.00 Å which may produce more realistic results. From optimized structures of six layers of eclipsed-AA and slipped-AA MOFs, it is found that the slipping affects the relative alignment between the atoms of MOF layers, resulting in changes in the interlayer distance due to the interlayer van der Waals or dispersion interactions.[84] It is expected that the change in interlayer distance and their relative alignment affects the gas adsorption and binding sites, which can be analysed through the comparative study of the adsorption of gas molecules for both eclipsed and most stable slipped-AA of Pc-MOFs. In eclipsed-AA structure, each layer is a sandwich between the two neighbouring layers while every top layer has a shift of 6.0 Å on the *xy*-plane in slipped-AA, therefore the six layers are eventually the two sets of AAA and AA'A" stacked layers, respectively (see **Figure 3.5**).

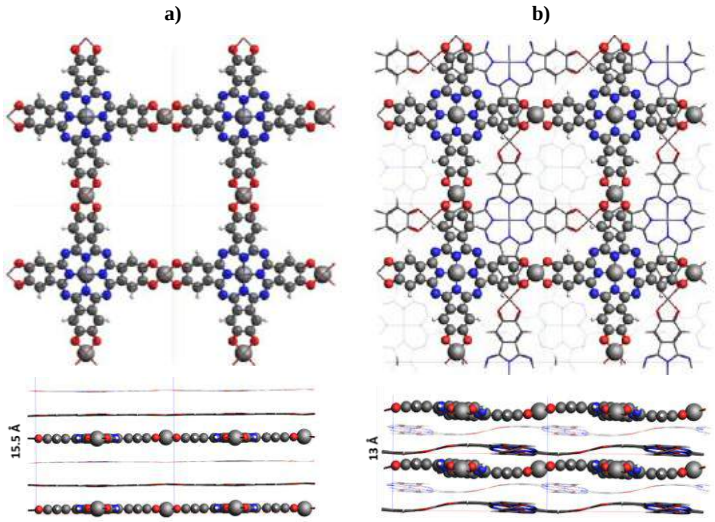

Figure 3.5. The top and side views of six layers of a) eclipsed-AA MOF, b) slipped-AA MOF, where every top layer has an offset of $x = y = 6.00$ Å.

3.4.3 NO Binding Sites in Eclipsed and Stable Slipped-AA Structures of Pc MOFs

3.4.3.1 NO Binding in Ni/Ni-Pc MOF

To identify the energetically preferred NO binding sites in the eclipsed-AA and slipped-AA structures of Ni/Ni-Pc MOFs, the binding energies of hundred Kick structures of NO@Ni/Ni-Pc-MOF are computed using DFTB simulations at the GFN1-xTB method. Among those hundreds of structures, the energetically most favourable binding geometries of NO in both eclipsed-AA and slipped-AA Ni/NiPc-

MOFs are displayed in **Figure 3.6(a & b)**. Generally, in eclipsed-AA as well as slipped-AA Ni/Ni-Pc MOF structures, it is found that the nitrogen of NO molecule prefers binding with oxygen atoms of inorganic nodes (NiO_4) due to the multiple reasons *i.e.*, high electron density as well as direct exposure to the porous channel of MOFs which provides higher intermolecular attraction.[45,85,86] Expectedly, in eclipsed-AA structure, the NO preferably sites between the equivalent oxygen atoms of two adjacent layers (shown in **Figure 3.6a)**. At this binding site of eclipsed MOF, mainly two nucleophilic oxygen atoms of neighbouring layers bind with NO molecules, thus the binding energy (E_b) of NO at this site is -155.3 kJ/mol. On the contrary, the most stable binding site for the NO molecule in slipped-AA Ni/Ni-Pc MOF is the same as in its eclipsed counterpart, however, in slipped structure, NO solely binds with a single oxygen atom of only one layer with a lower interatomic distance (1.42 Å) which is lower than that of eclipsed (1.89 Å). This close interaction in slipped-AA MOF gives rise to the strong binding energy of -243.5 kJ/mol. Thus, it is noted that the NO binding in slipped-AA of Ni/Ni-Pc MOF is energetically stronger with ∼100.0 kJ/mol of energy compared to the eclipsed-AA structure. The E_b, A_b, and D_b of NO onto the MOFs analogues are displayed in **Table 3.1**.

3.4.3.2 NO Binding in Ni/Cu-Pc MOF

The stable binding site of NO in slipped-AA MOF is surprisingly changed by replacing the tetrahedrally bonded Ni metal of NiO_4 with Cu. Unlike Ni/Ni MOF, in Ni/Cu MOF, the NO preferentially binds with the Ni metal and nitrogen atom of the NiPc unit rather than binding with the oxygen atom at the nodal site. The energy of this possible binding is -242.1 kJ/mol which is nearly equal to the energy of the most stable binding site of NO in Ni/Ni MOF. Due to the change in the possible stable binding site in Ni/Cu-Pc MOF, it can be postulated that the presence of Ni facilitates the binding of NO.[68] Among multiple binding possibilities of NO in slipped-AA Ni/Cu MOF, a similar binding as in the Ni/Ni MOF case, in which nitrogen of NO binds with the oxygen of MO_4, is also observed but the energy of this binding possibility is -207.1 kJ/mol, attributing the lower affinity of Cu binding NO molecules. The less stability of this particular binding site of NO is further strengthening our previous assumption which states that Ni exhibits more binding strength towards NO as compared to Cu. In contrast, the preferable binding site of the NO in eclipsed-AA Ni/Cu MOF structure is

consistent with the Ni/Ni AA MOF, where the nitrogen atom of NO binds with the oxygen atoms of two adjacent layers simultaneously with the binding energy of -113.0 kJ/mol. These results show that the adsorption of NO in Ni/Ni MOF is more feasible as compared to the Ni/Cu MOF.

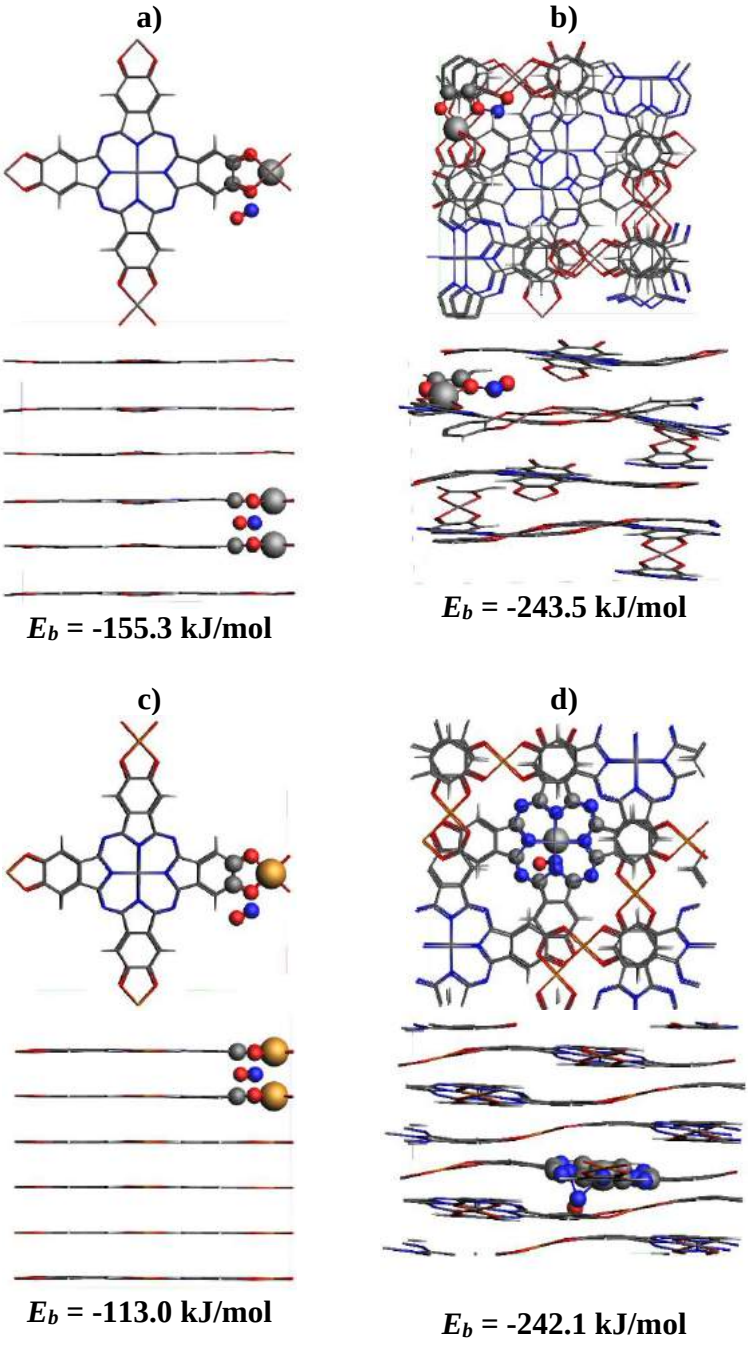

Figure 3.6. Top and side views of NO binding in eclipsed-AA a) Ni/Ni-Pc MOF, b) Ni/Cu-Pc MOF, c) slipped-AA Ni/Ni-Pc MOF, and d) Ni/Cu-Pc MOF with their binding energies (E_b).

3.4.3.3 NO Molecules Loading in MOFs

3.4.3.3.1 NO Loading in Eclipsed-AA and Slipped-AA Ni/Ni-Pc MOF

After judging the binding of NO in Ni/Ni- and Ni/Cu-Pc MOF, it is noted that in the eclipsed-AA structure, all oxygen sites are equivalent because of symmetry, therefore, there are 48 binding sites per considered MOF unit cell (six-layered). In order to examine the adsorption of the possible number of NO molecules, the E_b of the second NO molecule binding at two possible *anti*- and *syn*- positions are calculated in the adjacent layers (**Figure 3.7**). The increasing concentration of guest molecules has a negative impact on the binding stability due to the increasing Columbic repulsion between them.[87] The E_b of the second NO in eclipsed-AA MOF is determined to be -147.9 and -145.2 kJ/mol, respectively for *anti*- (**Figure 3.7a**) and syn-conformations (**Figure 3.7b**). It indicates that the binding stability of NO binding at *anti*-position is higher by ~2.0 kJ/mol because the NO---NO distance is over 6.40 Å, whereas, for *syn*-position, it is 3.41 Å, which causes higher repulsion. Similarly, the binding stability of increasing NO in slipped-AA MOF is reduced to the energies of -186.2 and -179.7 kJ/mol, respectively for *anti*- (**Figure 3.7c**) and *syn*-position (**Figure 3.7d**) binding.

Similarly, for further clarification, the six NO molecules are adsorbed around all the equivalent oxygen atoms of one hand of eclipsed-AA MOF in *anti*- and *syn*-fashion, see **Figure 3.7e&f**, respectively. In this case, due to a further increase in repulsion forces, the $E_{b/s}$ of *per* NO is reduced to -140.0 and -131.5 kJ/mol in *anti*- and *syn*-fashion, respectively. These results indicate that the *anti*- (opposite site) is more favourable for NO molecules binding as compared to the *syn*- (same) side because of lower repulsion due to the large intermolecular (NO----NO) distances between the adsorbed NO of two adjacent layers. Based on these results, it can be illustrated that despite being 48 symmetric oxygen atoms in a six-layered eclipsed structure but only 24 NO molecules can bind to minimize the intermolecular Columbic repulsion and to hinder the self-interactions, as seen in **Figure 3.7f**.

Thus, the binding of n^{th} (n = 24) NO in *anti*-fashion in eclipse-AA Ni/Ni- and Ni/Cu-Pc MOFs (**Figure 3.8a**) exhibits the E_b/s per NO of -129.7 and -93.1 kJ/mol, respectively, indicating the lowering of binding affinity with increasing the number of NO binds. Accordingly, it is interpreted that there are 24 active positions also present in slipped-AA MOF. Thus, the 24 NO molecules are manually added in slipped-AA

MOF at the positions where two adjacent NO molecules show the least repulsion (**Figure 3.8b**).

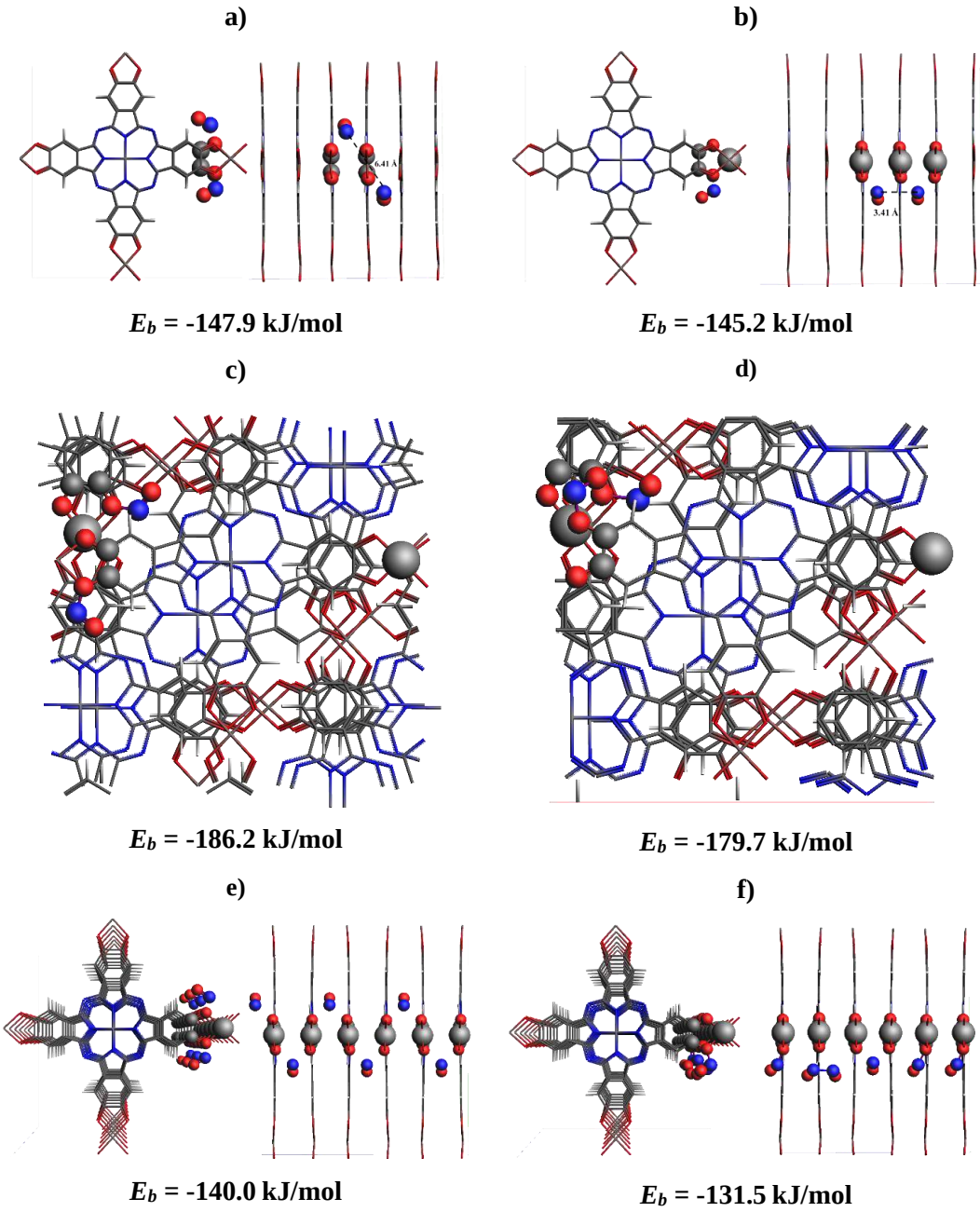

Figure 3.7. Optimized geometries of increasing concentration of NO molecules in eclipsed-AA two NO at a) *anti*-, b) *syn*-positions. Two NO in slipped-AA at c) *anti*-, d) *syn*-position. Six NO in eclipsed-AA at e) *anti*- and f) *syn*-positions.

The binding energies per NO in Ni/Ni- and Ni/Cu-Pc MOFs are -151.6 and -137.4 kJ/mol, respectively. From these results, it is observed that the binding stability of the number of NO molecules on the slipped-AA structure is higher than the eclipsed-AA counterpart. Thus, it can be concluded that the interlayer slip has a positive effect on

the molecule binding due to multiple reasons *i.e.*, a) open metal sites for direct binding of the molecule,[88] b) exposed all other active sites for binding[89] and c) per oxygen atom for per NO molecules due to the unsymmetric nature.[46] In comparison, the NO binding affinity of Ni/Ni-Pc MOF has more pronounced than that of the Ni/Cu-Pc analogue, manifesting that Ni metal facilitates the NO binding.

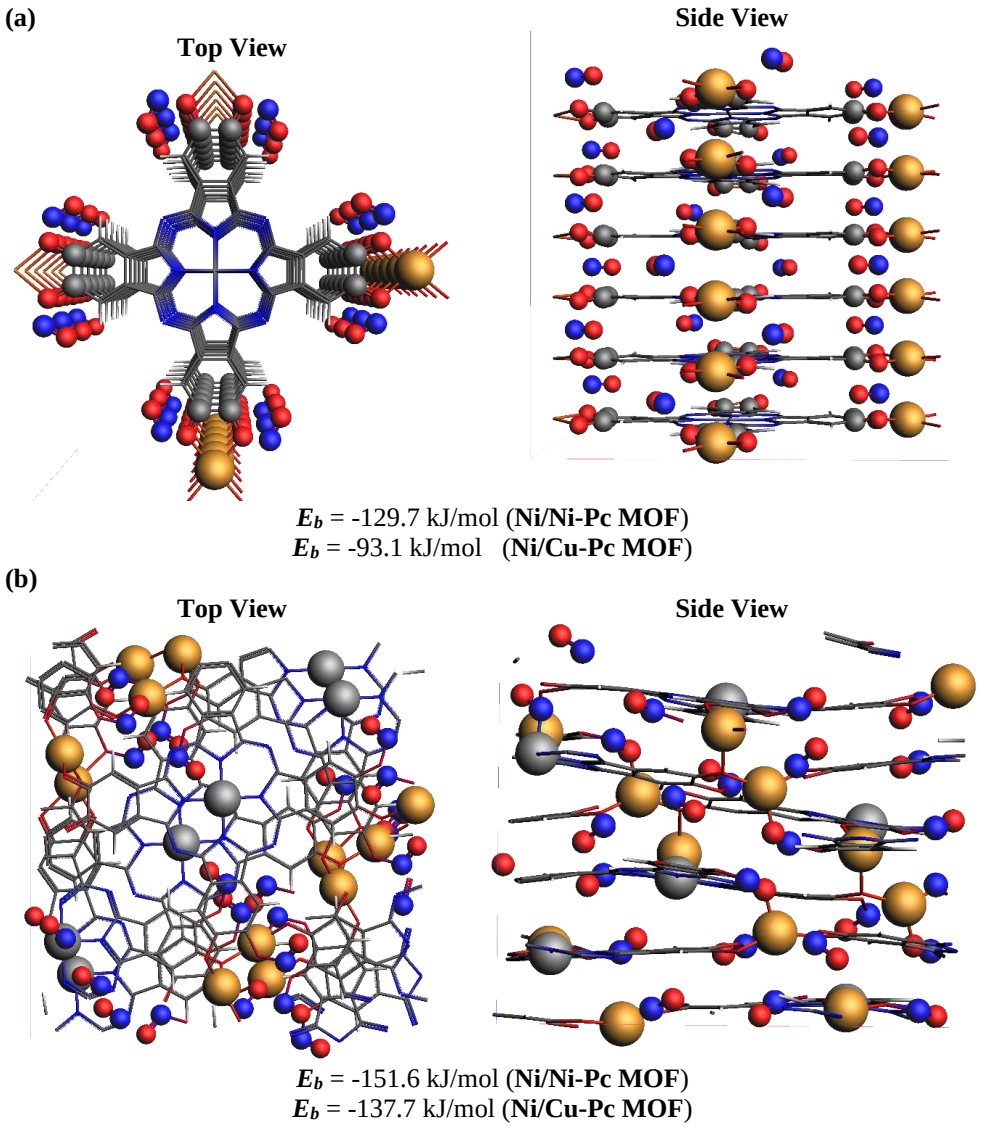

Figure 3.8. Twenty-four NO binding in (a) eclipsed-AA, and (b) slipped-AA MOFs. Chemical composition; gold may be Cu and Ni in the case of Ni/Cu and Ni/Ni-Pc MOFs, respectively.

After loading 24 NO molecules in eclipsed or slipped MOF structures, all the active oxygen sites are fully occupied with the minimum repulsion between adsorbed NO molecules. Further study to measure the next active site for binding of the 25th NO molecule in saturated Ni/Ni-Pc MOF is essential. Here we kicked one more NO

molecule in both eclipsed-AA and slipped-AA MOFs that have already filled with 24 NO molecules. By optimizing the 10 kicked structures containing an additional NO molecule, we get a deeper understanding of the possibility of new upcoming NO molecule adsorption. Note that since all the oxygen sites are fully loaded with 24 NO molecules, the added NO could not bind with the remaining oxygen atoms due to the Columbic repulsion caused by the nearly adsorbed NO molecules on either side. In the eclipsed-AA structure, the three possible binding positions of additional NO are depicted, however, only the lowest energy configuration is considered, where the nitrogen of NO binds with the nitrogen atom of the NiPc unit (**Figure 3.9a**).

For the most stable geometry, the binding energy and interatomic distance between additional NO molecule and nitrogen of NiPc in eclipsed-AA are -85.9 kJ/mol and 1.41 Å, respectively. The relative stability of the structure where NO binds with the N-site of NiPc is approximately 70.0 kJ/mol is lower as compared to the oxygen site of the NiO_4 node.

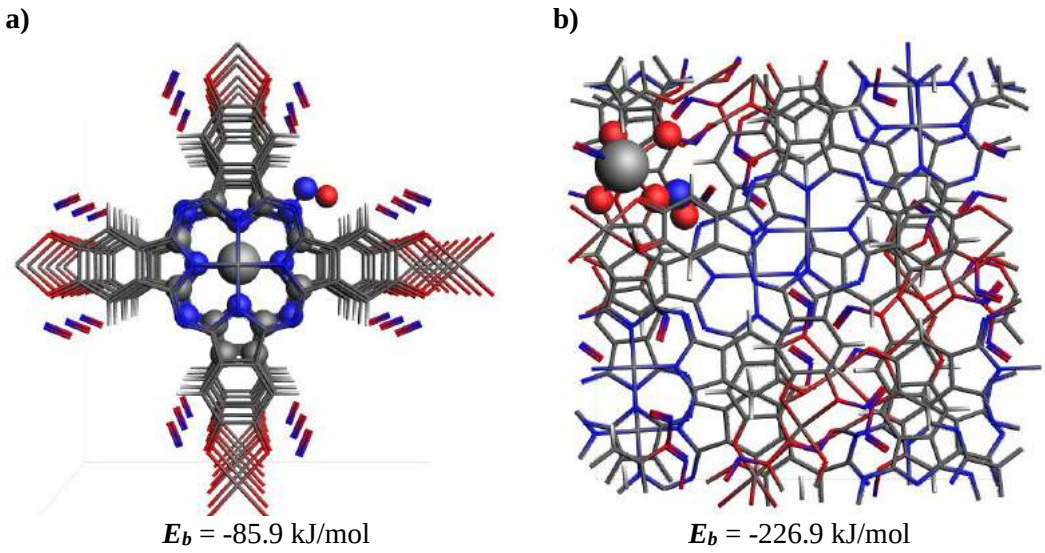

Figure 3.9. Binding of 25th NO molecule onto a) eclipsed-AA, and b) slipped Ni/Ni-Pc MOFs.

Similarly, the same method is also applied to slipped-AA Ni/Ni-Pc MOF. The binding energy and geometric analysis show that the most stable binding of additional NO molecule in slipped structure is that where nitrogen of NO binds with the 25th oxygen atom of the NiO_4, the same binding which has been seen in the above cases of slipped-AA, with the E_b and interatomic distance of -226.9 kJ/mol and 1.40 Å, respectively. Here, it can be concluded that due to the unsymmetric nature as well as the exposure

of every active position such as metal atoms and electron-rich oxygen atoms, the slipped-AA structures have a higher capacity of NO loading with ultra-high stability.

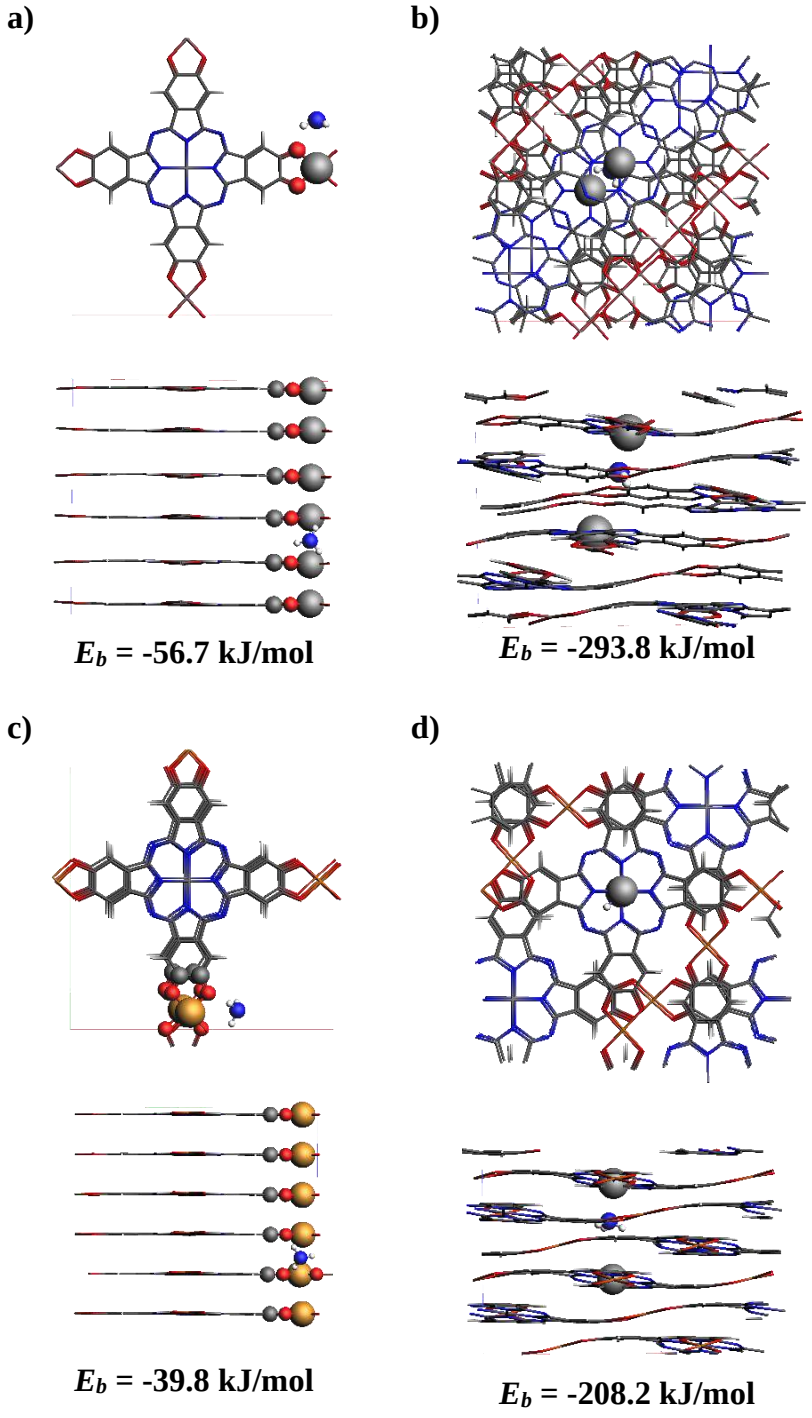

Figure 3.10. Top and side views of NH_3 binding in eclipsed-AA a) Ni/Ni-Pc MOF, b) Ni/Cu-Pc MOF, c) slipped-AA Ni/Ni-Pc MOF, and d) Ni/Cu-Pc MOF with their binding energies (E_b).

3.4.4 NH_3 Binding

3.4.4.1 NH_3 Binding in Ni/Ni-Pc MOF

Similar to NO, a hundred structures of each MOF *i.e.*, eclipsed-AA and slipped-AA of Ni/Ni and Ni/Cu were generated by adding NH_3 molecules stochastically, followed by their optimization at GFN1-xTB method implemented in SCM-AM2020.101 version. The energetically favourable NH_3 binding sites both in eclipsed-AA and slipped-AA structures of Ni/Ni-Pc MOFs were first analysed (**Figure 3.10a**). Like NO, the NH_3 molecule binds with the oxygen atoms of the NiO_4 unit of two adjacent layers. The interaction takes place through the electron-deficient H-atoms of NH_3 and electron-dense oxygen sites. Such types of interaction between NH_3 and adsorbent with only exposed oxygen site are rarely reported because of their lesser stability.[90,91] Thus, the computed E_b for these interactions is only -56.7 kJ/mol, indicating fewer chances of competitive adsorption in the eclipsed-AA structure of Ni/Ni-Pc MOF. On the other hand, the interaction of NH_3 *via* N-site with an open metal site of MOFs is a preferential binding and has extensively been reported in the literature.[92–97] Similar binding is observed between NH_3 and slipped-AA structure of Ni/Ni-Pc MOF, where nitrogen of NH_3 binds with the central metal (Ni) of the NiPc unit. Due to the high polarity and strong coordination ability of the central metal of phthalocyanine, it is expectedly superior in the activity of binding NH_3 molecule based on the previous reports.[98,99] Thus, the kicked NH_3 molecule is preferably bonded with the central Ni-site in NiPc of two repeating units of a slipped-AA structure, with the E_b of -293.8 kJ/mol, which is 200 fold higher than the eclipsed-AA counterpart. The intermolecular binding distance between the nitrogen of NH_3 and NiPc is 2.46 Å.

3.4.4.2 NH_3 Binding in Ni/Cu-Pc MOF

Similar to Ni/Ni-Pc MOF, the NH_3 molecule prefers to bind with the Ni of NiPc unit upon adsorption in slipped-AA Ni/Cu-Pc MOF due to the electrostatic interactions between lone pairs of NH_3 and cationic nature of Ni (Ni^{2+}). The calculated E_b, in this case, is -208.2 kJ/mol. In comparison to the Ni/Ni-Pc analogues, the binding stability of MOF is reduced by approximately 100.0 kJ/mol in Ni/Cu-Pc. Thus, it is found that upon replacing the Ni metal atom with Cu in the node unit, the adsorption affinity of the resulting MOF is significantly decreased. In the eclipsed-AA structure, the NH_3 molecule binds to the oxygen atoms of the CuO_4 nodal unit of the two adjacent layers.

The E_b of NH_3 with eclipsed-AA Ni/Cu MOF is -39.8 kJ/mol, indicating the least binding affinity as compared to the slipped structure of the same MOF as well as the eclipsed and slipped structure of Ni/Ni-Pc MOF.

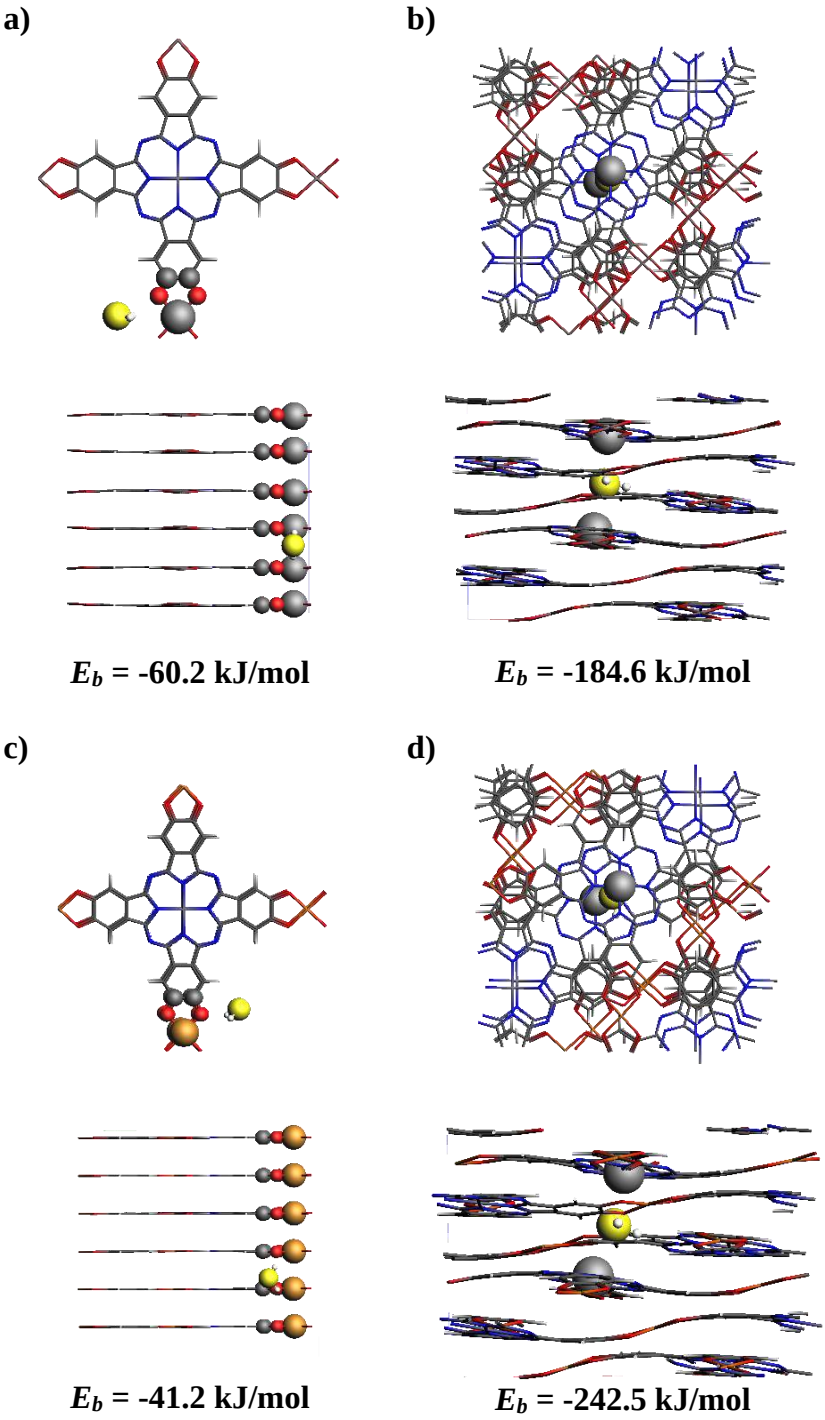

Figure 3.11. Top and side views of H_2S binding in eclipsed-AA a) Ni/Ni-Pc MOF, b) Ni/Cu-Pc MOF, c) slipped-AA Ni/Ni-Pc MOF, and d) Ni/Cu-Pc MOF with their binding energies (E_b).

3.4.5 H_2S Binding

3.4.5.1 H_2S Binding in Ni/Ni-Pc MOF

Like NO and NH_3, the binding stability of H_2S molecules in Ni/Ni- and Ni/Cu-Pc MOFs is studied. Moreover, the effect of slipping configurations with eclipsed-AA and slipped-AA on binding properties is also studied by stochastically adding H_2S molecules and optimizing resulting in 100 structures on each analogue of MOF. As shown in **Figure 3.11**, the binding strength of H_2S in the slipped-AA structure is higher compared to the eclipsed-AA Ni/Ni-Pc MOF. The central metal site of the phthalocyanine unit is expected to have a higher affinity for binding H_2S through the sulfur site.[100] Thus, in slipped-AA MOF, the H_2S molecule strongly binds to the central Ni^{2+} of NiPc unit with the intermolecular distance between S of H_2S and Ni^{2+} of NiPc is 2.89 Å (**Figure 3.11b**), which is much closer to the S---Ni binding distance by Tang *et al.*,[101] Due to the strong electrostatic interaction between S^{2-} and Ni^{2+} (**Figure 3.11a**), the binding stability is remarkably high which is -184.7 kJ/mol. In the eclipsed-AA structures, the central Ni metal site is not freely available for binding, the H_2S simultaneously binds through the hydrogen atoms with the oxygen atoms of the NiO_4 of two neighbouring layers. These types of binding interactions are less stable and only exist in case of limited active sites[102] thus, the E_b is quite low which is -60.2 kJ/mol. In addition, the intermolecular distances (H---O) are comparatively high (3.33 Å), this attributes to the lowest binding affinity of H_2S in the eclipsed-AA structure of Ni/Ni-Pc MOF.

3.4.5.2 H_2S binding in Ni/Cu-Pc MOF

Upon replacing Ni from a metal node with Cu, there is no significant variation observed except varying binding stability. Similar to Ni/Ni-Pc MOF, in the most stable binding interaction, the H_2S molecule strongly binds with the Ni^{2+} of NiPc of slipped-AA Ni/Cu-Pc MOF (**Figure 3.11c**), with a binding distance of 2.90 Å, due to the strong electrostatic interactions present between interacting atoms. The observed E_b, in this case, is -242.5 kJ/mol, attributing the strong binding stability of the slipped-AA structure. In the eclipsed-AA structure, the binding stability of H_2S is fivefold lower than in slipped structure because of the unavailability of active Ni^{2+} sites. Therefore, the H_2S binds, through electron-deficient hydrogen atoms, with the electron-dense oxygen atoms of CuO_4 unit of adjacent layers in eclipsed-AA structure (**Figure 3.11d**).

Although the hydrogen atoms of H_2S closely interact with oxygen atoms (2.26 Å) in this case, stability is still lower than slipped structure because of electrostatic forces[103,104] play their role in stabilizing the sulfur atom of H_2S on the metal site of NiPc unit.

3.5 Conclusions

Herein, the binding affinity and the interlayer slipping effect on NO, NH_3, and H_2S adsorption in layered 2D Ni/Ni- and Ni/Cu-Pc MOFs were explored. First, the various MOF slipped structures are considered and the most stable stacking geometries are determined by generating potential energy landscape. Subsequently, the adsorption of the small gas molecules in the most stable slipped structure (top layer offset 6.00 Å) and perfectly stacked eclipsed (zero offsets) are studied. Since the neighbouring layers are completely stacked in eclipsed-AA structures, resulting in limited site availability for binding guest molecules. In this case, the oxygen atoms, covalently bonded with a metal node, provide the energetically preferred molecule binding sites. Thus, the molecules prefer to bind the available oxygen atoms of two adjacent layers simultaneously, with binding energy contribution from both the MOF layers. In the eclipsed-AA structure of Ni/Ni-Pc, the binding energies of NO, NH_3, and H_2S are -155.0, -57.0, and -60.0 kJ/mol, respectively.

Next, the interlayer slipping of MOFs significantly affects the relative distance, stability, and alignment during the adsorption process. Due to the parallel interlayers slipping, the hidden active binding sites in eclipsed structures, are exposed and available for binding. Thus, the interlayer slipping drastically increases the binding stability. For slipped-AA of Ni/Ni-Pc MOF, the binding energies are found to be -243.0, -294.0, and -243.0 kJ/mol for NO, NH_3, and H_2S. This is because the guest molecules strongly bind only with one active position in slipped-AA structures due to the unsymmetric nature of the slipped-AA structure. Moreover, unlike eclipsed-AA, the molecules adsorb onto the freely available metals atom in slipped-AA, especially Ni, which is already a known binding position in phthalocyanine chemistry. It is also found that the nature of metal at the nodal position strongly affects the binding strength of molecules, especially in eclipsed-AA. For example, upon replacing Ni with Cu, the binding strengths of NO, NH_3, and H_2S molecules in eclipsed-AA of Ni/Cu-Pc MOF are reduced to the energies of -113.0, -40.0, and -41.0 kJ/mol, respectively. However,

the nature of metal does not produce a significant difference in the gas binding stability of the slipped-AA structure, which is probably due to the bimetallic nature of the phthalocyanine unit. For example, gas molecules prefer binding to the Ni atom inside the Pc-building unit rather than Cu at nodes, which reveals the high gas capturing affinity of Ni than Cu. Finally, these findings suggest; a) the slipped 2D MOFs are promising candidates for gas binding or adsorption, and b) the interlayer slipping can act as a potential parameter for designing new 2D MOFs with higher gas binding ability. Next, the gas loading capacity of both Ni/Ni- and Ni/Cu-Pc MOF and their structural analogues using GCMC simulations are discussed in Chapter 4.

3.6 References

1 M. H. Glantz, *Global Environ. Change*, 1992, **2**, 183–204.

2 H. Tian, K. Liu, J. Hao, Y. Wang, J. Gao, P. Qiu and C. Zhu, *Environ. Sci. Technol.*, 2013, **47**, 11350–11357.

3 S. J. Hall and P. A. Matson, *Nature*, 1999, **400**, 152–155.

4 W. XU, L. Z. LIU, M. LOIZIDOU, M. AHMED and I. G. CHARLES, *Cell Res.*, 2002, **12**, 311–320.

5 J. B. JOSHI, V. V. MAHAJANI and V. A. JUVEKAR, *Chem. Eng. Commun.*, 1985, **33**, 1–92.

6 Z. Hong, Z. Wang and X. Li, *Catal. Sci. Technol.*, 2017, **7**, 3440–3452.

7 J. Lin, W. Ho, X. Qin, C. Leung, V. K. Au and S. Lee, *Small*, 2022, **18**, 2105484.

8 K. Vikrant, V. Kumar and K.-H. Kim, *J. Mater. Chem. A Mater.*, 2018, **6**, 22391–22410.

9 H. Hasheminasab, Y. Gholipour, M. Kharrazi and D. Streimikiene, *J. Clean. Prod.*, 2018, **171**, 1215–1224.

10 T. S. Carpenter, S. M. Rosolina and Z.-L. Xue, *Sens. Actuators B Chem.*, 2017, **253**, 846–851.

11 K. Vikrant, V. Kumar, K.-H. Kim and D. Kukkar, *J. Mater. Chem. A Mater.*, 2017, **5**, 22877–22896.

12 K. Vikrant, V. Kumar, Y. S. Ok, K.-H. Kim and A. Deep, *TrAC Trends Analyt. Chem.*, 2018, **105**, 263–281.

13 N. Stock and S. Biswas, *Chem. Rev.*, 2012, **112**, 933–969.

14 Y. Yu, X.-M. Zhang, J.-P. Ma, Q.-K. Liu, P. Wang and Y.-B. Dong, *Chem. Commun.*, 2014, **50**, 1444–1446.

15 J. Zhang, L. Sun, C. Chen, M. Liu, W. Dong, W. Guo and S. Ruan, *J. Alloys. Compd.*, 2017, **695**, 520–525.

16 M. Ding, X. Cai and H.-L. Jiang, *Chem. Sci.*, 2019, **10**, 10209–10230.

17 C. Li, L. Zhang, J. Chen, X. Li, J. Sun, J. Zhu, X. Wang and Y. Fu, *Nanoscale*, 2021, **13**, 485–509.

18 M. Yao, J. Xiu, Q. Huang, W. Li, W. Wu, A. Wu, L. Cao, W. Deng, G. Wang and G. Xu, *Angew. Chem. Int. Ed.*, 2019, **58**, 14915–14919.

19 H. T. B. Pham, J. Y. Choi, S. Huang, X. Wang, A. Claman, M. Stodolka, S. Yazdi, S. Sharma, W. Zhang and J. Park, *J. Am. Chem. Soc.*, 2022, **144**, 10615–10621.

20 M. G. Campbell, D. Sheberla, S. F. Liu, T. M. Swager and M. Dincă, *Angew. Chem. Int. Ed.*, 2015, **54**, 4349–4352.

21 I. Stassen, J.-H. Dou, C. Hendon and M. Dincă, *ACS Cent. Sci.*, 2019, **5**, 1425–1431.

22 B. Wang, Y. Luo, B. Liu and G. Duan, *ACS Appl. Mater. Interfaces*, 2019, **11**, 35935–35940.

23 J. Park, M. Lee, D. Feng, Z. Huang, A. C. Hinckley, A. Yakovenko, X. Zou, Y. Cui and Z. Bao, *J. Am. Chem. Soc.*, 2018, **140**, 10315–10323.

24 E. M. Miner, L. Wang and M. Dincă, *Chem. Sci.*, 2018, **9**, 6286–6291.

25 H. Nagatomi, N. Yanai, T. Yamada, K. Shiraishi and N. Kimizuka, *Chem. Eur. J.*, 2018, **24**, 1806–1810.

26 C. Lyu, Y. Gao, Z. Gao, S. Mo, M. Hua, E. Li, S. Fu, J. Chen, P. Liu, L. Huang and N. Lin, *Angew. Chem.*, 2022, **134**, e202204528.

27 Y. Jiang, I. Oh, S. H. Joo, Y.-S. Seo, S. H. Lee, W. K. Seong, Y. J. Kim, J. Hwang, S. K. Kwak, J.-W. Yoo and R. S. Ruoff, *J. Am. Chem. Soc.*, 2020, **142**, 18346–18354.

28 R. Wang, C. He, W. Chen, L. Fu, C. Zhao, J. Huo and C. Sun, *Nanoscale*, 2021, **13**, 19247–19254.

29 M. G. Campbell, S. F. Liu, T. M. Swager and M. Dincă, *J. Am. Chem. Soc.*, 2015, **137**, 13780–13783.

30 N. Zhu, L. Gu, J. Wang, X. Li, G. Liang, J. Zhou and Z. Zhang, *J. Phys. Chem. C*, 2019, **123**, 9388–9393.

31 S. Lu, H. Jia, M. Hummel, Y. Wu, K. Wang, X. Qi and Z. Gu, *RSC Adv.*, 2021, **11**, 4472–4477.

32 M. Wang, Z. Zhang, H. Zhong, X. Huang, W. Li, M. Hambsch, P. Zhang, Z. Wang, P. st. Petkov, T. Heine, S. C. B. Mannsfeld, X. Feng and R. Dong, *Angew. Chem.*, 2021, **133**, 18814–18820.

33 Y. Liu, J. Peng, W. Zhuge, Q. Huang, G. Xiang and L. Wei, *J. Electrochem. Soc.*, 2022, **169**, 046502.

34 W. Zhuge, Y. Liu, W. Huang, C. Zhang, L. Wei and J. Peng, *Sens Actuators. B Chem.*, 2022, **367**, 132028.

35 W. Li, L. Sun, J. Qi, P. Jarillo-Herrero, M. Dincă and J. Li, *Chem. Sci.*, 2017, **8**, 2859–2867.

36 P. Zhang, M. Wang, Y. Liu, S. Yang, F. Wang, Y. Li, G. Chen, Z. Li, G. Wang, M. Zhu, R. Dong, M. Yu, O. G. Schmidt and X. Feng, *J. Am. Chem. Soc.*, 2021, **143**, 10168–10176.

37 T. Q. Nguyen, M. C. S. Escaño and H. Kasai, *J. Phys. Chem. B*, 2010, **114**, 10017–10021.

38 T. Q. Nguyen, A. A. B. Padama, M. C. S. Escano and H. Kasai, *ECS Trans.*, 2013, **45**, 91–100.

39 A. Aykanat, Z. Meng, R. M. Stolz, C. T. Morrell and K. A. Mirica, *Angew. Chem.*, 2022, **134**, e202113665.

40 B. Mandal, J. S. Chung and S. G. Kang, *J. Phys. Chem. C*, 2018, **122**, 9899–9908.

41 Z. Meng, A. Aykanat and K. A. Mirica, *J. Am. Chem. Soc.*, 2019, **141**, 2046–2053.

42 G. te Velde, F. M. Bickelhaupt, E. J. Baerends, C. Fonseca Guerra, S. J. A. van Gisbergen, J. G. Snijders and T. Ziegler, *J. Comput. Chem.*, 2001, **22**, 931–967.

43 M. Campbell, in *Learn RStudio IDE*, Apress, Berkeley, CA, 2019, 39–48.

44 C. Kessler, R. Schuldt, S. Emmerling, B. v. Lotsch, J. Kästner, J. Gross and N. Hansen, *Microporous Mesoporous Mater.*, 2022, **336**, 111796.

45 A. Sharma, A. Malani, N. v. Medhekar and R. Babarao, *CrystEngComm.*, 2017, **19**, 6950–6963.

46 A. Sharma, R. Babarao, N. v. Medhekar and A. Malani, *Ind. Eng. Chem. Res.*, 2018, **57**, 4767–4778.

47 M. A. Addicoat, S. Fukuoka, A. J. Page and S. Irle, *J. Comput. Chem.*, 2013, **34**, 2591–2600.

48 O. v. Kharissova, B. I. Kharisov and L. T. González, *J. Mater. Res.*, 2020, **35**, 1424–1438.

49 J. C. Tan and A. K. Cheetham, *Chem. Soc. Rev.*, 2011, **40**, 1059.

50 A. E. Mattsson, R. Armiento, P. A. Schultz and T. R. Mattsson, *Phys. Rev. B*, 2006, **73**, 195123.

51 I. Y. Zhang, J. Wu and X. Xu, *Chem. Comm.*, 2010, **46**, 3057.

52 P. Deák, B. Aradi, T. Frauenheim, E. Janzén and A. Gali, *Phys. Rev. B*, 2010, **81**, 153203.

53 S. Spicher, M. Bursch and S. Grimme, *J. Phys. Chem. C*, 2020, **124**, 27529–27541.

54 S. Amirjalayer and R. Schmid, *J. Phys. Chem. C*, 2008, **112**, 14980–14987.

55 C. Chen, Z. Deng, R. Tran, H. Tang, I.-H. Chu and S. P. Ong, *Phys. Rev. Mater.*, 2017, **1**, 043603.

56 M. A. Addicoat, N. Vankova, I. F. Akter and T. Heine, *J. Chem. Theory Comput.*, 2014, **10**, 880–891.

57 D. E. Coupry, M. A. Addicoat and T. Heine, *J. Chem. Theory Comput.*, 2016, **12**, 5215–5225.

58 J. Wang, R. M. Wolf, J. W. Caldwell, P. A. Kollman and D. A. Case, *J. Comput. Chem.*, 2004, **25**, 1157–1174.

59 A. D. MacKerell, N. Banavali and N. Foloppe, *Biopolymers*, 2000, **56**, 257–265.

60 A. K. Rappe, C. J. Casewit, K. S. Colwell, W. A. Goddard and W. M. Skiff, *J. Am. Chem. Soc.*, 1992, **114**, 10024–10035.

61 P. G. Boyd, S. M. Moosavi, M. Witman and B. Smit, *J. Phys. Chem. Lett.*, 2017, **8**, 357–363.

62 M. Sugihara, V. Buss, P. Entel, M. Elstner and T. Frauenheim, *Biochemistry*, 2002, **41**, 15259–15266.

63 M. Nurhuda, C. C. Perry and M. A. Addicoat, *Phys. Chem. Chem. Phys.*, 2022, **24**, 10906–10914.

64 S. Grimme, C. Bannwarth and P. Shushkov, *J. Chem. Theory Comput.*, 2017, **13**, 1989–2009.

65 A. A. Otlyotov, A. D. Moshchenkov, L. Cavallo and Y. Minenkov, *Phys. Chem. Chem. Phys.*, 2022, **24**, 17314–17322.

66 G. te Velde, F. M. Bickelhaupt, E. J. Baerends, C. Fonseca Guerra, S. J. A. van Gisbergen, J. G. Snijders and T. Ziegler, *J. Comput. Chem.*, 2001, **22**, 931–967.

67 B. Hourahine, B. Aradi, V. Blum, F. Bonafé, A. Buccheri, C. Camacho, C. Cevallos, M. Y. Deshaye, T. Dumitrică, A. Dominguez, S. Ehlert, M. Elstner, T. van der Heide, J. Hermann, S. Irle, J. J. Kranz, C. Köhler, T. Kowalczyk, T. Kubař, I. S. Lee, V. Lutsker, R. J. Maurer, S. K. Min, I. Mitchell, C. Negre, T. A. Niehaus, A. M. N. Niklasson, A. J. Page, A. Pecchia, G. Penazzi, M. P. Persson, J. Řezáč, C. G. Sánchez, M. Sternberg, M. Stöhr, F. Stuckenberg, A. Tkatchenko, V. W. -z. Yu and T. Frauenheim, *J. Chem. Phys.*, 2020, **152**, 124101.

68 J. Yi, D. Si, R. Xie, Q. Yin, M. Zhang, Q. Wu, G. Chai, Y. Huang and R. Cao, *Angew. Chemie*, 2021, **133**, 17245–17251.

69 F. Haase, K. Gottschling, L. Stegbauer, L. S. Germann, R. Gutzler, V. Duppel, V. S. Vyas, K. Kern, R. E. Dinnebier and B. v. Lotsch, *Mater. Chem. Front.*, 2017, **1**, 1354–1361.

70 Z. Meng and K. A. Mirica, *Nano. Res.*, 2021, **14**, 369–375.

71 D. Sheberla, L. Sun, M. A. Blood-Forsythe, S. Er, C. R. Wade, C. K. Brozek, A. Aspuru-Guzik and M. Dincă, *J. Am. Chem. Soc.*, 2014, **136**, 8859–8862.

72 A. J. Clough, J. M. Skelton, C. A. Downes, A. A. de la Rosa, J. W. Yoo, A. Walsh, B. C. Melot and S. C. Marinescu, *J. Am. Chem. Soc.*, 2017, **139**, 10863–10867.

73 M. E. Foster, K. Sohlberg, C. D. Spataru and M. D. Allendorf, *J.Phys. Chem. C*, 2016, **120**, 15001–15008.

74 Y. Jiang, I. Oh, S. H. Joo, O. Buyukcakir, X. Chen, S. H. Lee, M. Huang, W. K. Seong, S. K. Kwak, J.-W. Yoo and R. S. Ruoff, *J. Am. Chem. Soc.*, 2019, **141**, 16884–16893.

75 K. S. Rawat, S. Borgmans, T. Braeckevelt, C. v. Stevens, P. van der Voort and V. van Speybroeck, *ACS Appl. Nano Mater.*, 2022, **5**, 14377–14387.

76 Y. Liu, W. Li, C. Yuan, L. Jia, Y. Liu, A. Huang and Y. Cui, *Angew. Chem.*, 2022, **134**, e202113348.

77 S. Noro and T. Nakamura, *NPG Asia. Mater.*, 2017, **9**, e433–e433.

78 C. Liu, Y. Xiao, Q. Yang, Y. Wang, R. Lu, Y. Chen, C. Wang and H. Yan, *Appl. Surf. Sci.*, 2021, **537**, 148082.

79 Z. Zhang and O. Š. Miljanić, *Organic Mater.*, 2019, **01**, 019–029.

80 S. T. Emmerling, R. Schuldt, S. Bette, L. Yao, R. E. Dinnebier, J. Kästner and B. v. Lotsch, *J. Am. Chem. Soc.*, 2021, **143**, 15711–15722.

81 Q. Yang and C. Zhong, *Langmuir*, 2009, **25**, 2302–2308.

82 Z. Li, X. Feng, Y. Zou, Y. Zhang, H. Xia, X. Liu and Y. Mu, *Chem. Commun.*, 2014, **50**, 13825–13828.

83 A. Giri and P. E. Hopkins, *Nano Lett.*, 2021, **21**, 6188–6193.

84 Z. Zhang, D. Dell'Angelo, M. R. Momeni, Y. Shi and F. A. Shakib, *ACS Appl. Mater. Interfaces*, 2021, **13**, 25270–25279.

85 Y. J. Choi, J. H. Choi, K. M. Choi and J. K. Kang, *J. Mater. Chem.*, 2011, **21**, 1073–1078.

86 M. Tong, Q. Yang, Y. Xiao and C. Zhong, *Phys. Chem. Chem. Phys.*, 2014, **16**, 15189–15198.

87 H. Sajid, M. Asif, K. Ayub, M. A. Gilani, M. S. Akhter and T. Mahmood, *Surf. Interfaces*, 2021, **27**, 101587.

88 R. Xue, C. Wang, Y. Wang, Q. Guo, E. Dai and Z. Nie, *Metals (Basel)*, 2022, **12**, 1442.

89 Y. Wang, W. Wang, Z. Zhang and P. Li, *Appl. Surf. Sci.*, 2022, **571**, 151355.

90 H. Sajid, T. Mahmood and K. Ayub, *J. Mol. Model.*, 2017, **23**, 295.

91 K. Tan, S. Zuluaga, Q. Gong, Y. Gao, N. Nijem, J. Li, T. Thonhauser and Y. J. Chabal, *Chem. Mater.*, 2015, **27**, 2203–2217.

92 M. Zhang, X. Huang and Y. Chen, *Phys. Chem. Chem. Phys.*, 2016, **18**, 28854–28863.

93 T. Watanabe and D. S. Sholl, *J. Chem. Phys.*, 2010, **133**, 094509.

94 W. An, X. Wu and X. C. Zeng, *J. Phys. Chem. C*, 2008, **112**, 5747–5755.

95 N. B. Shustova, A. F. Cozzolino, S. Reineke, M. Baldo and M. Dincă, *J. Am. Chem. Soc.*, 2013, **135**, 13326–13329.

96 S. Liu, Y. Liu, X. Gao, Y. Tan, Z. Shen and M. Fan, *Appl. Surf. Sci.*, 2020, **500**, 144032.

97 M. K. Rana, M. Sinha and S. Panda, *Chem. Phys.*, 2018, **513**, 23–34.

98 R. G. Parkhomenko, A. S. Sukhikh, D. D. Klyamer, P. O. Krasnov, S. Gromilov, B. Kadem, A. K. Hassan and T. v. Basova, *J. Phys. Chem. C*, 2017, **121**, 1200–1209.

99 G. S. S. Saini, S. Singh, S. Kaur, R. Kumar, V. Sathe and S. K. Tripathi, *J. Phys. Cond. Matter.*, 2009, **21**, 225006.

100 J. Prasongkit, S. Tangsukworakhun, R. Jaisutti and T. Osotchan, *Appl. Surf. Sci.*, 2020, **532**, 147314.

101 H. Wei, Y. Gui, J. Kang, W. Wang and C. Tang, *Nanomaterials*, 2018, **8**, 646.

102 E. Salih and A. I. Ayesh, *Superlattices Microstruct.*, 2020, **146**, 106650.

103 M. U. C. Braga, G. H. Perin, L. H. de Oliveira and P. A. Arroyo, *Microporous Mesoporous Mater.*, 2022, **331**, 111643.

104 Z. Zhai, X. Zhang, X. Hao, B. Niu and C. Li, *Adv Mater. Technol.*, 2021, **6**, 2100127.

Chapter 4

4 Superior Small Gas Adsorption of Interlayered Slipped 2D MOF: GCMC Simulations

The previous chapter focused on identifying the binding motifs of a single gas molecule (NO, NH_3, and H_2S) in the two structural variants (eclipsed and slipped) of Ni/Ni- and Ni/Cu-Pc MOFs followed energetic stability of their fully saturated MOFs with NO molecules. This chapter is focused on grand canonical Monte-Carlo (GCMC) simulations to study the bulk adsorption behaviour of eclipsed-AA and slipped-AA structures of Ni/Ni- and Ni/Cu-Pc MOFs. For this research, the GCMC simulations are implemented by combining RASPA and SC-AMS software(s) using PLAMS scripting. First, the gas adsorption isotherms *via* GCMC calculation in various software especially in RASPA are discussed. Next, the GCMC simulation setup for our calculations is described. This is followed by the GCMC results (adsorption isotherm) discussion for NO gas in MOF analogs, where the effects of the number of MD steps and temperature difference are explained. Lastly, the adsorption isotherm of NH_3 and H_2S are discussed at 298 K.

4.1 Abstract

The design and development of high-performing adsorbents for small toxic gas molecule capturing are extremely significant due to their increased concentration and atmospheric degradation. Herein, the superior gas loading or capturing affinity of the energetically stable structure (slipped-AA) of bimetallic-phthalocyanine MOFs is compared with their fully eclipsed-AA structure. The GCMC results show that the slipped-AA Ni/Ni-Pc MOF shows exceptionally high gas loading *i.e.*, 232 mg/g of NO, 6.5 mg/g of NH_3, and 272 mg/g of H_2S as compared to the 120, 2.2, and 179 mg/g of eclipsed-AA structures, respectively. These GCMC findings are well consistent with our quantum mechanics (QM) results (discussed in Chapter 3), which illustrate that the slipped-AA structures exhibit strong gas binding affinity due to the exposed and freely available active sites, indicating that the interlayer slipping of the

conductive 2D MOFs can be a promising feature for enhanced gas capture ability of materials.

4.2 Introduction

An atomistic simulation namely, grand canonical Monte-Carlo (GCMC) has broad applications in material sciences. With GCMC the adsorption behaviour of porous materials can accurately be predicted.[1,2] Thus, it has widely been used as a valuable tool for designing suitable adsorbents for small gas molecules[3] and their separations.[4,5] Since the GCMC calculations using inter-atomic potentials are faster and simpler than quantum mechanics, large-scale computations with GCMC for bulk or periodic structures are possible.[6–8] Within the scope of GCMC, both the gas molecules and bulk adsorbent materials are treated as rigid structures. From the statistical viewpoint, the GCMC ensembles correspond to μVT because the temperature (T) and volume (V) of the studied system are constant while the values of chemical potential (μ) are specified to establish the thermodynamic equilibrium. However, the number or amount of particles can fluctuate. For example, a small system with volume (V) and particles (N) coupled with a large reservoir (**Figure 4.1**). The volume and particles of the reservoir are represented as V′-V and N′-N, respectively. The temperature of both the reservoir and the system is the same. Here, the μ is specified as both system and the reservoir exchange the molecules, but the volume is fixed. A general description of GCMC (reservoir of particles) can be found in the book by Vlugt and coworkers.[9] These GCMC simulations are widely used in the adsorption studies of crystalline porous materials.

In gas adsorption studies, the pressure of gas molecules relates to μ, which is responsible for the control adsorption of gas molecules in porous frameworks. Large-scale GCMC studies on periodic MOF systems have been performed to account for their performance and structural-property relationships for adsorptive gas capturing and separation.[10–13] The application of GCMC simulations for large porous systems is associated with a serious challenge, such as the screening program must be efficient enough that can sieve through potentially hundred and thousands of structures under the condition of interest. In this context, Gowers *et al.*[14] conducted a survey to benchmark the computational accuracy and cost of many existing and freely available algorithms for GCMC simulations. For this purpose, Gowers and co-authors evaluated

the GCMC performance of several programs including, Towhee, Music, DL Monte, Cassandra, and Raspa for CO_2 adsorption in a MOF called IRMOF-1. This study showed that there is a significant difference in the statical value of a single Monte-Carlo step across different GCMC programs.

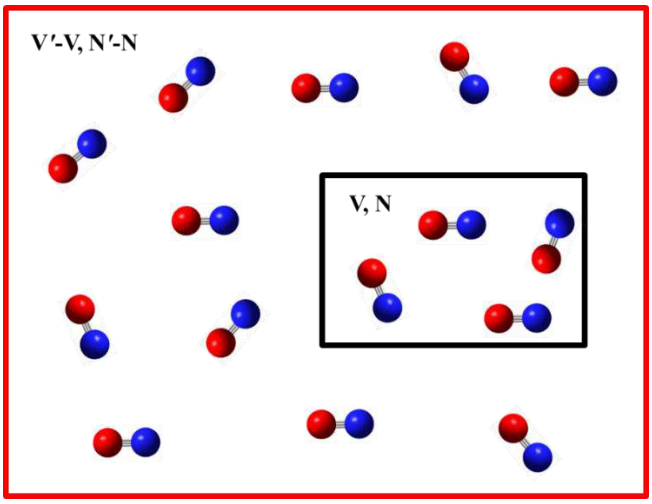

Figure 4.1. General representation of GCMC simulations, where a small system with the number of molecules (N) and fixed volume (V) is represented by the black box and the reservoir with V′-V volume and N′-N particles, shown in the red box.

Among these programs, RASPA[15] is the latest state-of-art algorithm for the implementation of force field-based approaches for large porous materials, especially MOFs.[16] RASPA contains implementations for computing adsorption isotherms of either single or multiple molecules, collective or self-diffusivities, energy minimization for reaction systems, and their visualizations. The RASPA code has the advantage of treating both rigid and flexible frameworks over other MC programs, such as MUSIC[17] which only treats rigid systems. A detailed implementation of RASPA in a number of different ensembles for porous materials with input and output structural features is well documented in the literature.[15,18,19] However, their discussion is beyond the scope of this chapter, therefore, the discussion here is restricted to the basic information used for this particular study.

Metal-Organic frameworks (MOFs) are promising candidates for more efficient gas capture applications due to the large internal surface area and metal-organic coordinate bonds which show enhanced adsorption capacity.[20–22] The highly tunable nature is one of the effective features of MOFs, they can be synthesized possibly as an ideal framework *via* the right combination of SBUs *i.e.*, metal clusters and organic linkers

for optimal performance. Since the number of MOFs with a variety of combinations that can be envisioned is essentially infinite, thus finding suitable SBUs with an ideal combination and optimal performance is a great challenge, which is practically impossible. In this context, molecular simulation techniques would be helpful to characterize all possible combinations and evaluate their performances. For the reliable prediction of energetic and gas adsorption properties in MOFs, it is essential to accurately describe the interactions between the gas molecules and the atoms of frameworks. Particularly, it is necessary to have a reliable force field that can accurately define the forces between atoms.

Currently, the Universal Force Field (UFF)[23] and another generic force field (*e.g.*, DREIDING[24]) are commonly used to reasonably estimate the thermodynamic and gas adsorption properties of MOFs. However, infinite distant MOFs with diverse chemical functionalities limit their use because these force fields fail to produce reasonable descriptions. Since many new force fields have been parametrized using *ab initio* molecular simulations to improve their accuracy for gas adsorption properties of MOFs. For example, Düren and coworkers used a genetic algorithm to parametrize many force field parameters using thousands of single-point *ab initio* calculations.[25] They claimed that the parametrized force field gives gas adsorption isotherms in good accord with experimental data along with the accurate prediction of adsorption mechanisms. Fang *et al.*,[26] developed transferable force fields by combining (classical) atomistic simulations and dispersion-corrected density DFT simulations. In this approach, 2-global scaling factors were incorporated in the (classical) 12-6 Lennard-Jones parameters, and these were optimized within the single-point DFT framework. Zang *et al.*,[27] however, could not determine this scaling factor for open-metal sites MOFs (CuBTC) with H_2O inside, rather an additional empirical term was added as a function of Cu-H_2O distance to correct the total energy of the system. These proposed methodologies of developing new force fields generalizable to a wide class of MOFs require high-level *ab initio* calculations, especially MP2 to probe pairwise interactions.[28,29] These calculations require significantly large computer time and resources, therefore, are limited to smaller clusters. Accordingly, the previously parametrized force fields were based on cluster calculations[30] because the traditional MP2 calculations are unaffordable for clusters with >100 atoms,[31] which poses limitations on the practical use of these force fields. Lin *et al.*,[31] proposed a new

approach of parametrizing accurate force fields from periodic exchange-correlation DFT functional with dispersion corrections included. Calero *et al.*,[32] provided transferable force fields for light gases adsorption on crystalline porous materials, however, they found some discrepancies in the results due to the kinetic impedimenta of cations present in the framework.

From a computational viewpoint, it has been shown that, although, many of the proposed force fields are reliable but are material specific *e.g.*, for open-metal site MOFs,[32] flexible MOFs,[33] zeolites.[34,35] In the case of 2D MOFs, there is no specific force field parameterized yet because π-interaction between the layers plays a significant role in the adsorption phenomenon.[36] However, the DREIDING force field[24] is extensively used in the gas adsorption studies of 2D covalent organic frameworks (COFs) because it showed good agreement with experimental results.[37–41] Literature reveals that the combined DREIDING and UFF is a well-accepted approach for modeling gas adsorption in MOFs, where LJ parameters are taken from DREIDING for MOF atoms, except inorganic part (*e.g.*, metal clusters), those treated with UFF.[42–44]

4.3 GCMC Simulations Setup

The gas adsorption isotherms of Pc-MOF were obtained *via* grand canonical Monte-Carlo (GCMC) calculations using RASPA-1.0[15] software. Adsorption isotherm can be obtained at a specified range of (increasing) pressures. To comply with the experimental conditions, the accessible pore volume of the framework is quite an essential parameter. In GCMC scope, it is referred to as a void fraction, an empty space accessible to the adsorbate molecules. The accessible pore volume of the framework was obtained at room temperature through *helium void-fraction*. The calculated pore volumes of eclipsed-AA Ni/Ni and Ni/Cu-Pc are 0.345 and 0.459 cm^3/g, whereas, the void fraction for slipped-AA analogues are 0.468 and 0.467 cm^3/g, respectively.

The gas molecule's interactions with framework atoms were defined by Lennard-Jones (LJ) potential and their partial charges. For this study, the LJ and point charges on adsorbed NO,[45] NH_3[46] and H_2S[47] were obtained from the literature (**Table 4.1**). The NO and H_2S were modeled as rigid molecules with partial charges assigned on each atom while NH_3 was a rigid and three-site model with two sites located at N and H

atoms and the third one at the center of mass (COM) to maintain the charge neutrality on NH_3.

Table 4.1. Lennard-Jones potential parameters and partial charges of the guest molecules used in this work.

Atoms	ϵ/k_b (K)	σ (Å)	q_i (e)
N_NO	79.50	3.01	+0.029
O_NO	96.94	2.87	-0.029
N_NH3	185.00	3.42	---
H_NH3	---	---	+0.41
NH3(COM)	---	---	-1.04
S_H2S	232.00	3.72	-0.38
H_H2S	---	---	-0.90

For this work, the van der Waals (vWD) interactions *i.e.*, dispersion as well as the repulsion between the interacting atoms were modeled with the (standard) LJ potentials

$$U_{LJ}(r_{ij}) = 4\varepsilon_{ij}\left[\left(\frac{\sigma_{ij}}{r_{ij}}\right)^{12} - \left(\frac{\sigma_{ij}}{r_{ij}}\right)^{6}\right] \tag{4.1}$$

Where, r_{ij} is the interacting distance between the two atoms i and j, while ε and σ are the LJ energy and length parameters, respectively, those were taken from the Universal Force Field (UFF)[23] and DREIDING[48] for the metallic parts (*i.e.*, Ni or Cu) and organic parts of MOFs, respectively. Defining the inter-atomic potentials for organic and inorganic parts of MOF with two different force fields is a popular approach in studying the adsorption isotherms of gases in MOFs.[49] Travert and co-workers[50] modeled the adsorption of a small gas (H_2S) in MIL-based MOFs by defining UFF and DREIDING potential respectively for inorganic and organic parts. A similar strategy was adopted here in modeling the adsorption of NO, NH_3, and H_2S in Ni/Ni- and Ni/Cu layered MOFs. Lorentz-Berthelot mixing rules were employed to describe the interaction parameters between gas molecules and atoms of MOF interaction parameters.

$$\epsilon_{ij} = \sqrt{\epsilon_i \epsilon_j}, \qquad \sigma = \frac{1}{2}(\sigma_i + \sigma_j) \tag{4.2}$$

Similar to the gas molecules, the partial charges on atoms of the framework need to be defined in order to calculate guest-MOF electrostatic interactions. For this purpose, the charge equilibration method (QEq) can be implemented in Raspa to assign partial

point charges to framework atoms.[51] Thus the QEq method was implemented to compute the point charges on the atoms of a single-unit cell of frameworks using Universal Force Field. The obtained charges are listed in the last column of the CIF files of frameworks.

The important critical parameters including temperature, pressure, and acentric factor of each involved molecule have to be defined separately, and separate input files for NO, NH_3, and H_2S were created. The critical constants, temperature (K), pressure (Pa), and acentric factor were defined in the first three rows of each input file. The accurate values of critical constants are necessary because they are used to calculate the fugacity using the Peng-Robinson equation of state. These values can be obtained from the literature. Somayajulu *et al.*[52] listed the critical constant for thousands of molecules. The values of critical constants for NO, NH_3, and H_2S are listed in **Table 4.2**.

Table 4.2. Critical constants values, including critical temperature (T_c) in Kelvin (K), critical pressure (P_c) in bar, and acentric factor (ω) for NO, NH_3, and H_2S.

Formula	T_c (K)	P_c (bar)	ω
NO	180.00	64.80	0.5896[53]
NH_3	405.40	11.35[54]	0.2560
H_2S	373.54	90.08	0.2420[55]

For GCMC simulations of both eclipsed-AA and slipped-AA MOFs, 2×2×4 supercells were used with the vWD cutoff distance of 25 Å. The Ewald summation method was used for the electrostatic interactions with a relative precision of 1×10^{-6}. During the GCMC simulations, the MOF atoms and gas molecules are kept rigid. In addition, the four distant moves for gas molecules were used including insertion and deletion with 100 % probability, while translation, and rotation with 50 % probability. In GCMC calculations, the MC cycles were varied such as 6×10^5, 2×10^5, and 2×10^4 for adsorption isotherm with 4×10^5, 1×10^5 and 1×10^4, respectively, for equilibration of the systems.

4.4 Results and Discussion

4.4.1 NO Adsorption Isotherm

The effect of interlayer slipping of MOFs on the NO adsorption is studied. Prior to the study of adsorption isotherm on different *e.g.*, eclipsed-AA and slipped-AA structures

of Ni/Ni- and Ni/Cu-Pc MOFs, a comparison between the number of MC steps was established in order to save the resources and reduce the computational cost. For this purpose, a GCMC simulation of NO adsorption on eclipsed-AA Ni/Ni-Pc MOFs is run with 20,000, 200,000, and 600,000 MD steps where the equilibration steps were 10,000, 100,000, and 400,000, respectively. However, comparisons between 20,000 and 200,000 were made for eclipsed-AA Ni/Cu-Pc MOF and slipped-AA Ni/Cu-Pc and Ni/Ni-Pc MOFs. Although, we used a small number of MC steps (20,000) for isotherm production, however, these steps can be as low as 12,000 cycles.[21] Zing *et al.*,[56] produced MOF adsorption isotherms with 20,000 GCMC cycles. Altundal *et al.*,[57] produced GCMC isotherms of small gas adsorption in COFs with 20,000 steps. The adsorption isotherms displayed in **Figure 4.2** illustrate that there is no significant variation in the adsorption capacity of MOFs analogs. In other words, the adsorption amount is independent of the number of MC steps.

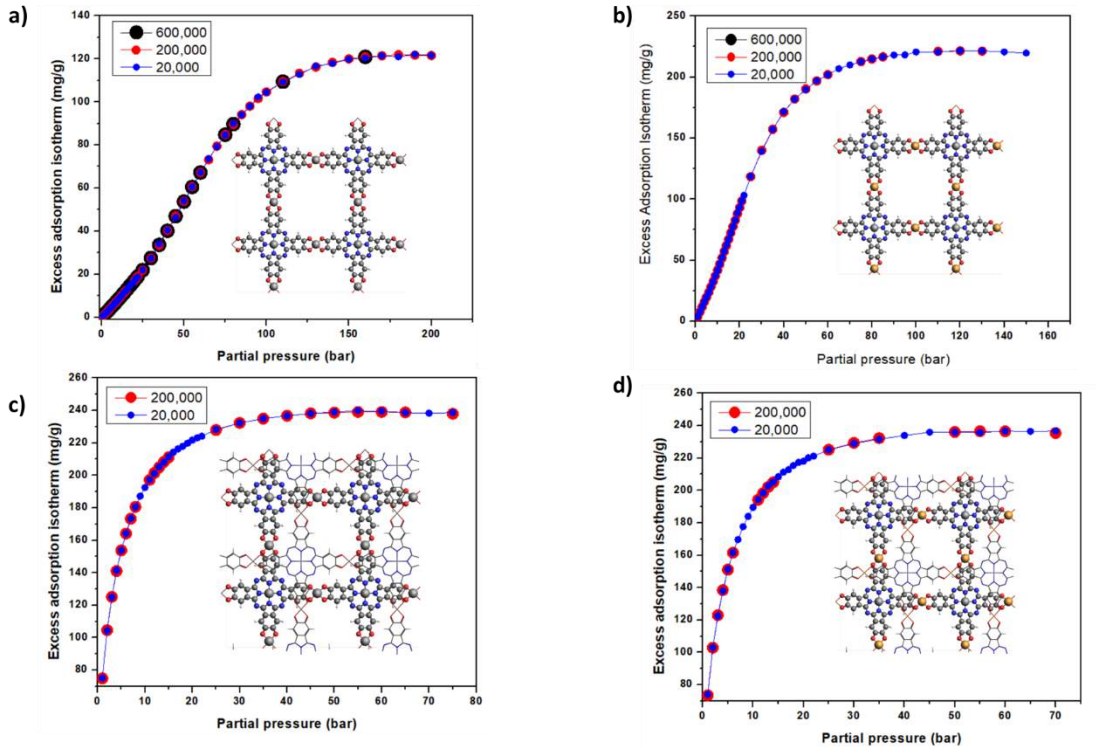

Figure 4.2. A comparison between the number of MD step and NO adsorption capacity of variation of eclipsed-AA a) Ni/Ni-Pc, b) Ni/Cu-Pc MOFs and slipped-AA c) Ni/Ni-Pc, d) Ni/Cu-Pc MOFs, insets are the periodic structures of corresponding MOFs.

Based on these results, it was decided to study the adsorption isotherms at the smallest but reasonable number of MC runs *i.e.* 20,000. In the subsequent step, the adsorption isotherm, corresponding to the excess amount of NO adsorption in the gravimetric unit (mg/g) as a function of partial pressure of MOF analogs at 298 K was estimated. Our quantum mechanics results suggested that the slipped-AA MOF structures are not only energetically stable but showed higher binding strength as compared to the eclipsed-AA geometries. Hence, it is expected to have a higher potential for gas adsorption of slipped-AA geometries, which is confirmed by the adsorption isotherms presented in **Figure 4.3**. It is shown that the NO adsorption capacities of slipped-AA MOF structures are huge, about 70 mg/g, even at very low pressure (1 bar); correspondingly, it is nearly zero for eclipsed-AA MOF structures. Moreover, the slipped-AA structures attain saturation at 30 bar with the NO adsorption amount of 230 mg/g. Whilst the saturation points for eclipsed-AA structures of Ni/Ni- and Ni/Cu-Pc MOFs are attained at 100 bar of pressure, the saturation amounts of NO are 104 and 220 mg/g, respectively.

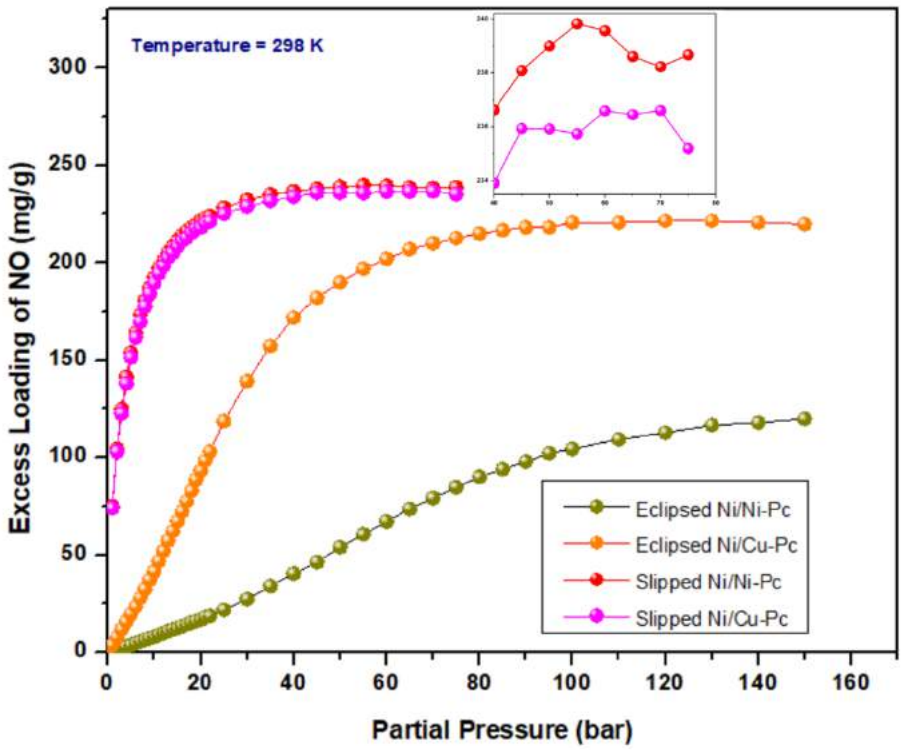

Figure 4.3. The GCMC simulations of NO adsorption isotherms at 289 K of eclipsed and slipped Ni/Ni- and Ni/Cu-Pc MOFs. Inset is the NO adsorption variation of slipped structures of Ni/Ni- and Ni/Cu-Pc MOFs between 60 & 90 bar pressure.

In comparison between the Ni and Cu metals, the adsorption capacities of Ni-containing MOFs (Ni/Ni-Pc) is 235 mg/g, however, it reduces to 232 mg/g upon replacing Ni metal atoms with Cu from inorganic connector units of slipped-AA MOF structures. In eclipsed-AA structures, due to the unavailability of metal sites, because such sites are hidden between the stacked layers, the adsorption capacity is not directly affected by the nature of metals. However, the pores volume of MOFs analogues plays an important role in adsorbing gas molecules,[58] especially in eclipsed-AA geometries. Prior to the GCMC simulations, the pore volumes of MOF structures are computed using "helium void-fraction" implemented in RASPA software, which are 0.468, 0.467, 0.4588, and 0.345 cm^3/g for AA-Ni/Ni-, AA-Ni/Cu-, slipped-AA Ni/Cu and slipped-AA Ni/Ni-Pc MOFs, respectively. Owing to the smallest pore volume, the eclipsed-AA Ni/Ni-Pc MOF shows the least NO adsorption capacity.

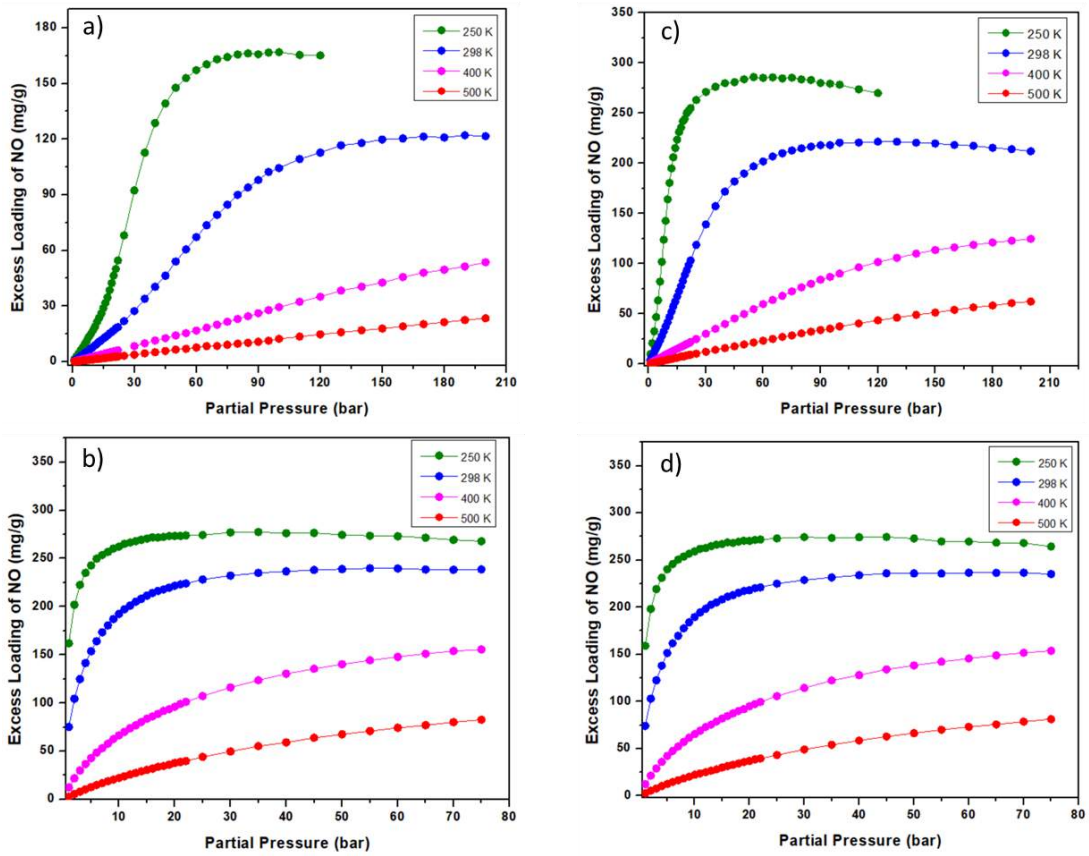

Figure 4.4. NO adsorption isotherms of eclipsed-AA a) Ni/Ni-, b) Ni/Cu- and slipped-AA c) Ni/Ni- and d) Ni/Cu-Pc MOFs at different temperatures.

4.4.1.1 Effect of Temperature

In this section, the NO adsorption capacities of MOFs at different temperatures including 250, 298, 400, and 500 K have been investigated and discussed, as shown in **Figure 4.4**. At the low temperature (250 K), all the MOF candidates show outstanding NO adsorption capacity *i.e.*, 167 mg/g of eclipsed-AA Ni/Ni-Pc, 285 mg/g of eclipsed-AA Ni/Cu-Pc, 277 mg/g of slipped-AA Ni/Ni-Pc, and 274 mg/g of slipped-AA Ni/Cu-Pc MOFs; correspondingly, the saturation is also attained at low pressure *e.g.*, 100, 75, 35, 45 and 35 bar. Moreover, it is found that the NO adsorption capacity decreases with increasing temperature due to the increasing kinetic energies of the guest molecules which weakens the attractive forces between NO molecules and MOF surfaces.[59] This lowering of the NO adsorption capacity of selected MOF is consistent with literature values.[60–62]

At the highest temperature *i.e.*, 500 K, the NO adsorption capacities of all the Pc-MOFs are decreased by approximately 80 wt% even at very high pressure of 190 bar for eclipsed-AA and 90 bar for slipped-AA structures. Moreover, these results further illustrate that the slipped-AA structures exhibit type I isotherms which reflect the monolayer adsorption of NO on the surface of exposed layers due to slipping. On the other hand, the eclipsed-AA structures of Pc-MOFs show type V isotherms,[63] which is more clear at a lower temperature (250 K). The type-V isotherm is typically for the adsorption on the porous site of the adsorbents,[64] thus, it can be concluded that the NO molecules adsorb on the porous/linker site of eclipsed-AA MOFs, which is similar to the GFN1-xTB results, discussed in Chapter 3.

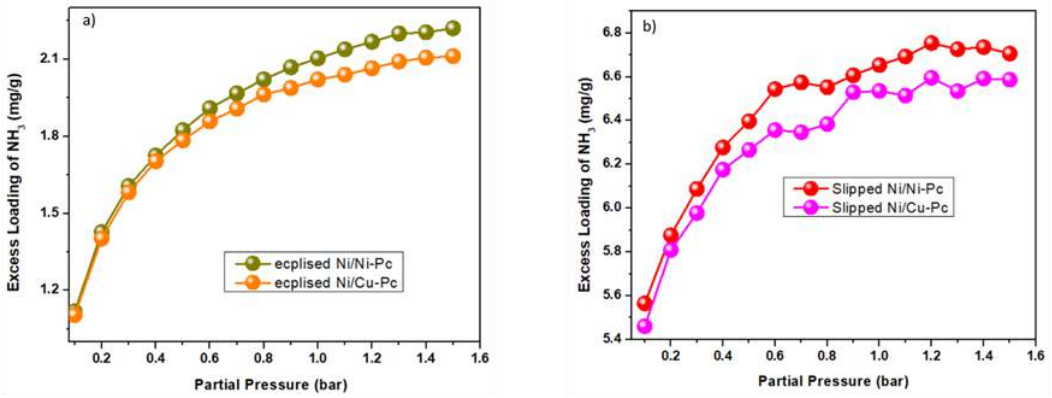

Figure 4.5. NH_3 adsorption isotherms of a) eclipsed-AA and b) slipped-AA of Pc-MOFs at 298 K.

4.4.2 NH_3 Adsorption Isotherm

The NH_3 adsorption isotherms of eclipsed-AA and slipped-AA Ni/Ni- and Ni/Cu-Pc MOFs are computed at 298 K, presented in **Figure 4.5**. Unlike NO adsorption, NH_3 adsorption takes place at low pressure (0.1-1.6 bar). **Figure 4.5** shows a significant difference between the amount of NH_3 adsorption on eclipsed-AA and slipped-AA structures of MOFs. For instance, the slipped-AA structures of MOF show higher NH_3 adsorption (>6.5 mg/g) as compared to the eclipsed geometries, which is well consistent with the binding energy results computed at GFN1-xTB. The higher adsorption isotherms of slipped-AA geometries are well consistent with the literature as well,[65] where the CO_2 adsorption capacity of slipped COF is higher than the perfect eclipsed structures. Upon increasing pressure, the adsorption capacity of Ni/Ni- and Ni/Cu-Pc MOFs are clearly separated, where the adsorption capacity of the former is higher than that of the latter, indicating that the molecule adsorption is facilitated by Ni metal in these MOFs. These findings are also in accord with the *ab initio* results.

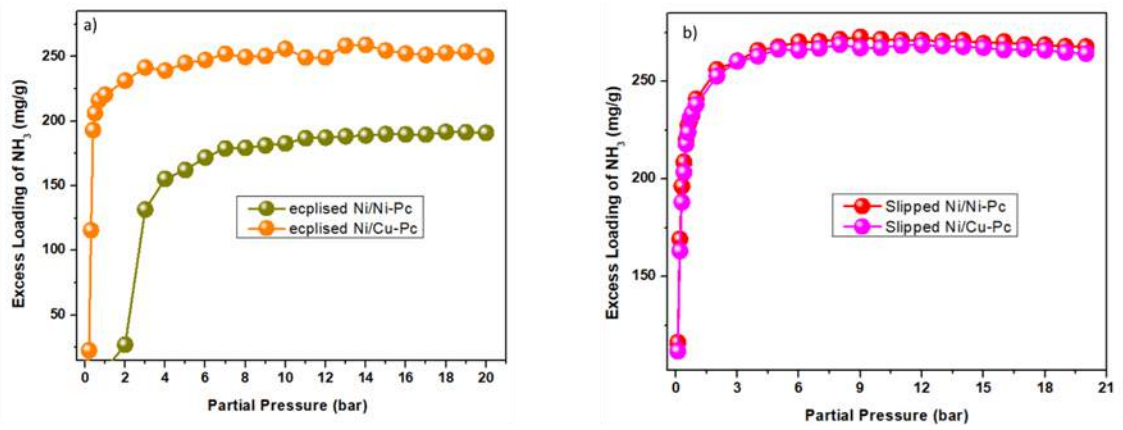

Figure 4.6. H_2S adsorption isotherms of eclipsed-AA and b) slipped-AA of Pc-MOFs at 298 K.

4.4.3 H_2S Adsorption Isotherm

Similar to NH_3, the H_2S adsorption isotherm is calculated at 298 K, and the applied pressure is varied between 1 to 20 bar, which is far higher than NH_3, indicating that the H_2S adsorption takes place at higher applied pressure. However, the adsorption saturation is attained between 0 and 2 bar of pressure. The H_2S adsorption capacity of slipped-AA MOF is higher as compared to the eclipsed structures (**Figure 4.6**). The maximum adsorption of H_2S at saturation is 270 and 267 mg/g of slipped-AA Ni/Ni- and Ni/Cu-Pc MOFs, respectively. The maximum adsorption is reduced to 179 and

252 mg/g of eclipsed-AA Ni/Ni- and Ni/Cu-Pc MOFs, respectively. This attributes to the higher capacity of H_2S adsorption in slipped-AA MOFs, which agrees well with the GFN1-xTB results, where the binding strength of H_2S is multifold higher than eclipsed-AA geometries.

4.5 Conclusions

The gas adsorption capacity and effect of interlayer slipping of 2D bimetallic-phthalocyanine MOFs are theoretically investigated using RASPA code via PLAMS scripting in SCM-AMS software. Interestingly, the most stable slipped structures of respective MOFs show unusual gas uptake. In particular, a slipped-AA of Ni/Ni-Pc MOF shows outstanding gas loading, which is approximately two-fold higher than the eclipsed-AA counterpart. The remarkable gas loading of slipped-AA structures is attributed to the strong interactions with the gas molecules. On addition, because these configurations exhibit exposed active sites, which facilitate more interactions with the molecules. Notably, the Ni in NiO_4 nodal units of Ni/Ni-Pc MOF also facilitates more strong interactions as compared to the Cu in CuO_4 of Ni/Cu-Pc MOF. Thus former show high adsorption capacity in all the cases except eclipsed-AA structures owing to the unavailability of metal sites. Lastly, these results manifest that interlayer slipping could produce a promising effect on the gas capturing of material, especially in 2D MOFs or COFs, *etc*.

4.6 References

1 D. J. Adams, *Mol. Phys.*, 1975, **29**, 307–311.

2 J. R. Errington, *Phys. Rev. E*, 2003, **67**, 012102.

3 S.-Y. Kim, A.-R. Kim, J. W. Yoon, H.-J. Kim and Y.-S. Bae, *Chem. Eng. J.*, 2018, **335**, 94–100.

4 Y.-S. Bae, B. G. Hauser, Y. J. Colón, J. T. Hupp, O. K. Farha and R. Q. Snurr, *Microporous Mesoporous Mater.*, 2013, **169**, 176–179.

5 Y. Wu, H. Chen, D. Liu, Y. Qian and H. Xi, *Chem. Eng. Sci.*, 2015, **124**, 144–153.

6 N. S. Bobbitt, J. Chen and R. Q. Snurr, *J. Phys. Chem. C*, 2016, **120**, 27328–27341.

7 S. Li, Y. G. Chung and R. Q. Snurr, *Langmuir*, 2016, **32**, 10368–10376.

8 Z. Qiao, C. Peng, J. Zhou and J. Jiang, *J. Mater. Chem. A Mater.*, 2016, **4**, 15904–15912.

9 T. J. H. Vlugt, J. P. J. M. van der Eerden, M. Dijkstra, B. Smit and D. Frenkel, *Introduction to Molecular Simulation and Statistical Thermodynamics*, Delft, The Netherlands, 2009.

10 C. E. Wilmer, O. K. Farha, Y.-S. Bae, J. T. Hupp and R. Q. Snurr, *Energy Environ. Sci.*, 2012, **5**, 9849.

11 X. Zeng, F. Chen and D. Cao, *J. Hazard. Mater.*, 2019, **366**, 624–629.

12 Y. G. Chung, J. Camp, M. Haranczyk, B. J. Sikora, W. Bury, V. Krungleviciute, T. Yildirim, O. K. Farha, D. S. Sholl and R. Q. Snurr, *Chem. Mater.*, 2014, **26**, 6185–6192.

13 M. Fernandez, T. K. Woo, C. E. Wilmer and R. Q. Snurr, *J. Phys. Chem. C*, 2013, **117**, 7681–7689.

14 R. J. Gowers, A. H. Farmahini, D. Friedrich and L. Sarkisov, *Mol. Simul.*, 2018, **44**, 309–321.

15 D. Dubbeldam, S. Calero, D. E. Ellis and R. Q. Snurr, *Mol. Simul.*, 2016, **42**, 81–101.

16 J. C. Umeh and T. A. Manz, *ACS Omega*, 2022, **7**, 44470–44484.

17 A. Gupta, S. Chempath, M. J. Sanborn, L. A. Clark and R. Q. Snurr, *Mol. Simul.*, 2003, **29**, 29–46.

18 M. Pardakhti, E. Moharreri, D. Wanik, S. L. Suib and R. Srivastava, *ACS Comb. Sci.*, 2017, **19**, 640–645.

19 Y. G. Proenza and R. L. Longo, *J. Chem. Inf. Model.*, 2020, **60**, 644–652.

20 P. G. M. Mileo, K. Ho Cho, J. Park, S. Devautour-Vinot, J.-S. Chang and G. Maurin, *J. Phys. Chem. C*, 2019, **123**, 23014–23025.

21 S.-Y. Kim, S.-I. Kim and Y.-S. Bae, *J. Phys. Chem. C*, 2020, **124**, 19538–19547.

22 K. Sladekova, C. Campbell, C. Grant, A. J. Fletcher, J. R. B. Gomes and M. Jorge, *Adsorption*, 2020, **26**, 663–685.

23 A. K. Rappe, C. J. Casewit, K. S. Colwell, W. A. Goddard and W. M. Skiff, *J. Am. Chem. Soc.*, 1992, **114**, 10024–10035.

24 S. L. Mayo, B. D. Olafson and W. A. Goddard, *J. Phys. Chem.*, 1990, **94**, 8897–8909.

25 L. Chen, C. A. Morrison and T. Düren, *J. Phys. Chem. C*, 2012, **116**, 18899–18909.

26 H. Fang, P. Kamakoti, J. Zang, S. Cundy, C. Paur, P. I. Ravikovitch and D. S. Sholl, *J. Phys. Chem. C*, 2012, **116**, 10692–10701.

27 J. Zang, S. Nair and D. S. Sholl, *J. Phys. Chem. C*, 2013, **117**, 7519–7525.

28 D. Hagberg, G. Karlström, B. O. Roos and L. Gagliardi, *J. Am. Chem. Soc.*, 2005, **127**, 14250–14256.

29 O. Engkvist, P.-O. Åstrand and G. Karlström, *Chem. Rev.*, 2000, **100**, 4087–4108.

30 A. L. Dzubak, L.-C. Lin, J. Kim, J. A. Swisher, R. Poloni, S. N. Maximoff, B. Smit and L. Gagliardi, *Nat. Chem.*, 2012, **4**, 810–816.

31 L.-C. Lin, K. Lee, L. Gagliardi, J. B. Neaton and B. Smit, *J. Chem. Theory. Comput.*, 2014, **10**, 1477–1488.

32 A. Martin-Calvo, J. J. Gutiérrez-Sevillano, J. B. Parra, C. O. Ania and S. Calero, *Phys. Chem. Chem. Phys.*, 2015, **17**, 24048–24055.

33 A. Thomas, R. Ahamed and M. Prakash, *RSC Adv.*, 2020, **10**, 39160–39170.

34 A. García-Sánchez, C. O. Ania, J. B. Parra, D. Dubbeldam, T. J. H. Vlugt, R. Krishna and S. Calero, *J. Phys. Chem. C*, 2009, **113**, 8814–8820.

35 L. Liu, L. Wang, D. Liu, Q. Yang and C. Zhong, *Green Energy Environ.*, 2020, **5**, 333–340.

36 J. Huang, J.-Q. Wu, B. Shao, B.-L. Lan, F.-J. Yang, Y. Sun, X.-Q. Tan, C.-T. He and Z. Zhang, *ACS Sustain. Chem. Eng.*, 2020, **8**, 10554–10563.

37 K. Gopalsamy, C. Desgranges and J. Delhommelle, *J. Phys. Chem. C*, 2017, **121**, 24692–24700.

38 R. Mercado, R.-S. Fu, A. v. Yakutovich, L. Talirz, M. Haranczyk and B. Smit, *Chem. Mater.*, 2018, **30**, 5069–5086.

39 M. Tong, Y. Lan, Z. Qin and C. Zhong, *J. Phys. Chem. C*, 2018, **122**, 13009–13016.

40 A. Sharma, R. Babarao, N. v. Medhekar and A. Malani, *Ind. Eng. Chem. Res.*, 2018, **57**, 4767–4778.

41 H. Xin, S. Zhou, S. Xu, W. Zhai, S. Liu, S. Liu, Z. Wang, X. Lu and S. Wei, *J. Mater. Sci.*, 2022, **57**, 6282–6292.

42 Z.-R. Tao, J.-X. Wu, Y.-J. Zhao, M. Xu, W.-Q. Tang, Q.-H. Zhang, L. Gu, D.-H. Liu and Z.-Y. Gu, *Nat. Commun.*, 2019, **10**, 2911.

43 J.-F. Lu, M.-L. Liu, C.-B. Zhao, P. Huang, Y.-H. Gao, N. Zheng, Q. Wang, L.-X. Jin, X.-H. Yu and H.-G. Ge, *Inorg. Nano-Met. Chem.*, 2021, 1–8.

44 L. Li, Y. Duan, S. Liao, Q. Ke, Z. Qiao and Y. Wei, *Chem. Eng. J.*, 2020, **386**, 123945.

45 W. Sun, L.-C. Lin, X. Peng and B. Smit, *AIChE J.*, 2014, **60**, 2314–2323.

46 P. Z. Moghadam, P. Ghosh and R. Q. Snurr, *J. Phys. Chem. C*, 2015, **119**, 3163–3170.

47 M. Ramdin, S. P. Balaji, J. M. Vicent-Luna, J. J. Gutiérrez-Sevillano, S. Calero, T. W. de Loos and T. J. H. Vlugt, *J. Phys. Chem. C*, 2014, **118**, 23599–23604.

48 S. L. Mayo, B. D. Olafson and W. A. Goddard, *J. Phys. Chem.*, 1990, **94**, 8897–8909.

49 S. Vandenbrande, T. Verstraelen, J. J. Gutiérrez-Sevillano, M. Waroquier and V. van Speybroeck, *J. Phys. Chem. C*, 2017, **121**, 25309–25322.

50 L. Hamon, H. Leclerc, A. Ghoufi, L. Oliviero, A. Travert, J.-C. Lavalley, T. Devic, C. Serre, G. Férey, G. de Weireld, A. Vimont and G. Maurin, *J. Phys. Chem. C*, 2011, **115**, 2047–2056.

51 S. Demir, N. Bilgin, H. M. Cepni, H. Furukawa, F. Yilmaz, C. Altintas and S. Keskin, *Dalton Trans.*, 2021, **50**, 16587–16592.

52 G. R. Somayajulu, *J. Chem. Eng. Data*, 1989, **34**, 106–120.

53 R. W. Hankinson and G. H. Thomson, *AIChE J.*, 1979, **25**, 653–663.

54 Y. Zhao, X. Dong, M. Gong, H. Guo, J. Shen and J. Wu, *J. Chem. Eng. Data*, 2016, **61**, 3883–3889.

55 M. MOSHFEGHIAN, A. SHARIAT and R. N. MADDOX, *Chem. Eng. Commun.*, 1988, **73**, 205–215.

56 X. Zhang, Q.-R. Zheng and H.-Z. He, *J. Taiwan Inst. Chem. Eng.*, 2022, **138**, 104479.

57 O. F. Altundal, Z. P. Haslak and S. Keskin, *Ind. Eng. Chem. Res.*, 2021, **60**, 12999–13012.

58 Z. Liu, G. An, X. Xia, S. Wu, S. Li and L. Wang, *J. Mater. Chem. A Mater.*, 2021, **9**, 6188–6195.

59 F. Hou, J. Jin, H. Yang, Y. Wang and S. Li, *Appl. Surf. Sci.*, 2019, **475**, 1033–1042.

60 X. Li, L. Zhu, Q. Xue, X. Chang, C. Ling and W. Xing, *ACS Appl. Mater. Interfaces*, 2017, **9**, 31161–31169.

61 S. Yu, G. Jing, S. Li, Z. Li and X. Ju, *Int. J. Hydrogen Energy*, 2020, **45**, 6757–6764.

62 C. U. Deniz, H. Mert and C. Baykasoglu, *Comput. Mater. Sci.*, 2021, **186**, 110023.

63 A. Chakraborty and B. Sun, *Appl. Therm. Eng.*, 2014, **72**, 190–199.

64 M. Burhan, M. W. Shahzad and K. C. Ng, *Int. J. Low Carbon Technol.*, 2018, **13**, 292–297.

65 A. Sharma, A. Malani, N. v. Medhekar and R. Babarao, *CrystEngComm.*, 2017, **19**, 6950–6963.

Chapter 5

5 Thermal Conductivity (*k*) of 2D Benzobisoxazole Covalent Organic Frameworks *via* Non-equilibrium Molecular Dynamics Method

In this chapter, collaborative work with Dr. Psaras McGrier's research group is discussed entitled, "*Thermal Conductivity of Two-Dimensional Benzobisoxazole-Linked Covalent Organic Frameworks with Nanopores: Implications for Thermal Management Applications*". This research has recently been published in the ACS Journal "*ACS Appl. Nano Mater. 2022, 5, 10, 13787–13793*". Herein, Dr. Psaras and coworkers reported the thermal conductivity (*k*) of layered benzobisoxazole (BBO)-based covalent-organic frameworks (COFs) using experimental techniques *i.e.*, longitudinal and steady-state heat-flow method. We contributed to this research in order to verify the experimentally computed thermal conductivity of the COFs by performing non-equilibrium molecular dynamics (NEMD) simulations using SCM-AMS2022.101 software. Based on this study, we wrote a tutorial that how to calculate the thermal conductivity of porous materials using SCM-AMS software that has been published on the SCM website and can be found here, "https://www.scm.com/highlights/thermal-management-conductivity-of-2d-covalent-organic-frameworks-with-nanopores/".

5.1 Abstract

In this chapter, the Nonequilibrium molecular dynamics (NEMD) method was used to study the thermal conductivity (*k*) *via* heat flow method in three BBO-COFs at 80 K and 300 K using Amsterdam Modeling Suite (AMS)2021.101 by Software for Chemistry and Materials (SCM) is explained. The finite size effect, the effect of unit cell size from one (1) to four (4) on the thermal transport of **BBO-COF** has also been investigated. The thermal conductivity value of 4×4 unit cells **BBO-COF** as high as 0.326 W/mK are obtained at 300 K, indicating that the NEMD requires sufficient phonon modes in order to establish suitable scattering or transport modes through the conduction zone which can be achieved by increasing the unit cell size. Our results

also indicate that the heat flow is proportional to the temperature, however, independent of the pore size.

5.2 Introduction

Thermal conductivity (*k*) is a measure of how well a specific material conducts heat, which governs by the lattice vibrations (phonon).[1] The knowledge of thermal conductivity is fundamentally important for energy transportation, conversion, or storage, and effective thermal conductivity is critically important to ensure the reliability and performance of materials in optical and electronic devices. Designing thermally conductive porous and crystalline frameworks is attracting increasing interest due to their high porosity, mechanical strength, low density, and exceptional energy storage properties.[2–4] It is essentially appealing to relate the rate of gas loading and unloading without a sharp rise or drop in temperature due to heat generation during energy diffusion.[5,6] The sharp rise and drop in temperature require adsorbent frameworks with high thermal conductivity. In this regard, new classes of porous frameworks including metal-organic frameworks (MOFs) and covalent-organic frameworks (COFs) have been developed.[7,8] MOFs are formed by the union of metallic clusters and organic linkers *via* coordination bonds. There are a few examples of MOF thermal conductivity; for instance, Wilmer and co-workers explored the thermal transport of MOFs within various aspects *e.g.*, the effects of; missing organic linkers,[9] the presence of gas adsorbates,[10–12] functionalization,[13] structural flexibility,[14] interpenetrations of MOF crystals, pores size and shape.[15] Although these molecular dynamic studies have shown the linear relation between these architectures and the thermal conductivity,[16] typical MOFs still show low thermal conductivity *e.g.*, <2.00 W/mK, which can obstruct the rapid heat transport during gas diffusion.[17]

Recently, an emerging class of porous materials with high chemical stability is COF. Depending upon the functionality and topology, these COFs are promising materials for applications in gas adsorption,[18] energy storage,[19] and optoelectronic devices.[20,21] Knowing their thermal transport properties would improve their role in these and other properties. In porous COF materials, heat propagates by thermal conductance through in-plane bonds or through the pores. In the latter case, thermal transport depends on the pore size. Freitas *et al.*,[4] initially reported the thermal conductivity of some COFs including COF-300, and RIO-*N* (*N* = 1, 4 & 20) as a function of pore size using the

experimental transient plane source technique. The measured values of these COFs range between 0.038 and 0.048 W/mK, which was inversely correlated with pore sizes. Like experimental studies, limited theoretical studies with respect to the thermal transport properties of COFs[22] especially 2D-COFs have been reported.[23–25] Hopkins *et al.*,[26] recently demonstrated the outstanding tunable response of anisotropic thermal conductivity of a 2D-COF (COF-5) using the EGK approach (see next section). Specifically, their results showed an increase in cross-plane heat transport upon increasing gas density inside the pores, whereas, the in-plane heat flow was decreased, indicating that heat conduction was taking place *via* adsorbed gas diffusion and collision with the framework. Similar results, *e.g.*, the increase of out-plane thermal transport of COFs before and after gas adsorption, are obtained in a study by Rahman *et al.*,.[27] Their atomic simulations also showed that the thermal conductivity of COF varies as a function of pore size. For example, COFs with <2 nm of pore diameters exhibit solid-gas scattering, which leads to a monotonic decrease in both in-plane and out-plane heat flow rates. On the other hand, COFs with >2nm of pores diameter, the gas adsorbates in 1D pores channels can lead to a drastic increase in cross-plane thermal properties. Although these studies indicate that 2D COFs with 1D channels show interesting thermal transport properties, the thermal conductivities of 2D COFs as a function of both pore size and the functional group have not been examined yet. Herein, we performed nonequilibrium molecular dynamics (NEMD) for novel benzobisoxazole (BBO) COF and derivatives in order to study their thermal conductivity dependence on pore size and functional groups by replacing small SBUs (phenyl nodes) with triphenylene and triazine triphenylene, respectively (see **Figure 5.1**). The thermal conductivities of BBO-COFs are measured at low (80 K) and high (300 K) temperatures by using the two different local thermostats (see next section for details) at desired temperatures. Interestingly, the thermal conductivities of BBO-COF and derivatives are increased with increasing temperature and are independent of the pore size of COFs. Experimental results generated using the longitudinal, steady-state heat flow method yield similar results at the range of temperature (80 to 300 K).[28]

5.3 Molecular Dynamic Simulation Methodology

Theoretically, there are two basic approaches for estimating the thermal conductivity of materials, a) Equilibrium Green-Kubo method (EGK)[29] and b) Non-equilibrium

Molecular dynamics (NEMD).[30,31] EGK method relates the linear response theory to the fluctuation of the heat flow in a "homogeneous" equilibrium system and requires the auto-correlation function, which makes the approach computationally highly demanding.[32] NEMD is convenient to calculate the *k* of periodic materials because it mimics the natural heat transport process and simulates the *k* through Fourier law.[33] In AMS-SCM software,[34] the NEMD is the only method that can be implemented to calculate thermal conductivity. There are two different approaches to studying *k* using NEMD.

- A thermostat method measures the amount of heat transferred between the well-defined heat sink and the source regions at desired temperatures using two distant thermostats. This method only requires standard thermostats and calculates the heat accumulated at each thermostat as a function of time.
- The heat flow approach measures the induced temperature gradient at the given heat flow rate.

In this study, the NEMD approach was used to describe the temperature-dependent *k* of BBO COF(s), implemented in SCM-AMS2021.1.[34] In the NEMD simulation setup, the COF is divided into three zones *i.e.*, heat source and sink regions and conduction region. The in-plane *k* of BBO COF was determined using Fourier's equation;

$$Q = k\frac{\Delta T}{L} \tag{5.1}$$

Where the temperature gradient is represented by ΔT along the conduction zone represented by *L* between the source and sink region whereas, the heat flux (Q) was calculated from the computed energy transfer rate as,

$$Q = \frac{\left(\frac{dE}{dt}/2\right)}{S} \tag{5.2}$$

where S represents the cross-sectional area and divided by two was used due to the periodic conditions *i.e.*, the heat is transferring in both directions of the cold regions.

Before the NEMD calculations, the COF structures were first energetically relaxed by optimizing using the GFN1-xTB[35] method. Subsequently, the NEMD simulations were performed using the Universal Force Field.[36] Where the BBO COF(s) were initially equilibrated at 80 K and 300 K in two separate calculations using the "global" Berendsen thermostat for 3×10^5 steps. Next, the two local Nosé-Hoover[37–39]

thermostats were set to realize the cold and hot thermal baths. The simulations with Nosé-Hoover thermostats at 80 ±10 or 300±10 were run for 1×10^6 with MD steps of 1 fs. Owing to the separate hot and cold thermostats, the NEMD method shows a finite-size effect,[24] it occurs when the length of the simulation unit cell is not large enough to define the phonon mean free path.[40] This is because, in a small unit cell, phonon modes may not be enough to establish adequate transport through the conduction zone.[41] Therefore, the effect of unit cell size on the thermal conductivity of BBO COF(s) has been investigated. For this purpose, the unit cells of BBO COFs ranged from 1 to 4 in the *a* and *b* directions.

5.4 Results and Discussion

In this research, the thermal conductivity (*k*) of three BBO COF derivatives including 1,3,5-triformylbenzene (TFB), 1,3,5-tris(4-formylphenyl)benzene (TFPB), and tris(4-formylphenyl)triazine (TFPT), named BBO-COF-1, BBO-COF-2, and BBO-COF-3, respectively are reported (**Figure 5.1**).

Figure 5.1. Structures of BBO-COF derivatives, reprinted with permission from Erica *et al.*,[28] from the American Chemical Society.

5.4.1 Thermal Conductivity as a Function of Pore Size

Our NEMD calculations are based on the prototypical BBO-COFs with hexagonal lattices with pore sizes of 1.3, 1.7, and 2.5 nm for BBO-COF-1, BBO-COF-2, and BBO-COF-3, respectively, as schematics in **Figure 5.1**. **Table 5.1** shows the thermal conductivity of BBO-COFs as a function of gas pore sizes. At 80 K, the thermal conductivity of 1×1 lattice units of BBO-COF-1, BBO-COF-2, and BBO-COF-3 are 0.059, 0.085, and 0.185 W/mK, respectively. A similar trend is observed for BBO-

COFs at 300 K temperature. The thermal conductivity increases with increasing the pore size due to the additional channels of heat flow introduced[27] through the additional aromatic groups along the walls of the BBO-COFs, indicating the enhanced stacked or π-π interactions, which improves the phonon transportation.[42]

5.4.2 Temperature-dependent Thermal Conductivity

In order to calculate the temperature-dependent thermal conductivity of BBO-COFs, the NEMD calculations are simulated with two local thermostats at 80 and 300 K temperatures. **Table 5.1** reveals that the BBO-COFs show temperature-dependent thermal conductivity. For example, the thermal conductivity of 4×4-unit cells of BBO-COF-1, and BBO-COF-2 at 80 K are 0.195, and 0.146 W/mK; correspondingly, upon increasing temperature to 300 K their conductivity to 0.326, and 0.230 W/mK, respectively. Although, this behaviour is not consistent with the other COFs reported in the literature.[24] This unusual temperature dependence thermal conductivity behaviour results from the enhanced anharmonic Umklapp process, which can only observe in high-quality crystalline materials in which phonon scattering mechanisms are negligible.[43,44] Surprisingly, in the large unit cell (4×4) of BBO-COF-3, the thermal conductivity decreases from 0.294 W/mK to 0.231 W/mK upon increasing temperature from 80 to 300 K. This is likely because benzene rings are replaced with the triazine rings are more aligned in the out-plane direction in BBO-COF-3, leads to a decrease of microscopic order of crystallinity.[22,45]

Table 5.1. Thermal conductivity of BBO-COF-1, BBO-COF-2, and BBO-COF-3 at 80 K and 300 K. The unit of values is W/mK.

	80 K				**300 K**			
BBO-	**1×1**	**2×2**	**3×3**	**4×4**	**1×1**	**2×2**	**3×3**	**4×4**
COF-1	0.059	0.141	0.163	0.195	0.072	0.251	0.275	0.326
COF-2	0.085	0.122	0.143	0.146	0.156	0.169	0.274	0.230
COF-3	0.185	0.204	0.110	0.294	0.357	0.330	0.197	0.231

5.4.3 Finite-Size Effect and Thermal Conductivity

Finite size effects are produced when the lattice size of the simulation cell is not considerably larger than the mean free path of phonons.[40] Thus in small simulation cells, there may not be adequate phonons to establish desired scattering modes. The size of simulation unit cells varies between 2 to 10 Å depending upon the unit cell size

as well as the type of MD simulations.[41] In this research, the effect of simulation cell size on the thermal transport properties of BBO-COFs has also been investigated. To examine this, the simulation cell of BBO-COFs ranged from 1×1 to 4×4-unit cells at a range of temperatures (80-300 K).

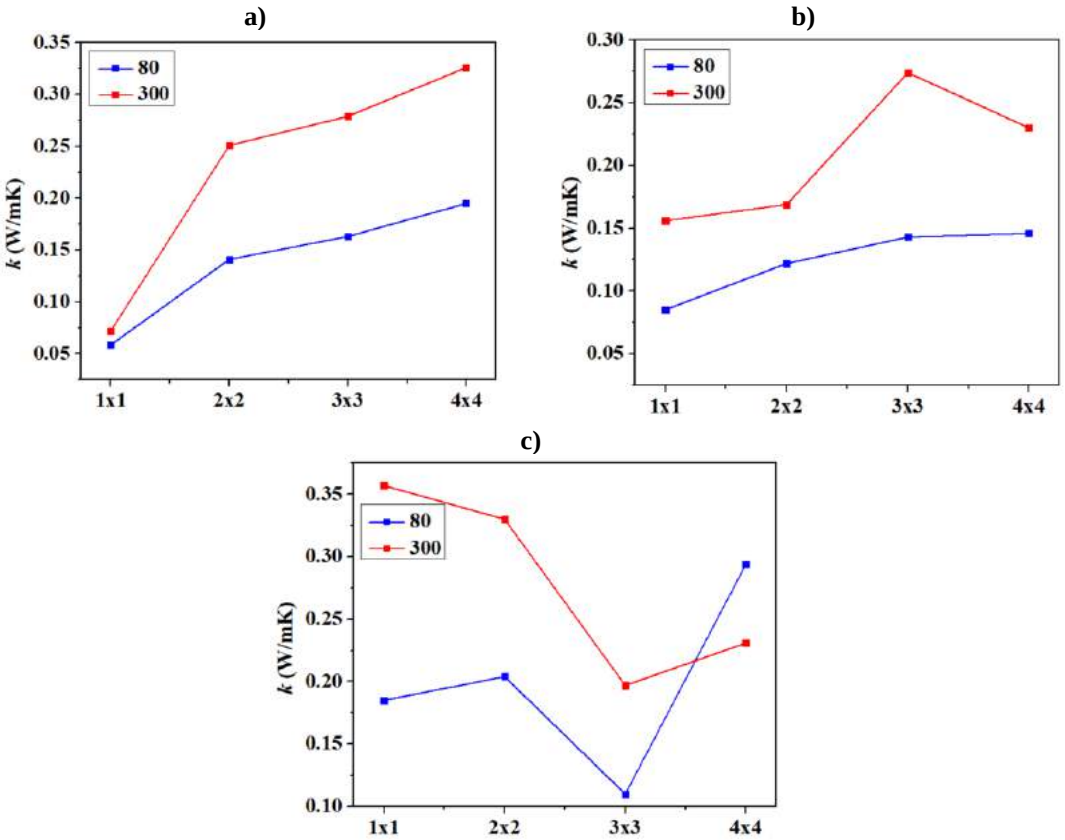

Figure 5.2. Unit cell size effect on the calculated thermal conductivity of a) BBO-COF-1, b) BBO-COF-2, and c) BBO-COF-3. Reprinted with permission Erica *et al.*,[28] from the American Chemical Society.

Figure 5.2 shows that the thermal conductivities of BBO-COFs significantly change with the simulation cell length. In the case of small pores COF (BBO-COF-1), the thermal conductivity increases sharply from 0.072 to 0.251 W/mK at a high temperature (300 K) as the cell length is enlarged from 1×1 to 2×2. However, this change becomes steep when the cell length increases further, manifesting that a 2×2-unit cell is sufficient to produce a converged value,[24] specifically, when the pore size of COF is ~1.5 nm. Similarly, the change is congruent upon increasing the pore size of BBO-COF to ~2.00 nm in BBO-COF-2 with a small exception in the 3×3 lattice at 300 K. Surprisingly, strange behaviour is noticed for BBO-COF-3, where the ultimate decrease is noticed in the thermal conductivity upon increasing the unit cell size at

high temperature (300 K), whereas, the opposite trend is seen at 80 K, indicating the unusual behaviour of BBO-COF-3 due to unknown reasons. However, this might be due to the triazine-aligned out-of-plane of the crystallinity.[45] It is deduced that the phonon means free paths of BBO-COFs are less than 2-unit cells, which is close to the other COFs as well as MOFs in the literature.[24,46,47]

The computed accumulated energies of hot and cold thermostats with finite size effect and linear fit heat flow rate at 80 and 300 K, as a result of NEMD simulations, are displayed in the Appendix.

5.5 Conclusions

In summary, the thermal conducting properties of BBO-COFs have been studied using the nonequilibrium molecular dynamic (NEMD) method. The pore size effect, temperature dependence, and finite size effect are analysed to estimate the heat transfer. The main conclusions are:

a) The thermal conductivities of BBO-COFs are directly related to the pore sizes e.g., the experimentally reported pore sizes of BBO-COF-1, BBO-COF-2, and BBO-COF-3 are 1.3, 1.7, and 2.5 nm, respectively. The thermal conductivity of BBO-COF-3 is more than double as compared to that of BBO-COF-1. The increasing thermal conductivity with pore sizes is probably due to the adding additional aromatic benzene rings in BBO-COF-2 which produce extra phonons in the system. Similarly, by replacing the benzene rings of BBO-COF-2 with triazine in BBO-COF-3, further phonon channels are increased along the wall of the COF.
b) The estimated thermal conductivities of one simulation cell of BBO-COFs range between 0.059 and 0.185 W/mK at 80 K. And they are in the order of BBO-COF-1 > BBO-COF-2 > BBO-COF-3. As the temperature of the simulated BBO-COFs is increased from 80 K to 300 K, the thermal conductivities increase between 0.072 to 0.357 W/mK.
c) The optimal mean free paths of phonon for BBO-COFs are two-unit cells i.e., ~3 nm, similar to some COFs and MOFs. The further increase in mean free paths for phonons results in low conductivity for BBO-COF-3.

Our computational modeling results support the experimental findings which reveal a direct relationship between the heat transport properties and the applied temperature.

5.6 References

1 A. M. Evans, A. Giri, V. K. Sangwan, S. Xun, M. Bartnof, C. G. Torres-Castanedo, H. B. Balch, M. S. Rahn, N. P. Bradshaw, E. Vitaku, D. W. Burke, H. Li, M. J. Bedzyk, F. Wang, J.-L. Brédas, J. A. Malen, A. J. H. McGaughey, M. C. Hersam, W. R. Dichtel and P. E. Hopkins, *Nat. Mater.*, 2021, **20**, 1142–1148.

2 X. Zhang, A. Chen, M. Zhong, Z. Zhang, X. Zhang, Z. Zhou and X.-H. Bu, *Electrochem. Energ. Rev.*, 2019, **2**, 29–104.

3 J. Li, X. Jing, Q. Li, S. Li, X. Gao, X. Feng and B. Wang, *Chem. Soc. Rev.*, 2020, **49**, 3565–3604.

4 S. K. S. Freitas, R. S. Borges, C. Merlini, G. M. O. Barra and P. M. Esteves, *J. Phys. Chem. C*, 2017, **121**, 27247–27252.

5 F. Jeremias, V. Lozan, S. K. Henninger and C. Janiak, *Dalton Trans.*, 2013, **42**, 15967.

6 M. F. de Lange, K. J. F. M. Verouden, T. J. H. Vlugt, J. Gascon and F. Kapteijn, *Chem. Rev.*, 2015, **115**, 12205–12250.

7 C. Dey, T. Kundu, B. P. Biswal, A. Mallick and R. Banerjee, *Acta. Crystallogr. B Struct. Sci. Cryst. Eng. Mater.*, 2014, **70**, 3–10.

8 S.-Y. Ding and W. Wang, *Chem. Soc. Rev.*, 2013, **42**, 548–568.

9 M. Islamov, H. Babaei and C. E. Wilmer, *ACS Appl. Mater. Interfaces*, 2020, **12**, 56172–56177.

10 M. E. DeCoster, H. Babaei, S. S. Jung, Z. M. Hassan, J. T. Gaskins, A. Giri, E. M. Tiernan, J. A. Tomko, H. Baumgart, P. M. Norris, A. J. H. McGaughey, C. E. Wilmer, E. Redel, G. Giri and P. E. Hopkins, *J. Am. Chem. Soc.*, 2022, **144**, 3603–3613.

11 H. Babaei and C. E. Wilmer, *Phys. Rev. Lett.*, 2016, **116**, 025902.

12 H. Babaei, A. J. H. McGaughey and C. E. Wilmer, *ACS Appl. Mater. Interfaces*, 2018, **10**, 2400–2406.

13 H. Babaei, J.-H. Lee, M. N. Dods, C. E. Wilmer and J. R. Long, *ACS Appl. Mater. Interfaces*, 2020, **12**, 44617–44621.

14 K. B. Sezginel, S. Lee, H. Babaei and C. E. Wilmer, *J. Phys. Chem. C*, 2020, **124**, 18604–18608.

15 H. Babaei, A. J. H. McGaughey and C. E. Wilmer, *Chem. Sci.*, 2017, **8**, 583–589.

16 L. Han, M. Budge and P. Alex Greaney, *Comput. Mater. Sci.*, 2014, **94**, 292–297.

17 H. Zhang, P. Deria, O. K. Farha, J. T. Hupp and R. Q. Snurr, *Energy Environ. Sci.*, 2015, **8**, 1501–1510.

18 H. Furukawa and O. M. Yaghi, *J. Am. Chem. Soc.*, 2009, **131**, 8875–8883.

19 S. S. Han, J. L. Mendoza-Cortés and W. A. Goddard III, *Chem. Soc. Rev.*, 2009, **38**, 1460.

20 G. H. v. Bertrand, V. K. Michaelis, T.-C. Ong, R. G. Griffin and M. Dincă, *Proc. Natl. Acad. Sci.*, 2013, **110**, 4923–4928.

21 S.-L. Cai, Y.-B. Zhang, A. B. Pun, B. He, J. Yang, F. M. Toma, I. D. Sharp, O. M. Yaghi, J. Fan, S.-R. Zheng, W.-G. Zhang and Y. Liu, *Chem. Sci.*, 2014, **5**, 4693–4700.

22 H. Ma, Z. Aamer and Z. Tian, *Mater. Today Phys.*, 2021, **21**, 100536.

23 D. Feng, Y. Feng, Y. Liu, W. Zhang, Y. Yan and X. Zhang, *J. Phys. Chem. C*, 2020, **124**, 8386–8393.

24 Y. Liu, Y. Feng, Z. Huang and X. Zhang, *J. Phys. Chem. C*, 2016, **120**, 17060–17068.

25 A. Giri, A. M. Evans, M. A. Rahman, A. J. H. McGaughey and P. E. Hopkins, *ACS Nano.*, 2022, **16**, 2843–2851.

26 A. Giri and P. E. Hopkins, *Nano. Lett.*, 2021, **21**, 6188–6193.

27 M. A. Rahman, C. J. Dionne and A. Giri, *ACS Appl. Mater. Interfaces*, 2022, **14**, 21687–21695.

28 E. M. Moscarello, B. L. Wooten, H. Sajid, L. D. Tichenor, J. P. Heremans, M. A. Addicoat and P. L. McGrier, *ACS Appl. Nano. Mater.*, 2022, **5**, 13787–13793.

29 C. Carbogno, R. Ramprasad and M. Scheffler, *Phys. Rev. Lett.*, 2017, **118**, 175901.

30 P. K. Schelling, S. R. Phillpot and P. Keblinski, *Phys. Rev. B*, 2002, **65**, 144306.

31 L. Hu, W. J. Evans and P. Keblinski, *J. Appl. Phys.*, 2011, **110**, 113511.

32 B. Dongre, T. Wang and G. K. H. Madsen, *Model. Simul. Mat. Sci. Eng.*, 2017, **25**, 054001.

33 D. J. Evans, *Phys. Lett. A*, 1982, **91**, 457–460.

34 G. te Velde, F. M. Bickelhaupt, E. J. Baerends, C. Fonseca Guerra, S. J. A. van Gisbergen, J. G. Snijders and T. Ziegler, *J. Comput. Chem.*, 2001, **22**, 931–967.

35 C. Bannwarth, E. Caldeweyher, S. Ehlert, A. Hansen, P. Pracht, J. Seibert, S. Spicher and S. Grimme, *WIREs Comput. Mol. Sci.*, , DOI:10.1002/wcms.1493.

36 A. K. Rappe, C. J. Casewit, K. S. Colwell, W. A. Goddard and W. M. Skiff, *J. Am. Chem. Soc.*, 1992, **114**, 10024–10035.

37 S. Nosé, *J. Chem. Phys.*, 1984, **81**, 511–519.

38 W. G. Hoover, *Phys. Rev. A (Coll Park)*, 1985, **31**, 1695–1697.

39 G. J. Martyna, M. L. Klein and M. Tuckerman, *J. Chem. Phys.*, 1992, **97**, 2635–2643.

40 A. J. H. McGaughey and M. Kaviany, *Phys. Rev. B*, 2005, **71**, 184305.

41 X. Zhang and J. Jiang, *J. Phys. Chem. C*, 2013, **117**, 18441–18447.

42 Y. Xu, X. Wang, J. Zhou, B. Song, Z. Jiang, E. M. Y. Lee, S. Huberman, K. K. Gleason and G. Chen, *Sci Adv*, 2018, **3**, eaar3031.

43 W. N. dos Santos, J. A. de Sousa and R. Gregorio, *Polym. Test.*, 2013, **32**, 987–994.

44 W. D. KINGERY and M. C. McQUARRIE, *J. Am. Ceram. Soc.*, 1954, **37**, 67–72.

45 H. Ma, E. O'Donnel and Z. Tian, *Nanoscale*, 2018, **10**, 13924–13929.

46 B. L. Huang, A. J. H. McGaughey and M. Kaviany, *Int. J. Heat Mass Transf.*, 2007, **50**, 393–404.

47 B. L. Huang, Z. Ni, A. Millward, A. J. H. McGaughey, C. Uher, M. Kaviany and O. Yaghi, *Int. J. Heat Mass Transf.*, 2007, **50**, 405–411.

Chapter 6

6 Modeling of Enzymatic Immobilization with Hybrid QM/MM Approach

6.1 Abstract

The design and development of effective catalytic systems is a fundamental aspect of sustainable methodologies for chemical production. The biocatalytic applications of the covalent organic frameworks (COFs) are predicted to have much to offer in the coming years. Due to their long-term operational stability and hierarchical porous structures, COFs are considered promising support for bulk biomolecules *i.e.*, enzyme immobilizations. Herein, we show how a newly synthesized COFs-foam with hierarchical pores serves as an ideal host for three different bulk enzymes (~10,000 atoms each) namely, *β*-glucosidase (BGL), cellobiohydrolase (CBH), and endoglucanase (EG). For this purpose, we performed hybrid QM/MM simulations to determine the enzyme binding site on COF- foam as well as their thermodynamic stabilities in order to support the experimental findings. The detailed implementations of Molecular Dynamics (MD) and hybrid QM/MM methods have been described in this Chapter. The results reveal that the hierarchical pores of COF-foam are thermodynamically the most favourable position for enzyme binding. The binding stability of the three enzymes is as follows, EG > BGL > CBH based on the number of hydrogen bonds between the atoms of the enzyme(s) and COF-foam.

6.2 Introduction

Enzymes, nowadays, are gaining increasing importance in the chemical and pharmaceutical industries[1,2] because of their significant role in organic synthesis reactions in terms of improved reaction yield.[3] However, the incompatibility of many enzymes with high pH, solvents, and temperature reduces their industrial importance.[4,5] For this purpose, porous materials, such as hydrogen-bonded organic frameworks (HOFs), metal-organic frameworks (MOFs), and covalent organic frameworks (COFs) are promising candidates for enzyme immobilization.[3,6] Over the last decade, interest in COFs has increased considerably owing to their stability,

tunable pore size, high surface area, and ease of functionalization.[7,8] Thus, the tunable functionalities and well-defined structures of COFs make them suitable hosts for enzyme support and immobilization. In this context, our experimental collaborator; Dr. Rahul Banerjee Group contributed an immobilization of bulk enzyme molecules in a new class of COFs called COF-foams.[9,10] Owing to their microporous nature, the foams COFs offer a wide pore volume for gas adsorption and diffusion which may enhance the catalytic performance of enzymes. In this study, by using experimental techniques, Banerjee *et al.*,[11] argue the higher enzyme immobilization efficiency of COF-foam, facilitating through the weak noncovalent interactions. In order to justify the role of noncovalent interaction in enzyme immobilization on COF-foam, computational modeling is highly demanding. Moreover, the improved catalytic performance of COF-foam upon encapsulation of three enzymes (BGL, CBH, and EG) does not only relate to the relative loading of three enzymes (studied experimentally) but also relates to the relative enzymes' adsorption positions. In simple, the distance between the enzyme and COF-foam and the surrounding pore environment also has a significant impact on the catalytic performances.[12] The lack of suitable experimental techniques to determine the exact preferred adsorption sites for each enzyme and their stability at the atomic level motivated us to perform atomistic quantum mechanical modeling for such enzyme@COF-foam systems.

For this purpose, we performed computational modeling *via* molecular dynamics (MD) and hybrid QM/MM simulations to determine the enzyme's preferable adsorption sites on COF-foam and their binding energies, respectively. Due to the ability to maintain accuracy in defining chemical rearrangements in less computational time, the hybrid QM/MM method is currently a method of choice for modeling biomolecules, such as enzymes.[13,14] The hybrid approach divides a bulk system containing thousands of atoms into two regions; an important electronic region that directly involves in chemical processes and requires highly accurate quantum mechanical (QM) description. On the other hand, the remaining part is treated with low cost and less accurate molecular mechanics (MM) or classical force field method. The computational cost in the hybrid approach is typically reduced by employing a small size of the QM part.[15] The hybrid approach was first developed by Warshel and Levitt *et al.*,[16] in 1970s. Through the years, a variety of different hybrid QM/MM approaches have been developed in varying features, a) the types of schemes for

computing the energies of QM or MM regions, b) how the boundary between QM and MM regions are considered, and c) how the interactions between MM and QM part are treated.[15] A comparison of different QM/MM hybrid methods falls beyond the scope of this chapter, but many excellent review articles can be found in the literature.[17–24] However, the basic theoretical introduction to the hybrid QM/MM approaches is listed in Chapter 1, section 1.3. The hybrid QM/MM approach has a wide range of applications in enzyme modeling, especially structural refinement, validating enzyme mechanistic methods, protein engineering, drug discovery, and many more.[15] Here, we used the hybrid QM/MM method for rationalizing the enzyme immobilization on layered foam-based COFs and to validate the experimental findings. We performed these simulations on Amsterdam Modeling Suite, a chemical modeling software by Software for Chemistry and Materials. The detail is given in the subsequent section.

6.3 Computational Methodology

The MD and QM/MM simulations were performed in SCM-AMS2022.101.[25] First, a monolayer of TpAzo-COF was constructed and optimized with relaxed parameters and without any geometric constraints using GFN1-xTB method. Next, by using the optimized monolayer, a 4×4×4 unit cell (a = 132.98 Å, b = 132.98 Å) of AA-stacked TpAzo-COF was generated (**Figure 6.1**). The 4×4×4 unit cell of TpAzo-COF was considered an adequate model to evaluate the non-covalent interactions between adsorbed enzymes and TpAzo-COF because the large lattices parameters ensured that the lack of self-interactions between repeated units of enzymes in the periodic clusters. The estimated average distance ($D_{EN---EN}$) between two repeated adsorbed units of enzymes are 66, 78, and 86 Å for BGL@TpAzo-COF, CBH@ TpAzo-COF, and EG@ TpAzo-COF, respectively.

Even though, *ab initio* methods are recommended for the accurate estimation of the noncovalent interaction energies specifically in the bulk biological molecules[26] *i.e.*, enzymes. However, semi-empirical methods are even computationally very expensive for the large enzymes, containing ~10k especially, those under study here. Thus, in order to reduce the computational cost, the interaction geometries of three enzymes namely BGL; β-glucosidase, CBH; cellobiohydrolase, and EG; endoglucanase adsorbed in layered TpAzo-COF were first relaxed using Universal Force Field in

Molecular Dynamics simulations.[27] For this purpose, each enzyme was placed in five different orientations on the TpAzo-COF, then fifteen structures were equilibrated at room temperature with applied a global Nosé-Hoover[28,29] thermostat. The MD calculations were implemented with 200,000 steps along with the 0.25 fs. In these calculations, the (bottom) two layers of TpAzo-COF were fixed to maintain stacking interactions between the layers, which hinders the top layers from deformation.

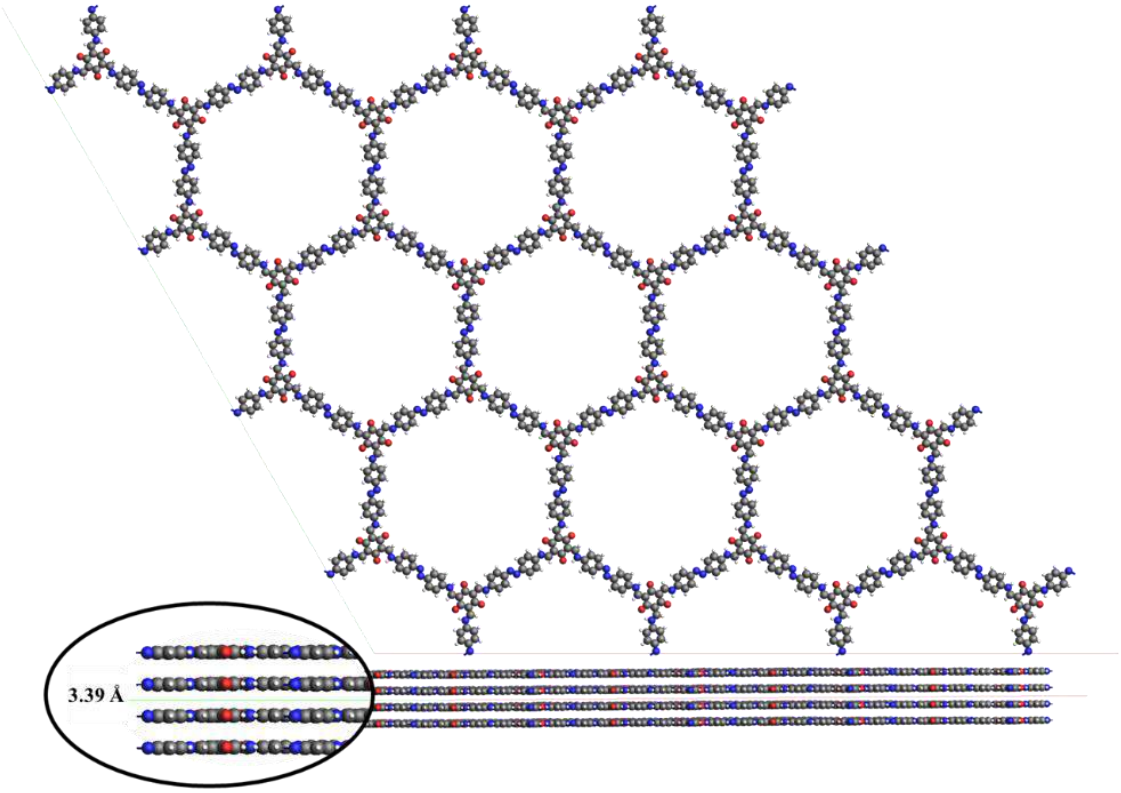

Figure 6.1. Front and side view of 4×4 unit cell of bare TpAzo-COF with layer separation of 3.39 Å.

Next, the final geometries of each MD run were further simulated using a hybrid approach called QM/MM; Quantum Mechanics/Molecular Mechanics[30] to estimate the noncovalent interaction energies accurately between enzymes and TpAzo-COF within the limited computational cost. The QM/MM calculations were implemented in a Hybrid engine of the SCM-AMS2022.101 version. Furthermore, the interacting atoms of enzymes with the cut-off of 15 Å were described as a separate zone and computed with the fast GFN-xTB method, while UFF was applied to the rest of the atoms. The interaction energies (E_{int}) of enzymes and TpAzo-COF were calculated as,

$$E_{int} = E_{En-TpAzoCOF} - \left(E_{En} + E_{TpAzoCOF}\right) \quad (6.1)$$

where, E_{En}, $E_{TpAzoCOF}$, and $E_{En-TpAzoCOF}$ are the single-point QM/MM energies for enzymes, TpAzo-COF, and their complexes, respectively.

At last, the volume and accessible surface area of enzymes are analyzed with a 1.86 Å (N_2) probe in Zeo++ software.[31] The calculated accessible surface areas and volumes of enzymes are shown in **Table 6.1**.

Table 6.1. Accessible surface areas (ASA) and volumes of BGL, CBH, and EG enzymes.

Enzymes	Surface Area (Å^2)	Volume (Å^3)
BGL	16240	97880
CBH	13565	74660
EG	15489	82340

6.4 Results and Discussion

The interaction geometries and energies of BGL, CBH, and EG enzymes with five different interacting conformers each are computed using QM/MM calculations, the resulting energies and structures are given in **Table 6.2** and **Figure 6.2-6.4**, respectively. Each conformer is named enzyme@TpAzo-COF_*n*, where *n* is the number of conformers from 1 to 5.

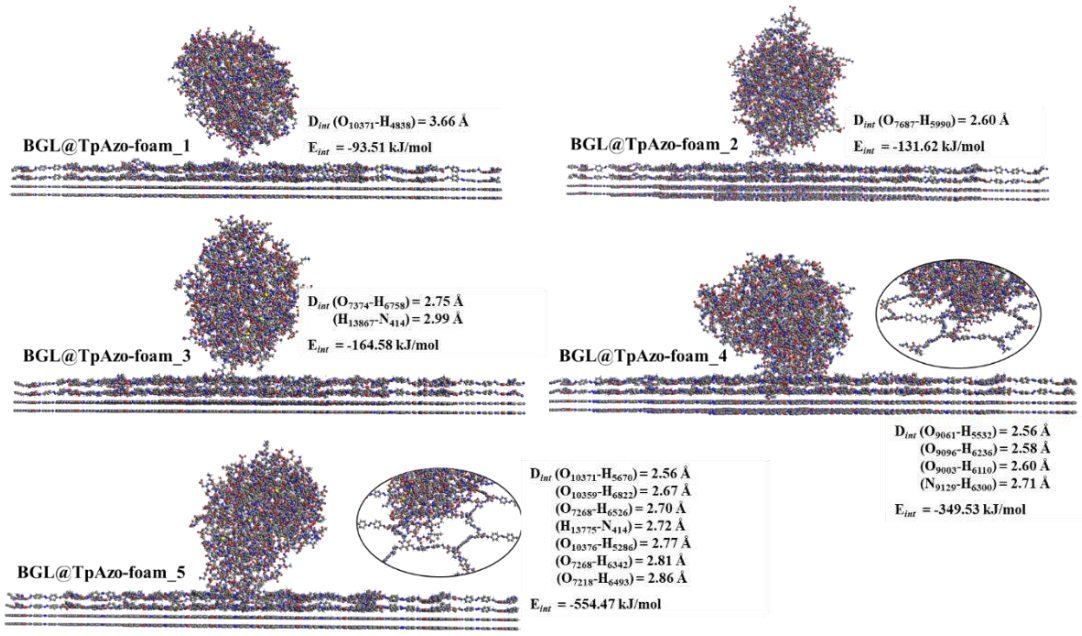

Figure 6.2. Interaction conformers of BGL@TpAzo-COF_*n* with intermolecular distances and interaction energies.

In BGL enzyme interaction, the maximum stability is observed for the BGL@TpAzo-COF_5, where the E_{int} is -554.5 kJ/mol, which is followed by the BGL@TpAzo-COF_4, the E_{int} is -349.5 kJ/mol. In both the BGL@TpAzo-COF_5 and BGL@TpAzo-COF_4, the BGL enzyme interacts with closet intermolecular distances. In these cases, the closest intermolecular distance (D_{int}) between the BGL enzyme and TpAzo-COF layers is 2.56 Å. Unlike them, the enzyme binds on the surface of TpAzo-COF in BGL@TpAzo-COF_2 and BGL@TpAzo-COF_3, as a result, the number of H-bonds in such interaction is reduced. Since, the H-bonding plays an essential role in adsorbing bio-molecules, such as amino acids and nitrogenous organic bases.[32,33] Due to the more than seven (7) H-bonds between the BGL enzyme and TpAzo-COF atoms, the structure_5 exhibits remarkable stability. However, the stability of the structures is decreased when the number of H-bonds decrease. Therefore, the interaction energies of BGL@TpAzo-COF_2 and BGL@TpAzo-COF_3 increase to -131.6 and -164.6 kJ/mol, respectively. However, the lowest negative energy is observed for the BGL@TpAzo-COF_1 *i.e.*, -93.5 kJ/mol. In addition, the largest intermolecular distance (3.66 Å) is observed in BGL@TpAzo-COF_1, which reveals the lowest stability of this structure.

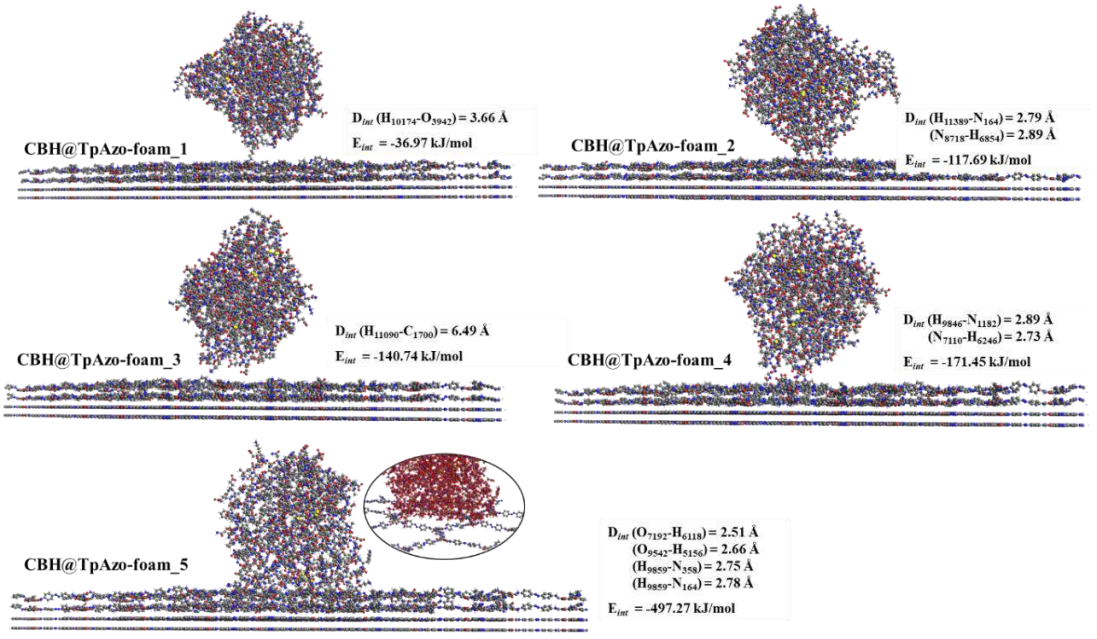

Figure 6.3. Interaction conformers of CBH@TpAzo-COF_*n* with intermolecular distances and interaction energies.

Similarly, in CBH@TpAzo-COF_5, the highest stability is noticed for structure_5 because the maximum atoms of CBH enzyme and TpAzo-COF are interacting. For

CBH@TpAzo-COF _5, the E_{int} is -497.3 kJ/mol, illustrating the significant stability with four H-bonds. However, the number of H-bonds reduce to two in CBH@TpAzo-COF_4, resulting in the lowering of negative E_{int} to -171.5 KJ/mol. For the structures CBH@TpAzo-COF_1, CBH@TpAzo-COF_2, and CBH@TpAzo-COF_3, the interactions are occurring on the surface of the COF layers with the D_{int} around 3.00 Å. The E_{int} of CBH enzymes with TpAzo-COF is -37.0, -117.7, and -140.7 kJ/mol respectively in CBH@TpAzo-COF_1, CBH@TpAzo-COF_2, and CBH@TpAzo-COF_3 conformers. Furthermore, the weak dispersion forces dominate in stabilizing these CBH@TpAzo-COF structures.

In comparison to BGL and CBH, the EG@TpAzo-COF_*n* are highly stabilized because of the maximum number of H-bonds present between the EG enzyme and TpAzo-COF. The D_{int}(s) between the interacting atoms of EG enzyme and TpAzo-COF in structure_1 to structure_5 are ranging between 2.31 and 2.72Å; correspondingly, the E_{int}(s) range between -270.9 to -667.6 kJ/mol. Thus, it can be inferred that the EG interacts more strongly with TpAzo-COF due to the greatest amount of observable H-bonding interactions, followed by the BGL whereas, the CBH shows the least interaction.

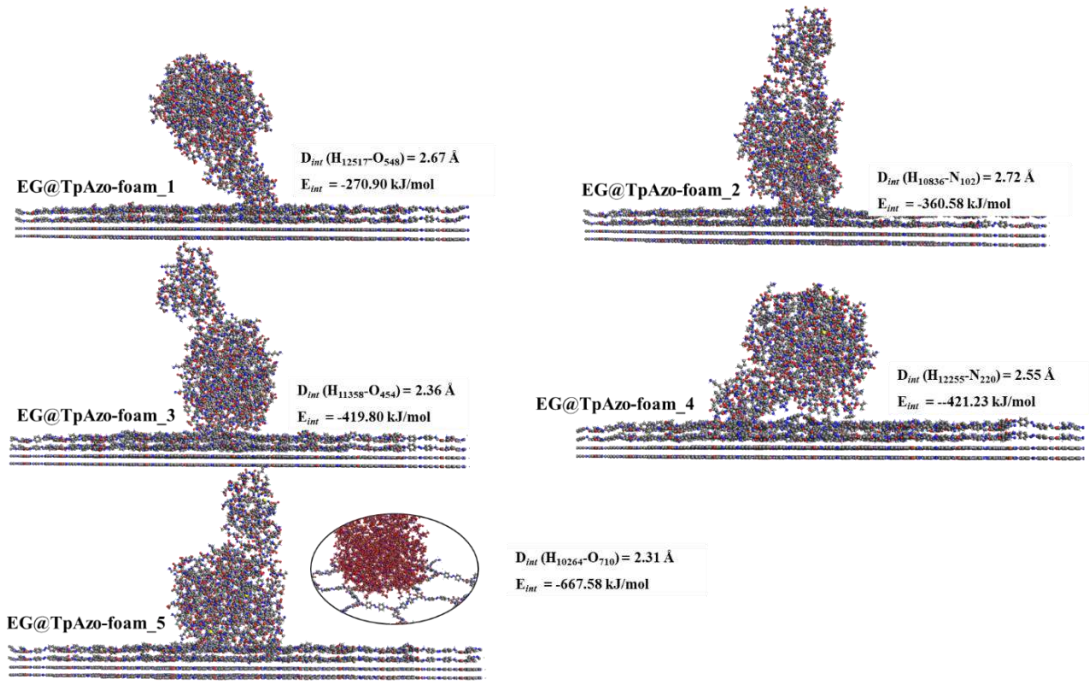

Figure 6.4. Interaction conformers of EG@TpAzo-COF_*n* with intermolecular distances and interaction energies.

6.5 Conclusions

Molecular Dynamics (MD) and hybrid QM/MM calculations have been undertaken to analyse the preferable interaction site of three different enzymes (BGL, CBH, and EG) on TpAzo-COF with their (non-covalent) interaction distances and energies. In order to model the adequate interaction of the enzymes, each enzyme molecule is placed above a 4×4 supercell of the 4 layers of TpAzo-COF. To avoid the COF structure from deformation, the bottom two layers of TpAzo-COF are held fixed. Each enzyme molecule was placed above the COF with five different orientations. MD simulations were run with 50 ps at room temperature (298 K), followed by the QM/MM simulations for binding energies calculations. The calculated binding energies are as follows; EG@TpAzo-COF (-667.6 kJ/mol) > BGL@TpAzo-COF (-554.47 kJ/mol) > CBH@TpAzo-COF (-497.3 kJ/mol). The number of possible H-bonding(s), hydrogen atoms of enzymes, and TpAzo-COF approaching each other is probably the main reason for stabilizing these structures. For example, the EG enzyme interacts strongly with COF because of the greatest number of observable H-bonds.

Table 6.2. Key Enzyme-TpAzo foam interactions, distances (D_{int}), energies (E_{int}), and separation between enzymes of unit cells.

BGL				
Species	**A_{int}**	**D_{int} (Å)**	**E_{int} (kJ/mol)**	**D_{E---E} (Å)**
BGL@TpAzo-COF_1	O_{10371}-H_{4838}	3.66	-93.5	76.6
BGL@TpAzo-COF_2	O_{7687}-H_{5990}	2.60	-131.6	84.9
BGL@TpAzo-COF_3	O_{7374}-H_{6758} H_{13867}-N_{414}	2.75 2.99	-164.6	82.6
BGL@TpAzo-COF_4	N_{9070}-H_{5052} O_{9061}- H_{5532} O_{9003}-H_{6110} O_{9069}-H_{6236} N_{9129}-H_{6300}	2.98 2.56 2.60 2.58 2.71	-349.5	83.1
BGL@TpAzo-COF_5	N_{124}-H_{13722} H_{12001}-N_{360} H_{13770}-N_{414} H_{13775}-N_{414} H_{12411}- O_{550} H_{12408}-O_{614} O_{9848}-H_{4710} O_{10376}-H_{5286} O_{10371}-H_{5670} O_{7268}-H_{6342}	2.93 2.90 2.94 2.72 2.96 2.91 2.90 2.77 2.56 2.81	-554.5	72.6

	O_{10376}-H_{6438} O_{7218}-H_{6493} O_{7268}- H_{6526} N_{7257}- H_{6558} O_{7260}- H_{6558} O_{10359}- H_{6822}	2.87 2.86 2.70 2.89 2.89 2.67		
Enzyme-2 (CBH_homology)				
CBH@TpAzo-COF_1	H_{10174}-C_{3942}	3.56	-37.0	77.4
CBH@TpAzo-COF_2	H_{11389}-N_{164} N_{8718}-H_{6854}	2.79 2.89	-117.7	73.5
CBH@TpAzo-COF_3	H_{9846}-N_{1182} N_{7110}-H_{6246}	2.89 2.73	-171.5	76.0
CBH@TpAzo-COF_4	H_{11090}-C_{1700}	6.49	-140.7	80.4
CBH@TpAzo-COF_5	H_{9859}-N_{164} H_{12166}-N_{164} H_{9859}-N_{358} H_{12018}-O_{612} H_{9871}-O_{806} H_{9874}-O_{806} O_{7169}-H_{4966} O_{9542}-H_{5156} O_{7192}-H_{6118} O_{8735}-H_{6494} O_{7192}-H_{6886}	2.78 2.83 2.75 2.95 2.88 2.79 2.91 2.66 2.51 2.81 2.89	-497.3	82.7
Enzyme-3 (endogluconase)				
EG@TpAzo-COF_1	H_{12516}-O_{548} H_{12517}-O_{548} O_{9440}-H_{5220} O_{9446}-H_{5220} O_{9659}-H_{5476} O_{9446}-H_{5640} N_{9665}-H_{5860} O_{9683}-H_{5924}	2.82 2.67 2.78 2.82 2.89 2.70 2.73 2.80	-270.9	92.1
EG@TpAzo-COF_2	H_{10836}-N_{102} H_{10804}-O_{550} O_{7884}-H_{6054} O_{7830}-H_{6246}	2.85 2.72 2.88 2.85	-360.6	92.1
EG@TpAzo-COF_3	H_{11337}-N_{414} H_{11338}-N_{414} H_{11358}-O_{454} H_{11360}-O_{454} H_{11354}-O_{486} H_{11358}-O_{486} H_{11076}-O_{550} H_{11036}-O_{614} O_{8403}-H_{4838} O_{8216}-H_{4838} O_{8184}-H_{5670}	2.85 2.75 2.36 2.77 2.48 2.80 2.84 2.77 2.76 2.65 2.65	-419.8	82.0

	O_{8205}-H_{5734} N_{8417}-H_{5862} N_{8400}-H_{5990} O_{8391}-H_{6558}	3.00 2.66 2.81 2.96		
EG@TpAzo-COF_4	H_{12255}-N_{220} H_{12255}-N_{220} N_{8545}-H_{4710} N_{9373}-H_{5596} O_{9539}-H_{5662} O_{9535}-H_{6430} N_{9380}-H_{6652}	2.75 2.55 2.89 2.91 2.81 2.67 2.83	-421.2	79.6
EG@TpAzo-COF_5	H_{10877}-N_{156} H_{10514}-N_{230} H_{10485}-N_{414} H_{10264}-O_{710} H_{10845}-O_{734} H_{11984}-O_{806} H_{11987}-O_{806} H_{11994}-O_{806} H_{11993}-N_{1190} O_{7347}-H_{5156} O_{9120}-H_{5350} O_{9123}-H_{5350} O_{7239}-H_{6054} O_{7283}-H_{6276} O_{7282}-H_{6308} O_{7282}-H_{6308} O_{7265}-H_{6630} O_{7283}-H_{6854}	2.78 2.96 3.00 2.31 2.88 2.80 2.98 2.83 2.97 2.78 2.97 2.38 2.78 2.95 2.88 2.71 2.49 2.94	-667.6	82.9

6.6 References

1 P. J. O'Brien and D. Herschlag, *Chem. Biol.*, 1999, **6**, R91–R105.

2 S. Simić, E. Zukić, L. Schmermund, K. Faber, C. K. Winkler and W. Kroutil, *Chem. Rev.*, 2022, **122**, 1052–1126.

3 E. T. Hwang and S. Lee, *ACS. Catal.*, 2019, **9**, 4402–4425.

4 H. Cui, L. Zhang, L. Eltoukhy, Q. Jiang, S. K. Korkunç, K.-E. Jaeger, U. Schwaneberg and M. D. Davari, *ACS Catal.*, 2020, **10**, 14847–14856.

5 C. Wang, L. Yue and I. Willner, *Nat. Catal.*, 2020, **3**, 941–950.

6 T. Man, C. Xu, X.-Y. Liu, D. Li, C.-K. Tsung, H. Pei, Y. Wan and L. Li, *Nat. Commun.*, 2022, **13**, 305.

7 S. Kandambeth, K. Dey and R. Banerjee, *J. Am. Chem. Soc.*, 2019, **141**, 1807–1822.

8 H. S. Sasmal, S. Bag, B. Chandra, P. Majumder, H. Kuiry, S. Karak, S. sen Gupta and R. Banerjee, *J. Am. Chem. Soc.*, 2021, **143**, 8426–8436.

9 A. K. Mohammed, S. Usgaonkar, F. Kanheerampockil, S. Karak, A. Halder, M. Tharkar, M. Addicoat, T. G. Ajithkumar and R. Banerjee, *J. Am. Chem. Soc.*, 2020, **142**, 8252–8261.

10 S. Karak, K. Dey, A. Torris, A. Halder, S. Bera, F. Kanheerampockil and R. Banerjee, *J. Am. Chem. Soc.*, 2019, **141**, 7572–7581.

11 S. Paul, M. Gupta, K. DEY, A. K. Mahato, S. Bag, A. Torris, B. Gowd, H. Sajid, M. A. Addicoat, S. Datta and R. Banerjee, *Chem. Sci.*, 2023, D3SC01367G.

12 C. Wang, Z. Wang, S. Mao, Z. Chen and Y. Wang, *Chin. J. Catal.*, 2022, **43**, 928–955.

13 J. Gao, S. Ma, D. T. Major, K. Nam, J. Pu and D. G. Truhlar, *Chem. Rev.*, 2006, **106**, 3188–3209.

14 H. J. Kulik, *Phys. Chem. Chem. Phys.*, 2018, **20**, 20650–20660.

15 R. P. Magalhães, H. S. Fernandes and S. F. Sousa, *Isr. J. Chem.*, 2020, **60**, 655–666.

16 A. Warshel and M. Levitt, *J. Mol. Biol.*, 1976, **103**, 227–249.

17 A. J. Mulholland, *Drug Discov. Today*, 2005, **10**, 1393–1402.

18 K. E. Ranaghan and A. J. Mulholland, *Int. Rev. Phys. Chem.*, 2010, **29**, 65–133.

19 M. Dal Peraro, P. Ruggerone, S. Raugei, F. L. Gervasio and P. Carloni, *Curr. Opin. Struct. Biol.*, 2007, **17**, 149–156.

20 H. M. Senn and W. Thiel, *Angew. Chem. Int. Ed.*, 2009, **48**, 1198–1229.

21 K. M. Merz, *Acc. Chem. Res.*, 2014, **47**, 2804–2811.

22 L. W. Chung, W. M. C. Sameera, R. Ramozzi, A. J. Page, M. Hatanaka, G. P. Petrova, T. V. Harris, X. Li, Z. Ke, F. Liu, H.-B. Li, L. Ding and K. Morokuma, *Chem. Rev.*, 2015, **115**, 5678–5796.

23 R. Lonsdale, J. N. Harvey and A. J. Mulholland, *Chem. Soc. Rev.*, 2012, **41**, 3025.

24 H. Lin and D. G. Truhlar, *Theor. Chem. Acc.*, 2007, **117**, 185.

25 G. te Velde, F. M. Bickelhaupt, E. J. Baerends, C. Fonseca Guerra, S. J. A. van Gisbergen, J. G. Snijders and T. Ziegler, *J. Comput. Chem.*, 2001, **22**, 931–967.

26 M. Nurhuda, C. C. Perry and M. A. Addicoat, *Phys. Chem. Chem. Phys.*, 2022, **24**, 10906–10914.

27 A. K. Rappe, C. J. Casewit, K. S. Colwell, W. A. Goddard and W. M. Skiff, *J. Am. Chem. Soc.*, 1992, **114**, 10024–10035.

28 W. G. Hoover, *Phys. Rev. A (Coll Park)*, 1985, **31**, 1695–1697.

29 S. Nosé, *Mol. Phys.*, 1986, **57**, 187–191.

30 M. Svensson, S. Humbel, R. D. J. Froese, T. Matsubara, S. Sieber and K. Morokuma, *J. Phys. Chem.*, 1996, **100**, 19357–19363.

31 T. F. Willems, C. H. Rycroft, M. Kazi, J. C. Meza and M. Haranczyk, *Microporous. Mesoporous Mater.*, 2012, **149**, 134–141.

32 Z. Hasan, M. Tong, B. K. Jung, I. Ahmed, C. Zhong and S. H. Jhung, *J. Phys. Chem. C*, 2014, **118**, 21049–21056.

33 A. Shankar, A. Jagota and J. Mittal, *J. Phys. Chem. B*, 2012, **116**, 12088–12094.

Chapter 7

7 Thioether- and Imine-based Covalent Organic Frameworks for Effective Mercury Capturing

A major challenge in atmospheric remediation is the design of porous adsorbents containing dense accessible binding sites with high and rapid pollutants capturing affinity. Herein, Prof. Phillip J. Milner's research group demonstrated the ideal adsorbent properties of a two-dimensional (2D) covalent organic framework (COF) bearing thioether and imine functional groups with well-defined porous pockets for Hg adsorption and removal. Experimental results illustrate that the COF exhibits about 95 % efficiency in Hg capturing, affording 789 mg/g of Hg loading capacity. In the computational part of the study, we proved that both the thioether and imine functional groups demonstrate an ultrahigh binding affinity towards mercury. For this purpose, we performed geometry optimizations on an extended tight binding semi-empirical method. A detailed discussion regarding the computational modeling approach and its results is described in this chapter.

7.1 Introduction

As a serious threat to human health and the atmosphere, metal ions, especially Hg^{2+} produce serious health damage to mankind, called Minamata disease.[1] The deletion of Hg^{2+} from the environment as well as the polluted water to the minimum concentration is a serious issue.[2–4] In this context, the adsorption using porous frameworks is much superior as compared to traditional chemical reaction approaches. This is because adsorption is the most simple and cost-effective approach.[5] In addition, the adsorption capacity, stability over a wide range of pH (1-14), and reusability are important parameters for suitable porous adsorbents in the adsorption process.[6] Traditionally used porous adsorbents, including, activated carbon and zeolites usually have low adsorption capacity.[7,8] Other than such porous adsorbent, Metal-organic frameworks (MOFs) have been designed and developed for Hg^{2+} adsorption and removal based on their huge surface areas, however, stable

performance in reaction conditions is still challenging.[9,10] The first successful example of using covalent-organic frameworks (COFs) with thioether functionality for selective removal of Hg^{2+} was published by Wang *et al.*[11] however, the less stability and limited capacity precluded its implementation. Thus, a porous adsorbent with high adsorption capacity and stability in a range of reaction conditions remains a challenge in adsorption science.

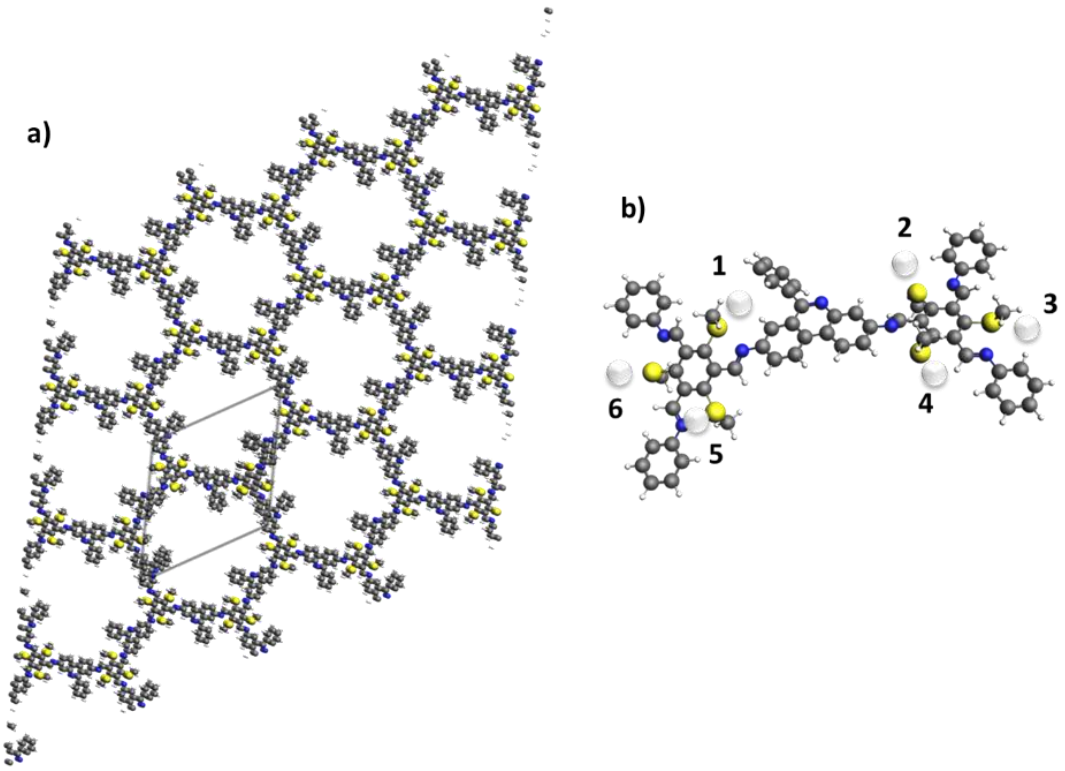

Figure 7.1. a) 4×4 supercell representation of thioether-COF, 1×1 unit cell is highlighted in the center of the figure, b) non-periodic/molecular cut unit of COF, terminal carbons are saturated with hydrogen atoms, also representing the suitable positions of mercury adsorption with their numbering given in **Table 7.1**a. Chemical representation: grey; carbon, blue; nitrogen, yellow; sulfur, small grey; hydrogen, large whitish grey; mercury atoms. The numbers 1 to 6 represent the six possible binding sites of Hg atoms on this unit.

Huang and co-workers designed a new layered COF based on the imine-linked skeleton and thioether groups, which provide high stability in harsh conditions and high Hg^{2+} removal capacity.[12] Moreover, Ma *et al.*[13] studied the effectiveness of Hg^{2+} removal based on the well-established Hg-S (thioether) ligation chemistry, by modifying a COF-V *via* introducing thioether and sulfur functionalities. Based on the

hard and soft approach, the installation of more sulfur (S) atoms, such as thioether groups as hard binding sites per unit cell of COF, could enhance the efficiency of binding soft metal species.[10] Herein, our experimental collaborator Prof. Phillip J. Milner designed a new **TpSMe-DPP** COF, where **TpSMe** stands for 2,4,6-tris(methylthio)benzene-1,3,5-tricarbaldehyde and **DPP** stands for 3,8-diamine-6-phenylphenanthridine COF (**Figure 7.1**) to remove Hg^{2+} based on the hard-soft approach (Hg-thioether bond). In this research, we performed computational screening in order to determine the Hg^{2+} binding site on **TpSMe-DPP** COF. For this purpose, Hg^0, Hg^{2+}, and $HgCl_2$ are separately placed and optimized on a newly designed **TpSMe-DPP** COF containing six thioether groups per unit cell, which is the highest among previously reported thioether-based COFs. It is found that the thioether functional group provides excellent pockets for binding Hg^{2+}. Further details are listed in the subsequent sections of the chapter.

7.2 Computational Methodology

The simulations were performed using the tight binding method *i.e.*, GF1-xTB through the DFTB engine in SCM-AMS-2020.101 software.[14]

First, the geometries optimization of the smallest molecular unit of **TpSMe-DPP** and their periodic structures were undertaken. In order to create the molecular unit of the **TpSMe-DPP** COF, the smallest unit cell was extracted from a periodic monolayer while the terminal carbons were saturated with hydrogens to resume the original bond order (**Figure 7.1b**). The non-periodic molecular model of **TpSMe-DPP** COF was used to analyze the most stable binding site for Hg^0 and Hg^{2+}. Next, a periodic monolayer of **TpSMe-DPP** COF (with a unit cell of 28.99 × 29.13 × 15.00 Å) was optimized with fully relaxed lattice parameters, which is followed by the addition of four layers with an interlayer separation of 3.87 Å.

All the **TpSMe-DPP** COF representatives, including the molecular unit and periodic 4-layer structure, were subsequently investigated for Hg adsorption. The adsorption energies (E_d) are determined as,

$$E_d = E_{(Hg-TpSME-DPP)} - \left[E_{(Hg)} + E_{(TpSMe-DPP)}\right] \quad (7.1)$$

where E_{rel} (relative energy) is defined as the energy difference between the most negative adsorption energy and others with similar structures.

Table 7.1. Binding distances (Å) between the atoms of **TpSMe-DPP** COFs (S or N) and Hg atoms, adsorption (E_d), and relative energies (E_{rel}) for a) one Hg and b) two Hg bindings.

	S--Hg^0 Å	**N--Hg^0** Å	***E*$_d$** kJ/mol	***E*$_{rel}$** kJ/mol	**S--Hg^0** Å	**Hg^0--Hg^0** Å	***E*$_d$** kJ/mol	***E*$_{rel}$** kJ/mol
	Hg^0@COF				**Hg^{2+}@COF**			
	One Hg atom				**Two Hg atoms/ions**			
1	3.45	4.32	-85.7	0.00	3.77	12.63	-52.3	0.03
2	3.57	4.17	-83.1	2.65	3.79	16.43	-52.1	0.27
3	3.60	4.28	-83.5	2.18	3.60	19.78	-52.4	0.00
4	3.78	3.45	-83.8	1.90	3.53	8.37	-51.7	0.61
5	3.57	3.95	-83.6	2.13	3.58	8.58	-50.6	1.74
6	3.48	5.03	-80.2	5.46	3.77	12.63	-52.3	0.03

Stochiometric calculation based on experimental results:

The experimental isotherm illustrates that the adsorption capacity of Hg on COF is about 789mg/g. Therefore:

a) For a periodic COF monolayer:

A periodic monolayer of COF contains 90 carbon, 57 hydrogens, 9 nitrogen, and 6 sulfur atoms.

Molar Mass of a periodic COF monolayer = 1456.86 g/mol.

The number of moles in 1g of COF = 0.00068640775 mol.

b) For Hg

The number of moles in 789mg of Hg = 0.00393339648 mol

By taking the ratio of Hg/COF moles: 0.00393339648/0.00068640775 = 5.73 atoms

Thus 5.73 Hg atoms are adsorbed per COF monolayer.

Therefore, in four layers of COF, we get 23 Hg atoms per COF unit cell.

7.3 Results and Discussion

7.3.1 Hg^0 Binding in Molecular TpSMe-DPP COF Unit

To determine the most suitable binding site, the Hg atom was placed on all the possible positions *e.g.*, thioether and imine functional groups of the molecular unit.

These manually identified positions were further checked with fifty additional **Hg@TpSMe-DPP** COF geometry optimizations, where the Hg binding position was determined using the Kick3 algorithm.[15] The adsorption energies, distances (*S*---*Hg*), and relative energies in each structure are given in **Table 7.1**. The *S* of the thioether group is the most suitable site for soft metal (Hg) adsorption based on the hard-soft adsorption approach.[16] In a molecular structure of **TpSMe-DPP** COF, there are 6-non-equivalent thioether units, thus the adsorption affinity of each thioether site is calculated. Among them, the most stable adsorption site is observed at position-1 (**Figure 7.1b**), with E_d of -85.7 kJ/mol (**Table 7.1**). At position-1, Hg adsorbs more closely on *S* of thioether with a distance of 3.45 Å. Other than the binding distance, position-1 is additionally stabilized by van der Waals forces between the Hg atom and the aromatic phenyl ring of **TpSMe-DPP** COF. Owing to the asymmetric structure of the **TpSMe-DPP** COF, the E_{rel} of all active thioether groups are well-conserved and vary within a range of approximately 5.0 kJ/mol.

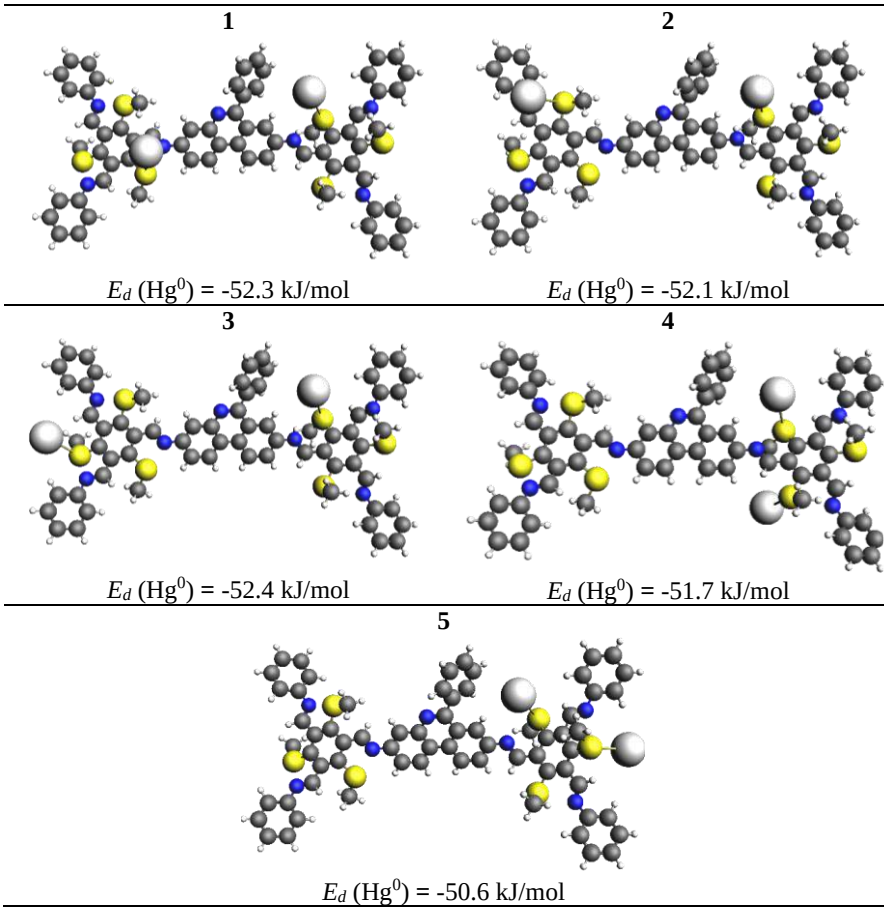

Figure 7.2. The illustration of multiple (two) Hg atoms (Hg^0) or ions (Hg^{2+}) bonding sites on the molecular COF.

7.3.2 Binding of $HgCl_2$ on Periodic TpSMe-DPP COF

The **TpSMe-DPP** COF adsorbs 789 mg/g Hg, proposed by experimental work. The stochiometric calculation illustrates that there are about 5.76 Hg atoms are adsorbed per **TpSMe-DPP** unit cell. In other words, a total of 23 Hg or $HgCl_2$ are adsorbed on four π-π* stacked layers of **TpSMe-DPP** (see section 7.2). This is close to saturation, wherein a fully saturated structure, 24 $HgCl_2$ can adsorb at all available thioether pockets on a four-layered periodic COF structure. Therefore, 24$HgCl_2$ adsorbed **TpSMe-DPP** structure was optimized, and found that half or 12$HgCl_2$ molecules simultaneously bonded with the thioether and the imine functionalities. The remaining twelve $HgCl_2$ adsorb solely on thioether groups due to the unavailability of the imine pocket (**Figure 7.3a**). In this case, the average E_d per $HgCl_2$ is -201.9 kJ/mol. **Figure 7.3b** shows the geometry, where all the 24$HgCl_2$ are adsorbed and fixed to the *S* of the thioether sites, in this case, the average adsorption energy per $HgCl_2$ is slightly decreased to -195.4 kJ/mol. This binding behaviour of $HgCl_2$ with thioether and imine, on availability, is according to the literature.[16]

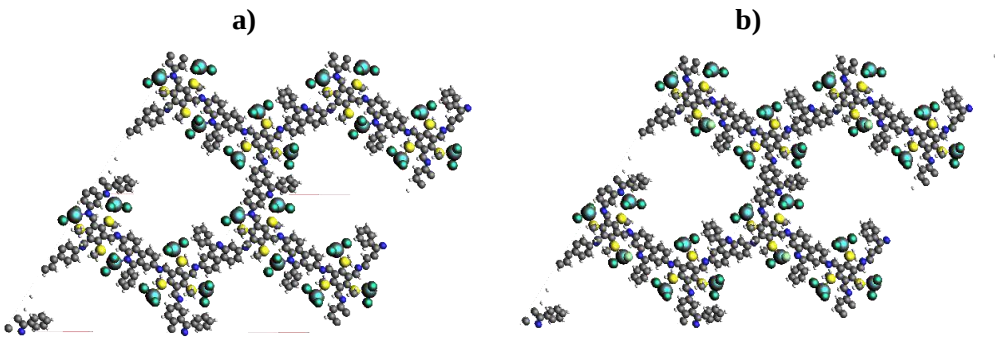

Figure 7.3. Saturated **TpSMe-DPP** COF with $HgCl_2$; a) fully relaxed geometry with 12$HgCl_2$ bonded simultaneously in **TpSMe-DPP** COF, b) constrained optimized geometry where all the $HgCl_2$ are bonded with thioether site of **TpSMe-DPP** COF. Chemical composition; yellow; S, blue; N, grey; C, white; H, highlights are adsorbed $HgCl_2$.

In order to model the experimental data, where 23$HgCl_2$ molecules are adsorbed per 4-layers of **TpSMe-DPP** COF, a $HgCl_2$ molecule is removed from the fully saturated structure. There are 6 different possibilities for removing $HgCl_2$ molecules, from each of the unique sites, as depicted in **Figure 7.4**. All the possibilities are optimized with fully relaxed geometric parameters, and the resulting adsorption energies per $HgCl_2$

are given in **Table 7.2a**. The adsorption stabilities are slightly reduced when a $HgCl_2$ molecule is removed from positions where adsorption takes place with only S of thioether. In contrast, removing a $HgCl_2$ where adsorption occurs with thioether and imine functionalities simultaneously is less favorable *e.g.,* from position-1 and position-6.

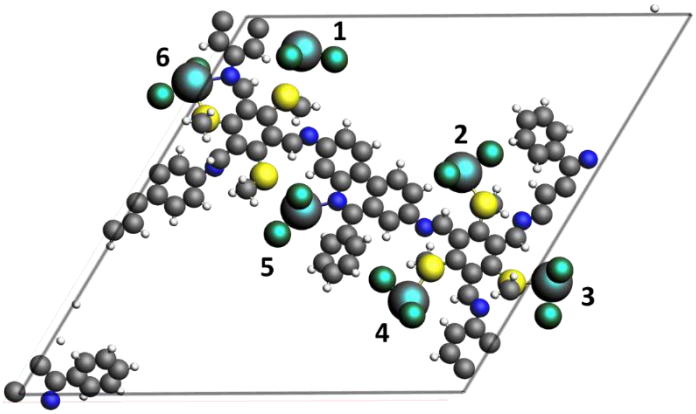

Figure 7.4. Six possibilities of removing one $HgCl_2$ to create $23HgCl_2$ containing **TpSMe-DPP** COFs (right). Chemical composition; yellow; S, blue; N, grey; C, white; H, highlights are adsorbed $HgCl_2$.

Table 7.2. Binding distances (Å) between **TpSMe-DPP** COF atoms and $HgCl_2$, adsorption energies (E_d), and relative binding energies (E_{rel}) (kJ/mol); a) $23HgCl_2$, b) $4HgCl_2$ adsorbed in **TpSMe-DPP** COF.

	S---$HgCl_2$ (Å)	**N---$HgCl_2$** (Å)	**E_d** (kJ/mol)	**E_{rel}** (kJ/mol)
a) $23HgCl_2$@COF				
1	3.58	2.89	-198.8	5.5
2	2.65	---	-204.3	0.0
3	2.67	---	-200.2	4.1
4	2.64	---	-200.7	3.6
5	3.50	2.41	-202.1	2.3
6	2.60	2.77	-199.3	5.0
b) $4HgCl_2$@COF				
1	3.03	2.41	-221.1	0.00
2	3.05	2.53	-213.8	7.3
3	2.59	2.53	-210.4	10.7
4	2.61	---	-194.3	26.8
5	2.64	---	-188.5	32.7
6	2.63	---	-180.2	40.9

Lastly, for further verification of stable binding sites in the periodic **TpSMe-DPP** COF, a layer of $HgCl_2$ molecules was separately adsorbed on the six possible thioether functional groups (**Figure 7.5**). The adsorption energies per $HgCl_2$ of these possibilities were found between -180.2 and -221.2 kJ/mol (**Table 7.2b**). In structures 1-3, $HgCl_2$ binds with the thioether and imine groups simultaneously, thus these structures exhibit the highest negative adsorption energies (> 210.0 kJ/mol). However, the structures in which $HgCl_2$ only binds with the thioether unit (Structures 4-6) exhibit relatively low stability with the adsorption energy of 30 kJ/mol or lower.

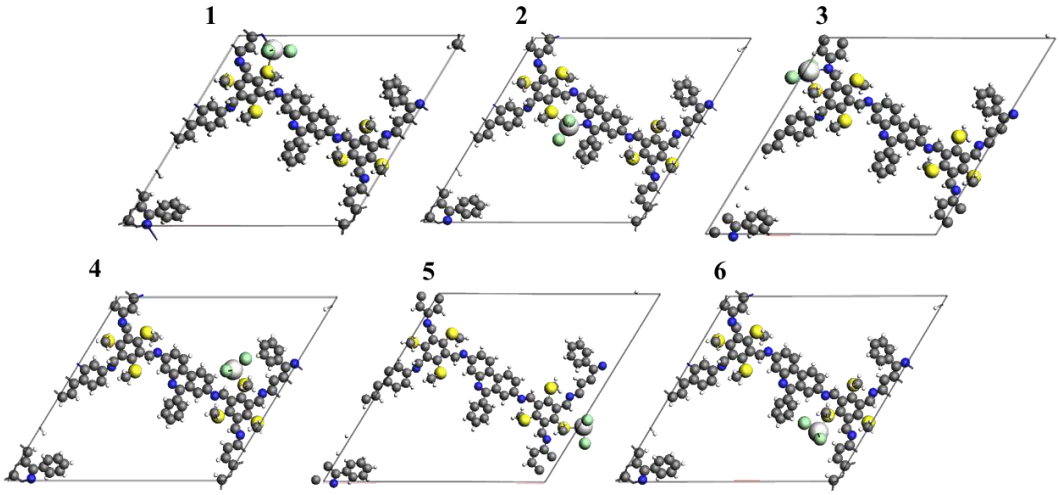

Figure 7.5. Six possible binding positions of $HgCl_2$ on a unit cell of **TpSMe-DPP** COF.

7.4 Conclusions

In summary, we presented the deployment of **TpSMe-DPP** COF with dense of thioether and imine functional groups as an amenable adsorbent for Hg adsorption and removal. The **TpSMe-DPP** COF exhibits high Hg^0 and Hg^{2+} adsorption capacity *i.e.*, 789 mg/g. More importantly, thioether and imine functional groups provide active pockets for effective mercury adsorption with the strongest adsorption strength. The binding energies per $HgCl_2$ are ~200.0 kJ/mol in a periodic **TpSMe-DPP** COF supercell. Our computational findings are in accord with the experimental data that available thioether and imine functionalities are appealing adsorption sites with remarkable affinity for mercury binding.

7.5 References

1 M. McNutt, *Science (1979)*, 2013, **341**, 1430–1430.

2 F.-S. Zhang, J. O. Nriagu and H. Itoh, *Water. Res.*, 2005, **39**, 389–395.

3 M. Wdowin, M. M. Wiatros-Motyka, R. Panek, L. A. Stevens, W. Franus and C. E. Snape, *Fuel*, 2014, **128**, 451–457.

4 Y. Zheng, A. D. Jensen, C. Windelin and F. Jensen, *Prog. Energy Combust. Sci.*, 2012, **38**, 599–629.

5 D. A. Atwood and M. K. Zaman, in *Recent Developments in Mercury Science*, Springer-Verlag, Berlin/Heidelberg, pp. 163–182.

6 Y. Shin, G. E. Fryxell, W. Um, K. Parker, S. V. Mattigod and R. Skaggs, *Adv. Funct. Mater.*, 2007, **17**, 2897–2901.

7 C. Huang and D. Blankenship, *Water Res.*, 1984, **18**, 37–46.

8 G. Blanchard, M. Maunaye and G. Martin, *Water Res.*, 1984, **18**, 1501–1507.

9 Q.-R. Fang, D.-Q. Yuan, J. Sculley, J.-R. Li, Z.-B. Han and H.-C. Zhou, *Inorg. Chem.*, 2010, **49**, 11637–11642.

10 J. He, K.-K. Yee, Z. Xu, M. Zeller, A. D. Hunter, S. S.-Y. Chui and C.-M. Che, *Chem. Mater.*, 2011, **23**, 2940–2947.

11 S.-Y. Ding, M. Dong, Y.-W. Wang, Y.-T. Chen, H.-Z. Wang, C.-Y. Su and W. Wang, *J. Am. Chem. Soc.*, 2016, **138**, 3031–3037.

12 N. Huang, L. Zhai, H. Xu and D. Jiang, *J. Am. Chem. Soc.*, 2017, **139**, 2428–2434.

13 Q. Sun, B. Aguila, J. Perman, L. D. Earl, C. W. Abney, Y. Cheng, H. Wei, N. Nguyen, L. Wojtas and S. Ma, *J. Am. Chem. Soc.*, 2017, **139**, 2786–2793.

14 G. te Velde, F. M. Bickelhaupt, E. J. Baerends, C. Fonseca Guerra, S. J. A. van Gisbergen, J. G. Snijders and T. Ziegler, *J. Comput. Chem.*, 2001, **22**, 931–967.

15 M. A. Addicoat, S. Fukuoka, A. J. Page and S. Irle, *J. Comput. Chem.*, 2013, **34**, 2591–2600.

16 A. Zhang, X. Liu, J. Hong, R. Guo, Y. Zhou and Y. Ai, *Sci. Total Environ.*, 2022, **838**, 156082.

Chapter 8

8 Transition State Search for the Formation of *Bis*-imine and Benzimidazole Based 1D COFs

The synthesis and design of one-dimensional (1D) covalent-organic frameworks (COFs) and their crystalline diversity using different secondary building units (SBUs), ranging from small secondary building units to large and even infinite building blocks is largely undeveloped. Here, experimental collaborators reported 1D COF formations with different unit cell sizes using the reticular chemistry, where the linker units vary from small (benzaldehyde) to large (tetraldehyde). In this study, we demonstrated the energy barriers of these novel 1D COFs formation and their growth upon varying the secondary linker units using computational modeling techniques. For this purpose, we performed density functional theory (DFT) simulations to elaborate the ground state energies of *bis*-imine (*cis*- & *trans*-) and benzimidazole structures of COF, which is followed by the energy barrier calculations *via* transition state search for the COF formation.

8.1 Introduction

The self-assembly of crystalline structures usually depends on the interaction between the secondary building units (SUBs).[1] There is a wide range of practical conditions over which high-quality crystals can be created depending on the nature of interactions between SBUs. The growth mechanisms of crystallites are ranging from the incorporation of small SBUs or monomer linkers to the attachment of large analogues.[2,3] The covalent-organic framework is a new class of crystalline materials, constructed *via* covalently bonded rigid SBUs.[4–6] By varying the SBUs, the pore size, shape, and skeleton of COFs can be modified.[7–10] Hence, the crystalline COFs have gained enormous attentions in practical applications including chemical separation,[11] energy storage,[12] gas storage,[13] and many more.[14–16] Topologically, the COFs are indeed classified into two-dimensional (2D)[17–19] and three-dimensional (3D).[20,21] The electronic properties and applications of covalent frameworks are strongly correlated with their structural topologies, e.g., 2D COFs perform exceptionally in electron conduction due to the high charge delocalization[22–24] and 3D COFs show great

potential in energy storage due to high Brunauer-Emmett-Teller (BET) surface area.[25,26] It is understood that the extension of framework structures has a remarkable effect on their inherent properties. It is important to design new topologies of COF in order to extend their applications in the future.[27–30]

In this context, Yaghi and coworkers have recently designed a new one-dimensional (1D) topology of COF (COF-76)[31] by combining excessive TAA[9] and TFPPY[10]. Very recently, Goa *et al.*,[32] combined TFPPY with DABP[11] to afford another new 1D-COF. Conceptually, the framework topology in 1D-COF is constructed from strong covalent linkages between SBUs in one-dimension and non-covalent interaction *e.g.*, π-π interactions or hydrogen bonding in other two-dimensions.[33] The reticular chemistry features numerous theoretically accessible COF structures ranging from small organic SBUs,[34,35] but the synthesis of COFs from large units remains a major challenge.[36]

Herein, our experimental collaborators build a novel 1D-COF by reacting a di-amine functional group containing backbone with aldehydic groups, *e.g.*, small unit benzaldehyde and large tetrahdehyde. These aldehydic groups are then used as linkers in obtaining 1D COF. Being a computational chemist, we report an atomic level feasibility of these hierarchically composed crystalline 1D COFs starting from small linker molecules (benzaldehyde) to the large units (tetraldehyde). We elaborately screened all the possible products including cis-, trans-bis-imine, and benzimidazole by thermodynamic analysis using a computational modeling approach. It is found that the benzimidazole product is energetically unstable. Furthermore, the 1D COF structures formation with various products is emphasized with energy barrier calculations, where the transition states of bis-imine (*cis* & *trans*) and benzimidazole formations are successfully optimized, revealing the bis-imine formations, especially *trans* product formation energetically feasible, followed by *cis*-*bis*-imine and then benzimidazole product. Subsequently, the energetic feasibility of such COFs upon using large tetraldehyde linker units (rather than small benzaldehyde units) is

[9] tris(4-aminophenyl)amine

[10] tetrakis(p-formylpheyl)pyrene

[11] diaminobenzophenone

elaborated. It is found that the crowdedness of linkers hinders the 1D COF formation due to increasing steric repulsions in the body of crystal systems.

8.2 Computational Methodology

Both bis-imine and imidazole products and their corresponding transition states were studied using DFT: B3LYP[37] calculations with DZP[38] basis set as implemented in the SCM-AMS version 2022.101.[39,40] Additionally, the Grimme dispersion (D3) corrections were also applied to refine the total dispersion energies.[41] Prior to the transition state search at high-level DFT, the reaction steps from the reactant (Di-amine) to the products (bis-imine and imidazole) *via* intermediates and transition states were scanned using potential energy scan search (PES) of AMS software with a fast extended tight bonding semiempirical GFN1-xTB[42] method, followed by geometry optimization of intermediates and transition states with vibrational frequencies at B3LYP-D3/DZP method. The successful transition states were confirmed by the one imaginary frequencies for all transition states.

8.3 Results and Discussion

8.3.1 Geometry Optimizations and Relative Energies of Bis-imine (*cis* and *trans*) and Imidazole Products

First, the geometry optimization of the reactant (di-imine) and corresponding products, including cis-, trans-bis-imine, and imidazole are carried out at the high-level DFT i.e., BLYP-D3/DZP level of theory, resulting the total electronic energies (E_{rel}) of products, relative to the reactant with small connector units (benzaldehyde), are computed (**Figure 8.1**) in order to estimate their stability. **Figure 8.1** illustrates that the bis-imine products are energetically more stable or favorable, and the relative energies of *cis*- and *trans*-bis-imine are exothermic e.g., -5.63 and -17.9 kJ/mol, respectively. The formation of benzimidazole is energetically unfavorable because of the high endothermic relative energy which is 35.4 kJ/mol.

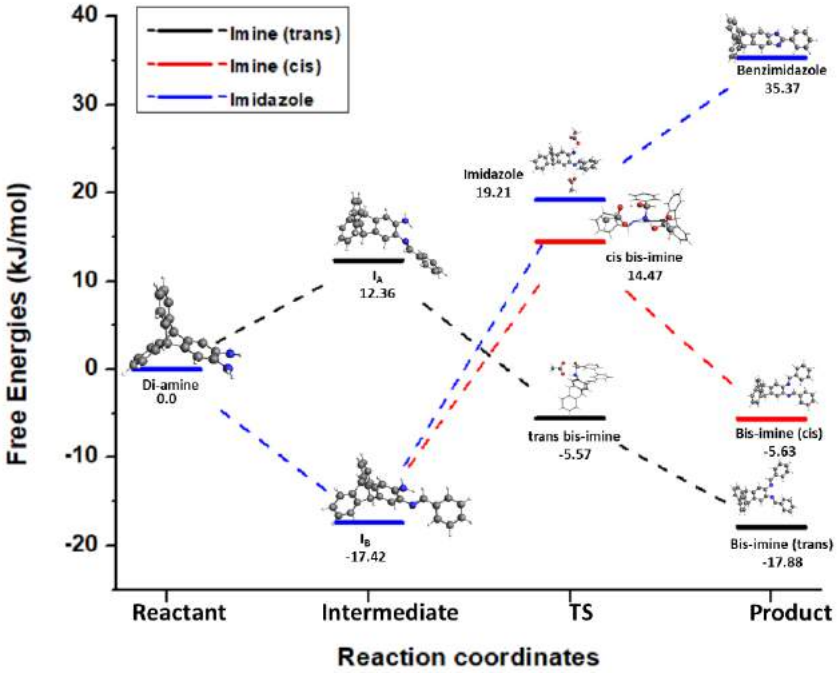

Figure 8.1. Combined reaction mechanisms with relative free energies for the formation of (*cis* and *trans*) bis-imine and benzimidazole products.

8.3.2 Transition State (TS) Search

8.3.2.1 TS with Small Linker Unit

The reaction paths from reactant to products, including intermediates and transition states are first estimated at the GFN1-xTB method in order to get the valid structures at a minimum computational cost. Subsequently, the total energies as well as Gibb's free energies of benzaldehyde-containing products are computed at BLYP-D3/DZP method. Vibrational frequency calculations were performed to determine the nature of the stationary points obtained. It is found that the bis-imine (*cis* and *trans*) formations are more feasible with only one transition state each. In bis-imine formations, a benzaldehyde molecule attacks the amine group of the di-imine reactant, in the presence of an acetic acid catalyst, to produce intermediates *e.g.*, IA (**Figure 8.2a**) and IB (**Figure 8.2b**) for *trans*- and *cis*- products, respectively. The formation energies of IA and IB are 12.4 and -17.4 kJ/mol, respectively. In the next step, the addition of another benzaldehyde molecule, in the presence of the acetic acid catalyst, takes place on the second amine group of intermediates. The transition states for both reactions are successfully optimized with the activation barrier of -5.6 and 14.5 kJ/mol respectively for *trans*- and *cis*-bis-imine products. The reaction mechanism of both

trans- and *cis*-bis-imine products with the relative energies of each step are shown in **Figure 8.2**.

A)

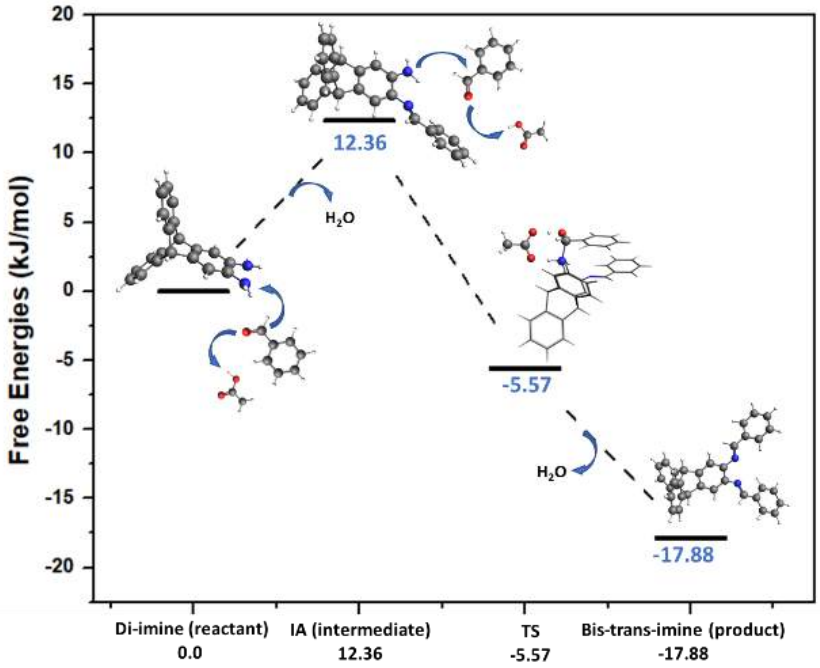

B)

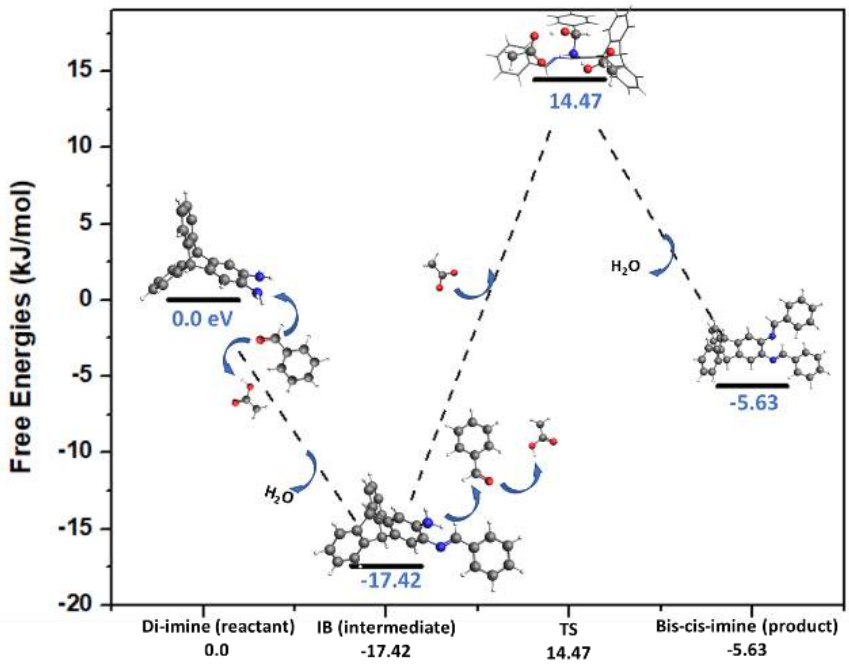

Figure 8.2. Reaction mechanisms with relative free energies for the formation of A) *trans*-, and B) *cis*-bis-imine products.

On the other hand, the benzimidazole formation takes place in two steps, containing two intermediates and two transition states, as shown in **Figure 8.3**. After the formation of intermediate (IB) with relative energy of -17.4 kJ/mol, the two acetic acid

molecules are involved in proton transformation, where the first transition state (TS-1) was successfully obtained with the energy barrier of 19.2 kJ/mol. In the next transition state, an acetate ion extracts an extra proton from the system, the energy barrier for TS-2 is 67.2 kJ/mol. Finally, the benzimidazole product is synthesized with a relative energy of 35.4 kJ/mol.

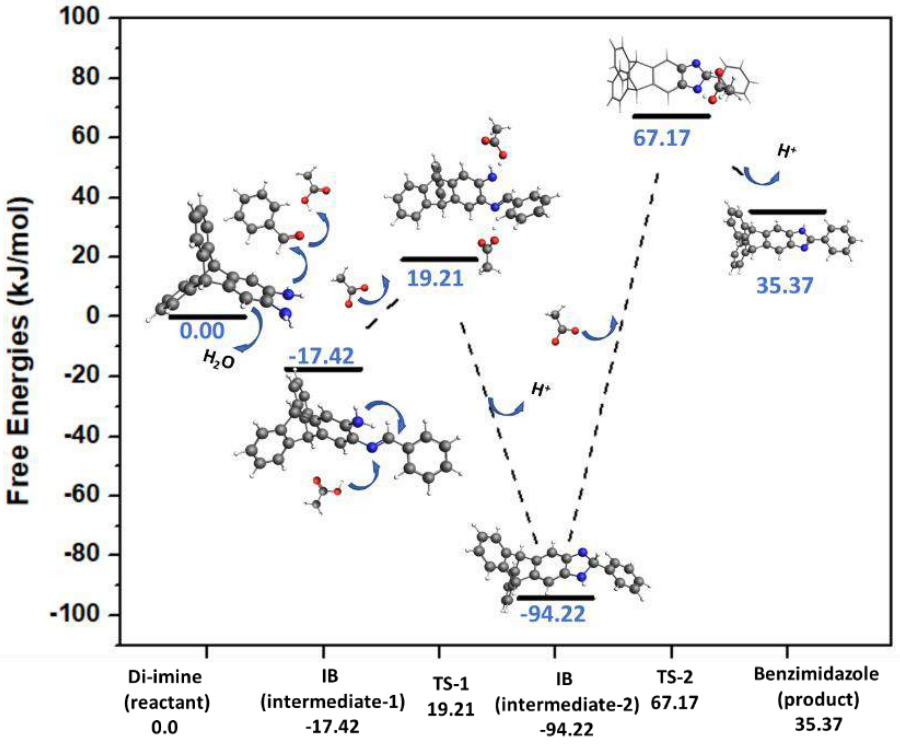

Figure 8.3. Reaction mechanism for the formation of benzimidazole product.

8.3.2.2 TS with Large Linker Unit

After describing the reaction mechanism of bis-imine and benzimidazole products formation with small benzaldehyde linker units, subsequently, similar reaction mechanisms are performed with large tertaldehyde linker units. Due to the overcrowdedness of the systems, successful optimization of transition states without any geometry constraints is impossible in a limited computational cost, thus, the reaction paths for Bis-imine (*cis* and *trans*) are computed with a single point energy calculations at BLYP-D3/SZ level of DFT. The reaction barriers for bis-imine formations as a function of reaction coordinates are displayed in **Figure 8.4**. The energy sequence in acetaldehyde-containing reactions is quite similar to the benzaldehyde reaction mechanism. For example, the *trans*-bis-imine product is highly stable with a ground state energy of -218.1 kJ/mol as compared to -173.9 kJ/mol for

the *cis*-bis-imine product. The energy barriers of both reactions are found to be 215.6 and 315.3 kJ/mol for trans- and cis-imines, respectively, manifesting that the *trans*-bis-imine formation is feasible as compared to the *cis*-analogs.

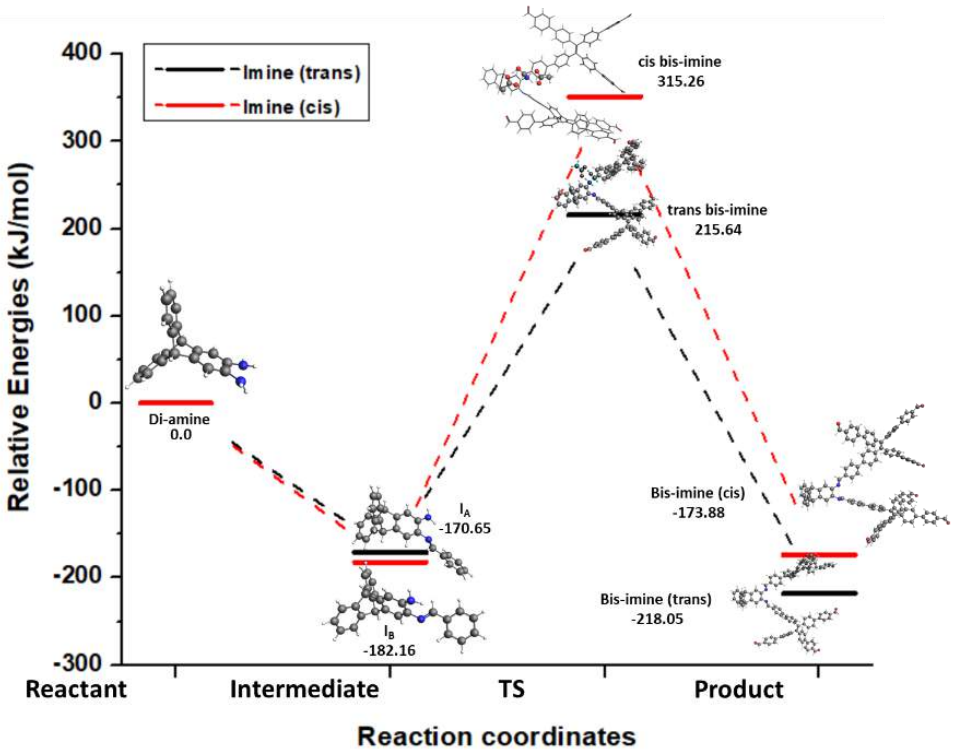

Figure 8.4. Reaction mechanisms for the formation of *trans*-, and *cis*-bis-imine products containing tetraldehyde linker units.

8.4 Conclusions

In this study, we reported computational modeling of hierarchically composed crystalline 1D COFs formation *via* energy barrier calculation using DFT simulations. Furthermore, the energy barrier of designed COFs with small benzaldehyde linker units is compared with their analogues containing large tetraldehyde linker units. Based on the reaction products of COF formations containing small linkers, the activation barriers of cis-bis-imine, trans-bis-imine, and benzaldehyde formation are 14.5, -5.6, and 19.2 kJ/mol, respectively. These results illustrate that the *trans-bis*-imine-based COF formation is energetically the most achievable. However, upon replacing the benzaldehyde unit with the tetraldehyde linkers, the energy barriers increase to 215.6 and 315.3 kJ/mol for trans- and cis-products. These values reveal that the in the large linker units the steric repulsions play a significant role with hinder the crystallinity of COFs.

8.5 References

1 V. Nguyen and M. Grünwald, *J Am Chem Soc*, 2018, **140**, 3306–3311.

2 J. J. de Yoreo, P. U. P. A. Gilbert, N. A. J. M. Sommerdijk, R. L. Penn, S. Whitelam, D. Joester, H. Zhang, J. D. Rimer, A. Navrotsky, J. F. Banfield, A. F. Wallace, F. M. Michel, F. C. Meldrum, H. Cölfen and P. M. Dove, *Science*, 2015, **349**, aaa6760.

3 J. de Yoreo and S. Whitelam, *MRS Bull.*, 2016, **41**, 357–360.

4 A. P. Côté, A. I. Benin, N. W. Ockwig, M. O'Keeffe, A. J. Matzger and O. M. Yaghi, *Science*, 2005, **310**, 1166–1170.

5 J. R. Hunt, C. J. Doonan, J. D. LeVangie, A. P. Côté and O. M. Yaghi, *J. Am. Chem. Soc.*, 2008, **130**, 11872–11873.

6 Y. Li, W. Chen, G. Xing, D. Jiang and L. Chen, *Chem. Soc. Rev.*, 2020, **49**, 2852–2868.

7 Y. Song, Q. Sun, B. Aguila and S. Ma, *Adv. Sci.*, 2019, **6**, 1801410.

8 J. W. Crowe, L. A. Baldwin and P. L. McGrier, *J. Am. Chem. Soc.*, 2016, **138**, 10120–10123.

9 Y. Li, W. Chen, W. Hao, Y. Li and L. Chen, *ACS Appl. Nano. Mater.*, 2018, **1**, 4756–4761.

10 H.-S. Xu, S.-Y. Ding, W.-K. An, H. Wu and W. Wang, *J. Am. Chem. Soc.*, 2016, **138**, 11489–11492.

11 Z. Wang, S. Zhang, Y. Chen, Z. Zhang and S. Ma, *Chem. Soc. Rev.*, 2020, **49**, 708–735.

12 A. F. M. EL-Mahdy, C. Young, J. Kim, J. You, Y. Yamauchi and S.-W. Kuo, *ACS Appl. Mater. Interfaces*, 2019, **11**, 9343–9354.

13 Q. Gao, X. Li, G.-H. Ning, H.-S. Xu, C. Liu, B. Tian, W. Tang and K. P. Loh, *Chem. Mater.*, 2018, **30**, 1762–1768.

14 J.-C. Wang, X. Kan, J.-Y. Shang, H. Qiao and Y.-B. Dong, *J. Am. Chem. Soc.*, 2020, **142**, 16915–16920.

15 S. Rager, A. C. Jakowetz, B. Gole, F. Beuerle, D. D. Medina and T. Bein, *Chem. Mater.*, 2019, **31**, 2707–2712.

16 Q. Fang, J. Wang, S. Gu, R. B. Kaspar, Z. Zhuang, J. Zheng, H. Guo, S. Qiu and Y. Yan, *J. Am. Chem. Soc.*, 2015, **137**, 8352–8355.

17 P. Wang, Q. Xu, Z. Li, W. Jiang, Q. Jiang and D. Jiang, *Adv. Mater.*, 2018, **30**, 1801991.

18 S. B. Alahakoon, S. D. Diwakara, C. M. Thompson and R. A. Smaldone, *Chem. Soc. Rev.*, 2020, **49**, 1344–1356.

19 E. L. Spitler, B. T. Koo, J. L. Novotney, J. W. Colson, F. J. Uribe-Romo, G. D. Gutierrez, P. Clancy and W. R. Dichtel, *J. Am. Chem. Soc.*, 2011, **133**, 19416–19421.

20 Q. Fang, S. Gu, J. Zheng, Z. Zhuang, S. Qiu and Y. Yan, *Angew. Chem. Int. Ed.*, 2014, **53**, 2878–2882.

21 G. Lin, H. Ding, R. Chen, Z. Peng, B. Wang and C. Wang, *J. Am. Chem. Soc.*, 2017, **139**, 8705–8709.

22 A. M. Rice, E. A. Dolgopolova, B. J. Yarbrough, G. A. Leith, C. R. Martin, K. S. Stephenson, R. A. Heugh, A. J. Brandt, D. A. Chen, S. G. Karakalos, M. D. Smith, K. B. Hatzell, P. J. Pellechia, S. Garashchuk and N. B. Shustova, *Angew. Chem. Int. Ed.*, 2018, **57**, 11310–11315.

23 X. Feng, L. Liu, Y. Honsho, A. Saeki, S. Seki, S. Irle, Y. Dong, A. Nagai and D. Jiang, *Angew. Chem. Int. Ed.*, 2012, **51**, 2618–2622.

24 X. Chen, M. Addicoat, S. Irle, A. Nagai and D. Jiang, *J. Am. Chem. Soc.*, 2013, **135**, 546–549.

25 E. Klontzas, E. Tylianakis and G. E. Froudakis, *J. Phys. Chem. C*, 2008, **112**, 9095–9098.

26 Y. Pramudya and J. L. Mendoza-Cortes, *J. Am. Chem. Soc.*, 2016, **138**, 15204–15213.

27 M. S. Lohse and T. Bein, *Adv. Funct. Mater.*, 2018, **28**, 1705553.

28 H. Wang, H. Wang, Z. Wang, L. Tang, G. Zeng, P. Xu, M. Chen, T. Xiong, C. Zhou, X. Li, D. Huang, Y. Zhu, Z. Wang and J. Tang, *Chem. Soc. Rev.*, 2020, **49**, 4135–4165.

29 S. Kandambeth, K. Dey and R. Banerjee, *J. Am. Chem. Soc.*, 2019, **141**, 1807–1822.

30 Y.-B. Zhang, J. Su, H. Furukawa, Y. Yun, F. Gándara, A. Duong, X. Zou and O. M. Yaghi, *J. Am. Chem. Soc.*, 2013, **135**, 16336–16339.

31 H. L. Nguyen, C. Gropp and O. M. Yaghi, *J. Am. Chem. Soc.*, 2020, **142**, 2771–2776.

32 Z. Chen, K. Wang, X. Hu, P. Shi, Z. Guo and H. Zhan, *ACS Appl. Mater. Interfaces*, 2021, **13**, 1145–1151.

33 H.-S. Xu, Y. Luo, X. Li, P. Z. See, Z. Chen, T. Ma, L. Liang, K. Leng, I. Abdelwahab, L. Wang, R. Li, X. Shi, Y. Zhou, X. F. Lu, X. Zhao, C. Liu, J. Sun and K. P. Loh, *Nat. Commun.*, 2020, **11**, 1434.

34 N. W. Ockwig, O. Delgado-Friedrichs, M. O'Keeffe and O. M. Yaghi, *Acc. Chem. Res.*, 2005, **38**, 176–182.

35 M. O'Keeffe, M. A. Peskov, S. J. Ramsden and O. M. Yaghi, *Acc. Chem. Res.*, 2008, **41**, 1782–1789.

36 H. L. Nguyen, F. Gándara, H. Furukawa, T. L. H. Doan, K. E. Cordova and O. M. Yaghi, *J. Am. Chem. Soc.*, 2016, **138**, 4330–4333.

37 I. Y. Zhang, J. Wu and X. Xu, *Chem. Commun.*, 2010, **46**, 3057.

38 G. A. Petersson, A. Bennett, T. G. Tensfeldt, M. A. Al-Laham, W. A. Shirley and J. Mantzaris, *J. Chem. Phys.*, 1988, **89**, 2193–2218.

39 G. te Velde, F. M. Bickelhaupt, E. J. Baerends, C. Fonseca Guerra, S. J. A. van Gisbergen, J. G. Snijders and T. Ziegler, *J. Comput. Chem.*, 2001, **22**, 931–967.

40 Y. J. Bomble, *J. Am. Chem. Soc.*, 2006, **128**, 3103–3103.

41 S. Grimme, J. Antony, S. Ehrlich and H. Krieg, *J. Chem. Phys.*, 2010, **132**, 154104.

42 C. Bannwarth, S. Ehlert and S. Grimme, *J. Chem. Theory. Comput.*, 2019, **15**, 1652–1671.

Chapter 9

9 Conclusions and future perspective

In this research, *ab initio*, (GC)MC, MD, and MM/QM hybrid simulations have been undertaken to understand the behaviours including, gas binding mechanisms, adsorption isotherms, thermal transport properties, binding of bulk enzymes and soft metals (*e.g.*, mercury) of the periodic 2D (layered) MOFs and COFs.

Covalent Organic Frameworks (COFs) and Metal-Organic Frameworks (MOFs) are subclasses of crystalline polymers constructed by the periodic connection of secondary building units (SBUs) *via* organic and metallic linkers, respectively. These materials have shown great potential in gas storage applications due to their diverse (0D to 3D) crystalline nature. Among them, 2D analogs are ideal candidates for gas storage applications due to their perpendicular π-π interactions between the stacked 2D layers and periodically aligned 1D porous nature. In such materials, layer-by-layer π-interactions have a substantial effect on the electrical conductivity and catalytic properties. Based on the previous reports, where the effects of MOF geometries including metal units, heteroatoms, and organic linkers on the electrical band nature and catalytic properties have been widely discussed (see Chapter 2), it is found that the information about the effect of interlayer slipping and metal node on gas adsorption properties of such materials is still lacking. In order to fill this gap in the literature, we systematically explored the effect of neighboring layer slipping on NO, NH_3, and H_2S adsorption in 2D bimetallic Phthalocyanine MOF (see Chapter 3). It is found that oxygen atoms at metal nodes (MO_4) of the neighboring layer of the perfect stacked (eclipsed-AA) structure of MOFs provide the thermodynamically (energetically) preferred gas binding sites. In these structures, gas molecules prefer binding adjacent layers simultaneously due to the symmetric nature of eclipsed-AA. However, the parallel slipping of MOF layers affects the relative strength and alignment of gas adsorption. For this purpose, the simplified models of Pc-MOFs are used, and the potential energy landscape at GFN1-xTB method suggests the optimum slipping distance of around 6.00 Å in the *xy-plane* due to the lowest Columbic repulsion between the atoms of adjacent layers. This parallel slipping affects the binding energies drastically, as for stable slipped-AA structures of Ni/Ni-Pc and Ni/Cu-Pc MOFs, the NO binding energies are -243.5 and -242.1 kJ/mol as compared to -155.3

and -113.0 kJ/mol in eclipsed-AA structures, respectively. The layer slipping of MOFs also affects the number of binding sites. At the stable slipped-AA structure (6.00 Å), the number of binding sites increases because the active positions are shifted in space, resulting in the gas molecules prefer binding directly to the top metal sites. Hence, for slipped-AA structures, gas loading capacity increases due to the availability of a large number of active positions. For example, the gas (NO) loading capacity of the optimal slipping structure (slipped-AA) is almost double as compared to the eclipsed-AA structure, especially for the Ni/Ni-Pc MOF. Moreover, the changing nature of metal from Ni to Cu at the node position has not had a significant effect on the gas adsorption capacity in the slipped-AA structure, probably due to the dual nature of the phthalocyanine unit. Interestingly, the molecule adsorption takes place on Ni metal inside the body of phthalocyanine units upon replacing Ni with Cu at the node position, revealing that gas adsorption is facilitated by Ni rather than Cu. With these findings, it can be suggested that slipping in 2D MOFs is an essential parameter in the rational designing of new 2D frameworks with higher gas adsorption capacity than traditionally used materials. In the future, we are intending to extend this study to explore the effect of interlayer slipping on different heteroatoms or groups (S & NH and their mixed functional groups) containing 2D Pc-MOFs for gas adsorption applications.

Subsequently, the thermal conductivity of porous 2D COF namely benzobisoxazole (BBO-COF), and its structural derivatives with increased pores size has been studied *via* Non-Equilibrium Molecular Dynamics (NEMD) simulations. For this purpose, the BBO-COF structures are initially equilibrated at the desired temperature (*i.e.*, 80 and 300 K) using a "global" Berendsen thermostat. Subsequently, the heat flow is estimated by applying the local Nosé-Hoover thermostats at 80 ±10 or 300±10 K temperature to differentiate the hot and cold regions. The finite size effect on the thermal conductivity of COF structures from 1×1 to 4×4 lattices is also investigated, which reveals that the accurate estimation of thermal properties requires sufficient phonon modes that can be achieved by using the large unit cell size. The thermal conductivity values of various unit cell sizes *i.e.*, from 1 to 4 of parent BBO-COF are increased from 0.059 to 0.195 W/mK (at 80 K); correspondingly, the values vary from 0.072 to 0.326 W/mK at higher temperature (300 K). In simple, NEMD results reveal that the conductivity of BBO-COF increases with increasing temperature, which is

well consistent with the experimental findings. Moreover, this study also reveals that the thermal transport property of the BBO-COF is independent of the pore size. This research has been published in *ACS Applied NanoMaterials* and can be found in *ACS Appl. Nano Mater. 2022, 5, 10, 13787–13793*". Based on this study, our tutorial about the method of computing the thermal conductivity of periodic porous materials using SCM-AMS has also been published in the Software for Chemistry and Materials Manual, which can be accessed *via* "https://www.scm.com/highlights/thermal-management-conductivity-of-2d-covalent-organic-frameworks-with-nanopores/".

Next, the adsorption behaviour of three bulk enzymes; namely BGL, CBH, and EG, containing ~10,000 atoms each, on experimentally synthesized 2D-COFs (called TpAzo-COF) has been investigated. In this work, the hybrid QM/MM calculations have been performed for modeling enzyme binding on layered COF in order to rationalize the experimental findings. The bulk structures of enzymes as well as the COF limits the use of accurate DFT simulations. In this context, the hybrid QM/MM approach has an advantage over expensive DFT and inaccurate force field studies. QM/MM method divided the bulk systems into two parts *e.g.*, QM and MM parts based on the methods applied. QM part is the region of interest, containing a limited number of atoms that are simulated through accurate QM methods while the remaining atoms are the MM region, studied *via* fast force field. A detailed description of hybrid methods has been listed in Chapter 1 (see section 1.3) and Chapter 6 (see section 6.1). The QM/MM findings reveal that the 1D porous channel of 4×4×4 lattices of 2D COF is energetically the most favourable site for enzyme bindings, however, due to the bulkiness of enzyme molecules, most of their active positions remain unattended, and thus the adsorption takes place onto the surface of COF near the porous site. However, the stability of enzyme binding depends on the number of strong hydrogen bonds between the atoms of enzymes and COF. For example, the interaction strength of three enzymes is as follows; EG > BGL > CBH, which depends on the numbers of hydrogen bonds *i.e.*, 18, 16, 11 for binding EG, BGL, and CBH on COF, respectively. Overall findings are well agreed with the experimental study. The revised manuscript of this research has been submitted to the *Journal of the American Chemical Society*.

In the next study, the mercury (Hg) adsorption on newly designed COF called TpSMe-DPP has been successfully modeled computationally. Herein, the preferable adsorption site of mercury, atomic (Hg^0) as well as molecular (Hg^{2+}) in TpSMe-DPP

COF is explored by optimizing the structures at the GFN1-xTB method. The energetic stability reveals that the thioether and imine functionalities are the most suitable sites for Hg binding. In the TpSMe-DPP COF structure, there are six thioethers and three imine groups are available for Hg binding. There are six Hg molecules that can bind simultaneously in a single unit cell of TpSMe-DPP COF. Among them, three $HgCl_2$ molecules bind simultaneously with both functionalities whereas the remaining three molecules only bind at thioether groups due to the unavailability of imine groups. These findings reveal the 95 % efficiency of TpSMe-DPP COF which is well consistent with the experimental results *e.g.*, the Hg adsorption capacity of TpSMe-DPP COF is about 789 mg/g. Currently, the research article on this work is in the writing-up stages, we and collaborators are aiming to submit the work to the *Journal of the American Chemical Society*.

Lastly, the activation barriers *via* transition state calculations using DFT simulations have been computed in order to study the effect of different secondary building units *e.g.*, small benzaldehyde and large tetraldehyde, on the growth of 1D COFs. The energetic stability of products including (*cis*- and *trans*-) *bis*-imine and benzimidazole reveals that the *trans*-*bis*-imine formation is energetically feasible with the formation energy -17.88 kJ/mol, followed by the *cis*-*bis*-imine (-5.63 kJ/mol). The benzimidazole formation is a highly endothermic process, where the obtained formation energy is +35.4 kJ/mol. Moreover, unlike *bis*-imine products, the benzimidazole formation is a two-step process, which makes it energetically unfavorable. In comparison between SBUs, it is found that the activation barrier for *trans*-*bis*-imine containing benzaldehyde linker is about 12.4 kJ/mol, however, it increases to 215.6 kJ/mol upon replacing with large (tetraldehyde) linker units, indicating that increasing the size of the linker is energetically disfavoured for the COF growth due to the increasing steric crowding.

Undoubtedly, from the study on porous materials presented in this thesis, the importance of interlayer slipping in the gas adsorption of 2D MOFs is evident. Overall, this research suggests that interlayer slipping in 2D frameworks is an essential parameter in designing adsorbents with enhanced gas adsorption capacities. Another problem here though is achieving accurate modeling of 2D layered frameworks using the extended tight binding GFN1-xTB method. The non-covalent interaction term in the algorithm, allows the method to be employed for the accurate

screening of noncovalent (π-π) interactions between the neighbouring layers and their binding energies with gas molecules which are not applicable *via* DFT and force field due to high computational demand and low accuracy, respectively. Finally, the knowledge earned here will not only assist in the development of improved MOF sensors with a high ratio of gas adsorption but gives an example of using xTB method in quick modeling of stacked frameworks within a short time span.

Our study and many others illustrate that the 2D-MOFs are the ideal candidates for applications in gas binding and energy storages due to their distinctive structures and dimensional porosities.[1] This is because their geometric structures, electronic behaviour, and mechanical & chemical properties can be feasibly modified at the molecular level through varying SBUs including organic linkers, inorganic nodes, and heteroatom linkages.[2] Thermal management is one of the most fundamental properties for ensuring the optimal performance of porous crystals in energy transport processes;[3] however, the practical implementation of thermal properties in gas storage of such materials has been overlooked.[4] Energetically, gas adsorption is an exothermic process, rapid loading and unloading of gases result in a sharp rise and drop in temperature, respectively which undermines the advantages of using a framework as an ideal adsorbent. In other words, the energy storage *e.g.*, filling and unfilling of gases depends on the thermal efficiency of frameworks.[5] In order to fulfil their promise as ideal adsorbents, it is necessary for MOFs to maintain the balance between gas adsorption and thermal properties. However, very little is known about how to tune the thermal properties of MOFs,[6] especially 2D-MOFs. Broadly, the MOFs that have been investigated so far exhibit thermal conductivity lower than 0.4 W/mK.[7–9] To the best of our knowledge, these have been the open questions a) how adsorbed gas molecules influence the thermal conductivity of 2D MOFs and b) how the structural diversity *e.g.*, interlayer slipping of MOFs affects the thermal management of such materials. Based on the literature studies on the thermal management of other (3D) MOFs,[10] it is expected that the in-plane thermal transport ability of 2D-MOFs will be increased upon molecules adsorption due to the addition of extra heat transfer channels in the system. Moreover, the interlayer slipping may affect the out-of-plane thermal properties due to the decreasing Columbic repulsions between the neighbouring layers when the top layers shift to energetically stable offsets. In future work, we will be

extending adopted approaches (in this work) to study the effect of gas adsorption and interlayer slipping on the thermal management of 2D-Pc MOFs.

9.1 References

1 H.-C. Zhou, J. R. Long and O. M. Yaghi, *Chem. Rev.*, 2012, **112**, 673–674.

2 M. Zhao, Y. Huang, Y. Peng, Z. Huang, Q. Ma and H. Zhang, *Chem. Soc. Rev.*, 2018, **47**, 6267–6295.

3 X. Xu, J. Chen, J. Zhou and B. Li, *Adv. Mater.*, 2018, **30**, 1705544.

4 H. Babaei, M. E. DeCoster, M. Jeong, Z. M. Hassan, T. Islamoglu, H. Baumgart, A. J. H. McGaughey, E. Redel, O. K. Farha, P. E. Hopkins, J. A. Malen and C. E. Wilmer, *Nat. Commun.*, 2020, **11**, 4010.

5 M. Beckner and A. Dailly, *Appl. Energy*, 2016, **162**, 506–514.

6 K. J. Erickson, F. Léonard, V. Stavila, M. E. Foster, C. D. Spataru, R. E. Jones, B. M. Foley, P. E. Hopkins, M. D. Allendorf and A. A. Talin, *Adv. Mater.*, 2015, **27**, 3453–3459.

7 D. Liu, J. J. Purewal, J. Yang, A. Sudik, S. Maurer, U. Mueller, J. Ni and D. J. Siegel, *Int. J. Hydrogen Energy*, 2012, **37**, 6109–6117.

8 B. L. Huang, Z. Ni, A. Millward, A. J. H. McGaughey, C. Uher, M. Kaviany and O. Yaghi, *Int. J. Heat Mass Transf.*, 2007, **50**, 405–411.

9 B. L. Huang, A. J. H. McGaughey and M. Kaviany, *Int. J. Heat Mass Transf.*, 2007, **50**, 393–404.

10 L. Han, M. Budge and P. Alex Greaney, *Comput. Mater. Sci.*, 2014, **94**, 292–297.

Appendix A – Python Scripts Used in the Research

Bilayer geometries were generated from optimised monolayers and X gas molecules were inserted stochastically.

Python code for generating layers slipped structures

ASE; Atomic Simulation Environment, a Python module for visualizing, manipulating, running, and analyzing atomistic simulations, is employed. Before creating the slip geometries, eclipsed-AA geometries of the analogs of MOFs with two stacked layers were created from their optimized monolayer using the python coding below. The command for this script is "**python script.py filename.XYZ**".

1. Lines 1 to 6 export the necessary libraries for atoms and mathematical expressions from the ASE module.
2. Lines 8 to 13 present the arguments for selecting the file containing monolayer coordinates.
3. Line 14 argues to read the coordinates.
4. Lines 18 & 23 command that the interlayer distance between two layers of MOFs along the *z*-plane should be 3.3 Å.
5. Lines 20 and 21 use the Cell Module from ASE to explain the unit size of two the layers of cell.
6. Line 25 commands to create supercell with lattice parameters of 1×1×2 which generates two stacked layers.
7. Lines 31 and 32 command to save the bilayer structure in a new CIF file with the name of "AA.CIF".

```python
from ase.atom import Atom
from ase.atoms import Atoms
from ase.io import read, write
from math import sin,cos,pi,sqrt
import numpy as np
import sys

if len(sys.argv) == 2:
    qcin1 = sys.argv[1]
    qc_base = qcin1.split('.')[0]
else:
    print ('Incorrect filetype')
    sys.exit()
monolayer = read(qcin1)
#orig_coords=monolayer.get_positions()

#Now change the cell
interlayer_dist = 3.3
print("!!! you might want to change the interlayer distance")
cell_a = sqrt(monolayer.cell[0,0]**2 + monolayer.cell[0,1]**2 + monolayer.cell[0,2]**2 )
cell_b = sqrt(monolayer.cell[1,0]**2 + monolayer.cell[1,1]**2 + monolayer.cell[1,2]**2 )

monolayer.cell[2,2] = interlayer_dist

bilayer = monolayer * (1,1,2)

#x-axis and a-axis correspond

#for n_shift in xrange(1,11):
#bilayer.positions[len(monolayer):]+=[0.5,0,0]
filename='AA.cif'
write(filename,bilayer)
```

After creating a bilayer structure, another python code was used to generate 361 slip structures with the slipping offset of 0.5 Å in *x*-, *y*-, and *xy*-plane. In the python script below, a build function was used to make offsets in all the directions with the indices from 0.0 to 9.0 Å. This script generates 361 coordinates in CIF format titled, "SlipAA_XY_*x*-index_*y*-index.cif" representing each geometry separately.

```python
#!/usr/bin/python
#from __future__ import print_function
from ase.atom import Atom
from ase.atoms import Atoms
from ase.io import read, write
from math import sin,cos,pi,sqrt
import numpy as np
import os
import shutil
import itertools
import sys


if len(sys.argv) == 2:
    qcin1 = sys.argv[1]
else:
    print ('Incorrect filetype')
    sys.exit()



bilayer = read(qcin1)

def Building_XY(x_index, y_index):
    # Creating a folder for each of the slipped files
    Folder_name = 'SlipAA_XY_'+str(x_index)+'_'+ str(y_index)
    if not os.path.exists(Folder_name):
        os.makedirs(Folder_name)
    else:
        pass
    #for n_shift in xrange(1,11):
    bilayer.positions[len(bilayer)/2:]+=[x_index,y_index,0]
    #Creat File name and write into the file
    filename='slipAA.cif'
    write(filename,bilayer)


    #copy the file into the new directory
    shutil.copy2(filename,Folder_name)
    os.remove(filename)
    return


Indices = [0.0, 0.5, 1.0, 1.5, 2.0, 2.5, 3.0, 3.5, 4.0, 4.5, 5.0, 5.5, 6.0, 6.5, 7.0, 7.5, 8.0, 8.5, 9.0]
#Indice = [0.5]
for x in Indices:
    for y in Indices:
    bilayer = read(qcin1)
        Building_XY(x, y)
```

Implementation of SCM-AMS parameters on slip structural coordinates

Afterwards, the SCM-AMS parameters were implied on each CIF file by using another python code given below. This script not only applies essential parameters but also save the files as AMS run jobs in separate folders.

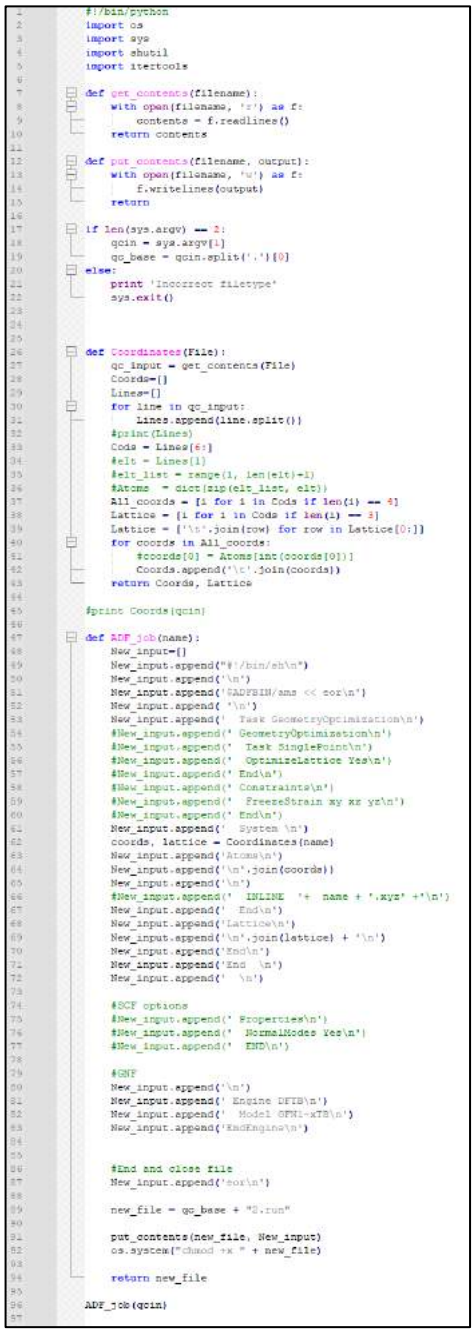

```
#!/bin/python
import os
import sys
import shutil
import itertools

def get_contents(filename):
    with open(filename, 'r') as f:
        contents = f.readlines()
    return contents

def put_contents(filename, output):
    with open(filename, 'w') as f:
        f.writelines(output)
    return

if len(sys.argv) == 2:
    qcin = sys.argv[1]
    qc_base = qcin.split('.')[0]
else:
    print 'Incorrect filetype'
    sys.exit()


def Coordinates(File):
    qc_input = get_contents(File)
    Coords=[]
    Lines=[]
    for line in qc_input:
        Lines.append(line.split())
    #print(Lines)
    Cods = Lines[6:]
    #elt = Lines[1]
    #elt_list = range(1, len(elt)+1)
    #Atoms  = dict(zip(elt_list, elt))
    All_coords = [i for i in Cods if len(i) == 4]
    Lattice = [i for i in Cods if len(i) == 3]
    Lattice = ['\t'.join(row) for row in Lattice[0:]]
    for coords in All_coords:
        #coords[0] = Atoms[int(coords[0])]
        Coords.append('\t'.join(coords))
    return Coords, Lattice

#print Coords(qcin)

def ADF_job(name):
    New_input=[]
    New_input.append("#!/bin/sh\n")
    New_input.append('\n')
    New_input.append('$ADFBIN/ams << eor\n')
    New_input.append( '\n')
    New_input.append('  Task GeometryOptimization\n')
    #New_input.append(' GeometryOptimization\n')
    #New_input.append('  Task SinglePoint\n')
    #New_input.append('  OptimizeLattice Yes\n')
    #New_input.append(' End\n')
    #New_input.append(' Constraints\n')
    #New_input.append('  FreezeStrain xy xz yz\n')
    #New_input.append(' End\n')
    New_input.append('  System \n')
    coords, lattice = Coordinates(name)
    New_input.append('Atoms\n')
    New_input.append('\n'.join(coords))
    New_input.append('\n')
    #New_input.append('  INLINE  '+  name + '.xyz' +'\n')
    New_input.append('  End\n')
    New_input.append('Lattice\n')
    New_input.append('\n'.join(lattice) + '\n')
    New_input.append('End\n')
    New_input.append('End  \n')
    New_input.append('  \n')

    #SCF options
    #New_input.append(' Properties\n')
    #New_input.append('  NormalModes Yes\n')
    #New_input.append('  END\n')

    #GNF
    New_input.append('\n')
    New_input.append(' Engine DFTB\n')
    New_input.append('  Model GFN1-xTB\n')
    New_input.append('EndEngine\n')


    #End and close file
    New_input.append('eor\n')

    new_file = qc_base + ".run"

    put_contents(new_file, New_input)
    os.system("chmod +x " + new_file)

    return new_file

ADF_job(qcin)
```

- Before running this script, the ".run" files were generated using command "**for f in SlipAA_XY_*/*.cif; do mybabel -o run $f; done**".
- Followed by the slurrm script (below) to run the above python code. For this purpose, the above code file should be moved to a "Job_creation" folder in "src"

on the Linux machine. GFNSP_cif.py is the name of script to create a job for single point energy calculations.

```
for i in Slip*
do
cd $i
for f in *run
do
python ~/src/Job_creation/GFNSP_cif.py $f
done
cd ../
done
```

Finally, the calculations were submitted to the queue system using submit.sh script with command; "**sbatch submit.sh**".

```
#!/bin/bash
#SBATCH --ntasks=8
#SBATCH --nodes=1
#SBATCH --mem-per-cpu=6000M   # memory per CPU core
#SBATCH --job-name=Ni/Cu
#SBATCH --time=20-48:00:00
source /etc/bashrc

module load apps/dftbplus

cd SlipAA_XY_0.0_0.0
./slipAA.run > slipAA.out
cd ../

cd SlipAA_XY_0.0_0.5
./slipAA.run > slipAA.out
cd ../

cd SlipAA_XY_0.0_1.0
./slipAA.run > slipAA.out
cd ../

cd SlipAA_XY_0.0_1.5
./slipAA.run > slipAA.out
cd ../

cd SlipAA_XY_0.0_2.0
./slipAA.run > slipAA.out
cd ../

cd SlipAA_XY_0.0_2.5
./slipAA.run > slipAA.out
cd ../
```

Python script for the extraction of electronic energies

After simulating the 361 single-point energy calculations for each MOF analogue, the electronic energies were extracted using another python code (given below).

```
out = open('energy_data.out','a')
Indices = [0.0, 0.5, 1.0, 1.5, 2.0, 2.5, 3.0, 3.5, 4.0, 4.5, 5.0, 5.5, 6.0, 6.5, 7.0, 7.5, 8.0, 8.5, 9.0]
#x = [0, 5]

for value in (Indices):
    x = [0.0, 0.5, 1.0, 1.5, 2.0, 2.5, 3.0, 3.5, 4.0, 4.5, 5.0, 5.5, 6.0, 6.5, 7.0, 7.5, 8.0, 8.5, 9.0]
    for i in (x):
        #values = str(x)
        file = open('SlipAA_XY_' + str(value)+'_'+ str(i)+'/slipAA.out','r')
        data = file.readlines()
        Results=[]
        for line in data:
            if ' Start   directory: /users/' in line:
                directory_name = line
                #print(line)
                file_names = directory_name.split('/')[7]
                Results.append(file_names)

        for linenum, line in enumerate(data):
            if 'AMS application finished' in line:
                NT = linenum + 1
                NORMAL TERMINATION = data[NT]
        for lines in data:
            if len(lines.split())==4 and lines.split()[0] == 'Total'  and  lines.split()[1] == 'Energy' and lines.split()[2] == '(hartree)':
                Energy = (str(lines.split()[3]))
                #print(Energy)
                Results.append(Energy)
                #print(Results)
                data = str(Results)
                #print(data)
                A = data.split(',')[0]
                Name = A.split("'")[1]
                #print(Name)
                ABC = str(data.split(',')[1])
                Energy = str(ABC.split("'")[1])
                #print(Energy)
                #out.write(str(Results)+ '\t'+ (NORMAL TERMINATION)+'\n')
                out.write((Name)+ '\t'+ (Energy)+'\t'+(NORMAL_TERMINATION))
```

By running the script with the command "**python script.py**", a new file with .out extension was saved, containing names of structures in column-1, electronic energies in column-2, and Normal termination message in the column-3.

Convert .out file to Excel sheet

After getting list of energies in .out files, another script was used to convert it into excel sheet.

```
#This script will work in hamilton (Linux)
# In hamilton need to activate virtual environment
#for the first time install pandas using command; pip install pandas
import pandas as pd
#for editing in excell sheet need to install library; pip install aspose-cells

df = pd.read_csv('energy_data.out', sep='\t')

df=df.to_excel('energy_data.xlsx', 'Sheet1', index=False)
```

Relative energies with respect to the eclipsed-AA structures and generate Excel sheet

The script below was written to generate an Excel worksheet containing the relative energies with respect to the eclipsed-AA structure.

```
import openpyxl
from openpyxl.styles import Font
#from openpyxl.reader.excel import load_workbook
#from openpyxl import load_workbook
#from openpyxl import Workbook
#print(openpyxl.__version__)

#Took help from these videos:
    #https://www.youtube.com/watch?v=8z6lLhMsyDM
    #https://www.youtube.com/watch?v=JjeSXWIX9SY


'''make a sheet'''
#wb = openpyxl.Workbook()

'''Load filename.xlsx'''
wb = openpyxl.load_workbook('energy_data.xlsx')

'''change the sheet name'''
ws = wb['Sheet1']
ws.title = 'Energies'
'''del col_3 with ----'''
ws.delete_cols(3)

'''add title in row one''''''First add a row on top'''
ws.insert_rows(1, 1)

'''adding title using enumerate, start=1 means that adding title should start with column 1'''
for col_idx, title in enumerate(('Names', 'Energies (au)', 'Erel (kcal/mol)', 'Erel_round'), start=1):
    ws.cell(row=1, column=col_idx, value=title)

'''To apply font on column one'''
for i in range(1, ws.max_column+1):
    ws.cell(row=1, column=i).font = Font(bold=True, name='Arial', size=10)


'''To apply font on column one'''
for i in range(1, ws.max_column+1):
    ws.cell(row=1, column=i).font = Font(bold=True, name='Arial', size=10)

'''Insert colum for adding formula'''
#ws.insert_cols(3)
#select rows from 2 to infinity. Here max_row+1 means till last row

for i in range(2, ws.max_row+1):
    #print(i)
    #select values of column 2 (energies)
    Energies = float(ws.cell(row=i, column=2).value)
    #print(Energies)
    #select the energy of first/AA structure
    initial = float(ws.cell(row=2, column=2).value)
    #write a formula
    Erel = (initial - Energies)*627.51
    #append formula to column 3, title Erel
    ws.cell(row=i, column=3).value = Erel

'''Add round function'''
for i in range(2, ws.max_row+1):
    Erel = ws.cell(row=i, column=3).value
    formula = round(Erel, 0)
    ws.cell(row=i, column=4).value = formula
'''save a sheet'''
wb.save('Excel_sheet_Final.xlsx')
```

Potential Energy Surfaces (PESs) plots

RStudio is an IDE: integrated development program, a language-based program for statistical computing and graphical visualization of data. Therefore, R and RStudio were used to plot the PESs for slipped structures based on theory relative energies.

```
1.      Import Excel file to R
2.      install.packages("ggplot2")
3.      Install.packages("ggthemes")
4.      Library(ggplot2)
5.      Library(ggthemes)
6.      Then write this script


> ggplot(Excel_file_name, aes(x=X, y=Y, colour = Energies))+
    geom_point(size=6)+
    scale_colour_gradientn(colours=rainbow(6))+
    scale_x_continuous(name = "X-axis shift", breaks=c(0,1,2,3,4,5,6,7,8,9))+
    scale_y_continuous(name = "Y-axis shift", breaks=c(0,1,2,3,4,5,6,7,8,9))+
    labs(title ="Title_name", color="Energy\n (kcal/mol)")+
    theme_minimal()+
    theme(text = element_text(size=20, face="bold"))+
    coord_fixed(ratio = 1)



7.      Finally save as 700, 700 pxicel
```

Binding energies and Excel worksheet

Another python code was written to produce list of binding energies of hundreds and thousands of structures with only one command.

```
import openpyxl
from openpyxl.styles import Font
import sys
#from openpyxl.reader.excel import load_workbook
#from openpyxl import load_workbook
#from openpyxl import Workbook
#print(openpyxl.__version__)

#Took help from these videos:
    #https://www.youtube.com/watch?v=8z6lLhMeyDM
    #https://www.youtube.com/watch?v=JieSXWIX9SY

if len(sys.argv)==3:
    Surface = sys.argv[1]
    Molecule = sys.argv[2]

'''make a sheet'''
#wb = openpyxl.Workbook()

'''Load filename.xlsx'''
wb = openpyxl.load_workbook('energy_data.xlsx')

'''change the sheet name'''
ws = wb['Sheet1']
ws.title = 'Energies'
'''del col_3 with ---'''
ws.delete_cols(3)

'''add title in row one''''''First add a row on top'''
ws.insert_rows(1, 1)

'''adding title using enumerate, start=1 means that adding title should start with column 1'''
for col_idx, title in enumerate(('Names', 'Energies (au)', 'Eint (kcal/mol)', 'Erel_round'), start=1):
    ws.cell(row=1, column=col_idx, value=title)

'''To apply font on column one'''
for i in range(1, ws.max_column+1):
    ws.cell(row=1, column=i).font = Font(bold=True, name='Arial', size=10)


'''To apply font on column one'''
for i in range(1, ws.max_column+1):
    ws.cell(row=1, column=i).font = Font(bold=True, name='Arial', size=10)

'''Insert colum for adding formula'''
#ws.insert_cols(3)
#select rows from 2 to infinity. Here max_row+1 means till last row

for i in range(2, ws.max_row+1):
    #print(i)
    #select values of column 2 (energies)
    Energies = float(ws.cell(row=i, column=2).value)
    #Energies = ws.cell(row=i, column=2).value
    #print(Energies)
    #select the energy of first/AA structure
    #initial = ws.cell(row=2, column=13).value


    #initial2 = ws.cell(row=3, column=13).value
    #write a formula
    Eint = (Energies-(float(Surface) + float(Molecule)))*2625.5
    #Eint = (Energies-(initial2 + initial))*2625.5
    #append formula to column 3, title Erel
    ws.cell(row=i, column=3).value = Eint

'''Add round function'''
for i in range(2, ws.max_row+1):
    Eint = ws.cell(row=i, column=3).value
    formula = round(Eint, 0)
    ws.cell(row=i, column=4).value = formula
'''save a sheet'''
wb.save('Excel_sheet_Final.xlsx')
```

Neighbour list

The python script below was used to print the name of closest atoms of MOFs interacting to the atoms of guest molecules within distance of 3.00 Å.

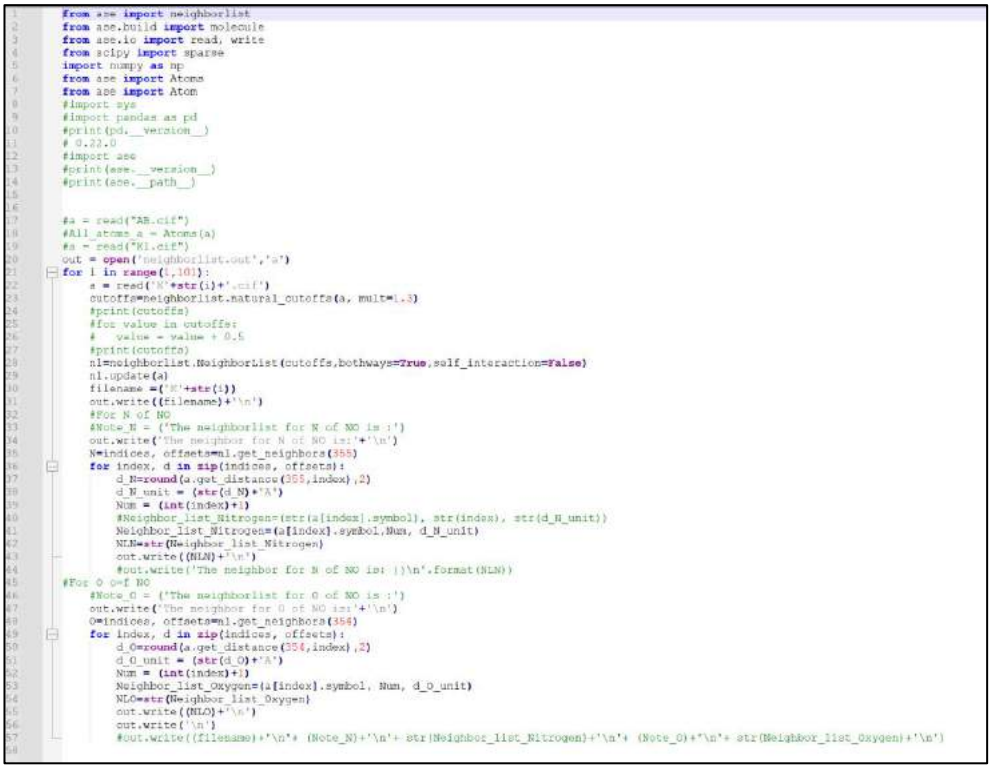

```
from ase import neighborlist
from ase.build import molecule
from ase.io import read, write
from scipy import sparse
import numpy as np
from ase import Atoms
from ase import Atom
#import sys
#import pandas as pd
#print(pd.__version__)
# 0.22.0
#import ase
#print(ase.__version__)
#print(ase.__path__)


#a = read("AB.cif")
#All_atoms_a = Atoms(a)
#a = read("K1.cif")
out = open('neighborlist.out','a')
for i in range(1,101):
    a = read('K'+str(i)+'.cif')
    cutoffs=neighborlist.natural_cutoffs(a, mult=1.3)
    #print(cutoffs)
    #for value in cutoffs:
    #   value = value + 0.5
    #print(cutoffs)
    nl=neighborlist.NeighborList(cutoffs,bothways=True,self_interaction=False)
    nl.update(a)
    filename ='K'+str(i)
    out.write((filename)+'\n')
    #For N of NO
    #Note_N = ('The neighborlist for N of NO is :')
    out.write('The neighbor for N of NO is:'+'\n')
    N=indices, offsets=nl.get_neighbors(355)
    for index, d in zip(indices, offsets):
        d_N=round(a.get_distance(355,index),2)
        d_N_unit = (str(d_N)+'A')
        Num = (int(index)+1)
        #Neighbor_list_Nitrogen=(str(a[index].symbol), str(index), str(d_N_unit))
        Neighbor_list_Nitrogen=(a[index].symbol,Num, d_N_unit)
        NLN=str(Neighbor_list_Nitrogen)
        out.write((NLN)+'\n')
        #out.write('The neighbor for N of NO is: {}\n'.format(NLN))
#For O of NO
    #Note_O = ('The neighborlist for O of NO is :')
    out.write('The neighbor for O of NO is:'+'\n')
    O=indices, offsets=nl.get_neighbors(356)
    for index, d in zip(indices, offsets):
        d_O=round(a.get_distance(356,index),2)
        d_O_unit = (str(d_O)+'A')
        Num = (int(index)+1)
        Neighbor_list_Oxygen=(a[index].symbol, Num, d_O_unit)
        NLO=str(Neighbor_list_Oxygen)
        out.write((NLO)+'\n')
        out.write('\n')
        #out.write((filename)+'\n'+ (Note_N)+'\n'+ str(Neighbor_list_Nitrogen)+'\n'+ (Note_O)+'\n'+ str(Neighbor_list_Oxygen)+'\n')
```

The small gas adsorption isotherms for eclipsed-AA and slipped-AA Ni/Ni- and Ni/Cu-Pc MOF were performed using the GCMC; grand canonical Monte-Carlo simulations. The simulations were performed in RASPA-1.0 (ref) using the external interface PLAMS functionality. For this purpose, a PLAMS script was written;

Set-input & simulation parameters: The information of RASPA input is wrapped into a Settings class, followed by the important parameters for simulations, including types of calculations, number of equilibration and production cycles, and applied force field.

Execution parameters are defined e.g., defining MOF.cif, applied reaction condition and finally, the MC moves.

Job-setting describes the name of the job and submits it to the queuing system.

Results including excess adsorption isotherm at each pressure are produced. Finally, a new file is generated in the working folder entitled; “Isotherm.out”.

```python
from ase.io import read, write

#=============Set-Input=====================
s = Settings()

#=============Simulation-parameters=========
s.input.simulationtype ='MonteCarlo'
s.input.numberofinitializationcycles = 2000
s.input.numberofcycles = 1000*20000
s.input.printevery = 100 #1000
s.input.forcefield = 'ExampleMOFsForceField'
s.input.restartfile = 'no'
s.input.usechargesfromcifile = 'yes'
#=============Execution-parameterrs=========
s.input.framework, h = 0
s.input.framework.frameworkname = 'NiMIAAcharge'
s.input.framework.unitcells = '2 2 3'
s.input.heliumvoidfraction = 6.345
s.input.externaltemperature = 298.15
s.input.externalpressure = '1e1 1e4 2e4'
#s.input.cutoff = 24.0

s.input.computenumberofmoleculeshistogram = 'yes'
s.input.writonumberofmoleculeshistogramevery = 5000
s.input.numberofmoleculeshistogramsize = 1100
#s.input.numberofmoleculesrange = 80

s.input.computeenergyhistogram = 'yes'
s.input.writeenergyhistogramevery = 5000
s.input.energyhistogramsize = 400
s.input.energyhistogramlowerlimit = -110000
s.input.energyhistogramupperlimit = -20000

s.input.Component['0'] = Settings()
s.input.Component['0'].molsculename = 'N2oside'
s.input.Component['0'].moleculedefinition = 'ExampleDefinitions'
s.input.Component['0'].translationprobability = 0.5
s.input.Component['0'].reinsertionprobability =  0.5
s.input.Component['0'].swapprobability = 1.0
s.input.Component['0'].rotationprobability = 0.5
#s.input.Component['0'].idealgasrosenbluthweight = 1.00132
s.input.Component['0'].creatonumberofmolecules = 0

#=============Job-run=======================
job = RaspaJob(name='test', settings=s)
#jobrun = job.run()

#=============get queueing system===========
gr = GridRunner(parallel=True, maxjobs=1, grid='slurm')
gr.settings.special.export = '--export='
#jobrun = job.run(jobrunner=gr, queue='nodes', node=2, J='something', C='')
jobrun = job.run(jobrunner=gr, walltime='20-48:00:00', queues'nodes', exports'value')

#=============Results=======================
#isotherm=jobrun.get_isotherm(output_folder='Output/System_0/', get_std=True, get_unit=True, search_x='Partial pressure', search_y='Average loading excess')
isotherm=jobrun.get_isotherm(output_folder='Output/System_0/', search_x='Partial pressure', search_y='Average loading excess', get_unit=True)
#isotherm=jobrun.get_isotherm()
print(isotherm)

#=============write results in newfile===
newfile = open('Isotherm.out','w')
for values in isotherm:
    values = str(values)
    newfile.write(values+ '\n')
```

Appendix B – Tutorial for NonEquilibrium Molecular Dynamics Simulations in SCM-AMS Software

NEMD simulation setup in SCM-AMS software

The input for NEMD simulations consists of two steps;

a) equilibration of the system at the desired temperature (80 K and 300 K in our case) using a global Berendsen thermostat.

b) thermal conductivity calculations;

As discussed above, the thermal conductivity can be calculated by two different approaches, depending upon the requirement *e.g.*, thermal conductivity calculations via heat flow rate by applying local thermostats with fixed temperature and *via* temperature gradient with fixed heat flow rate.

System equilibration: Before setting up the NEMD calculations, the equilibration of the system at a given temperature is necessary in order to achieve thermal equilibrium. Thermal equilibrium is the state where heat is equally distributed throughout the system at a given temperature. In other words, it is the condition where the temperature of each atom of the system becomes the same.

- In the equilibration step, the Molecular dynamics calculations are set with the Universal Force Field.

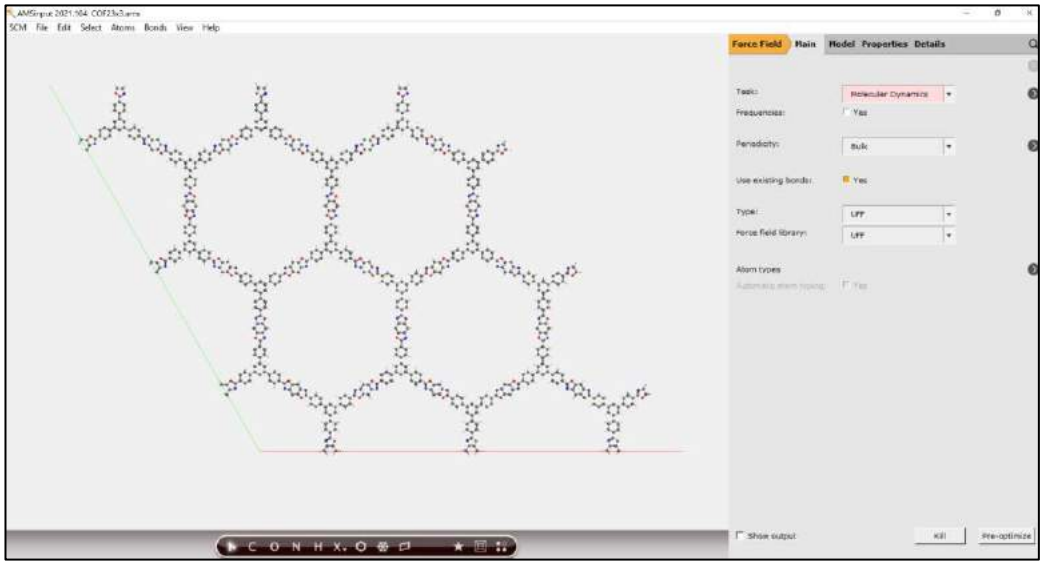

- The MD parameters are set to $3x10^5$ number of steps with 1fs time scale and an initial temperature of 80 K (or 300 K in separate input).

- A global thermostat is set by selecting the “Berendsen”, the temperature of 80 K, with a damping constant of 1000 fs. (don’t forget to select “All” from the “Atoms in region” section.

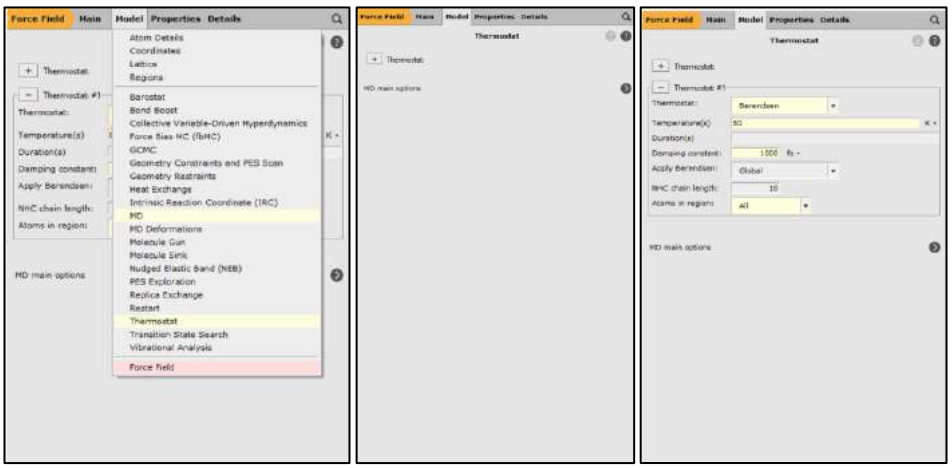

- All set for step 1, our input will look like this:

```
"$AMSBIN/ams" << eor

Task MolecularDynamics      (This input is to perform MD calculations)

MolecularDynamics           (MD block to set the parameters)

   NSteps 300000            (These are the number of MD steps)
   TimeStep 1               (Time scale of 1 fs)

   InitialVelocities        (To set the temperature)

      Temperature 80        (To equilibrate the system at 80 K, depending upon the requirement)

   End                      (block end)

   Thermostat               (Thermostat block to set the parameters)
```

Can be acquired from the literature

```
    Type Berendsen          (Global Berendsen type of thermostat is applied)
    Temperature 80          (Desired temperature: should be equal to the temp of MD calculation)
    Tau 1000                (Damping constant value; here this value should be higher)
  End                       (block end)
End                         (whole block end)
System
  Atoms
    Coordinates             (x y z coordinates of the system, have been removed here)
  End
  Lattice
    62.7 0.0 0.0
    31.2 54.2 0.0           (lattice parameters)
    0.0 0.0 3.37
  End
  BondOrders
    values                  (bond order of all atoms, has been removed here)
  End
End


Engine ForceField (UFF is used which sets a default here)
EndEngine
eor
```

- After running the calculations the results illustrate that the system is equilibrated at the desired temperature.
- The final equilibrated geometry will be used for the next step.

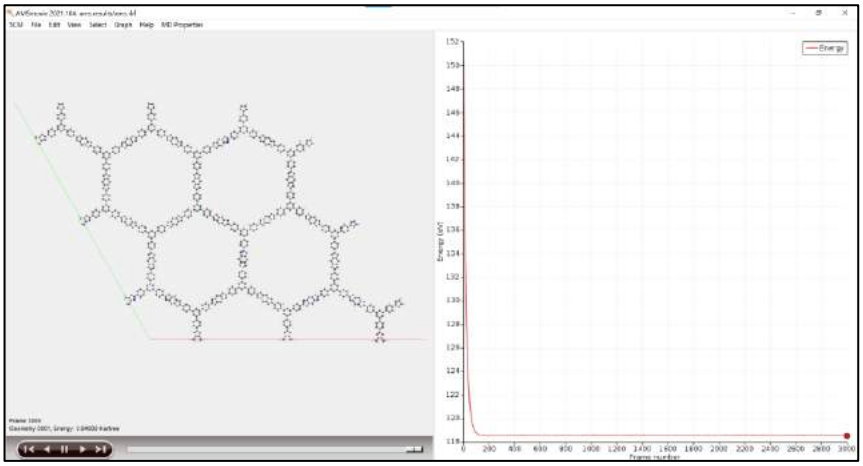

Thermal conductivity calculations: After the equilibration of the system, remake an input from the final geometry of the equilibrated system to simulate NEMD calculations.

- A common characteristic of the NEMD method is that a structure should split into different regions, including hot, cold, and conduction, each with its own thermostat.
- In AMS, these zones can be generated by the region sub-block in the Model section.
- Defining the regions is a more crucial part of these calculations. In thermal conductivity calculations, a system is basically divided into three parts: a) hot region, referred a heat source, b) cold region called a heat sink, and c) conduction region, where heat travels from the hot to the cold bath.
- The selection of atoms for hot and cold regions is a crucial part, the hot and cold regions should be symmetrically apart from all the sides in periodic systems, and both regions must be spatially separated by a reasonably-sized conduction zone. As we can notice from the example below that the red island is the hot region from where heat enters the system, while the green wavy line represents the cold region which is equidistant to the hot region from both ends.

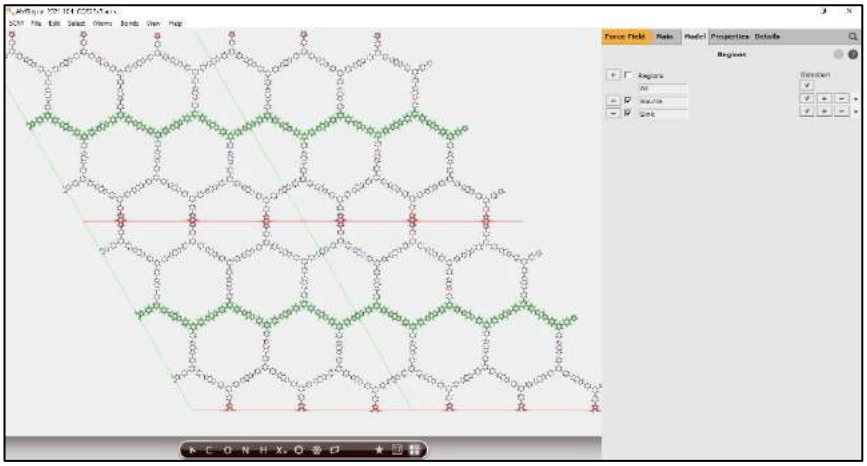

- The hot region (source of heat) is a region from where heat enters the system which is red highlighted. While the green highlighted region represents the cold bath (sink), through this region heat leaves the system. As our selected system is periodic, thus conduction zone between the source and sink in all directions i.e. all across the unit cell boundaries.

Input to calculate the *k* via the thermostat method: In the thermostat method, the two (local) Nosé-Hoover thermostats are applied to recognize the hot and cold baths. The temperature of the hot bath is set to be 80+10 (300+10) and the cold bath 80-10 (300-10), with a damping constant of 10 fs. Don't forget to specify the "Atoms in the region" as "source" and "Sink" for the "hot" and "cold" regions, respectively.

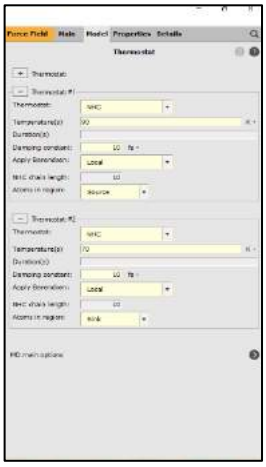

- Finally set the MD parameters, No. of steps 1 x 10^6 with time 1fs, and temperature of conduction zone remain 80 K (300 K).

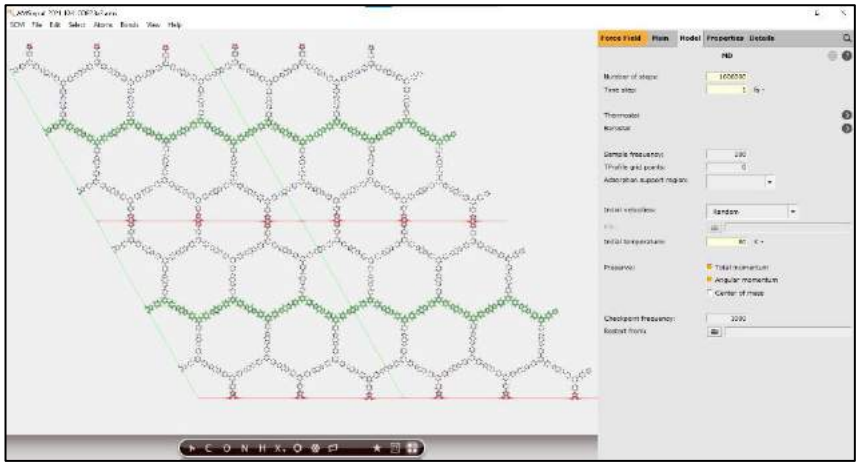

- The final input looks like this:

```
"$AMSBIN/ams" << eor

Task MolecularDynamics   (MD calculations)

MolecularDynamics        (MD block starts to set parameters)

   NSteps 1000000        (No. of MD steps increased)
   TimeStep 1            (Time steps for MD calculations)

   InitialVelocities     (Defines the temperature of conduction zone)

      Temperature 80     (Conduction zone's temp is set to be desired value (80 K in our case))

   End

   Thermostat            (Thermostat block starts for the hot region to define the parameters)

      Type NHC           (Local Nosé-Hoover thermostat for the hot region)

      Temperature 90     (Temp of a hot bath is set to be 90 K)

      Tau 10             (Damping constant should be between 10 and 20)

      Region Source      (Defining that it is the hot region)

   End                   (Thermostat block for the hot region ends)

   Thermostat            (Thermostat block starts for the cold region to define the parameters)

      Type NHC           (Local Nosé-Hoover thermostat for the cold region)

      Temperature 70     (Temp of the cold bath is set to be 70 K)

      Tau 10             (Damping constant should be between 10 and 20)

      Region Sink        (Defining that it is a cold region)
```

Can be acquired from the literature

```
   End                    (Thermostat block for the cold region ends)
End
System
   Atoms
      C -4.329850319771174 7.98705133175566 -0.6323655535702611
      C -3.737705794759909 9.231969904859076 -0.4324230437168098
      C 10.58633933736407 3.311594327324605 2.053232582128115 region=Source
      N 11.6943898255502 2.642096018866664 2.243278820819794 region=Source
      C -14.78770809897013 25.96067922902425 -0.313836061279315 region=Sink
      C -14.15312181163548 27.20704165450094 -0.09740472960534986 region=Sink
   End
   Lattice
      values
   End
   BondOrders
      values
   End
End
Engine ForceField
EndEngine
eor
```


Heat flow rate and thermal conductivity from the thermostat method of NEMD simulations: After the completion of calculations, the results will show the energy graph, however extra graphs can be added by clicking the "Add graph" in the open list.

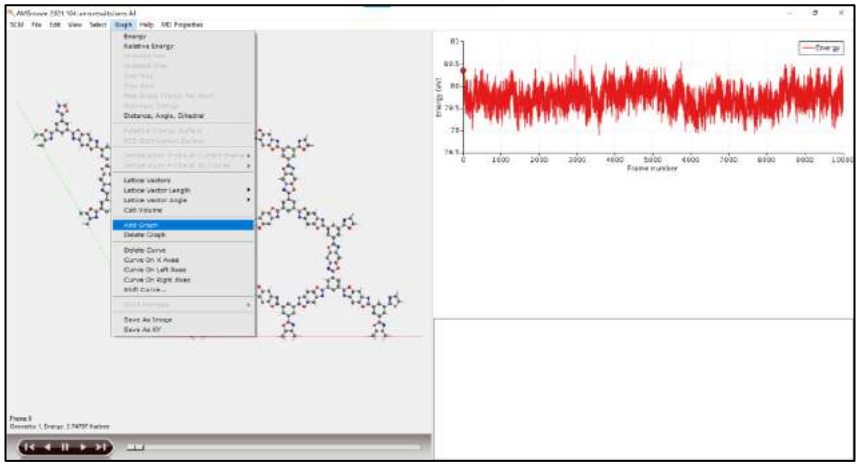

- In ams.rkf file, the MD results, including thermostat energies, are available in the MD Properties section, in variables *i.e.*, 'NHCTstat1Energy and NHCTstat2Energy'. The variable "XXXX" is a four-letter abbreviation of the Thermo-/NHCT (NHCT' for an NHC thermostat) and the digits 1 and 2 are indexes of the thermostat e.g., 1 for hot and 2 for cold.
- The figure below shows the energy of the thermostat coupling to the heat source region is decreasing because heat is transferred from the thermostat to the atoms in the source region. The energy of the thermostat coupling to the heat sink region is increasing because heat is transferred from the atoms in the sink region to the thermostat.

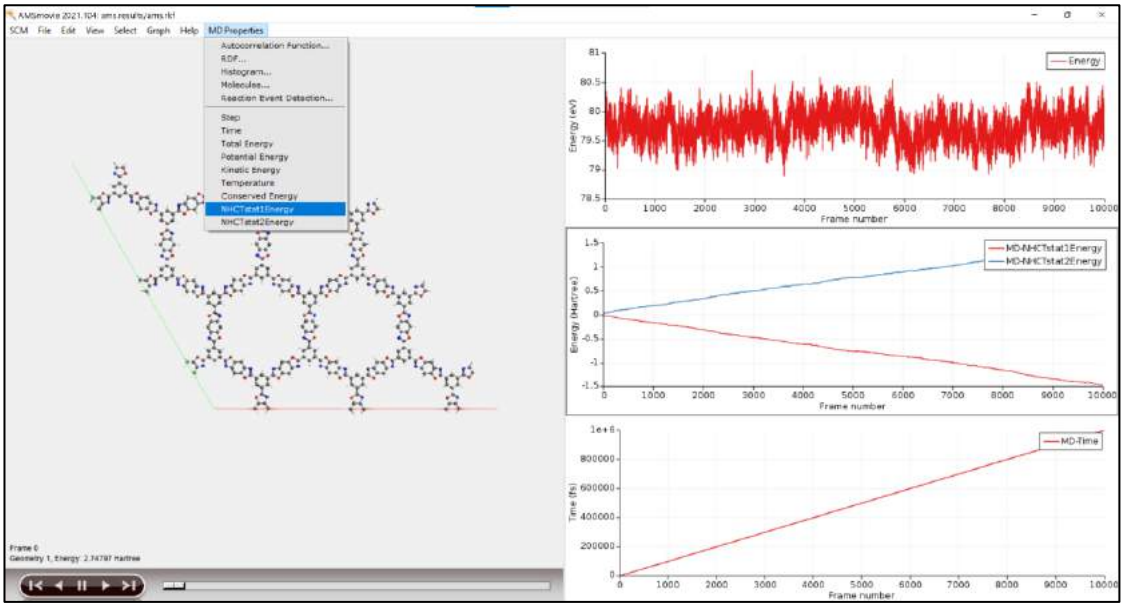

- The unit of the energies and time can be changed by double-clicking on the axis labeling, shown in the figure below.

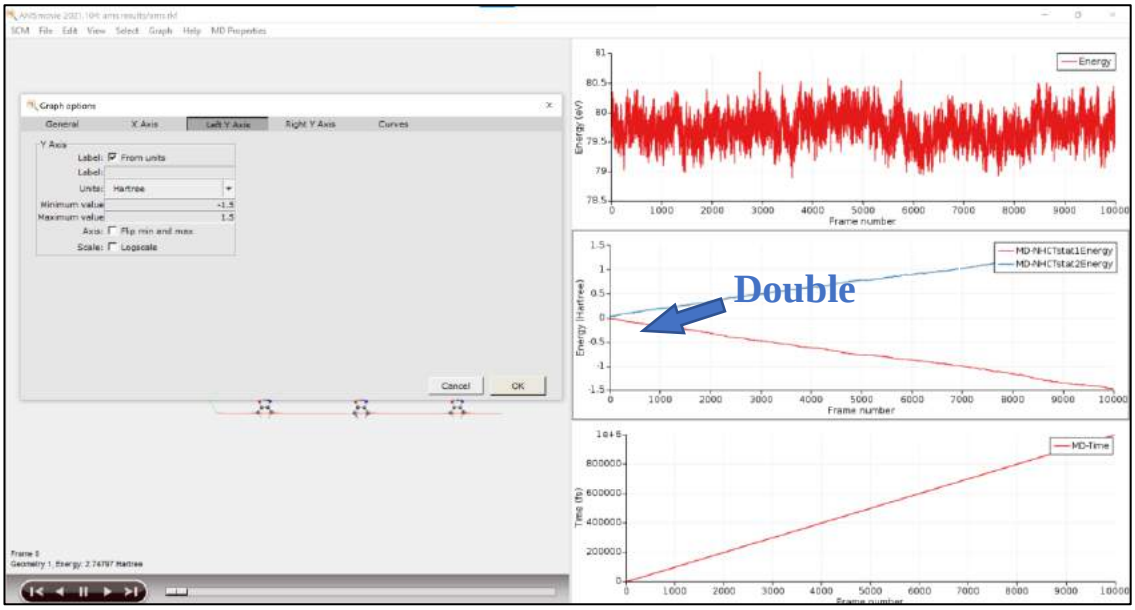

- *The heat flow rate is basically the flow of heat from the hot to the cold region of the system through the conduction zone.*
- The absolute values of the slopes of the hot and sink regions should be the same; otherwise, it means energy is not conserved. The absolute slope of the sink region is the energy transfer rate (heat flow rate) which should be divided by 2 because in a periodic system the heat transfers in two directions.

$$Q = \left(\frac{dE}{dt} \Big/ 2 \right)$$

- The slope is extracted from the graph.

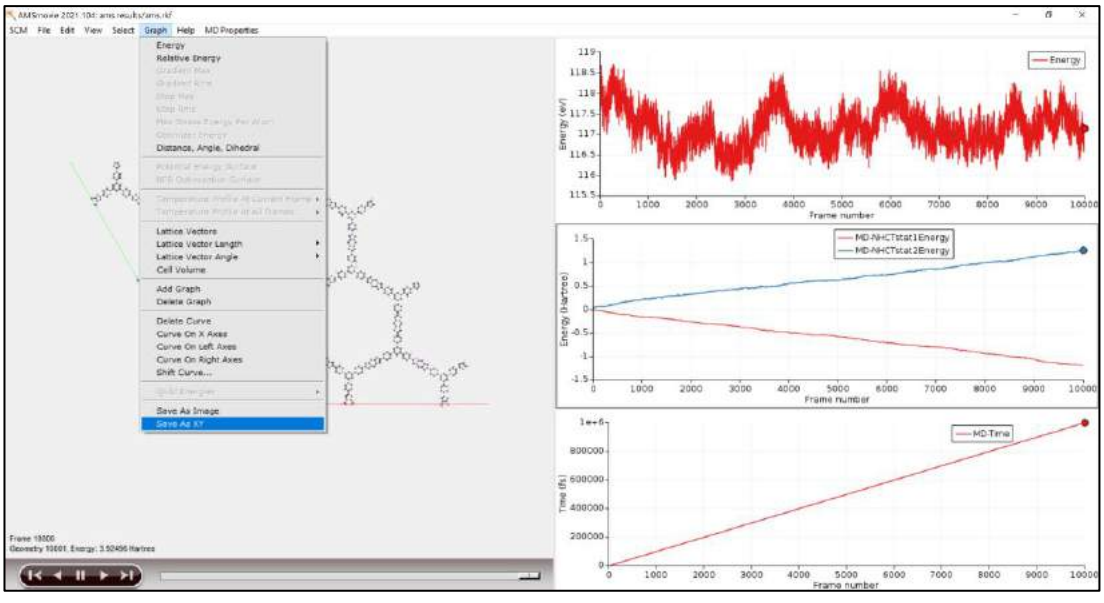

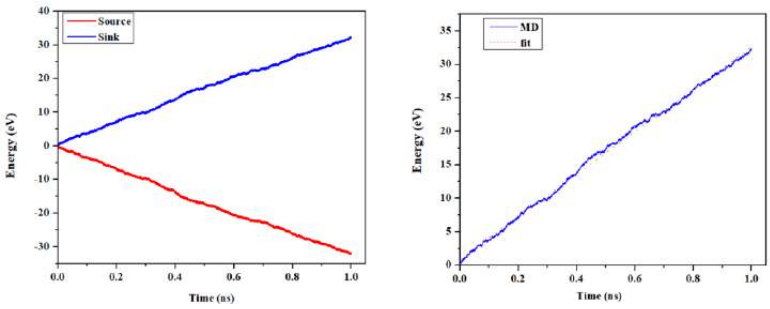

- The thermal conductance in the system can be calculated as

$$k = \left(\frac{Q}{S\Delta T}\right)$$

where S is the cross-sectional area, from where heat enters the system and ΔT is the temperature difference, which is 20 K here.

Some important literature about NEMD simulations for the thermal conductivity of periodic materials are:

Input to calculate the *k* via the Heat-exchange method: In the heat-exchange method, the temperature gradient is measured at a given heat flow rate.

- After defining the region of new input generated from the equilibrated structure at desired temperature needs to be set as given below.

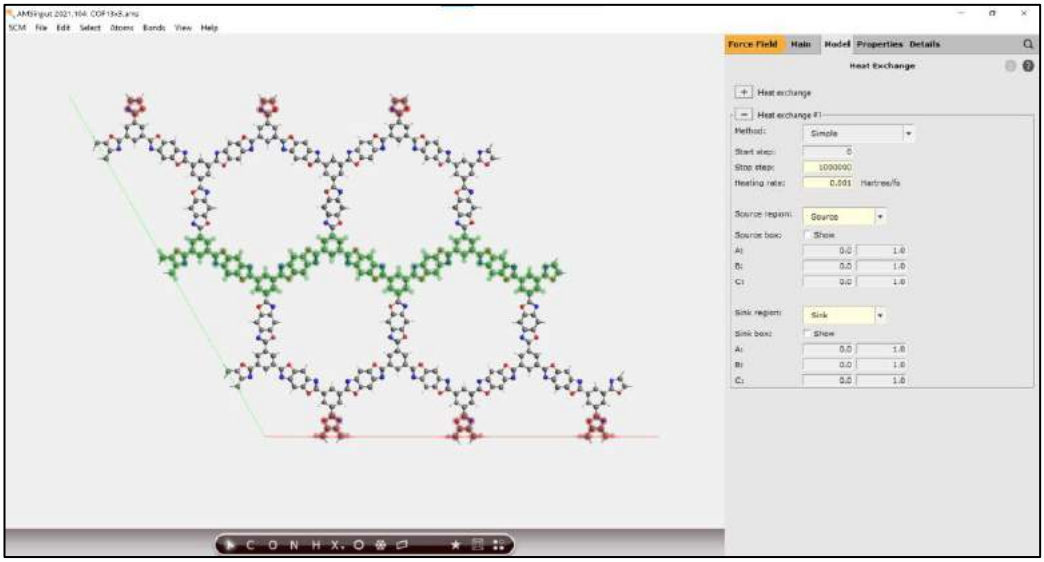

- This method can be implemented in SCM-AMS in 3-variants, including simple heat exchange, HEX, and eHEX. In the heat exchange method, the atom velocities are scaled down (or up) by a factor equivalent to the amount of heat deposited or

withdrawn from the source or the sink regions, respectively, without considering the conservation of the total momentum of thermostats. In the HEX method, the total momentum is conserved, which introduces a small drift in the total energy of the system. The eHEX algorithm is an improved version of HEX by a third-order integration correction, which removes the drift.

- Heating rate defines the rate of energy added to the hot thermostat and removed from the cold thermostat. A heating rate of 1.00 Hartree/fs corresponds to 0.00436 Watts of power transferred. Here the Heating rate should be logical, a very high heating rate can cause pyrolysis in the structure.
- The temperature gradient can be calculated as the absolute slope of Tempgradiant results from the MD Properties section (as we did in calculating heat flow rate in the thermostat method).
- The thermal conductivity (*k*) can be calculated via Fourier Law as listed above.

Energy accumulation graphs for BBO-COFs during NEMD calculations

BBO-COF-1 (80 K)

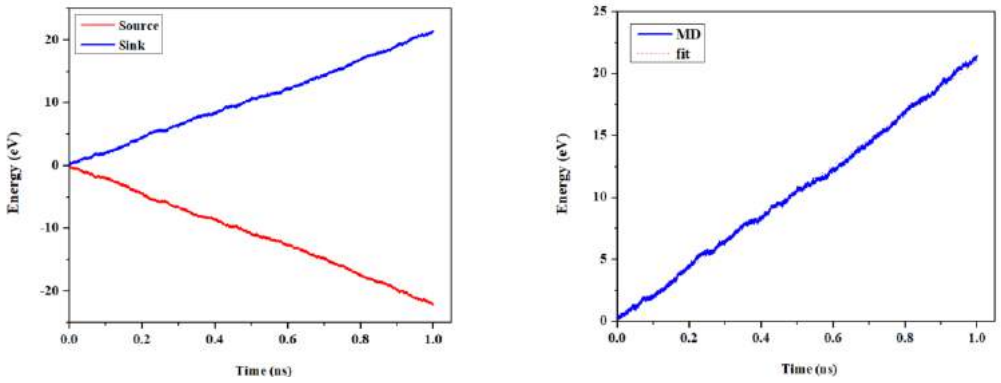

BBO-COF-1 (300 K)

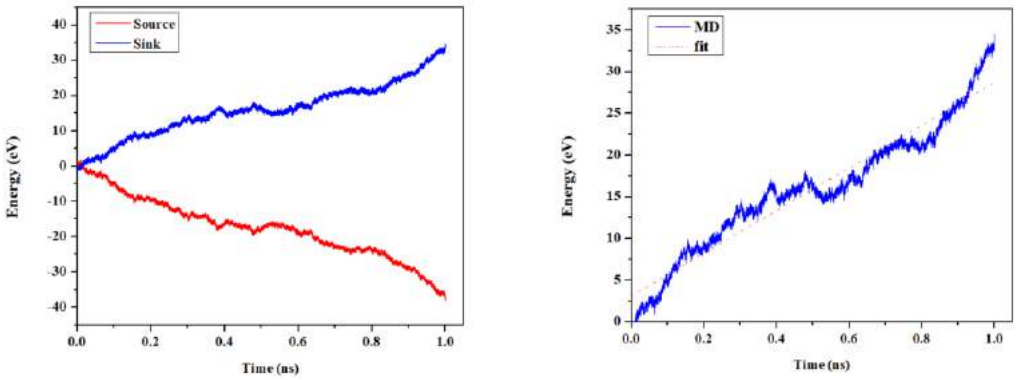

BBO-COF-2 (80 K)

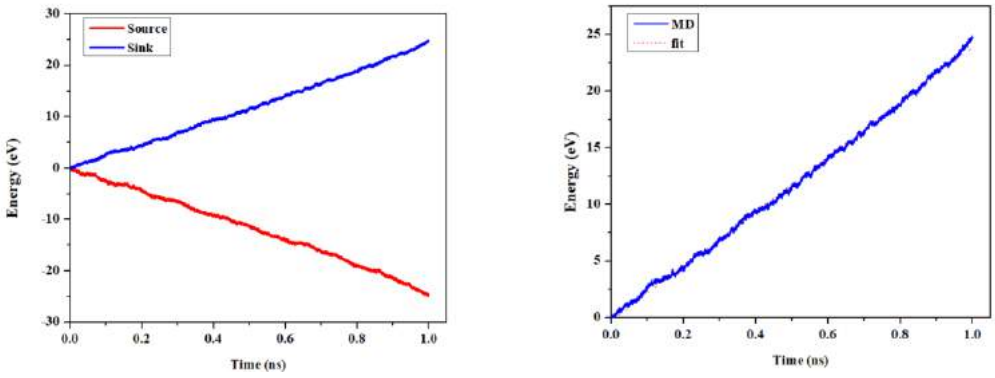

BBO-COF-2 (300 K)

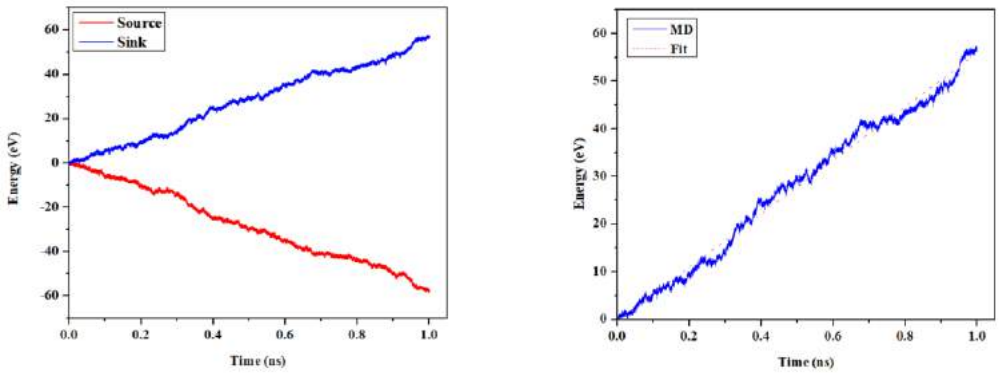

BBO-COF-3 (80 K)

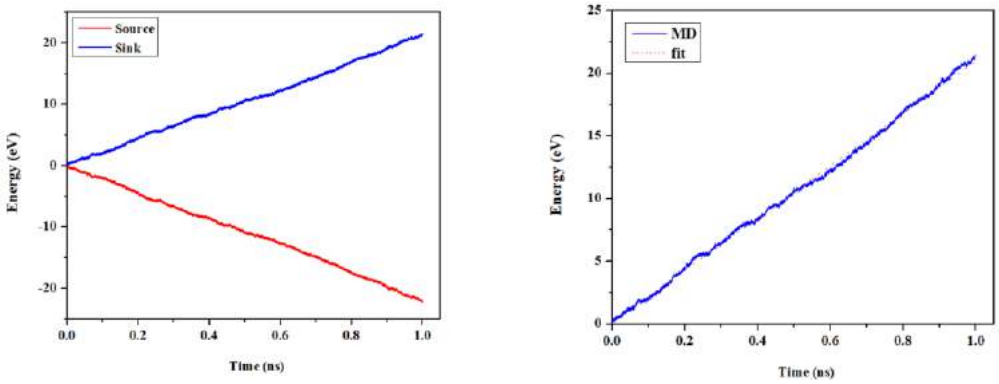

BBO-COF-3 (300 K)

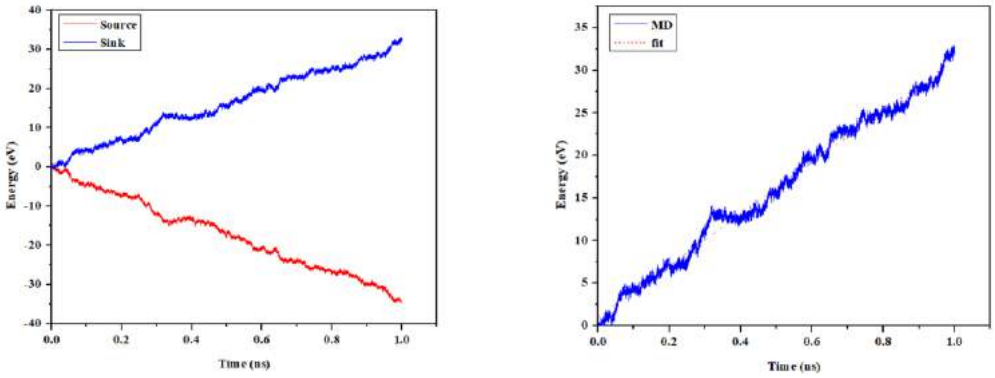

Figure 9.1. Energies (eV) accumulated in the source and sink (hot and cold thermostats, respectively) and the accumulated energy of the sink only with a linear fit as a function of time (ns) for 1×1 unit cells of BBO-COF-1, BBO-COF-2, and BBO-COF-3.

BBO-COF-1 (80 K)

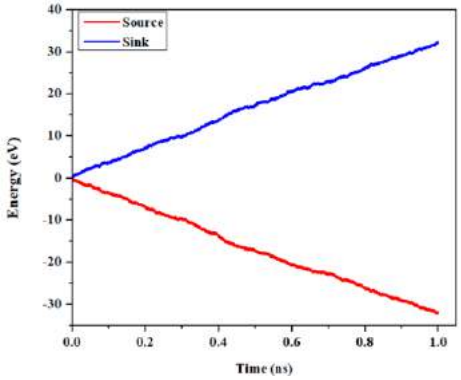

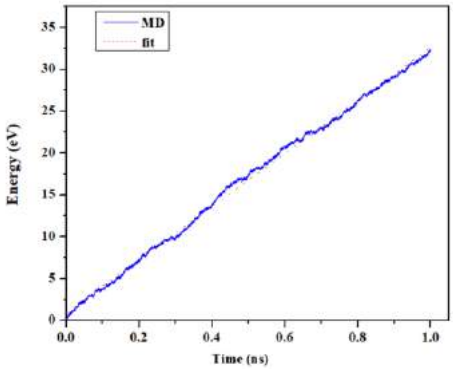

BBO-COF-1 (300 K)

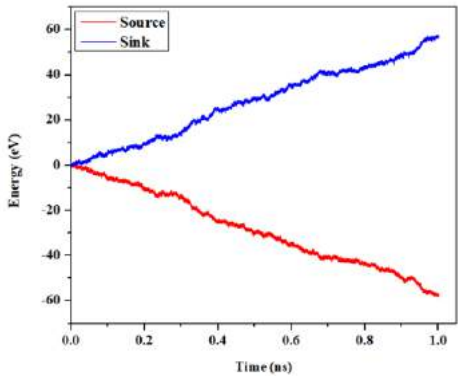

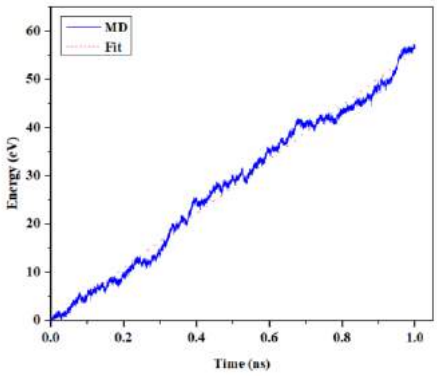

BBO-COF-2 (80 K)

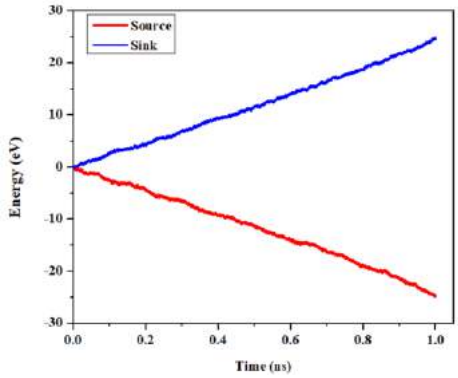

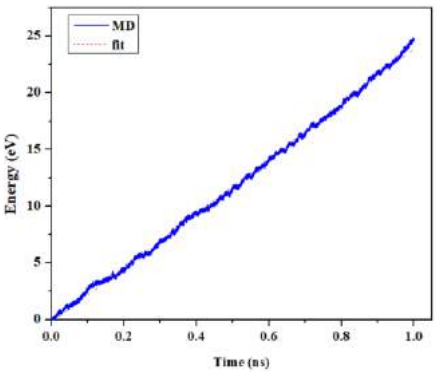

BBO-COF-2 (300 K)

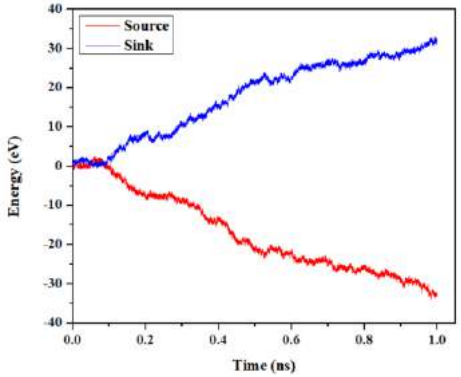

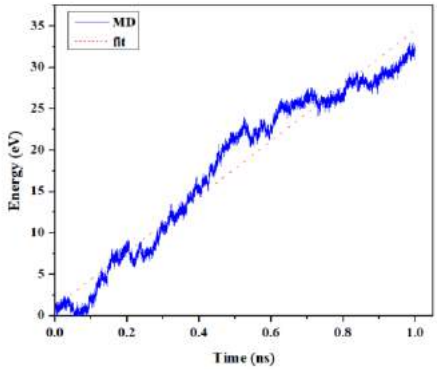

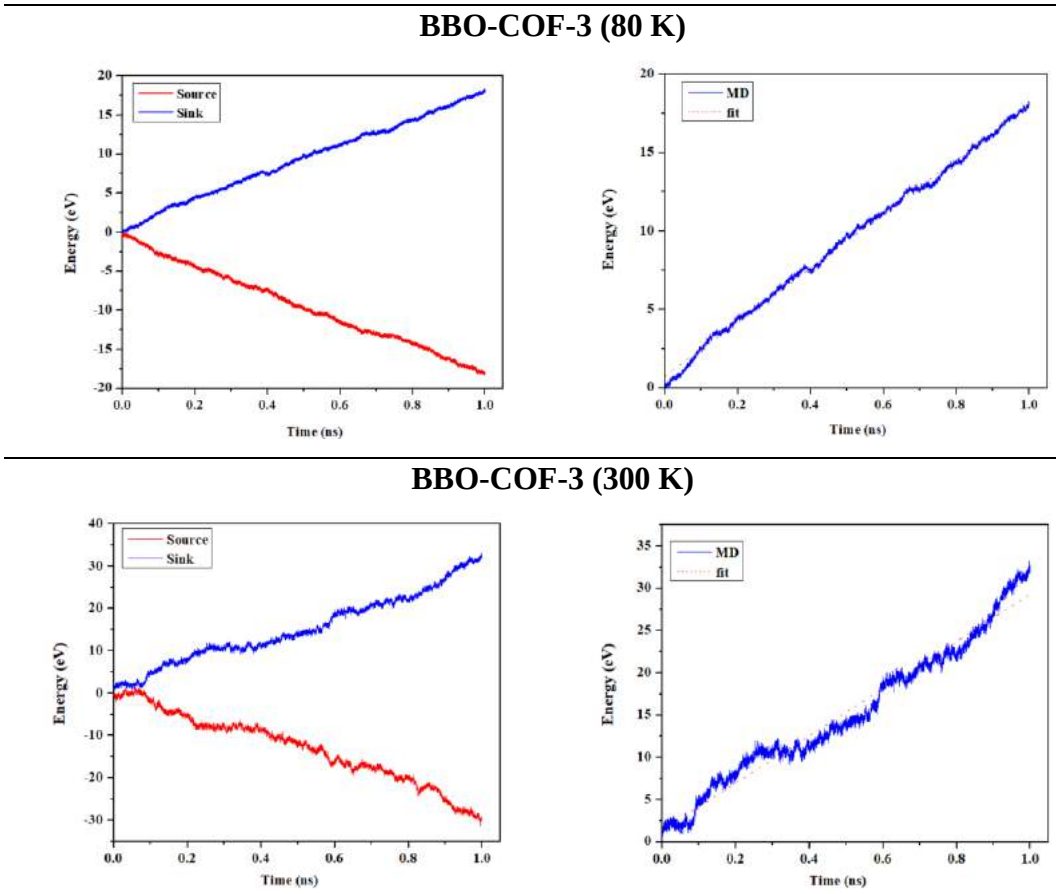

Figure 9.2. Energies (eV) accumulated in the source and sink (hot and cold thermostats, respectively) and the accumulated energy of the sink only with a linear fit as a function of time (ns) for 2×2 unit cells of BBO-COF-1, BBO-COF-2, and BBO-COF-3.

BBO-COF-1 (80 K)

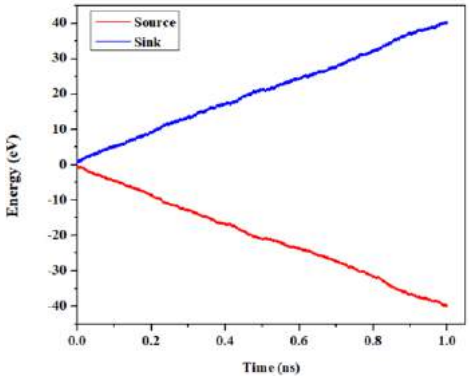

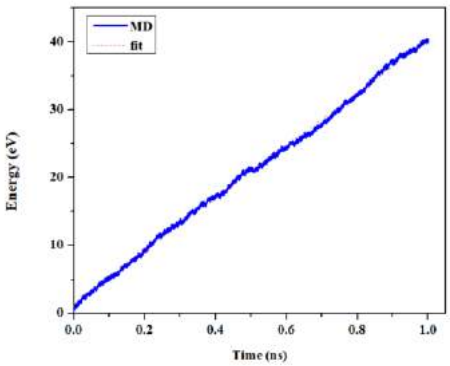

BBO-COF-1 (300 K)

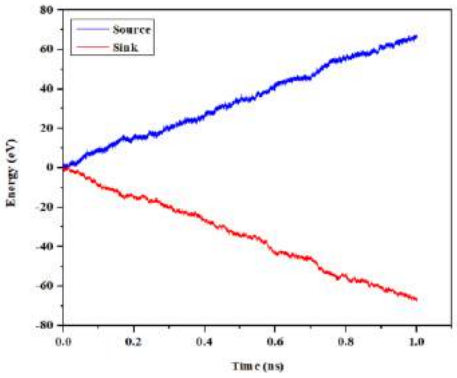

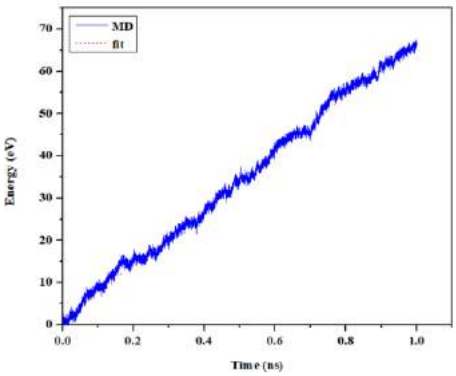

BBO-COF-2 (80 K)

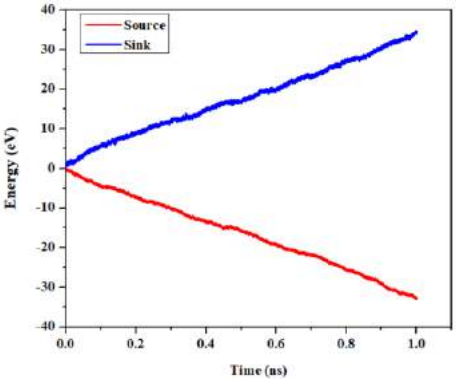

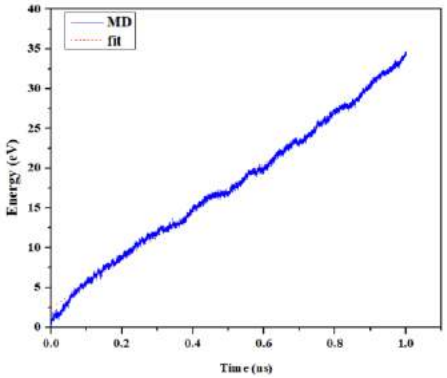

BBO-COF-2 (300 K)

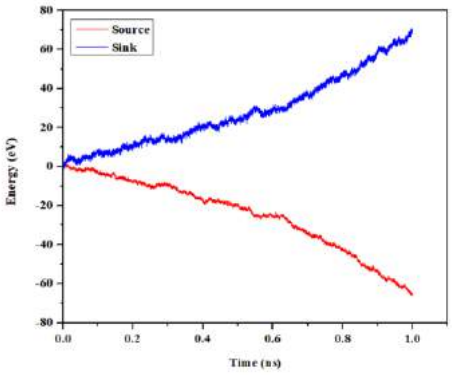

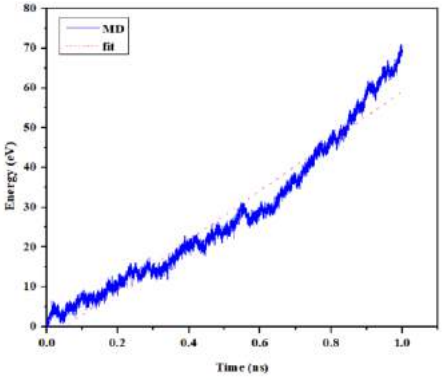

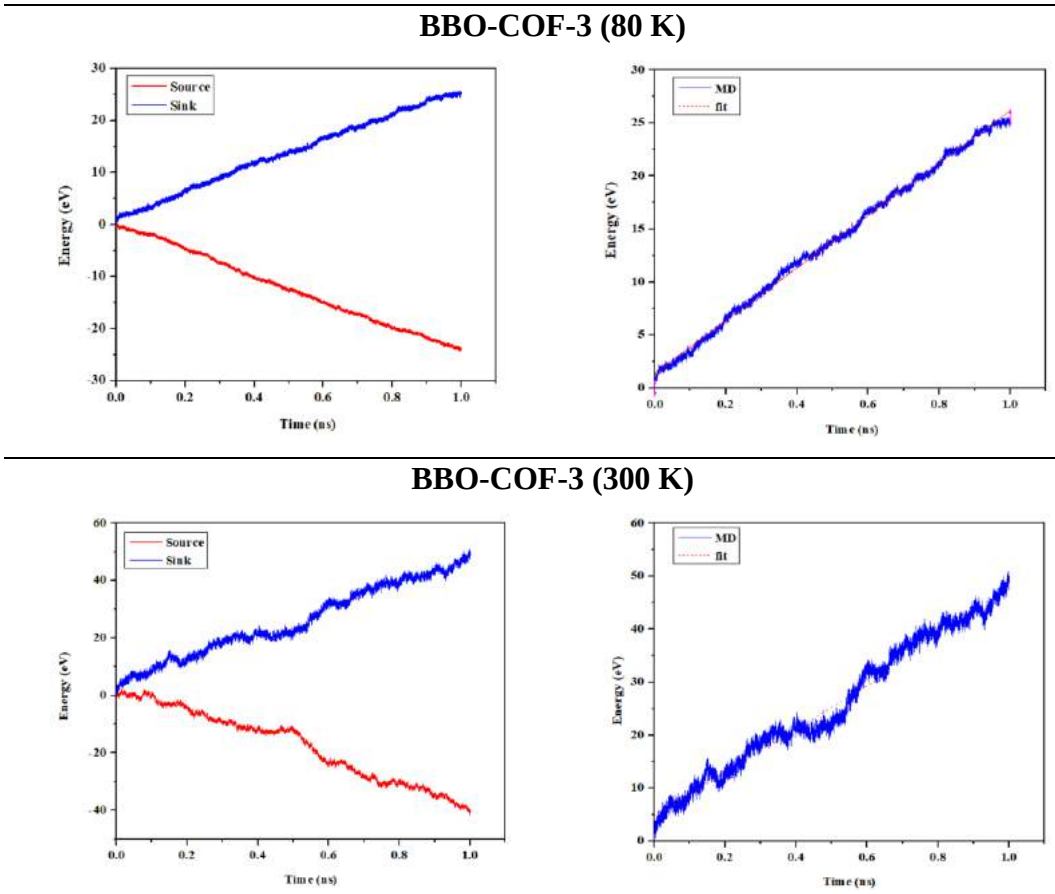

Figure 9.3. Energies (eV) accumulated in the source and sink (hot and cold thermostats, respectively) and the accumulated energy of the sink only with a linear fit as a function of time (ns) for 3×3 unit cells of BBO-COF-1, BBO-COF-2, and BBO-COF-3.

BBO-COF-1 (80 K)

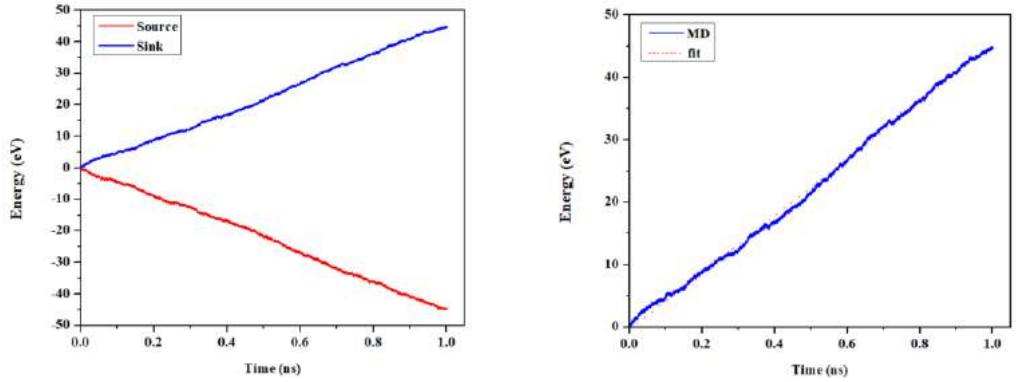

BBO-COF-1 (300 K)

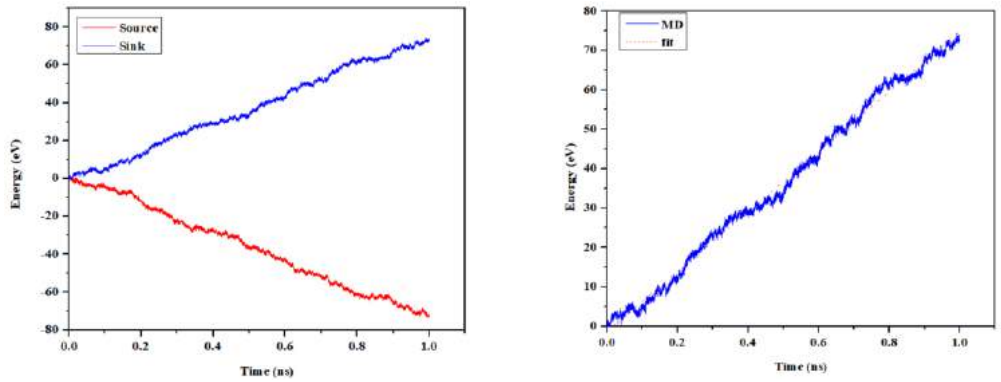

BBO-COF-2 (80 K)

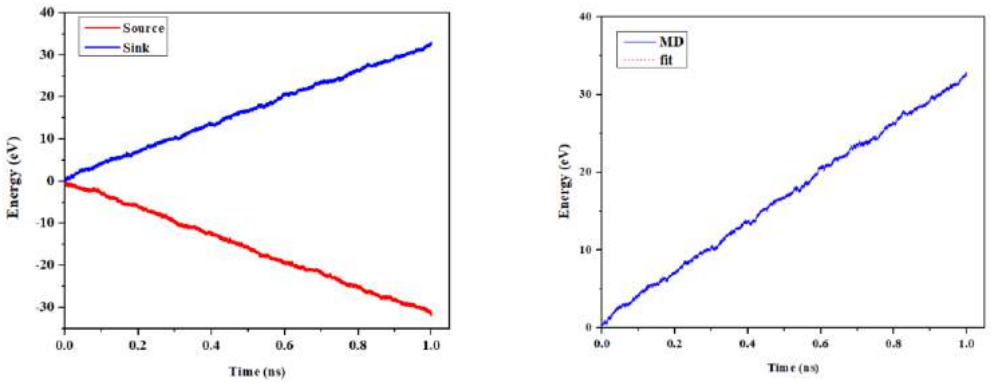

BBO-COF-2 (300 K)

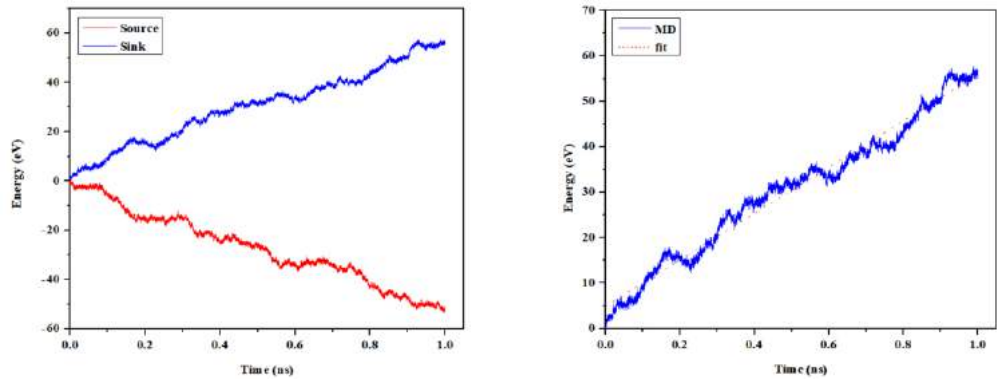

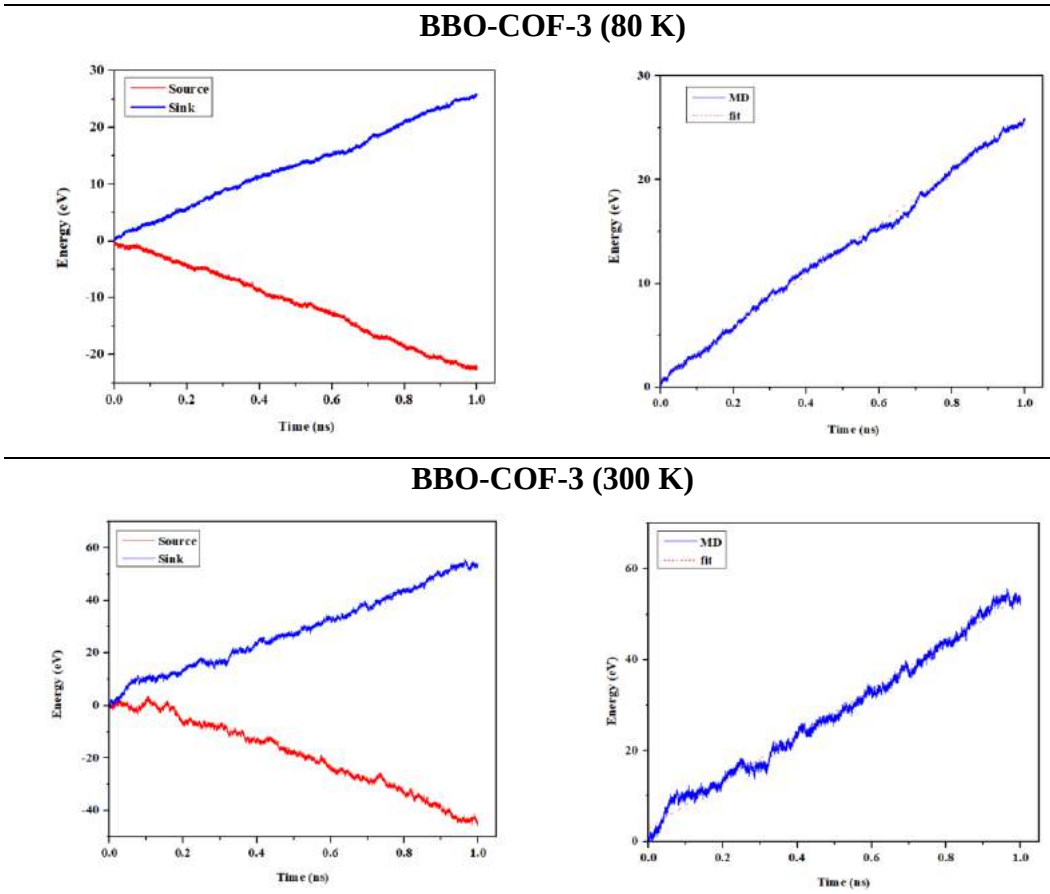

Figure 9.4. Energies (eV) accumulated in the source and sink (hot and cold thermostats, respectively) and the accumulated energy of the sink only with a linear fit as a function of time (ns) for 4×4 unit cells of BBO-COF-1, BBO-COF-2, and BBO-COF-3.